

國立交通大學
土木工程學系
碩士論文

反復扭剪夯實試驗之扭剪角度對
砂土密度及應力之影響

Change of Density and Stress in Sand Due to
Cyclic Torsional Shear Compaction

研 究 生：劉 政

指導教授：方永壽 博士

中 華 民 國 一 零 一 年 九 月

反復扭剪夯實試驗之扭剪角度對砂土密度及 應力之影響

Change of Density and Stress in Sand Due to Cyclic Torsional Shear
Compaction

研 究 生：劉 政

Student : Cheng Liu

指導教授：方永壽 博士 Advisor : Dr. Yung-Show Fang

國 立 交 通 大 學 土 木 工 程 學 系

碩士論文

A Thesis

Submitted to the Department of Civil Engineering

College of Engineering

National Chiao Tung University

in Partial Fulfillment of the Requirements

for the Degree of

Master of Engineering

in Civil Engineering

September, 2012

Hsinchu, Taiwan, Republic of China

中華民國一零一年九月

反復扭剪夯實試驗之扭剪角度對 砂土密度及應力之影響

研究生：劉 政

指導教授：方永壽 博士

國立交通大學土木工程學系碩士班

摘要

本論文以實驗方法探討反復扭轉剪力夯實造成砂質填土之地表沉陷量,土體內相對密度,垂直與水平應力及 CPT 試驗錐尖阻抗的改變。本研究使用自行設計建造之反復扭轉剪力夯實儀,施加靜態垂直應力及反復剪應力在土層表面。本研究以氣乾之渥太華砂為填土,填入 4 層高 150 mm 之疏鬆砂土。填土初始相對密度為 35.5 %,試體採用直徑為 300 mm 的鋼質圓盤施加垂直載重 9.2 kPa,然後施加反復剪應力,扭剪轉角分別為 $\pm 1^\circ$ 、 $\pm 3^\circ$ 、 $\pm 5^\circ$ 、 $\pm 7^\circ$ 及 $\pm 10^\circ$,反復扭剪作用為 20 次。本研究採用雷射測距儀量測土體表面沉陷量,埋設密度控制盒埋置於試體內部以量測土壤各點之相對密度,置於土壓力計試體內部以量測垂直及水平應力變化,以圓錐貫入儀測量土體各深度之錐尖阻抗值。根據實驗結果,本研究可獲得以下幾項結論:

1. 加載靜態垂直荷重於四層 150 mm 厚的試體表面,造成土體表面 15 至 22.3 mm 的沉陷量;平均表面沉陷量為 19 mm,沉陷量約為試體厚度 600 mm 的 3.2%。很明顯地,靜態垂直載重是夯實鬆砂有效的方法
2. 靜態垂直加載,砂土的相對密度從 35.5%增加大約至 62.0%,比緊砂要求的標準($D_r=70\%-85\%$)略低。
3. 與未夯實的鬆砂內的應力相比,靜態載重對於砂土中的垂直土壓力和側向土壓力的影響不顯著

4. 在垂直載重的作用後，上層之錐尖阻抗 q_c 有明顯的增加。受壓後正常化錐尖阻抗 $q_c / q_{c, \text{loose}}$ 由 1.0 增大至 4.6。
5. 在四層且每層為 150 mm 厚之土層的表面，經過以扭轉角度為 $\pm 10^\circ$ 扭轉 20 次後，平均表面沉陷量為 38.2 mm；由於反覆扭剪夯實造成額外的表面沉陷量約為 19.2 mm。很明顯地，反覆扭轉剪力是有效的夯實方法
6. 若靜態載重為 9.2 kPa，且試體厚度為 150 mm，以扭轉角度為 $\pm 5^\circ$ 扭剪 20 次後，土壤的相對密度可達 72% 至 84%。達成之土壤相對密度隨扭剪角度之加大而增加
7. 經過反覆扭剪夯實後，土層中的垂直土壓力沒有受到影響；然而，經過反覆扭剪夯實後，土層中側向土壓力增加從 27% 至 88%。
8. 在經過反覆扭剪夯實後，正常化的錐尖阻抗 $q_c / q_{c, \text{loose}}$ 從 4.6 增加至 9.0。實驗結果說明了反覆扭剪夯實明顯的增加土層中的錐尖阻抗。

關鍵字：土壤夯實；反復扭轉剪力；相對密度；砂；沉陷量；土壓力；錐尖阻抗

Change of Density and Stress in Sand Due to Cyclic Torsional Shear Compaction

Student: Cheng Liu

Advisor: Dr. Yung-Show Fang

Department of Civil Engineering

National Chiao Tung University

Abstract

This paper presents experimental data on the surface settlement change of relative density, vertical and horizontal stresses, and cone resistance in a cohesionless soil mass due to static vertical load and cyclic torsional shearing compaction. A new cyclic torsional shearing compactor was with a 300 mm-diameter circular shearing disc designed and constructed at National Chiao Tung University. Air-dry Ottawa sand was used as fill material. The initial relative density of the fill was 35.5 %. The static vertical load and cyclic torsional shearing were applied on the surface of the four 150 mm-thick lifts. Then cyclic shearing was applied with rotation angles of $\pm 1^\circ$, $\pm 3^\circ$, $\pm 5^\circ$, $\pm 7^\circ$ and $\pm 10^\circ$ for 20 cycles. Surface settlement of the fill was measured with a laser distance meter. Soil density cups were buried in the cohesionless specimen to monitor the relative density of soil. Soil pressure transducers were buried in the compacted fill to measure the change of the stress. A cone penetrometer used to measure cone resistance due to compaction. Based on the test results, the following conclusions were drawn.

1. With the vertical loading $q = 9.2$ kPa on the surface of the four 150 mm-thick soil lift, the induced surface settlements varied from 15.0 to 22.3 mm. The average surface settlement was 19.0 mm, which was about 3.2% of the soil thickness. Static vertical loading is an effective method to compact the loose fill.
2. Static vertical loading represents the dead load of the cyclic torsional shear compactor. After the application of $q = 9.2$ kPa, on the average, the relative density of soil increased from 35.5% to about 62%, which was less than the target

value $D_r = 70-85\%$ for dense sand.

3. As compared with that for uncompacted loose sand, the effects of static vertical loading on the vertical and horizontal earth pressure, in the compressed soil mass were not significantly.
4. The application of static vertical loading $q = 9.2$ kPa significantly increased the cone resistance of the compressed fill. The normalized cone resistance $q_c / q_{c, \text{loose}}$ increased from 1.0 to 4.6 due to static compression.
5. After 20 cycles of torsional shearing with the rotation angle of $\theta = \pm 10^\circ$ on the surface of the four 150 mm-thick lifts, the average surface settlement was 38.2 mm (volumetric strain = 6.4%). The extra surface settlement due to the torsional shearing compaction was about 19.2 mm. Cyclic torsional shearing compaction (static plus cyclic loads) is an effective method to densify loose soil.
6. With static load $q = 9.2$ kPa and the lift thickness of 150 mm, after 20 cycles of torsional shearing with angle θ of $\pm 5^\circ$, the relative density achieved was 72 to 84%. The compacted relative density increased with increasing θ angle.
7. The vertical earth pressure in the fill was not influenced by the cyclic shearing compaction. However, after cyclic shearing compaction, the horizontal earth pressure in the compacted fill increased from 27% to 88%.
8. After cyclic torsional shear compaction, the normalized cone resistance $q_c / q_{c, \text{loose}}$ increased from 4.6 to about 9.0. Test results showed the cyclic shearing compaction effects on the cone resistance in the fill was quite obviously.

Keywords: Cyclic torsional shearing; Relative density; Sand; Settlement; Compaction; Earth pressure; Cone resistance

Acknowledgements

The author wishes to give his sincere appreciation to his advisor, Dr. Yung-Show Fang for his enthusiastic advice and continuous encouragement in the past two years. If there is not the guidance from him, the thesis can not be accomplished.

Very special thanks are extended to Dr. Yi-Wen Pan, Dr. Jhih-Jhong Liao, Dr. An-Bin Huang, Dr. Shen-Yu Shan and Dr. Chih-Ping Lin for their teaching and valuable suggestions. In addition, the author also felt a great gratitude to the members of his supervisory committee, Dr. Huei-Wen Chang and Dr. Tao-Wei Feng for their suggestions and discussions.

The author must extend his gratitude to Dr. Tsang-Jiang Chen, Mr. Guan-Yu Chen, Mr. Ting-Yuen Huang, Mr. Min-Yi Huang, for their support and encouragement. Appreciation is extended to all my friends and classmates, especially for Mr. Yu-An Huang, Mr. Jia-Hao Dai, Yi-Chang Li, Mr. Cheng-You Li, Mr. Shiang-Ming Huang and Mr. Jhong-Yuan Huang for their encouragement and assistance.

Finally, the author would dedicate this thesis to his girlfriend, parents, brother and sister for their continuing encouragement and moral support.

Table of Contents

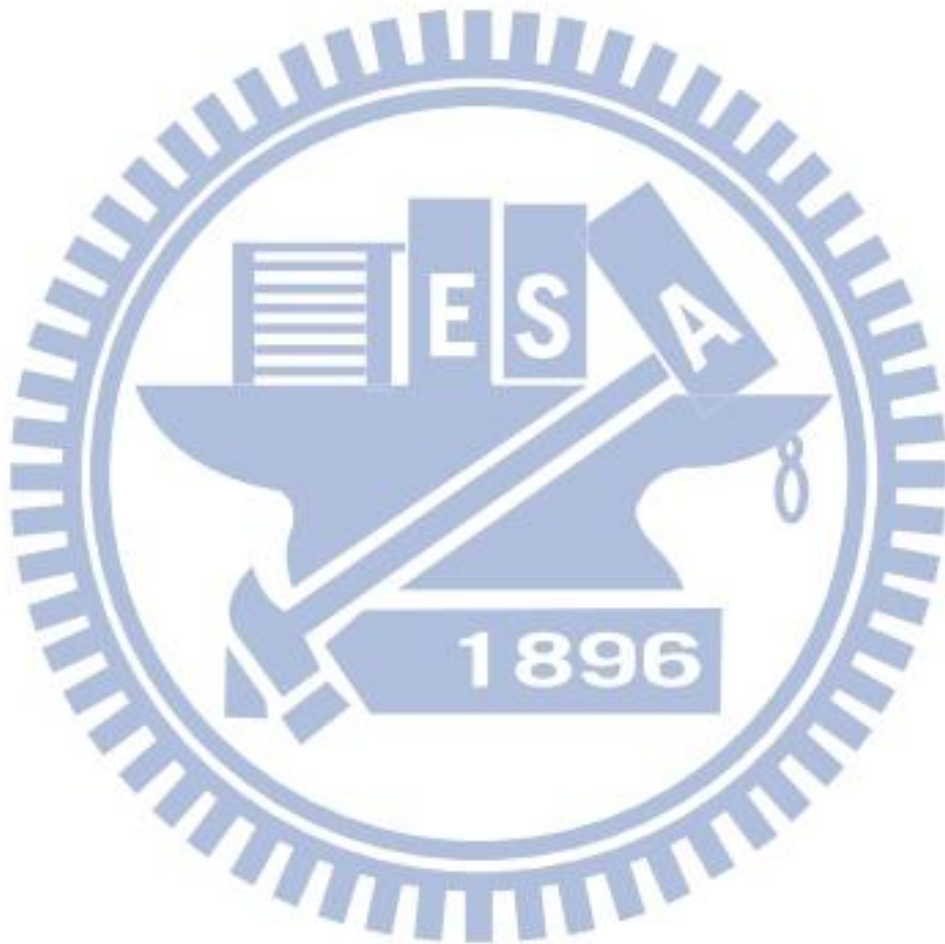
Abstract (in Chinese)	i
Abstract	iii
Acknowledgements	v
Table of Contents	vi
List of Tables	ix
List of Figures	x
List of Symbol	xvi
Chapter 1 Introduction	1
1.1 Objectives of Study	1
1.2 Research Outline	2
1.3 Organization of Thesis	3
Chapter 2 Literature Review	4
2.1 Soil Improvement with Densification	4
2.1.1 Densification Techniques	5
2.1.2 Soil Densification with Vibratory Compactor	5
2.2 Earth Pressure At-Rest	6
2.2.1 Coefficient of Earth Pressure At-Rest	6
2.2.2 Jaky's Formula	7
2.2.3 Study of Mayne and Kulhawy	8
2.3 Effects of Soil Compaction on Earth Pressure	9
2.3.1 Study of Duncan and Seed	9
2.3.2 Study of Chen and Fang	10
2.4 Cyclic Simple Shear Test	11
2.4.1 Study of Youd	12
2.4.2 Study of Hsu and Vucetic	12
2.5 Cyclic Torsional Simple Shear Test	13

2.5.1 Study of Ishibashi et al.....	14
2.6 Densification with Cyclic Torsional Shearing	14
2.6.1 Study of Yang.....	14
2.6.2 Study of Ren	15
2.6.3 Study of Chen	15
2.7 Assessment of Relative Density.....	16
2.8 Cone Penetration Test	17
2.8.1 Study of Jamiolkowski et al.	17
Chapter 3 Experimental Apparatus	19
3.1 Soil Bin	19
3.2 Soil Pressure transducer.....	20
3.3 Cyclic Torsional Shear Compactor	20
3.4 Cone Penetration Facility.....	22
3.5 Earth-Pressure Data Acquisition System	23
Chapter 4 Soil Characteristics	24
4.1 Soil Properties.....	24
4.2 Lubricated Side Wall Friction	25
4.3 Control of Soil Density	25
4.3.1 Air-Pluviation of Loose Ottawa Sand	25
4.3.2 Measurement of Soil Density.....	26
Chapter 5 Testing Procedure	28
5.1 Specimen Preparation	28
5.2 Application of Vertical Static Load	29
5.3 Application of Cyclic Torsional Shearing.....	29
5.4 Cone Penetration Test	30
Chapter 6 Test Results	32
6.1 Static Load Test.....	32
6.1.1 Settlement Due to Static Load	33

6.1.2 Density Change Due to Static Load.....	33
6.1.3 Stress Change Due to Static Load.....	34
6.1.4 Cone Resistance Change Due to Static Load.....	35
6.2 Applied Cyclic Torsional Shearing	35
6.3 Cyclic Torsional Shear Test	36
6.3.1 Surface Settlement Change Due to Cyclic Torsional Shearing.....	36
6.3.2 Density Change Due to Cyclic Torsional Shearing	37
6.3.3 Stress Change Due to Cyclic Torsional Shearing	38
6.3.4 Cone Resistance Change Due to Cyclic Torsional Shearing	39
Chapter 7 Conclusions.....	41
References.....	43
Tables.....	48
Figures.....	51
Appendix A: Calibration of Soil Pressure Transducer	184

List of Tables

Table2.1. Qualitative description of granular soil deposits.....	48
Table3.1. Characteristics of normal loading discs	49
Table4.1. Properties of Ottawa Sand.....	50



List of Figures

Fig. 2.1. Arrangement of uniform spheres	51
Fig. 2.2. Unit weight vs. depth relation for vibratory roller compaction	52
Fig. 2.3. Compacted unit weight profiles for 8-ft lift heights for 2, 5, 15, and 45 vibratory roller passes.....	53
Fig. 2.4. Approximate method for determining lift height required to achieve a minimum compacted relative density of 75% with five roller passes using data for a large lift height.....	54
Fig. 2.5. Development of in-situ stresses	55
Fig. 2.6. Principal Stresses on a Soil Element	56
Fig. 2.7. Jaky's Formulation of the Relationship between K_o on OC and Mobilized in OAB	57
Fig. 2.8. Simplified stress history of soil under K_o conditions.....	58
Fig. 2.9. Relationship between K_{onc} and $\sin \alpha$ for cohesionless soils	59
Fig. 2.10. Basic components of hysteretic K_o -loading/unloading model.....	60
Fig. 2.11. Comparison between Final Pressure Distributions Based on Incremental Analysis and Hand Solution.....	61
Fig. 2.12. Distribution of Horizontal Earth Pressure after Compaction	62
Fig. 2.13. Stress path of a soil element under compaction.....	63
Fig. 2.14. Horizontal Earth Pressure Estimated with Various Methods after Compaction	64
Fig. 2.15. NGI cyclic simple shear apparatus	65
Fig. 2.16. Stress conditions of a soil specimen cyclic horizontal shear stress	66
Fig. 2.17. Void ratio versus cyclic displacement for densification of a sand with successive cycles of shear	67
Fig. 2.18. Sketch of typical results of cyclic simple shear strain-controlled tests with definitions of volumetric cyclic threshold strain	68
Fig. 2.19. Torsional simple shear device.....	69

Fig. 2.20. Variation of cyclic volumetric strain as a function of cyclic shear strain.....	70
Fig. 2.21. Change of relative density with one-way and cyclic disc shearing versus normal stress.....	71
Fig. 2.22. Change of relative density due to cyclic disc shear with number of cycles	72
Fig. 2.23. Change of relative density due to cyclic disc shear at different depths with high of layer	73
Fig. 2.24. Surface settlement due to static vertical load at $N = 0$ to $N = 40$	74
Fig. 2.25. Distribution of relative density due to cyclic torsional shearing	75
Fig. 2.26. Distribution of relative density in lift 1 to 4	76
Fig. 2.27. Relationship between Relative density and q_c	77
Fig. 3.1. NCTU non-yielding model retaining wall and soil bin	78
Fig. 3.2. Soil-Pressure Transducer (Kyowa BE-2KCM17)	79
Fig. 3.3. Dimensions of cyclic torsional shear compactor	80
Fig. 3.4. Cyclic torsional shear compactor	81
Fig. 3.5. Bottom of shearing disc with radial fins.....	82
Fig. 3.6. Dimensions of a radial fin	83
Fig. 3.7. Bottom of shearing disc with SAFETY WALK	84
Fig. 3.8. Dimensions of normal loading discs	85
Fig. 3.9. Dimensions of torque loading frame	86
Fig. 3.10. Torque loading frame.....	87
Fig. 3.11. Dimensions of torque wrench	88
Fig. 3.12. Dimensions of digital torque wrench.....	89
Fig. 3.13. Torque wrench are installed on the cyclic torsional loading frame	90
Fig. 3.14. Cone penetration facility of CYCU	91
Fig. 3.15. Data acquisition system	92
Fig. 4.1. Grain size distribution of Ottawa sand	93
Fig. 4.2. Lubrication layer on the side wall	94
Fig. 4.3. Variation of friction Angle with normal stress	95


Fig. 4.4. Soil hopper.....	96
Fig. 4.5. Pluviation of Ottawa sand into soil bin	97
Fig. 4.6. Relationship among slot opening, drop height, and relative density	98
Fig. 4.7. Dimensions of soil density cup.....	99
Fig. 4.8. Soil density cup	100
Fig. 4.9. Soil density cups buried at different elevations	101
Fig. 4.10. Arrangement of soil density cups at same elevation.....	102
Fig. 4.11. Measurement of soil mass in density cup	103
Fig. 4.12. Distribution of relative density with depth	104
Fig. 5.1. Soil storage	105
Fig. 5.2. Sand hopper and electrical scale.....	106
Fig. 5.3. Sand hopper lifted by overhead crane	107
Fig. 5.4. Air-pluviation of Ottawa sand into soil bin	108
Fig. 5.5. Portable hanging ladders and bridge board hanging on side wall	109
Fig. 5.6. Level soil surface with a brush	110
Fig. 5.7. Check density cup horizontal with a bubble level.....	111
Fig. 5.8. Soil density cup and soil-pressure transducer placed on soil surface.....	112
Fig. 5.9. Soil density cups and soil-pressure transducer buried at different elevations ...	113
Fig. 5.10. Grid points on soil surface	114
Fig. 5.11. Hoist of CTSC into the soil bin	115
Fig. 5.12. 5×5 and 4×4 loading formations of disc shearing location	116
Fig. 5.13. Apply vertical static load on loose sand	117
Fig. 5.14. Fixed light dot from laser distance meter	118
Fig. 5.15. Apply cyclic torsional shear on loose fill	119
Fig. 5.16. Shear disc at initial position $\theta = 0^\circ$	120
Fig. 5.17. Shear disc rotated to $\theta = +5^\circ$	121
Fig. 5.18. Shear disc rotated to $\theta = -5^\circ$	122
Fig. 5.19. Application of cyclic torsional shear to loose sand	123

Fig. 5.20. Compacted soil surface after 4×4 formation of cyclic torsional shear at N = 5	124
Fig. 5.21. Compacted soil surface after 5×5 formation of cyclic torsional shear at N = 10	125
Fig. 5.22. Compacted soil surface after 4×4 formation of cyclic torsional shear at N = 20	126
Fig. 5.23. Soil density cups dug out of compacted soil mass	127
Fig. 5.24. Scraping of soils toward edge of density cup with a spatula	128
Fig. 5.25. Brush away soil particles from base plate of density cup	129
Fig. 5.26. Arrangement of cone penetration location	130
Fig. 5.27. Steel beam on top of soil bin for CPT test	131
Fig. 5.28. Electric motor and movable plate fixed to the steel beam by the screws	132
Fig. 5.29. Connect cone penetrometer with electric motor	133
Fig. 5.30. Cone penetrometer on soil surface	134
Fig. 6.1. Settlement measurement with laser distance meter	135
Fig. 6.2. Surface settlement due to static vertical loading	136
Fig. 6.3. Distribution of relative density due to static vertical loading	137
Fig. 6.4. Distribution of relative density due to static vertical loading	138
Fig. 6.5. Locations of SPT to measure distribution of earth pressure	139
Fig. 6.6. Distribution of vertical earth pressure with depth	140
Fig. 6.7. Distribution of horizontal earth pressure with depth	141
Fig. 6.8. Distribution of cone resistance in soil mass	142
Fig. 6.9. Distribution of relative density after static load	143
Fig. 6.10. Digital torque wrench	144
Fig. 6.11. Torque with number of cyclic for $\theta = \pm 1^\circ, \pm 3^\circ, \pm 5^\circ, \pm 7^\circ$ and $\pm 10^\circ$	145
Fig. 6.12. Variation of torque with shearing angle	146
Fig. 6.13. Determine the maximum torsional shear stress at the edge of the shearing disc due to the applied torque	147

Fig. 6.14. Maximum shear stress with shearing angle	148
Fig. 6.15. Settlement after cyclic torsional shearing.....	149
Fig. 6.16. Settlement after cyclic torsional shearing.....	150
Fig. 6.17. Distribution of relative density due to cyclic torsional shearing at $\theta = \pm 1^\circ$	151
Fig. 6.18. Distribution of relative density due to cyclic torsional shearing at $\theta = \pm 3^\circ$	152
Fig. 6.19. Distribution of relative density due to cyclic torsional shearing at $\theta = \pm 5^\circ$	153
Fig. 6.20. Distribution of relative density due to cyclic torsional shearing at $\theta = \pm 7^\circ$	154
Fig. 6.21. Distribution of relative density due to cyclic torsional shearing at $\theta = \pm 10^\circ$..	155
Fig. 6.22. Distribution of relative density after cyclic torsional shearing.....	156
Fig. 6.23. Relative density with shearing angle	157
Fig. 6.24. Distribution of vertical earth pressure after cyclic torsional shear at $\theta = \pm 1^\circ$..	158
Fig. 6.25. Distribution of vertical earth pressure after cyclic torsional shear at $\theta = \pm 3^\circ$..	159
Fig. 6.26. Distribution of vertical earth pressure after cyclic torsional shear at $\theta = \pm 5^\circ$..	160
Fig. 6.27. Distribution of vertical earth pressure after cyclic torsional shear at $\theta = \pm 7^\circ$..	161
Fig. 6.28. Distribution of vertical earth pressure after cyclic torsional shear at $\theta = \pm 10^\circ$	162
Fig. 6.29. Distribution of vertical stress after static loading and cyclic torsional shearing	163
Fig. 6.30. Normalized vertical stress after cyclic torsional shearing	164
Fig. 6.31. Distribution of horizontal earth pressure after cyclic torsional shear at $\theta = \pm 1^\circ$	165
Fig. 6.32. Distribution of horizontal earth pressure after cyclic torsional shear at $\theta = \pm 3^\circ$	166
Fig. 6.33. Distribution of horizontal earth pressure after cyclic torsional shear at $\theta = \pm 5^\circ$	167
Fig. 6.34. Distribution of horizontal earth pressure after cyclic torsional shear at $\theta = \pm 7^\circ$	168
Fig. 6.35. Distribution of horizontal earth pressure after cyclic torsional shear at $\theta = \pm 10^\circ$	

.....	169
Fig. 6.36. Distribution of horizontal stress after static loading and cyclic torsional shearing	170
Fig. 6.37. Normalized horizontal stress after cyclic torsional shearing	171
Fig. 6.38. Distribution of cone resistance after cyclic torsional shear at $\theta = \pm 1^\circ$	172
Fig. 6.39. Distribution of cone resistance after cyclic torsional shear at $\theta = \pm 3^\circ$	173
Fig. 6.40. Distribution of cone resistance after cyclic torsional shear at $\theta = \pm 5^\circ$	174
Fig. 6.41. Distribution of cone resistance after cyclic torsional shear at $\theta = \pm 7^\circ$	175
Fig. 6.42. Distribution of cone resistance after cyclic torsional shear at $\theta = \pm 10^\circ$	176
Fig. 6.43. Distribution of cone resistance after cyclic torsional shearing	177
Fig. 6.44. Distribution of $q_c / q_{c, \text{loose}}$ after cyclic torsional shearing	178
Fig. 6.45. Distribution of relative density after cyclic torsional shear at $\theta = \pm 1^\circ$	179
Fig. 6.46. Distribution of relative density after cyclic torsional shear at $\theta = \pm 3^\circ$	180
Fig. 6.47. Distribution of relative density after cyclic torsional shear at $\theta = \pm 5^\circ$	181
Fig. 6.48. Distribution of relative density after cyclic torsional shear at $\theta = \pm 7^\circ$	182
Fig. 6.49. Distribution of relative density after cyclic torsional shearing at $\theta = \pm 10^\circ$	183

List of Symbols



C_u	= Uniformity Coefficient
D_r	= Relative Density
D_{10}	= Diameter of Ottawa Sand whose Percent finer is 10%
D_{60}	= Diameter of Ottawa Sand whose Percent finer is 60%
e_{max}	= Maximum Void Ratio of Soil
e_{min}	= Minimum Void Ratio of Soil
f	= Frequency
G_s	= Specific Gravity
N	= Number of Cycle
T	= Torque
z	= Depth from Surface
σ	= Normal Stress
γ	= Unit Weight of Soil
τ_{max}	= Maximum Torsional Shear Stress
θ	= Disc Rotation Angle
ϕ	= Angle of Internal Friction of Soil
δ_i	= Angle of Interface Friction
δ_{sw}	= Angle of Side-Wall Friction
δ_w	= Angle of Wall Friction

Chapter 1

INTRODUCTION

In the construction of highway embankments, earth dams, and many other engineering structures, engineers are required to compact loose soils to increase their densities. The objective of the compaction operation is to improve the engineering properties of soil such as increasing shear strength, bearing capacity, and reducing permeability and settlement. Various techniques had been used to increase the bearing capacity of shallow foundations, to increase the factor of safety against possible slope failure of embankments and earth dams, and to reduce the shrinkage and swelling of soils.

1.1 Objectives of Study

Commonly used methods for soil improvement, included compaction, vibroflotation, dynamic compaction, compaction sand pile, blasting method, vibro rod, and stone columns. Most of these engineering methods may produce significant noise and vibration during construction, thus not suitable for use in the metropolitan area. In this study, the cyclic torsional shear compaction is introduced as an alternative construction method. With this compaction method, the relative density of sand could increase from 35.5% up 85%. This method produces low noise and no low vibration. The purpose of this study is to investigate the change of soil density, change of stress, and increase of CPT cone resistance in the soil mass due to compaction.

1.2 Research Outline

Air-dry Ottawa sand was placed in four lifts and each lift was compacted to achieve a relative density of 75%. Each compacted lift was 0.15 m thick. The instrumented nonyielding wall facility at National Chiao Tung University in Taiwan was used to investigate the effects of vibratory compaction on the change of stresses at the soil-wall interface.

Compaction is a particular kind of soil stabilization and one of the oldest methods for improving existing soil or man-placed fills. The objective of the compaction operation is to improve the engineering properties of soil such as increasing the fill's bearing capacity or reducing settlement. For granular soils, achieving a relative density of 70-75% is generally recommended (US Navy 1982). Hand tampers and vibratory compaction equipment are commonly used to compact the fills.

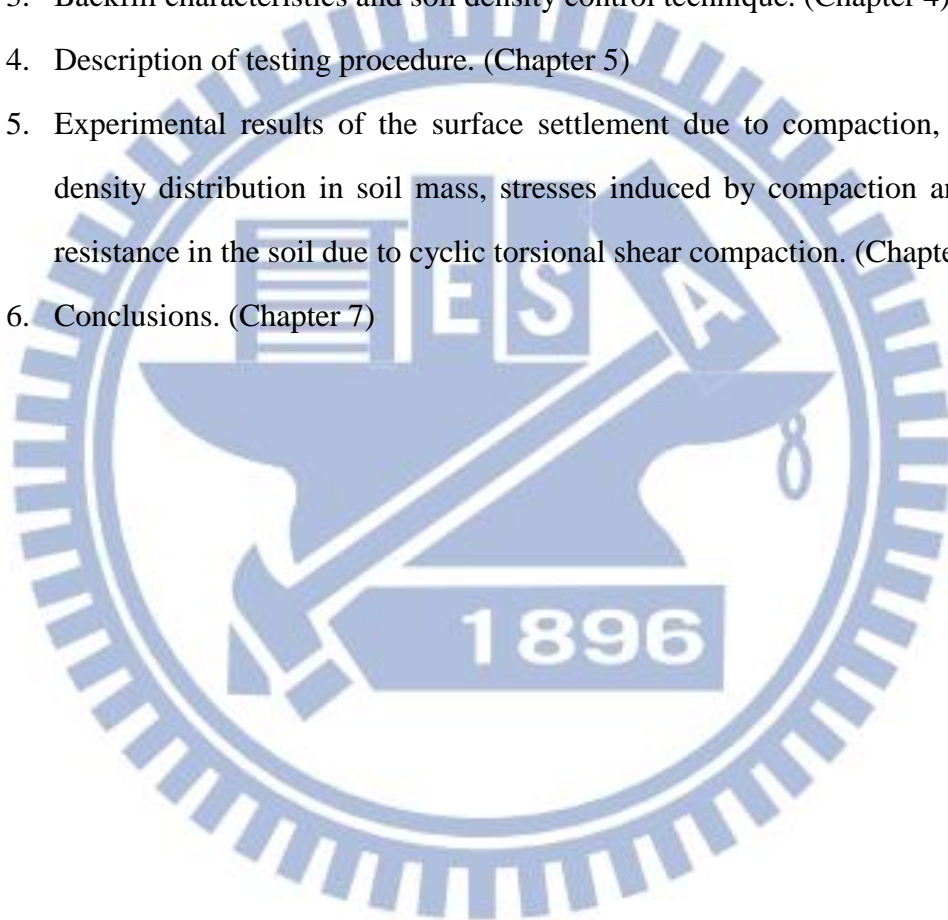
Conventionally, the earth pressure at rest is evaluated by the Jaky equation (Jaky 1944). Based on their laboratory tests, Sherif et al. (1984) found that the Jaky's equation ($K_o = 1 - \sin \phi$) gives good results when the backfill is loose sand, where K_o = coefficient of earth pressure at rest and ϕ = internal friction angle of soil. When the backfill behind the wall is either compacted or vibrated to increase its density, the magnitude of at-rest stresses increases due to densification.

This paper presents experimental data associated with the surface settlement, relative density, stresses, and cone resistance acting on a nonyielding wall at different stages of soil filling and compaction. Based on the experimental data, a possible mechanism of soil behavior under cyclic torsional shearing compacting is proposed. All of the experiments mentioned in this paper were conducted in the National Chiao Tung University (NCTU) nonyielding retaining wall facility, which is briefly described in the following section.

1.3 Organization of Thesis

This paper thesis divided into the following parts:

1. Review of past investigations regarding cyclic torsional shear compaction of cohesionless soils. (Chapter 2)
2. Description of the National Chiao Tung University non-yielding soil bin, cyclic torsional shear compactor and cone penetration device. (Chapter 3)
3. Backfill characteristics and soil density control technique. (Chapter 4)
4. Description of testing procedure. (Chapter 5)
5. Experimental results of the surface settlement due to compaction, relative density distribution in soil mass, stresses induced by compaction and cone resistance in the soil due to cyclic torsional shear compaction. (Chapter 6)
6. Conclusions. (Chapter 7)



Chapter 2

Literature Review

Das (2010) stated that the soil at a construction site may not always be totally suitable for supporting structures such as buildings, bridges, highways, and dams. For example, in granular soil deposits, the in situ soil may be very loose and perform a large elastic settlement under loading. In such a case, the soil needs to be densified to increase its unit weight and thus its shear strength.

Sometimes the top layers of soil are undesirable and must be removed and replaced with better soils on which the structural foundation can be built. The soil used as fill should be well compacted to sustain the desired structural load. Compacted fills may also be required in low-lying areas to raise the ground elevation for construction of the foundation.

To improve its engineering properties, contractors are generally required to compact the loose soils to increase their unit weights and reducing settlements. Previous studies associated with the compaction-induced effects such as the change of soil density, the change of stresses in the soil mass and mechanism of soils under compaction are discussed in this chapter.

2.1 Soil Improvement with Densification

Kramer (1996) defined the common soil improvement techniques to mitigate seismic hazards, soil improvement method were divided into four categories including (1) densification techniques (vibrofloatation, vibro rod, dynamic compaction, blasting,

and compaction grouting); (2) reinforcement techniques (stone columns, compaction piles, and drilled inclusions); (3) grouting and mixing techniques (permeation grouting, intrusion grouting, soil mixing, and jet grouting), and (4) drainage techniques. In this thesis, only the densification of cohesionless soil were discussed.

2.1.1 Densification Techniques

Fig. 2.1 shows two of the many possible ways that a system of equal-sized spheres can be packed. Looser systems than the simple cubic packing can be obtained by carefully constructing arches within the packing, but the simple cubic packing in Fig.2.1 (a) is the loosest of the stable arrangements. The dense packings in Fig.2.1 (b) represent the densest possible state for such a system. A dense packing of soil spheres can be reached by soil densification techniques.

2.1.2 Soil Densification with Vibratory Compactor

D'Appolonia et al. (1969) proposed the vibratory rollers are particularly useful for compacting granular soils. Fig. 2.2 shows the effects of compaction of a 8-ft lift dune sand after five passes by a vibratory roller. The low unit weight that remains in the uppermost zone is due to vibration and lack of confinement in sand. Fig. 2.3 shows the compacted unit-weight profiles for the same dune sand after 2, 5, 15, and 45 roller passes. For field compaction work, the specification requires that the granular soil be compacted to a certain minimum relative density at all depths. Determination of the height of each lift depends on the type of roller and the economic number of passes. The method for determination of the lift height is shown in Fig. 2.4. For soils at all depths to reach a minimum relative density $D_r = 75\%$, the lift thickness should be controlled to be less than 18 inch.

2.2 Earth Pressure At-Rest

2.2.1 Coefficient of Earth Pressure At-Rest

In Fig. 2.5(a), a soil element A located at depth z is compressed by the overburden pressure $\sigma = \gamma z$. During the formation of the deposit, the element A is consolidated under the pressure σ_v . The vertical stress induces a lateral deformation against surrounding soils due to the Poisson's ratio effect. Over the geological period, the horizontal strain is kept to be zero and the surrounding soil would develop a lateral stress to counteract the lateral deformation. A stable stress state will develop that the principal stresses acts σ_1 and σ_3 on the vertical and horizontal planes, as shown in Fig. 2.5(b).

The soil in a state of static equilibrium condition is commonly termed as the K_o condition. Donath (1891) defined the ratio of the horizontal stress σ_h to vertical stress σ_v as the coefficient of earth pressure at-rest, K_o , or

$$K_o = \frac{\sigma_h}{\sigma_v} \quad (2.1)$$

Since $\sigma_v = \gamma z$, then $\sigma_h = K_o \gamma z$, where γ is the unit weight of soil.

For an isotropic soil element shown in Fig. 2.6, if the soil behaved as an ideal elastic material, based on the mechanics of materials, the lateral strain ε_y can be expressed as:

$$\varepsilon_y = \frac{\sigma_y}{E} - \frac{\nu}{E}(\sigma_x + \sigma_z) \quad (2.2)$$

or

$$\varepsilon_h = \frac{\sigma_h}{E} - \frac{\nu}{E}(\sigma_h + \sigma_v) \quad (2.3)$$

where E is the elastic modulus and ν is the Poisson's ratio of the soil.

Base on the definition of the at-rest condition, the lateral strain would be zero ($\varepsilon_h = 0$) under the application of stress state and the $\sigma_h = K_o \sigma_v$. Then the

Eq. 2.3 can be written as:

$$\varepsilon_h = \frac{1}{E} (K_o \sigma_v - \nu K_o \sigma_v - \nu \sigma_v) = 0 \quad (2.4)$$

$$K_o = \frac{\nu}{1 - \nu} \quad (2.5)$$

It should be mentioned that Eq. 2.5 is applicable for the isotropic and elastic materials only. However, the behavior of soil element is more complex and far from these assumptions. It is evident that the relationship between K_o and elastic parameter, ν Eq. 2.5 is not practical for predicting in-situ horizontal stress.

2.2.2 Jaky's Formula

Several scholars attempted to set up a theoretical relationship between the strength properties of a soil and K_o . The empirical relationship to estimate K_o of coarse-grained soil is discussed in the following section.

Mesri and Hayat (1993) reported that Jaky (1944) established a relationship between K_o and maximum effective angle of internal friction ϕ by analyzing a talus of granular soil freestanding at the angle of repose. Jaky (1944) supposed that the angle of repose is analogous to the angle of internal friction ϕ . This is reasonable for a sedimentary, normally consolidated material. Jaky (1944) reasoned that the sand cone OAD in Fig. 2.7 is in a state of equilibrium and its surface and inner points are motionless. The horizontal pressure acting on the vertical plane OC is the earth pressure at-rest. Slide planes exist in the inclined sand mass. However, as OC is a line of symmetry, shear stresses can not develop on it. Hence OC is a principal stress trajectory. Based on the equations of equilibrium, Jaky expressed the coefficient of earth pressure at-rest K_o with the angle of internal friction,

$$K_o = (1 - \sin \phi) \frac{1 + \frac{2}{3} \sin \phi}{1 + \sin \phi} \quad (2.6)$$

In 1948, Jaky presented a modified simple expression given by Eq. 2.7.

$$K_o = 1 - \sin \phi \quad (2.7)$$

Mayne and Kulhawy (1982) reported that, the approximate theoretical relationship for K_o for normally consolidated soils supposed by Jaky appears valid for cohesionless soils. Using Jaky's equation to estimate the in-situ lateral earth pressure is reliable for most engineering purposes.

2.2.3 Study of Mayne and Kulhawy

Mayne and Kulhawy (1982) investigated the relationship between K_o and (over-consolidation ratio)OCR for the soil with primary loading–unloading–reloading conditions. They considered the simplified stress history depicted in Fig. 2.8 for a homogeneous soil deposit with horizontal ground surface. Stress path OA represents virgin loading of the soil deposit, associated with sedimentation and normally–consolidated conditions. As represented by Fig. 2.8, the at-rest coefficient remains constant during virgin compression (K_{onc}). Any reduction in the effective overburden stress results in overconsolidation of the soil, represented by path ABC. As shown in Fig. 2.8, it is obviously that the overconsolidation ratio, OCR which is defined as $\sigma_{v,max} / \sigma_v$ has a pronounced effect on the value of K_o . If loading is reapplied, the reload relationship subsequently will follow a path similar to CD in Fig. 2.8. Subsequent unloading and reloading is likely to cause stress path to occur within the loop ABCDA.

To evaluate the behavior of horizontal stresses during vertical loading–unloading–reloading conditions. Mayne and Kulhawy (1982) reviewed laboratory data of 171 different soils tested and reported by many researchers from various sources published in the geotechnical literature. Based on the method of

statistical analysis as indicated in Fig. 2.9, Mayne and Kulhawy (1982) concluded the approximate theoretical relationship for K_{onc} of normal consolidated soil introduced by Jaky (1944) is in good agreement with these data. Numerous investigators have suggested that K_{onc} may correlate with liquid limits, plasticity index, clay fraction, uniformity coefficient, void ratio, or other index properties of the soil. However, on the basis of findings, the data collected did not confirm any of these relationships. Mayne and Kulhawy (1982) deduced that only the effective stress friction angle, and prior stress history (OCR and OCR_{max}) are needed to predict approximate values of K_o .

2.3 Effects of Soil Compaction on Earth Pressure

Compaction of a loose soil can produce a stiff, low settlement-free and less permeable mass. It is usually accomplished by mechanical means that cause the density of soil to increase. At the same time the air voids were reduced.

Several theories and analytical methods had been proposed to analyze the residual lateral earth pressures induced by soil compaction. Most of these theories introduced the idea that compaction represented a form of over consolidation, where stresses resulting from a temporary or transient loading condition were retained following the removal of this load.

2.3.1 Study of Duncan and Seed

Duncan and Seed (1986) presented an analytical procedure for evaluation of peak and residual compaction-induced stresses either in the free field or adjacent to vertical, non-deflecting soil-structure interfaces. This procedure employs a hysteretic K_o -loading model shown in Fig. 2.10. The model is adapted to incremental analytical methods for the evaluation of peak and residual earth pressures resulting from the

placement and compaction of soil. When the surcharge is applied on the soil surface, it will increase the vertical stress and the horizontal stress. In Fig. 2.10, as the virgin loading is applied on the soil, both σ_v and σ_h increase along the K_o -line ($K_o = 1 - \sin\phi$). Nevertheless, when the surcharge is removed, σ_v and σ_h would decrease along the virgin unloading path. As virgin reloading was applied again, the increment of earth pressure is less than that induced by the first virgin loading.

Seed and Duncan (1983) brought up a simple hand calculation procedure which results in good agreement with the incremental procedure described above. In Fig. 2.11, it is apparent the simple hand solution has a good agreement with the incremental procedure.

2.3.2 Study of Chen and Fang

The distribution of horizontal earth pressure against the nonyielding wall after the compaction of soil Lift 1 to Lift 5 is shown in Fig. 2.12 (a) to (e). Each compacted lift was 0.3 m thick after compaction. The variation of lateral earth pressure was monitored by the soil pressure transducers mounted on the wall. After vibratory compaction, it is clear in Fig. 2.12 (a) to (e) that an extra horizontal normal stress Δh_{ci} was induced by compaction. The lateral stress distribution measured near the top of the backfill was almost identical to the passive earth pressure estimated with Rankine theory. From Fig. 2.12 (a) to (e), it is interesting to note that the compaction-influenced zone rose with the rising compaction surface. It was also interesting to note in Fig. 2.12(c) to (e) that, below the compaction-influenced zone, the measured horizontal stresses converged to the earth pressure at rest based on Jaky's equation. In Fig. 2.12, data points obtained from Tests C0903 and C1141 indicated that the experimental results were quite reproducible.

The stress paths of σ_v versus σ_h for soil elements adjacent to the surface of the

nonyielding wall are displayed in Fig. 2.13. Test data shown in Fig. 2.13(a) were measured by SPT 2 and SPT 102. In the figure, the path F1 represents the stress variation due to the “filling” of the loose Lift 1. It is clear that the stress path F1 is in good agreement with Jaky’s prediction. The filling of sand Lifts 1-5 stress (paths F1-F5) caused an obvious increase in vertical pressure.

Stress path C1 represents the stress variation due to the “compaction” on the surface of soil Lift 1. During the compaction of soil Lift 1 (stress path C1), the lateral earth pressure σ_h measured by SPT2 on the nonyielding wall increased significantly, but the vertical normal stress in soil mass was not affected by compaction. The compaction on Lift 2 (stress path C2) caused the h to increase further. However, the compaction on the surface of Lift 3 resulted in a lateral pressure reduction at SPT2 as indicated by the stress path C3. The compaction on the surface of Lifts 3 and 4 gradually brought the soil element located in front of SPT2 back to an at-rest stress condition. The horizontal earth pressure change was mainly caused by the compaction process, not soil filling. Similar trends can also be observed in Fig. 2.13 (b) and (c).

In Fig. 2.14, the experimental test results are compared with the design recommendations proposed by Broms (1971), NAVFAC DM-7.2 (US Navy 1982), Duncan and Seed (1986), Peck and Mesri (1987), and Duncan et al. (1991). Parameter values used in the pressure calculation such as the unit weight γ , relative density D_r , internal friction angle ϕ , wall friction angle δ , and cyclic compaction stress σ_{cyc} are shown in Fig. 2.14. The horizontal pressure distribution suggested by the Navy Design Manual DM-7.2 was based on the analytical method proposed by Ingold (1979). The pressure distribution determined with the method proposed by Duncan et al. (1991) was obtained from the design chart for vibratory plates with a cyclic compaction stress $q = 34.9 \text{ kN/m}^2$ (5 psi).

2.4 Cyclic Simple Shear Test

The cyclic simple shear test is a convenient method for determining the shear modulus and damping ratio of soils. It is also a convenient device for studying the liquefaction behavior of saturated cohesion less soils. In fig.2.15, Airey and Wood (1987) showed the NGI cyclic simple shear apparatus. In the cyclic simple shear test, a soil specimen, usually 20-30 mm high with a diameter of 60-80 mm, is subjected to a vertical effective stress σ_v and a cyclic shear stress τ_{cyc} , as shown in Fig. 2.16. The horizontal load necessary to deform the specimen is measured by the horizontal load cell, and the shear deformation of the specimen is measured by the linear variable differential transformer LVDT.

2.4.1 Study of Youd

Youd (1972) reported the experimental results regarding the void-ratio reduction of sand due to cyclic simple shearing. Fig. 2.17 shows the gradual densification of sand by repeated shear displacement in a simple shear test. Each cycle of shear straining reduces the void ratio of the soil by a certain amount, although at a decreasing rate. Decrease in volume of the sand, as shown in Fig. 2.17, can take place only if drainage occurs freely. In the figure, after 10,000 cycles, the void ratio of sand was reduced from 0.54 to 0.42. It is obvious from the figure that cyclic shearing is an effective measure to densify the cohesionless soil.

2.4.2 Study of Hsu and Vucetic

Hsu and Vucetic (2004) studied the volume decrease of dry or partially saturated sands subjected to several cycles of cyclic shear strain amplitudes γ_c . If the cyclic

shear strain amplitudes γ_{cl} are smaller than a certain threshold value called the volumetric cyclic threshold shear strain γ_{tv} ($\gamma_{cl} < \gamma_{tv}$), their volume will not change. Such cyclic behavior is depicted schematically in Fig. 2.17. In the figure the results of three cyclic strain-controlled direct simple shear (DSS) tests conducted on dry or partially saturated specimens are sketched. The variations of shear strain over time t are presented in Fig. 2.18(a). The resulting variations of vertical strain ε_v are presented in Fig. 2.18(b). The relationship between γ_c , the permanent cyclic vertical strain ε_{vc} , and the number of cycles N , is presented in Fig. 2.18(c). The strain ε_{vc} in Fig. 2.18(c) is taken as ε_v at the end of cycle N , and it is also called the cyclic settlement strain.

It can be seen in Fig. 2.18(c) how below certain γ_{tv} the soil does not settle ($\varepsilon_{vc} = 0$), while above it, it settles significantly ($\varepsilon_{vc} > 0$). Accordingly, the amplitude γ_{tv} represents the boundary between two fundamentally different types of volume change behavior. Below γ_{tv} , the soil particles are not displaced with respect to each other and the soil's mineral skeleton and volume remain practically unchanged during cycling loading. When the soil is subjected to $\gamma_c > \gamma_{tv}$, the particles are displaced with respect to each other irreversibly, resulting in permanent changes of the soil's volume and microstructure. It is clear in Fig. 2.18 that the cyclic shearing is an effective method to reduce the vertical strain of soil, and to densify the soil mass.

2.5 Cyclic Torsional Simple Shear Test

Fig. 2.19 shows the cyclic torsional simple shear device proposed by Ishibashi et al. in 1985. In this device, a hollow cylindrical specimen 71.1 mm in outside diameter, 50.8 mm in inside diameter, and 142.2 mm in height, can be subjected to independent variations of axial stress, inner and outer confining pressure, and torsional shear stress

or strain. Thus the device closely simulates the ideal in situ condition and enable us to apply a known value of the lateral confining stress.

Static and cyclic torsional shear stresses can be applied by MTS closed-loop servo-hydraulic linear actuator by means of a torque loading rod, ball bearing spline, and axial loading piston. The movement of the MTS actuator is corrected by feedback signals either from the torque transducer for cyclic stress controlled tests, or from the rotational LVDT for cyclic strain controlled tests. The specimen is subjected to the programmed cyclic motion by the MTS commanding unit without any effect of the piston friction and torsional distortion of the loading piston and transducers.

2.5.1 Study of Ishibashi et al.

Ishibashi et al. (1985) studied the volume change of a hollow cylindrical Ottawa sand specimen subjected to cyclic torsional shearing in drained conditions. The experiments were conducted under uniform cyclic shear strains and the following conclusions were drawn. In Fig. 2.20, relationships between the cyclic volumetric strain the uniform cyclic shear strain γ_{cyc} for a given number of cycle is nearly linear. It is clear in Fig. 2.17 that the volume reduction of the soil specimen is significantly influenced by the cyclic shear strain load γ_{cyc} and the number of cyclic shear stress application N .

2.6 Densification with Cyclic Torsional Shearing

2.6.1 Study of Yang

Yang (2002) used the disc-shearing instrument at Chung-Yuan University to study

the soil settlement due to cyclic torsional shearing. The diameter of the shearing disc was 198 mm. The diameter of the cylindrical sandy specimen was 200 mm, and the height of the soil specimen was 105 mm. The cyclic shear tests were carried out with initial relative densities from 30 % to 50 %, and normal stresses applied from 7 kPa to 150 kPa. One-way and cyclic (N=1) shear stresses were applied on Mai Liao sand, Vietnam sand, and Ottawa sand. Fig. 2.21 shows the relative density increase due to cyclic shearing (N=1) was about twice that due to one-way shearing.

2.6.2 Study of Ren

Ren (2006) studied the soil densification due to cyclic torsional shearing. The diameter of the sandy specimen was 200 mm and the height was 105 mm. The diameter of the shear disc was 198 mm. Mailiao sand, Ottawa sand and Vietnam sand were tested with an initial relative density of 30 %. Normal stresses of 20, 60 and 100 kPa, and the shear angle 10°, 20°, 30°, 60° and 90° were used for testing.

Fig. 2.22 showed the relative density of sand increased with increasing number of cyclic shear stress application N. The first 6 cycles of τ_{cyc} application was most effective. Fig. 2.23 showed a greater relative density increment was achieved at a shallow depth. Less D_r increment due to the cyclic shear stress was observed at a deeper depth.

2.6.3 Study of Chen

Chen (2011) presents experimental data on the settlement and relative density change due to cyclic torsional shearing compaction. A new cyclic torsional shearing compactor was designed and constructed at NCTU. The thickness (T) of the soil after compaction was 0.6 m. The initial relative density was $34.5\% \pm 2.3\%$ and the vertical

pressure on the surface loading was 9.2 kPa. Fig.2.24 showed the soil surface settlements after 1, 2, 5, 10, 20, 30 and 40 cycles of cyclic torsional shearing. It was obvious that the soil settlement increased with increasing number of cycles (N) of torsional shearing.

In the first 2 cycles of torque application, surface settlement increased significantly. However, after $N = 20$, the major part of settlement has accomplished, soil particles were sheared and reached a densely-packed condition. Therefore, it was difficult to increase the settlement any further with more cyclic shear application.

Fig. 2.25 showed the relative density distributions of the compacted specimen for $N = 1, 2, 5, 10, 20$ and 40. Test results showed that the density distribution increased with increasing number of cycles of torsional shearing.

In fig. 2.26, cyclic torsional shearing was applied on the surface of each 0.15m-thick lift, and the distribution of relative density in Lifts 1 to 4. Test results revealed that the trend of pressure distribution in each 0.15 m-thick lift was similar. The average relative density achieved in each lift was greater than the required value of 70 %.

2.7 Assessment of Relative Density

ASTM Test Designation D-4253 (2007) provide a procedure for determining the minimum and maximum dry unit weights of granular soils. These unit weights can be used to determine the relative density of soil compacted in the field. The term relative density is commonly used to indicate the in situ denseness or looseness of a granular soil. Relative density is defined as

$$D_r = \frac{e_{max} - e}{e_{max} - e_{min}} \times 100\% \quad (2.10)$$

Where e = in situ void ratio of the soil, e_{max} = void ratio of the soil in the loosest state, e_{min} = void ratio of the soil in the densest state.

Das (2010) reported that the value of D_r may vary from a minimum of 0 % for very loose soils to a maximum of 100 % for very dense soils. Soils engineers qualitatively describe the granular soil deposits according to their relative densities. In-place soils seldom have relative densities less than 20 to 30 %. Compacting a granular soil to a relative density greater than about 85 % is difficult. Lambe and Whitman (1969) reported that for dense soils the value of D_r was 65 to 85 % as shown in Table. 2.1. US Navy Design Manual NAVFAC DM-7 (1982) reported the relative density was 70 to 75 % can be obtained by proper compaction procedures. Vibration compaction generally is the most effective procedure.

2.8 Cone Penetration Test

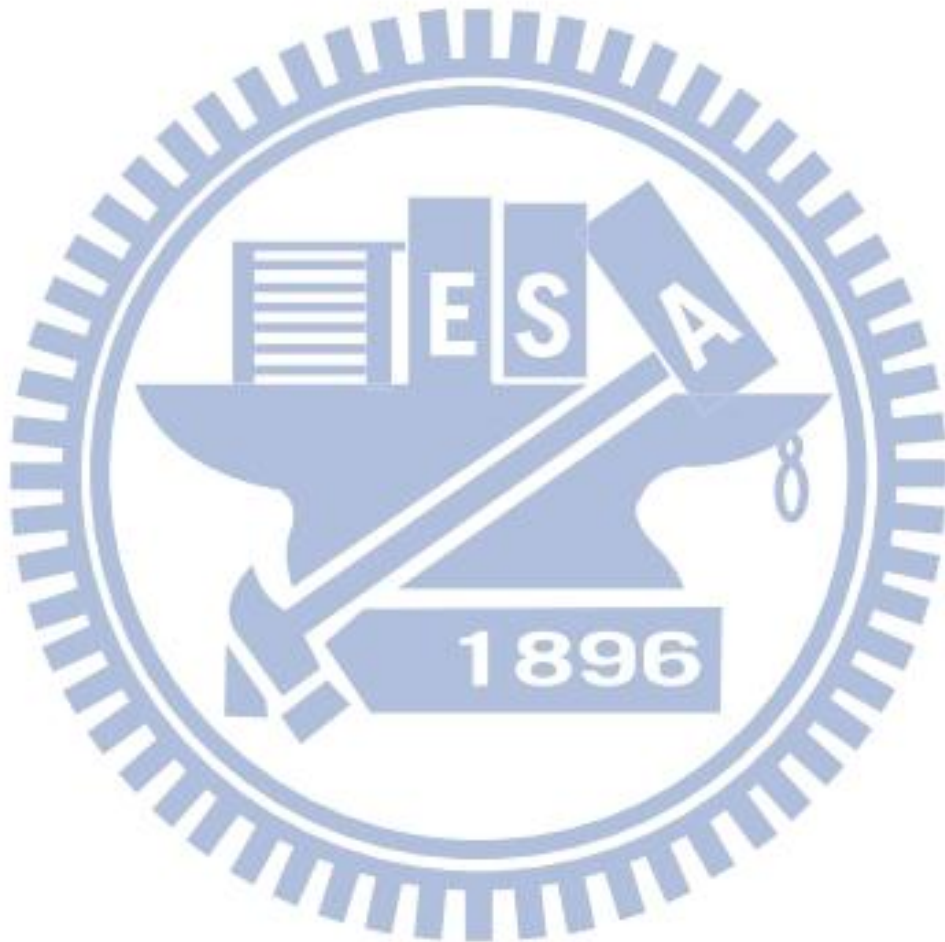
2.8.1 Study of Jamiolkowski et al.

The relationship between relative density of sand of the tip resistance q_c of CPT was investigated by Jamiolkowski et al. (1985). It was found that Fig. 2.27 illustrates the variation in cone resistance for a range of relative densities for different sands. The Ticino sand used by Baldi et al. (1986) was a clean, uniform silica sand with subangular grains and appears to have a moderate compressibility. Fig. 2.27 shows the range for five predominantly silica sands used under controlled laboratory conditions; field cases are likely to exhibit more variability. Base on the data in Fig.

2.27, the following relationship was established:

$$Dr = -98 + 66 \log_{10} [q_c / (\sigma_o')^{0.5}] \quad (2.11)$$

Where q_c is cone resistance (ton/m^2) and σ_o' is vertical effective stress (ton/m^2).



Chapter 3

Experimental Apparatus

To investigate the effects of cyclic torsional shear compaction on the relative density of in a cohesionless soil mass, the soil bin at National Chiao Tung University (NCTU) was used. All soil improvement experiments described in this chapter and there were conducted in the soil bin of the NCTU non-yielding model retaining wall facility. This chapter introduces the soil bin, soil pressure transducer, cyclic torsional shear compactor, cone penetration facility and data acquisition system used for laboratory experiments.

3.1 Soil Bin

The soil bin is designed to minimize the lateral deflection of sidewalls during testing. In Fig. 3.1, the soil bin was fabricated of steel plates with inside dimensions of 1,500 mm \times 1,500 mm \times 1,600 mm shown in Fig. 3.1 is 1,500 mm-wide, 1,600 mm-high, and 45 mm-thick. To achieve an at-rest condition, the wall material should be nearly rigid. It is hoped that the deformation of the model wall could be neglected when the soil bin is filled with cohesionless soil. In Fig. 3.1, twenty-four 20 mm-thick steel columns were welded to the four sidewalls to reduce any lateral deformation during loading. In addition, twelve C-shaped steel beams were also welded horizontally around the box to further increase the stiffness of the box.

Assuming a 1,500 mm-thick cohesionless backfill with a unit weight $\gamma = 17.1$ kN/m³, and an internal friction angle $\phi = 41^\circ$ was pluviated into the soil bin. A 45

mm-thick solid steel plate with a Young's modulus of 210 GPa was chosen as the wall material. The estimated deflection of the model wall would be only 1.22×10^{-3} mm. Therefore, it can be concluded that the lateral movement of the model wall is negligible.

The end-wall and sidewalls of the soil bin were made of 35 mm-thick steel plates. Outside the steel walls, vertical steel columns and horizontal steel beams were welded to increase the stiffness of the end-wall and sidewalls. If the soil bin was filled with dense sand, the estimated maximum deflection of the sidewall would be 1.86×10^{-3} mm. From a practical point of view, the deflection of the four walls around the soil bin can be neglected.

For this study, the thickness of the compacted soil is only 0.6 m-thick. The lateral earth pressure acting on the side wall would be lower than that due to a 1.5 m-thick backfill. As the results, the deflection of the side walls of the soil bin would be even less.

3.2 Soil Pressure transducer

To investigate the development of vertical stress σ_v and horizontal stress σ_h in the soil mass fill, eight soil pressure transducers (Kyowa BE-2KCM17, capacity = 98.1 kN/m²) buried in the compacted soil. The strain-gage-type soil pressure transducer buried in the fill is shown in Fig. 3.2. The radial extensions attached to the transducers are used to prevent possible rotation due to filling and compaction. Calibration of the soil pressure transducers are indicated in the Appendix A of this thesis. The diameter of the SPT sensing area is 22 mm.

3.3 Cyclic Torsional Shear Compactor

To enhance an effective soil compactor with less noise, and less vibration, a cyclic torsional shear compactor (CTSC) was developed at National Chiao Tung University (NCTU). Fig. 3.3 and 3.4 show the cyclic torsional shear compactor. The entire cyclic torsional shear compactor consists of four components, namely: (1) shearing disc; (2) normal loading discs; (3) torque loading frame; and (4) torque wrench. The design and construction of cyclic torsional shear compactor are discussed in this chapter. All of the experiments mentioned in this thesis were conducted with the NCTU cyclic torsional shear compactor, which is briefly introduced as follows.

To efficiently carry the applied cyclic shear stress from the disc to the soil, 12 steel radial steel fins were carved on the bottom of the shearing disc as shown in Fig. 3.5. Fig. 3.6 shows, the steel radial fin was 2 mm-thick, 4 mm-wide and wedge angle of the fin was 90° . During testing, the steel fin would cut into the soil mass. To provide adequate friction between the base of the disc and the soil, the bottom of the shearing disc is covered with a layer of anti-slip frictional material called SAFETY WALK (3M). The SAFETY WALK was attached to the disc bottom on the fan-shaped areas between the steel fins as shown in Fig. 3.7. Table 3.1 shows the dimension and mass of the normal loading discs. As shown in Fig. 3.8, the outside-diameter normal loading discs is 290 mm, the diameter of the screw rod hole is 21.6 mm, the diameter of the torque shaft hold is 43 mm, and the diameter of the hoist screw hole is 10.25 mm. Without any normal loading disc, the mass of the CTSC is 24.3 kg. Adding 2 pieces of 19.8 kg and 2 pieces of 1.05 kg loading discs, the total mass of the entire CTCS is 66.0 kg. It should be mentioned that this thesis is intended to report on the preliminary experimental data obtained from a light-weight cyclic torsional shear compactor.

Fig. 3.9 and Fig. 3.10 shows the dimensions of the torque loading frame at the top of the torsional shear device. The hoist ring was screwed on top of the frame so that

torsional shear compactor be lifted and lowered by the overhead crane in the laboratory. Two hexagon caps were fixed on the arms of the torque frame, which enable the torque wrench to be hooked up to the torque frame. The applied torque was transmitted from the torque wrench, to the torque frame, then to the torque shaft and shear disc as illustrated in Fig. 3.3.

Fig. 3.11 (a) shows, the three torque wrenches are 600, 430, and 128 mm long. Fig. 3.11 (b) shows the torque wrench made of stainless steel. During testing, proper wrench length was selected so that no collision between the torque wrench with the sidewall of the soil bin would occur. The torque wrench was attached to the torque loading frame to induce torsional shear on the loose fill.

The digital torque wrench shown in Fig. 3.12 and Fig. 3.13 was used to measure the torque applied to the soil. The digital torque wrench has a digital torque value readout. Accuracy in the clockwise direction was $\pm 1\%$, and the accuracy in the counterclockwise direction was $\pm 2\%$. Readout units included N-m, ft-lb, in-lb and kg-cm. The digital torque wrench made by OLY SCIENTIFIC Equipment Ltd. (model 921/200E) was 530 mm. Long the maximum operation range is 200 N-m. The square peg is 12.7 mm x 12.7 mm.

3.4 Cone Penetration Facility

The cone penetration facility was used to estimate the change of soil properties before and after cyclic shear compaction. This facility belong to Department of Civil Engineering, Chung Yuan Christian University (CYCU). Continuous measurements were obtained with the CPT facility. As shown in Fig. 3.14 (a) to (c), the CYCU CPT facility is composed of following these parts: (1) mini-cone penetrometer; (2) electric motor and speed control device; and (3) CPT data acquisition device (including micro signal conditioning device, DA-16 anlong to digital converter, and the lap-top

computer). A load cell was installed at the bottom of the penetrometer near the cone, to measure the cone resistance q_c . After connecting the cone penetrometer to the electric motor, the mini-cone was pushed into the soil mass at a constant speed. For this study, the speed of penetration was controlled to be 5.0 mm/s. The digital signals from the load cell of the cone penetrometer were filtered and amplified by micro signal conditioning device. Then, the experimental data were digitized by the D to A converter (USB DA-16). The digital signals were transmitted to the lab-top computer (Fig. 3.14 (b)) for storage and analysis. The mini-cone used for this study has a 60 degree apex angle and a diameter of 9 mm. The standard cone has a cross section area of 1000 mm². But the cross-section area of the mini-cone is only 63.62 mm².

3.5 Earth-Pressure Data Acquisition System

A earth-pressure data acquisition system was used to collect and store the considerable amount of earth pressure data generated during the tests. In the Fig. 3.15 (a) and (b) the data acquisition system is composed of the following four parts: (1) dynamic strain amplifiers (Kyowa: DPM601A and DPM711B); (2) AD/DA card (NI BNC-2090); and (3) Personal Computer. The analog signals from the sensors were filtered and amplified by the dynamic strain amplifiers. Then, the analog experimental data were digitized by an A/D-D/A card. The digital signals were then transmitted to the personal computer for storage and analysis. The software LabView was used for data collection and recording.

Chapter 4

Soil Characteristics

The characteristics of the fill used for soil improvement experiments are introduced in this chapter. The reduction of friction between the soil and lubricated side wall is discussed. The control and measurement of soil density distribution in the fill are also introduced.

4.1 Soil Properties

Air-dry Ottawa sand (ASTM C-778) was used throughout this investigation. Physical properties of the soil include $G_s = 2.65$, $e_{\max} = 0.76$, $e_{\min} = 0.50$, $D_{60} = 0.39$ mm, and $D_{10} = 0.26$ mm. Grain-size distribution of the backfill is shown in Fig. 4.1. Major factors considered in choosing Ottawa sand as the fill material are summarized as follows.

1. Its round shape, which avoids the effect of angularity of soil grains.
2. Its uniform distribution of grain size (coefficient of uniformity $C_u = 1.5$), which avoids the effects due to soil gradation.
3. High rigidity of solid grains, which reduces possible disintegration of soil particles under loading.
4. Its high permeability, which allows fast drainage and therefore reduces water pressure behind the wall.

4.2 Lubricated Side-wall Friction

To simulate the field condition of a infinite half space for the compaction constitute, the shear stress between the fill and the side walls of the soil bin should be minimized to nearly frictionless. To reduce the friction between side wall and fill Fang et al. (2004) suggested to was a lubrication layer fabricated with plastic sheets. Two types of plastic sheeting, one thick and two thin plastic sheets, were adopted to reduce the interface friction. All plastic sheets were hung vertically on the side walls before the backfill was deposited as shown in Fig. 4.2.

In this study, two thin (0.009 mm-thick) and one thick (0.152 mm-thick) plastic sheets were adopted for the soil improvement experiments. Fig. 4.3 shows the variation of side-wall friction angle δ_{sw} as a function of the normal stress σ_v for the plastic sheet method (1 thick + 2 thin sheeting) reported by Fang et al. (2004). The measured side-wall friction angle with this method is about 7.5° . For all experiments in this paper, the lubrication layers were wall applied on four side walls of the soil bin.

4.3 Control of Soil Density

4.3.1 Air-Pluviated of Loose Ottawa Sand

To achieve a uniform soil density in the backfill, Ottawa sand was deposited by air-pluviation method into the soil bin. The air-pluviation method had been widely used for a long period of time to reconstitute laboratory sand specimens. Rad and Tumay (1987) reported that pluviation is the method that provides reasonably homogeneous specimens with desired relative density. Lo Presti et al. (1992) reported

that the pluviation method could be performed for greater specimens in less time.

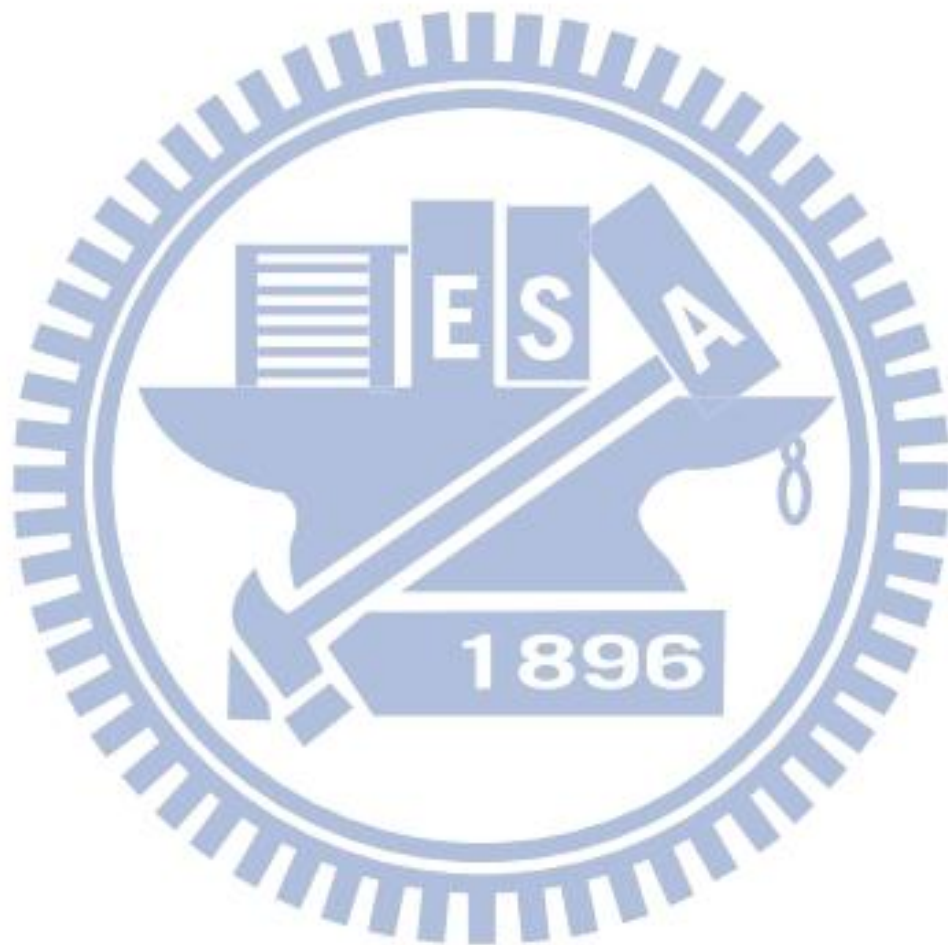
Das (2010) suggested that, for granular soil deposits, the relative density D_r of 15~50%, is defined as loose, $D_r = 50\sim70\%$ is defined as medium, and $D_r = 70\sim85\%$ is defined as dense. For the air-pluviation method, Fig. 4.4 shows the soil hopper let the sand flow through a calibrated slot opening at the lower end. A picture of the soil pluviating processes is shown in Fig. 4.5. To achieve a loose backfill, Chen (2003) adopted the drop height of 1.0 m and hopper slot opening of 15 mm. In this study, the drop height of 1.0 m and the hopper slot-opening of 15 mm were also selected to achieve the loose fill. In Fig. 4.6, the expected relative density of soil was about 35% by Ho (1999).

4.3.2 Measurement of Soil Density

To observe the distribution of soil density in the soil bin, soil density cups were made. The soil density cup made of acrylic is illustrated in Fig. 4.7. The circular cup wall was only 10 mm-high, so that the shear deformation and volume reduction could occur in the cup during testing. A picture of the soil density cup is shown in Fig. 4.8. During the preparation of the 0.6 m thick loose soil specimen, density cups were buried in the soil mass at different elevations and different locations in the backfill as shown in Fig. 4.9 and Fig. 4.10. After the loose soil had been filled up to 0.6 m from the bottom of the soil bin by air-pluviation, density cups were dug out from the soil mass carefully. Fig. 4.11 shows the mass of the cup and soil in the cap was measured with an electrical scale.

For a 0.6 m thick air-pluviated Ottawa sand layer, the distribution of soil density with depth is shown in Fig. 4.12. For the loose sand, the mean unit weight γ is 15.6 kN/m³, the mean relative density is $D_r = 35.5\%$ with the standard deviation of 0.8%.

Das (2010) suggested that for the granular soil deposit with a relative density $15\% \leq D_r \leq 50\%$ is defined as loose sand. The relative density achieved in Fig. 4.12 is quite loose and uniform with depth.



Chapter 5

Testing Procedure

The procedure to conduct the cyclic torsional shear tests are introduced in this chapter. The testing procedure can be divided into three parts: (1) specimen preparation; (2) application of vertical static load; (3) application of cyclic torsional shear; and (4) cone penetration. These parts will be introduced in the following sections with pictures. The “plastic-sheets” lubrication layers were hung on the sidewalls of the soil bin before testing.

5.1 Specimen Preparation

Fig. 5.1 shows air-dry Ottawa sand in the soil storage container. Fig. 5.2 shows sand was shoveled from the soil storage to the sand hopper, and the mass of the fill was measured with an electrical scale. Fig. 5.3 shows the sand hopper was lifted by overhead crane in the laboratory. Fig. 5.4 shows Ottawa sand was deposited by air-pluviation method into the soil bin. The drop height was controlled to be 1.0 m and the hopper slot-opening of 15 mm were selected to achieve a loose fill, Fig. 5.5 (a) and (b) show portable hanging ladders were placed on top of the sidewalls, and a bridge board was placed between the ladders. Throughout the test, the operator will stay on the bridge board to avoid any unexpected surcharge on the soil specimen.

Leveling of the pluviated soil surface by the graduate student with a brush is shown in Fig. 5.6. Four density cups were placed on each 50 mm-thick soil layer. A

total of 44 density cups were buried in the fill. Fig. 5.7 shows how check the density cup horizontal with a bubble level. Placement of a soil density cup and soil-pressure transducer on the soil surface is shown in Fig. 5.8. Fig. 5.9 shows density cups and soil-pressure transducers were buried in the soil mass at different elevations in the fill. Eight soil pressure transducers were placed at the depths of 100, 250, 400 and 550 mm. The soil pulviation and density cup placement operations were repeated until a backfill thickness $T = 0.6$ m was reached.

5.2 Application of Vertical Static Load

The procedure to apply the vertical static load q on top of the air-pluviated loose sand is introduced. The cyclic torsional shear compactor (24.3 kg) and the loading discs (41.7 kg) used to apply static load has a mass of 66 kg. Diameter of the circular footing is 0.3 m and the vertical static load $q = 9.2$ kPa. Fig. 5.10 illustrates the grid points for the vertical load application. For the first row of static load, the center of circular load was applied at 1A, 1C, 1E, 1G and 1I.

Fig. 5.11 shows the CTSC was hoisted with overhead crane into the soil bin. Fig. 5.12 (a) shows the vertical static load q was applied on the loose sand with 5x5 formation. Fig. 5.13 shows the circular static vertical load was applied on the surface of the fill with the 5x5 loading formation.

5.3 Application of Cyclic Torsional Shearing

In this study, the cyclic torsional shear was applied on the soil surface for $\theta = \pm 1^\circ$, $\pm 3^\circ$, $\pm 5^\circ$, $\pm 7^\circ$ and $\pm 10^\circ$. Fig. 5.14 showed a light dot from the laser distance meter on the angle steel bar was used as a fixed point to the soil surface. Fig. 5.15 shows the cyclic torsional shear was applied by the operator on the loose fill to increase its

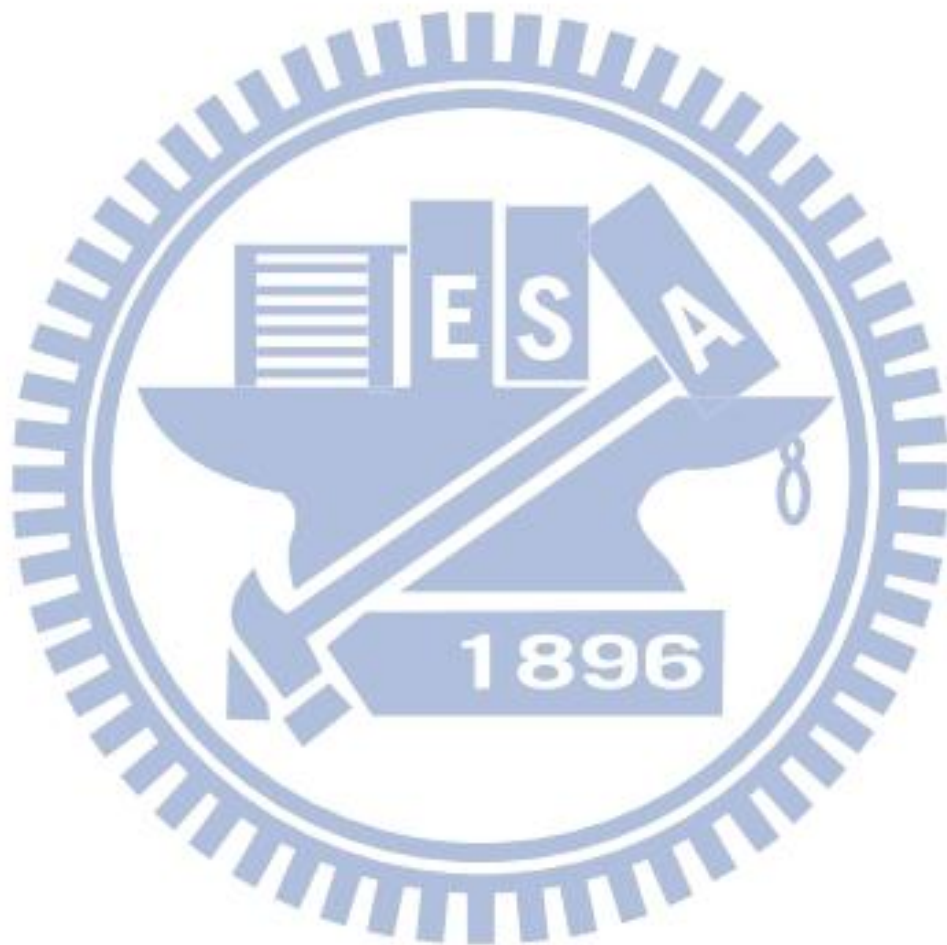
density. In Fig. 5.16, 5.17 and 5.18, with the guidance of the fixed light dot, the circular disc shears the soil from 0° to $+5^\circ$ and -5° . The application of cyclic torsional shear to loose sand is shown in Fig. 5.19.

For the test for with 20 shearing cycles ($N=20$), after the application of vertical static load, the torsional shear was first applied on the 4x4 loading formation (Fig. 5.12(b)) for the first 5 cycles, as shown in Fig. 5.20. To prevent disc penetration due to continuous shearing at the same spots, the shearing was moved to the 5x5 formation Fig. 5.12(a) from $N = 6$ to 10 as shown in Fig. 5.21. For $N = 11$ to 20, the shearing was applied on the 4x4 formation, as shown in Fig. 5.22. Fig. 5.23 shows, after compaction the soil density cup was carefully dug out of the soil mass. Fig. 5.24 (a) to (c) shows the density cup with a spatula. Fig. 5.25 (a) to (d) shows the brush away soil particles from base plate of the density cup. Soil mass in the cup was measured with an electrical scale and the density of the compacted soil could be determined.

5.4 Cone Penetration Test

In Fig. 5.26, the points of penetration in the soil bin were labeled as C1, C2, C3 and C4. The steel beam on the top of soil bin to support the CPT facility is shown in Fig. 5.27 (a). Fig. 5.27 (b) showed the beam was fixed on the soil bin with steel c-clamps. In Fig. 5.28, the electric motor and the movable plate was fixed to the steel beam by the screw. Fig. 5.29 shows the connection of cone penetrometer to the electric motor. Fig. 5.30 shows the cone was lowered to the surface of the soil mass. During penetrating, the speed of downward penetration of the mini-cone was controlled at 5 mm/s. After reaching the penetration depth of 400 mm, the testing was terminated. then, moved the electric motor on the movable plate to the next point and repeat the

penetration procedure. The sequence of testing would be C1, C2, C3 and C4. Test results measured by the load cell on the mini-cone were collected, stored and processed with the CPT data acquisition system.



Chapter 6

Test Results

This chapter shows experimental results regarding soil densification due to static vertical load and cyclic torsional shearing. The static vertical load applied of the fill was $q = 9.2$ kPa. The cyclic torque and shearing applied on the soil surface was measured and reported. The surface settlement, distribution relative density, vertical and horizontal stresses and cone resistance of the compacted fill due to the static vertical loading and cyclic torsional shearing were investigated. The rotation angle of the shearing disc varied for $\pm 1^\circ$, $\pm 3^\circ$, $\pm 5^\circ$, $\pm 7^\circ$ and $\pm 10^\circ$, and the number of loading cycle were set to be $N = 20$. To obtain a soil mass with a relative density greater than 70%, compaction was applied on the fill surface for 0.15 m-thick lifts.

6.1 Static Load Test

To separate the densification effects due to static and cyclic loadings, in this section, the surface of four 0.15 m-thick soil lifts was compressed with the static vertical loading only. Effects of soil densification such as the surface settlement, change of relative density, vertical and horizontal stresses and cone resistance in the compressed fill are investigated.

6.1.1 Surface Settlement Due to Static Load

The surface settlements of the four 0.15 m-thick compressed soil lifts due the static

weight of the compactor were discussed. The initial relative density of the loose fill was 35.5% (see Fig. 4.12). The applied static normal stress was $q = 9.2$ kPa. To achieve a uniform settlement, the vertical static loading was applied on the surface with the 5×5 formation (see Fig. 5.12 (a)). Fig. 6.1 showed the settlement measurement was carried out with the laser distance meter placed on top of the steel beam. The surface settlement measured at the centers of disc loading disc was shown in Fig. 6.2. For the four 150 mm-thick soil lifts, the accumulated minimum and maximum settlements were 15.0 and 22.3 mm. The average settlement was 19.0 mm, which was about 3.2% (volumetric strain $\epsilon_v = 3.2\%$) of the soil thickness. It is obvious that static vertical loading is an effective method to compact the loose fill. To limit the scope of this thesis, only $q = 9.2$ kPa was used throughout this study. It should be mentioned that the vertical strain distribution in the soil lift may not be uniform.

6.1.2 Density Change Due to Static Load

To investigate the density distribution in the compressed fill, density cups were buried in the soil mass at different elevations and locations in the four 0.15 m-thick soil lifts (see Fig 5.9). For the un-compacted loose soil, the average relative density was about 35.5%. In Fig. 6.3, Chen (2011) reported that, for a 0.6m-thick fill, after the application of static vertical load q , the density increase more near the surface and the density increase less at greater depths. The induced density change decreased with increasing depth. Fig. 6.4 shows, after applying the static vertical load 9.2 kPa on each lift, the relative density of fill increased. This static vertical loading represents the weight of the cyclic torsional shear compactor. On the average, the relative density increase was about 26.4% from 35.5% to 61.9%. It should be mentioned that the distribution of density is not uniform with depth. However, the relative density

achieved $Dr = 61.9\%$ is not enough to achieve the target of dense sand ($Dr = 70\%-85\%$).

6.1.3 Stress Change Due to Static Load

For comparison purposes, at the beginning of this study, experiments were conducted to investigate the stresses in an uncompacted loose fill. Air-pluviation method was adopted to prepare the fill and the relative density achieved for the loose sand was 35.5 %. Fig. 6.5 shows the location of soil pressure transducers to measure the distribution of vertical and horizontal stress with depth. SPT2, SPT3, SPT6 and SPT7 were buried in the soil mass to measure σ_v and SPT1, SPT4, SPT5 and SPT8 were used to measure σ_h . The vertical stress σ_v measured in the soil mass was shown in Fig. 6.6. In this figure, the vertical stress σ_v increased with increasing depth z . Test data were in fairly good agreement with the traditional equation $\sigma_v = \gamma z$. In this study, unit weight γ was 15.6 kN/m^3 for the loose sand. The distributions of horizontal earth pressure σ_h with depth were shown in Fig. 6.7. In the figure, the earth pressure profile induced by the 0.6 m-thick loose fill was approximately linear and was in good agreement with the Jaky's equation. Mayne and Kulhawy (1982), Mesri and Hayat (1993) reported that Jaky's equation was suitable for backfill in its loosest state. From a practical point of view, it was concluded that for a loose fill, the vertical and horizontal earth pressure in the soil mass can be properly estimated with the equation $\sigma_v = \gamma z$ and Jaky's equation, respectively.

To investigate the change of stresses due to static load, the loose fill was placed in four 0.15m-thick lifts as shown in Fig. 6.5. Static load q was applied each lift on the surface with the 5×5 formation (see Fig. 5.12) and then removed. Fig. 6.6 shows the vertical stress profile after the static vertical loading. It is clear in the figure that the vertical overburden pressure σ_v can be properly estimated with the equation $\sigma_v = \gamma z$.

As compared with the σ_v for loose sand the measured, σ_v increased slightly, probably because the compressed fill had a slightly higher density (see Fig. 6.4). It is clear in the figure that the static vertical load did not result insignificant residual stress in the vertical direction. It may be concluded that the effect of static loading on the vertical pressure σ_v was insignificantly. Fig. 6.7 shows the horizontal stress was also increased slightly after the application of the static vertical loading.

6.1.4 Cone Resistance Change Due to Static Load

Cone penetration tests were conducted to investigate the change of soil properties due to static loading on the loose fill. The fill is 600 mm-thick as shown Fig. 6.5. The bottom of the soil bin is a solid steel plate. Due to boundary effects, the cone resistance may suddenly increase, when the penetrometer approached the bottom of the soil bin. For this study, cone penetration was conducted for $z = 0$ to 400 mm. For Fig. 6.8 shows the cone resistance for the loose soil varied from 0 to 300 kPa. After static vertical loading, the cone resistance varied from 0 to 1681.2 kPa. It is obvious that static vertical loading significantly increase the tip resistance of the compressed fill.

Jamiolkowski et al. (1985) were reported that could make cone resistance converted to relative density. Fig 6.9 shows the cone resistance of static load transformed to the relative density by Jamiolkowski theory. It could be found the test result and the theory were agreement in the loose fill. However, it was not agreement after compressed. It was probability that the soil mass not big enough.

6.2 Applied Cyclic Torsional Shearing

Fig. 6.10 shows the torque applied on the soil surface was measured with a digital torque meter. For the number of loading cycle $N = 20$, the torque measured at $\theta = \pm 1^\circ$,

$\pm 3^\circ$, $\pm 5^\circ$, $\pm 7^\circ$ and $\pm 10^\circ$ was shown in Fig. 6.11. In figure, for different θ angles, the applied torque varied between -53 to 47.8 N-m. Fig. 6.12 shows the applied torque T as a function of shearing angle θ . Test results indicated that the applied torque does not change with increasing shearing angle. On the average, for $\theta = \pm 1^\circ$, $\pm 3^\circ$, $\pm 5^\circ$, $\pm 7^\circ$ and $\pm 10^\circ$, the applied torque was about ± 47.7 N-m. The variation of torque for the θ angle between 0° and $\pm 1^\circ$ should be studied in the future.

Fig. 6.13 indicates how to determine the maximum torsional shear stress τ_{\max} at the edge of the shearing disc due to the applied torque. A linear distribution of shear stress from the center to the edge of the disc was assumed. Fig. 6.14 shows the maximum shear stress as a function of the θ angle. Test results indicated that maximum shear stress with increasing θ value. On the average, for $\theta = \pm 1^\circ$, $\pm 3^\circ$, $\pm 5^\circ$, $\pm 7^\circ$ and $\pm 10^\circ$, the maximum shear stress was about 9.0 kPa. It is possible that, for θ angle greater than $\pm 1^\circ$, the slip between soil and shearing disc has already occurred compressed.

6.3 Cyclic Torsional Shear Test

6.3.1 Surface Settlement Due to Cyclic Torsional Shearing

After the application of the static loading, cyclic torsional shearing was applied on the surface of each lift. The cyclic shearing was applied on the circular areas of the 4×4 formation for $N = 1$ to 5, and 11 to 20. The shearing was applied on the 5×5 formation for $N = 6$ to 10 (see Fig. 5.12). Fig. 6.15 shows the surface settlements of the 0.6 m-thick fill after the disc rotation angle at $\pm 1^\circ$, $\pm 3^\circ$, $\pm 5^\circ$, $\pm 7^\circ$ and $\pm 10^\circ$. In the figure, the surface settlement increased with increasing shearing angle θ of torsional shearing. In the figure, the average settlement due to the static vertical loading $q = 9.2$

kPa was about 19 mm. After the cyclic disc rotation $\theta = \pm 10^\circ$ and $N = 20$ cycles of torque application, the average settlement was 38.2 mm. The extra settlement due to the torsional shearing cycles was about 19.2 mm, which was more than the settlement due to static vertical loading. It was obvious that cyclic torsional shearing (static and cyclic load) is an effective method to compact loose soil. Fig. 6.16 shows the variation of surface settlement from 19 to 38.2 mm with the disc rotation angle from 0° to $\pm 10^\circ$

6.3.2 Density Change Due to Cyclic Torsional Shearing

Fig. 6.17 to Fig. 6.21 show the distributions of relative density due to cyclic torsional shearing angle of $\theta = \pm 1^\circ, \pm 3^\circ, \pm 5^\circ, \pm 7^\circ$ and $\pm 10^\circ$. Fig. 6.19 shows the compaction could effectively increase the relative density up to 70% at all depths at the shearing angle $\theta = \pm 5^\circ$. However, the soil densification was effective only for the 150 mm-thick soil lift. To increase the effective compaction depth from 0.15 m to 0.30 m, it is possible that the radius of the compaction disc has to increase from 0.15 m to 0.30 m.

Fig. 6.22 shows the density distribution for $\theta = 0^\circ$ to $\pm 10^\circ$. In the figure, the relative density of compacted fill increased with increasing disc rotation angle θ . The US Navy design manual (NAVFAC DM-7.2) described that for coarse-grained, granular well-graded soils with less than 4 percent passing No. 200 sieve, 70 to 75 relative density can be obtained by proper compaction procedures. In this study, $Dr = 70\%$ is selected as the minimum required density. In Fig. 6.22 shows, with static load $q = 9.2$ kPa and the lift thickness of 150 mm, the relative density $Dr = 70\%$ can be achieved with 20 cycles of torsional shearing with angle θ greater than $\pm 5^\circ$. Fig. 6.23 shows increasing shearing angle θ would make the relative density more focused. It was also

found the shearing angle θ greater than $\pm 5^\circ$, the relative density $Dr = 70\%$ could be achieved. It should be mentioned that the effective depth of compaction could be influenced by the applied normal stress q , angle of disc rotation θ , and number of shearing cycle N . Further study should be carried out regarding these parameters.

6.3.3 Stress Change Due to Cyclic Torsional Shearing

The change of vertical stress σ_v and horizontal stress σ_h in the fill due to cyclic torsional shearing are reported in this section. Fig. 6.24 to Fig. 6.28 show the measured after 20 cycles of cyclic torsional shearing at shearing angle $\theta = \pm 1^\circ, \pm 3^\circ, \pm 5^\circ, \pm 7^\circ$ and $\pm 10^\circ$. In Fig. 6.24, little σ_v change was observed between the loose fill and compacted sand. Fig. 6.25 to Fig. 6.28 also show no significant σ_v change after torsional shearing compaction. The vertical earth pressure σ_v was affected neither by the cyclic torsional shearing τ_{cyc} , nor by the shearing angle θ as shown in Fig. 6.29. Fig. 6.30 shows the normalized σ_v with shearing angle θ . From $\theta = 0^\circ$ to 10° , the $\sigma_v / \gamma z$ ratio is a constant 1.0. Based the test results, the vertical earth pressure in the fill was not changed by the cyclic shearing compaction.

Fig. 6.31 to Fig. 6.35 show the distribution of horizontal stress after cyclic torsional shearing. Fig. 6.31 shows, after the compaction at the shearing angle $\theta = \pm 1^\circ$ for 20 cycles, as compared with that for uncompacted soil, the horizontal earth pressure σ_h increased a little. From Fig. 6.32 to 6.35, it was found that the horizontal pressure increased with increasing shearing angle θ . Fig. 6.36 shows the distribution of horizontal stress σ_h after cyclic shearing with $\theta = \pm 1^\circ, \pm 3^\circ, \pm 5^\circ, \pm 7^\circ$ and $\pm 10^\circ$. It was clear that the horizontal earth pressure in the compacted fill increased with increasing shearing angle θ . Fig. 6.37 shows normalized σ_h with the shearing angle θ . It was obviously that the $\sigma_h / K_0 \gamma z$ ratio increased with increasing shearing angle for $\theta = 0^\circ$

to $\pm 5^\circ$. For an angle θ greater than $\pm 5^\circ$, the curve of $\sigma_h / K_o \gamma z$ vs. θ became flat. It was obviously that the cyclic shearing compaction would influence the horizontal earth pressure in the compacted fill.

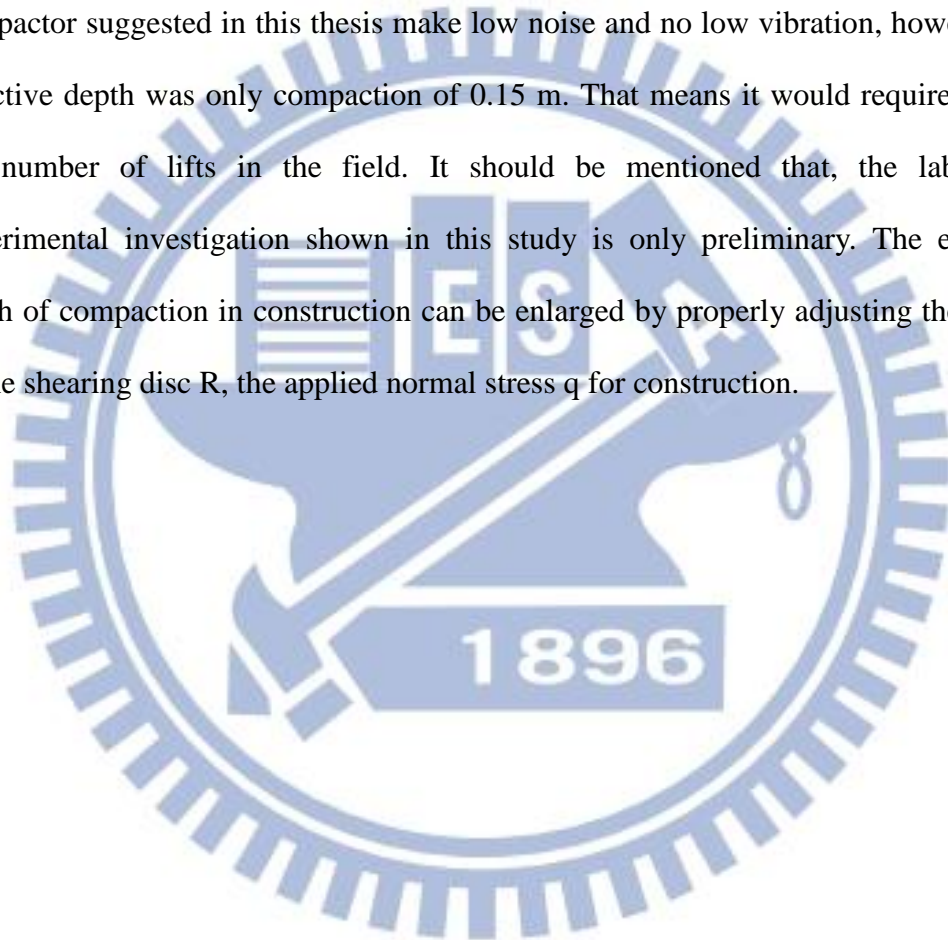
6.3.4 Cone Resistance Change Due to Cyclic Torsional Shearing

The change of CPT cone resistance in the fill due to cyclic shearing compaction is studied in this section. Fig. 6.38 to Fig. 6.42 shows the test result of cone resistance after 20 cycles of shearing at different the shearing angles. The cone resistance for loose sand and statically loaded sand are also shown in the figures. Fig. 6.38 shows, the cone resistance q_c has increased after compaction at shearing angle $\theta = \pm 1^\circ$. Fig. 6.39 to Fig. 6.42 show the tip resistance q_c at shearing angles of $\pm 3^\circ$, $\pm 5^\circ$, $\pm 7^\circ$ and $\pm 10^\circ$. As compared with that for loose fill, statically loaded fill, the cone resistance increased signification due to compaction. Fig. 6.43 shows the cone resistance increased significantly after cyclic shear compaction. Fig 6.44 showed the distribution of normalized q_c for uncompacted loose fill. For loose soil, the $q_c / q_{c, \text{loose}}$ was 1.0. In Fig 6.44, cone resistance ratio increased to about 4 times due to the static loading $q = 9.2$ kPa. After the application of static and cyclic shear compaction, the cone resistance increased up to about 6 times. The effects of static vertical load and cyclic shearing on the cone resistance of soil were quite obvious.

Fig. 6.45 to Fig. 6.49 show the cone resistance at different depths were converted to the relative density of soil with the method proposed by Jamiolkowski et al. (1985). In these figure, the calculated relative density of loose fill was compared with that measured in the lab. In fig 6.48, the test values were neared the calculated relative density at the shearing angle $\theta = \pm 7^\circ$ at the depth $z = 200$ mm to 300 mm. The cone resistance was very low at the depth $z = 0$ mm to 200 mm because of the extremely

low overburden and confining pressure. With such a thin soil fill ($H = 600 \text{ mm}$), it may not be a good idea to predict the distribution of soil density with the penetration test.

The effective depth of compaction plays an important role in field earthwork. Compaction with a smooth-wheel vibratory roller can easily reach an effective depth of compaction of 0.3 m. Although the compaction with the cyclic torsional shear compactor suggested in this thesis make low noise and no low vibration, however the effective depth was only compaction of 0.15 m. That means it would require double the number of lifts in the field. It should be mentioned that, the laboratory experimental investigation shown in this study is only preliminary. The effective depth of compaction in construction can be enlarged by properly adjusting the radius of the shearing disc R , the applied normal stress q for construction.



Chapter 7

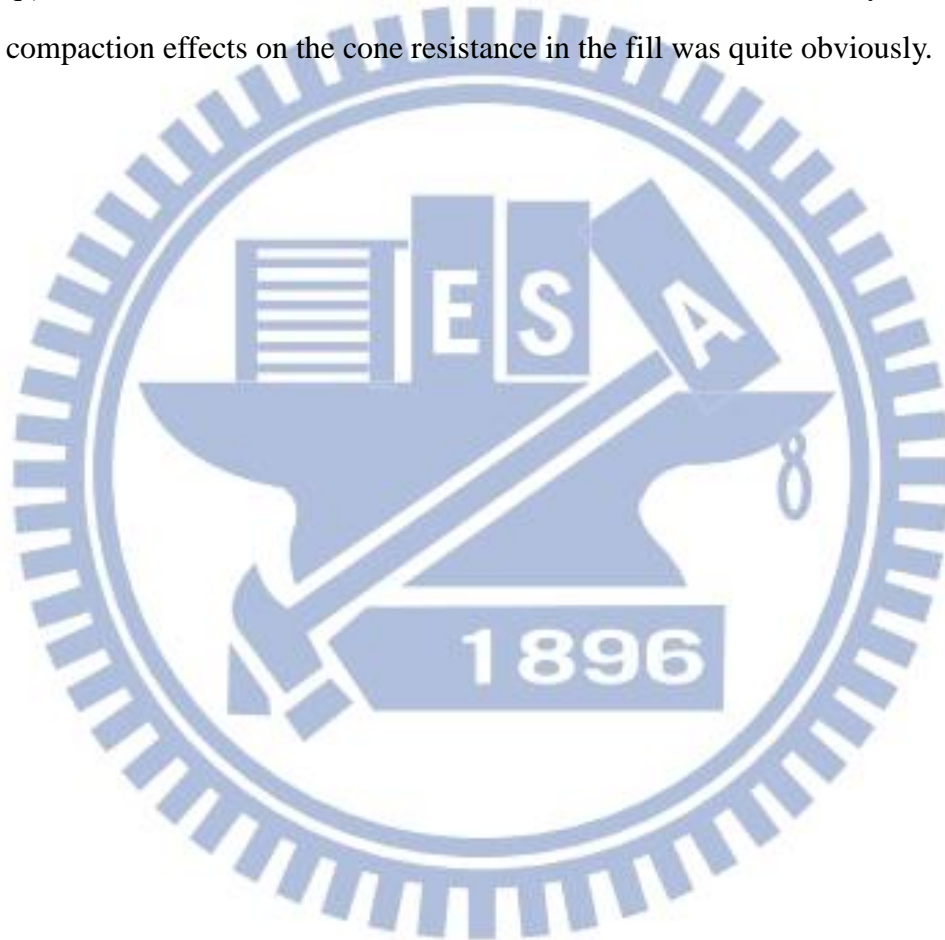
CONCLUSIONS

In this study, the surface settlement, change of relative density, stresses and cone resistance change in the soil due to static vertical loading, and cyclic torsional shearing compaction were investigated. Based on the experiment results, the following conclusions were drawn.

1. With the vertical loading $q = 9.2$ kPa on the surface of the four 150 mm-thick soil lift, the induced surface settlements varied from 15.0 to 22.3 mm. The average surface settlement was 19.0 mm, which was about 3.2% of the soil thickness. Static vertical loading is an effective method to compact the loose fill.
2. Static vertical loading represents the dead load of the cyclic torsional shear compactor. After the application of $q = 9.2$ kPa, on the average, the relative density of soil increased from 35.5% to about 62%, which was less than the target value $D_r = 70-85\%$ for dense sand.
3. As compared with that for uncompacted loose sand, the effects of static vertical loading on the vertical and horizontal earth pressure, in the compressed soil mass were not significantly.
4. The application of static vertical loading $q = 9.2$ kPa significantly increased the cone resistance of the compressed fill. The normalize cone resistance $q_c / q_{c, \text{loose}}$ increased from 1.0 to 4.6 due to static compression.
5. After 20 cycles of torsional shearing with the rotation angle of $\theta = \pm 10^\circ$ on the surface of the four 150 mm-thick lifts, the average surface settlement was 38.2 mm (volumetric strain = 6.4%). The extra surface settlement due to the torsional shearing compaction was about 19.2 mm. Cyclic torsional shearing compaction (static plus cyclic loads) is an effective method to densify loose soil.
6. With static load $q = 9.2$ kPa and the lift thickness of 150 mm, after 20 cycles of

torsional shearing with angle θ of $\pm 5^\circ$, the relative density achieved was 72 to 84%. The compacted relative density increased with increasing θ angle.

7. The vertical earth pressure in the fill was not influenced by the cyclic shearing compaction. However, after cyclic shearing compaction, the horizontal earth pressure in the compacted fill increased from 27% to 88%
8. After cyclic torsional shear compaction, the normalized cone resistance $q_c / q_{c, \text{loose}}$ increased from 4.6 to about 9.0. Test results showed the cyclic shearing compaction effects on the cone resistance in the fill was quite obviously.



References

1. ASTM D4253-93 (2007). "Standard Test Methods for Maximum Index Density and Unit Weight of Soils Using a Vibratory Table," Section four, Construction, Volume 04.08, Soil and Rock (I): D420-D5779 Annual Book of ASTM Standards, ASTM, Conshohocken, PA, USA.
2. Baldi, G., Bellotti, R., Ghionna, V., Jamiolkowski, M. and Pasqualini, E. (1986) "Interpretation of CPT s and CPTUs; 2nd part: drained penetration of sands". Proceedings of the Fourth International Geotechnical Seminar, Singapore, 143-56.
3. Borowicka, H., Influence of Rigidity of a Circular Foundation Slab on the Distribution of Pressures over the Contact Surface, *Proc. 1st Int. Conf. Soil Mech. Found. Eng.*, vol. 2, pp. 144-149, 1936.
4. Borowicka, H., The Distribution of Pressure under a Uniformly Loaded Elastic Strip Resting on Elastic-Isotropic Ground, 2d Cong. Int. Aaaoc. Bridge Struct. Eng., Berlin, Final report, vol. 8, no. 3, 1938.
5. Burgess, G. P. (1999). "Performance of Two Full-scale Model Geosynthetic Reinforced Segmental Retaining Walls," MS thesis, Royal Military College of Canada, Kingston, Ontario, 207.
6. Chang, S. Y., (2000), "Effect of Backfill Density on Active Earth Pressure," Master of Engineering Thesis, Dept. of of Civil Engineering, National Chiao Tung University, Hsinchu, Taiwan.
7. Chen, T. J., and Fang, Y. S, (2002). "A New Facility For Measurement of Earth Pressure At-Rest," *Geotechnical Engineering Journal*, SEAGS, 3(12), 153-159.
8. Chen, T. J., (2003). "Earth Pressures Due to Vibratory Compaction." Ph.D. Dissertation, National Chiao Tung University, Hsinchu, Taiwan.
9. Chen, T. J., and Fang, Y. S, (2008). "Earth Pressure Due to Vibratory Compaction", *Journal of Geotechnical and Geoenvironmental Engineering*, ASCE, 134 (4), 1-8.
10. Chen, K.Y., (2011). "Densification of Sand Due to Cyclic Torsional Shear

- Compaction.” Master of Engineering Thesis. Dissertation, National Chiao Tung University, Hsinchu, Taiwan.
11. D’Appolonia, D. J., Whitman, R. V., and D’Appolonia, E. (1969). “Sand Compaction with Vibratory Rollers.” *Journal of the Soil Mechanics and Foundations Division*, ASCE, 95(SM1), 263-284.
 12. Das, B. M., (1994), “Principal of Geotechnical Engineering. ” 3rd Edition, PWS Publishing Company, Boston.
 13. Das, B. M., (2011), “Principles of Soil Dynamics.”, 2nd Ed., Cengage Learning, Stamford, CT, USA.
 14. Das, B. M., (2010), “Principles of Geotechnical Engineering.”, 7th Ed., Cengage Learning, Stamford, CT, USA.
 15. Donath, A. D. (1891). “Untersuchungen ueber den erddruck auf stuetzwaende.” *Zeitschrift fuer Bauwesen*, Berlin.
 16. Duncan, J. M., and Seed, R. B. (1986). “Compaction-induced Earth Pressures under K_o -conditions.” *Journal of Geotechnical Engineering*, ASCE, 112(1), 1-22.
 17. Duncan, J. M., Williams, G. W., Sehn, A. L., and Seed, R. B. (1991). “Estimation earth pressures due to compaction.” *Journal of Geotechnical Engineering*, ASCE, 117(12), 1833-1847.
 18. Fang, Y. S. (1983). “Dynamic earth pressures against rotating walls.” Ph.D. dissertation, Department of Civil Engineering, University of Washington, Seattle, Washington.
 19. Fang, Y. S., Chen, T. J., Holtz, R. D., and Lee, W. F., (2004). “Reduction of Boundary Friction in Model Tests”, *Geotechnical Testing Journal*, ASTM, 27(1), 1-10.
 20. Filz, G. M., and Duncan J. M. “Earth Pressures due to Compaction: Comparison of Theory with Laboratory and Field Behavior.” *Transportation research record*, 1526, 28-37.
 21. Ho, Y. C., (1999), “Effects of Backfill Compaction on Passive Earth Pressure,”

- Master of Engineering Thesis, National Chaio Tung University, Hsinchu, Taiwan
22. Hsu, C. C., and Vucetic, M., (2004), "Volumetric Threshold Shear Strain for Cyclic Settlement," *Journal of Geotechnical and Geoenvironmental Engineering*, ASCE, 130 (11), 58-70.
23. Huang, Y. X., (2008) "A Study on the Disc Shearing Behavior of Sand in a Mid-size Soil Tank," Master of Engineering Thesis, Chung Yuan Christian University, Chungli, Taiwan.
24. Ingold, T. S. (1979). "Retaining wall performance during backfilling." *Journal of the Geotechnical Engineering Division*, ASCE, 105(GT5), 613-626.
25. Ingold, T. S. (1979). "The effects of compaction on retaining walls." *Geotechnique*, 29(3), 265-283.
26. Ishibashi, I., and Sherif, M. A., (1974), "Soil Liquefaction by Torsional Simple Shear Device," *Journal of the Geotechnical Engineering Division*, ASCE, 100 (8), 871-888.
27. Ishibashi, I., Kawamura, M., and Bhatia, S. K., (1985), "Effect of Initial Shearing on Cyclic Drained and Undrained Characteristics of Sand." *Geotechnical Engineering Report 85-2*, School of Civil and Environmental Engineering, Cornell University, Ithaca, New York, USA.
28. Jaky, J. (1944). "The Coefficient of Earth Pressure at rest." *Journal for Society of Hungarian Architects and Engineers*, Budapest, Hungary, Oct., 355-358.
29. Jaky, J., (1948), "Pressure in Soils," *Proceedings, 2nd International Conference on Soil Mechanics and Foundation Engineering*, 1, 103-107.
30. Jamiolkowski, M., Ladd, C.C., Germaine, J.T. and Lancellotta, R. (1985) "New developments in field and laboratory testing of soils". State-of-the art report. *Proceeding of the 11th International Conference on Soil Mechanics and Foundation Engineering*, San Francisco, 1, 57-153, Balkema Pub., Rotterdam.
31. Johnson, A. W., and Sallberg, J. R. (1960). "Factors That Influence Field Compaction of Soil." Highway Research Board, *Bulletin* No. 272.
32. Kramer, S. L., (1996), "Geotechnical Earthquake Engineering", Prentice-Hall, Inc.,

Upper Saddle River, New Jersey.

33. Lo Presti, D. C. F., Pedroni, S., and Crippa, V. (1992). "Maximum Dry Density of Cohesionless Soils by Pluviation and by ASTM D 4253-83: A comparative study." *Geotechnical Testing Journal*, ASTM, 15(2), 180-189.
34. Mayne, P. W., and Kulhawy, F. H. (1982). " K_o -OCR Relationships in Soil." *Journal of Geotechnical Engineering Division*, ASCE, 108(GT6), 851-872.
35. McElroy, J. A. (1997). "Seismic Stability of Geosynthetic Reinforced Slopes: A shaking table study." MS thesis, University of Washington, Seattle, 286.
36. Mesri, G., and Hayat, T. M. (1993). "The Coefficient of Earth Pressure at rest." *Canadian Geotechnical Journal*, 30(4), 647-666.
37. Miura, K., Tsukada, Y., Tsubokawa, Y., Ishito, M., Nishimura, N., Ohtani, Y., and You, G. L., (2000), "Bearing capacity during earthquake of the spread footing reinforced with micropiles." *Proceedings, 12th World Conference on Earthquake Engineering*, pp. 1-8.
38. Peck, R. B., and Mesri, G. (1987). Discussion of "Compacted-induced earth pressures under K_o -conditions." *Journal of Geotechnical Engineering*, ASCE, 113(11), 1406-1408.
39. Rad, N. S., and Tumay, M. T. (1987). "Factors affecting sand specimen preparation by raining." *ASTM Geotechnical Testing Journal*, 10(1), 31-37.
40. Ren, F. Y., (2006) "A Study on the Influence of Type of Plate Shearing on the Relative Density of Loose Sand," Master of Engineering Thesis, Chung Yuan Christian University, Chungli, Taiwan.
41. Seed, R. B., and Duncan, J. M. (1983). "Soil-Structure Interaction Effects of Compaction-induced Stresses and Deflections." *Geotechnical Engineering Research Report No. UCB/GT/83-06*, Univ. of California Berkeley, CA.
42. Sowers, G. F., Robb, A. D., Mullis, C. H., and Glenn, A. J. (1957). "The Residual Lateral Pressures Produced by Compacting Soils." *Proceedings, 4th International Conference on Soil Mechanics and Foundation Engineering*, London, 243-247.
43. Terzaghi, K. (1934). "Large retaining-wall tests (I): Pressure of dry sand."

- Engineering News-Record*, 112, 136-140.
44. Terzaghi, K. (1941). "General wedge theory of earth pressure." *ASCE Transactions*, 106, 68-80.
45. Terzaghi, K. (1943). *Theoretical Soil Mechanics*, Wiley, New York.
46. Tzeng, S. K., (2002). "Horizontal Pressure on an Unyielding Wall due to Strip Loading on Backfill with Different Densities." MS thesis, Dept. of Civil Engineering, National Chiao Tung University, Hsinchu, Taiwan.
47. Robertson P. K. and Cabal K.L. (Robertson), (2009). "Guide to Cone Penetration Testing for Geotechnical Engineering." Gregg Drilling & Testing, Inc. Corporate Headquarters 2726 Walnut Avenue Signal Hill, California 90755.
48. US NAVY. (1982). "Foundations and Earth Structures." *NAVFAC Design Manual DM-7.2*. Naval Facilities Engineering Command, U.S. Government Printing Office, Washington, D. C., 60.
49. Vesic, A. S., (1973), "Analysis of Ultimate Loads of Shallow Foundations," *Journal of the Soil Mechanics and Foundations Division, ASCE*, 99 (1), 45-73.
50. Vesic, A. S., Banks, D. C., and Woodard, J. M. (1965). "An Experimental Study of Dynamic Bearing Capacity of Footings on Sand." *Proceedings, Sixth International Conference on Soil Mechanics and Foundation Engineering*, Montreal, Canada, II, 209-213.
51. Wang, F. J., (2005). "Effects of Adjacent Rock Face Inclination on Earth Pressure at-rest." MS thesis, Dept. of Civil Engineering, National Chiao Tung University, Hsinchu, Taiwan.
52. Yang, C. T., (2002) "A Study on Plate Shear to Improve Relative Density of Sand," Master of Engineering Thesis, Chung Yuan Christian University, Chungli, Taiwan.
53. Youd, T. L., (1972), "Compaction of Sand by Repeated Straining," *Journal of the Soil Mechanics and Foundations Division, ASCE*, 98 (7), 709-725.

Table2.1. Qualitative description of granular soil deposits

Relative density (%) Das (2010)	Relative density (%) Lambe and Whitman (1969)	Description of soil deposit
0 - 15	0 - 15	Very loose
15 - 50	15 - 35	Loose
50 - 70	35 - 65	Medium
70 - 85	65 - 85	Dense
85 - 100	85 - 100	Very dense

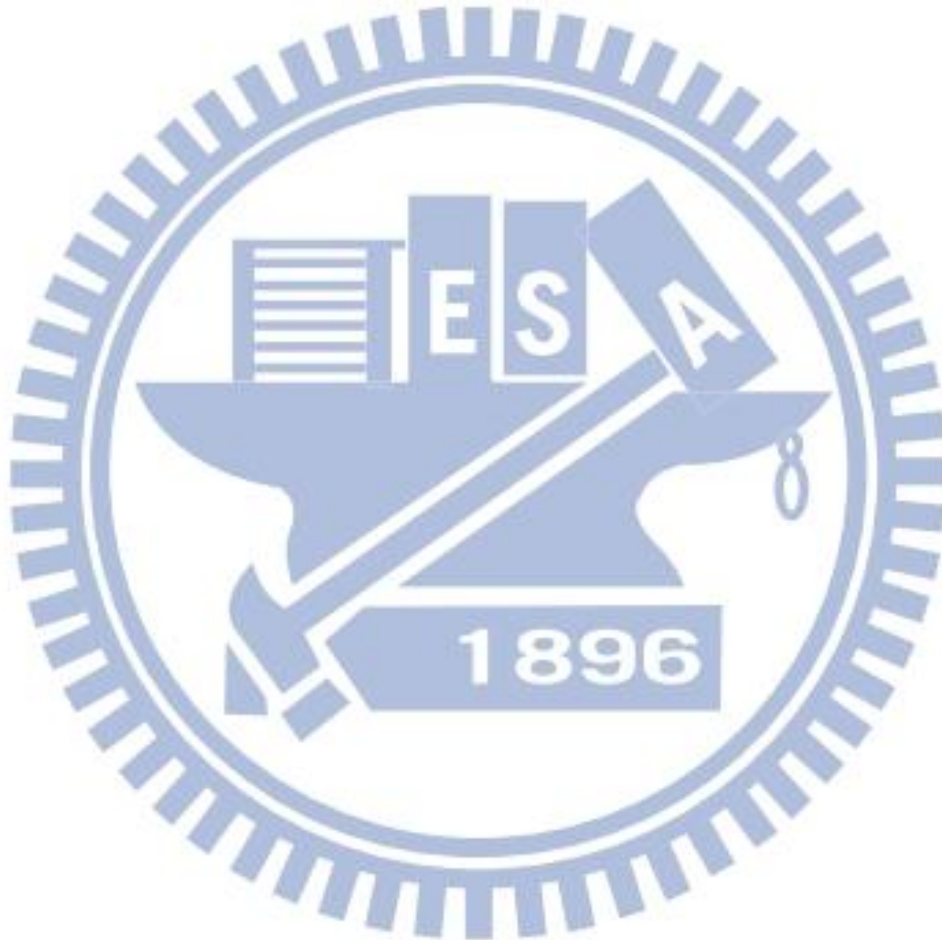


Table3.1. Characteristics of normal loading discs

Thickness Disc (mm)	37.5	20.0	10.0	3.0	2.0	1.0
Mass (kg)	19.80	9.60	4.80	1.55	1.05	0.50
Quantity Ordered	4	3	1	2	3	4

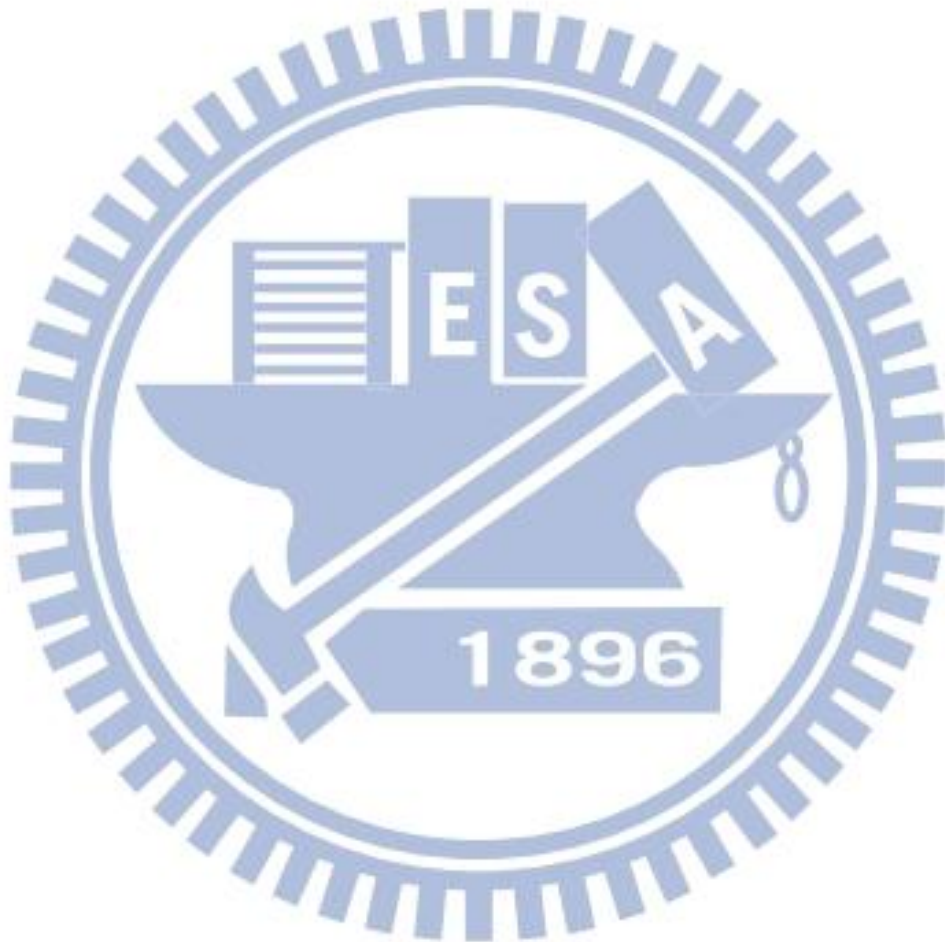
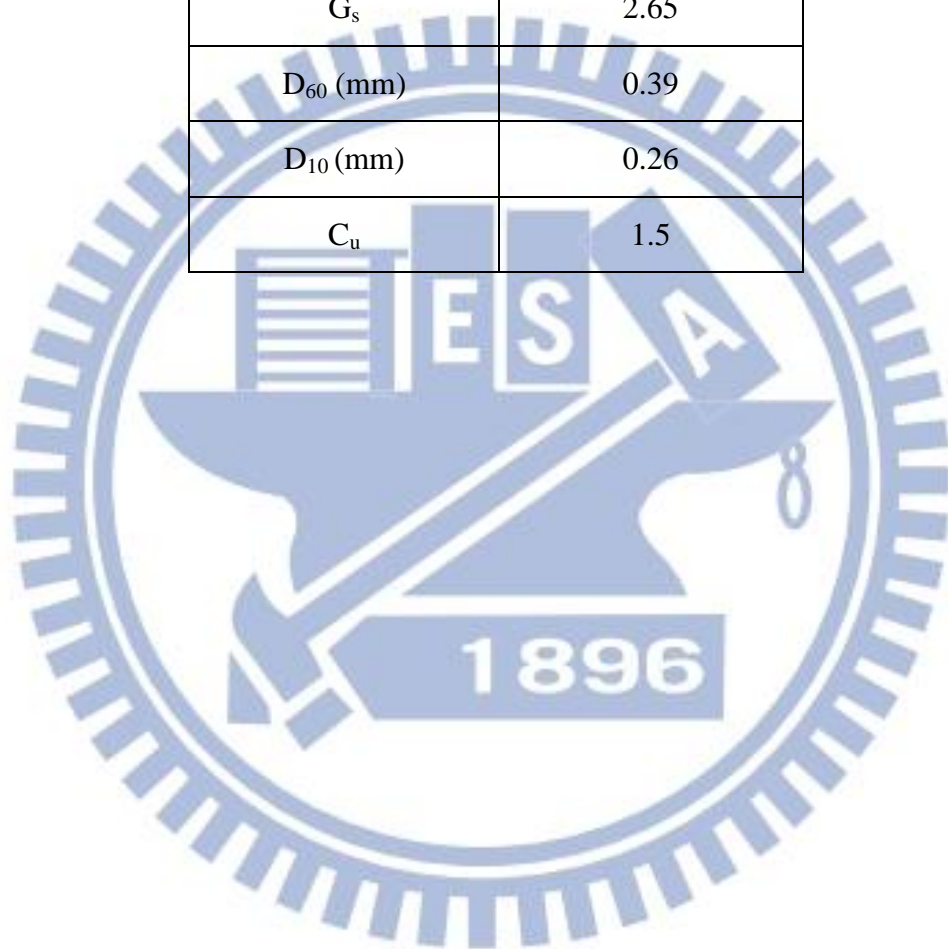


Table 4.1. Properties of Ottawa Sand (after Chen, 2003)

Shape	Rounded
e_{\max}	0.76
e_{\min}	0.50
G_s	2.65
D_{60} (mm)	0.39
D_{10} (mm)	0.26
C_u	1.5



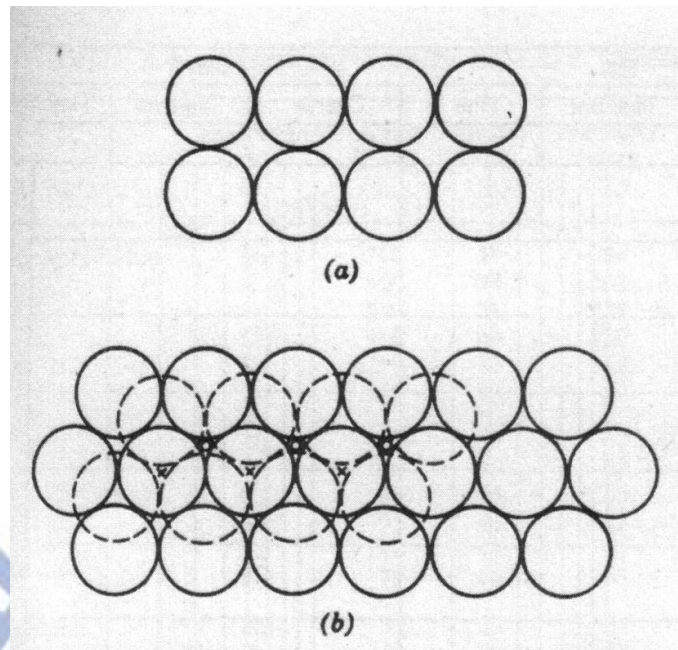


Fig. 2.1. Arrangement of uniform spheres (after Deresiewicz, 1958)

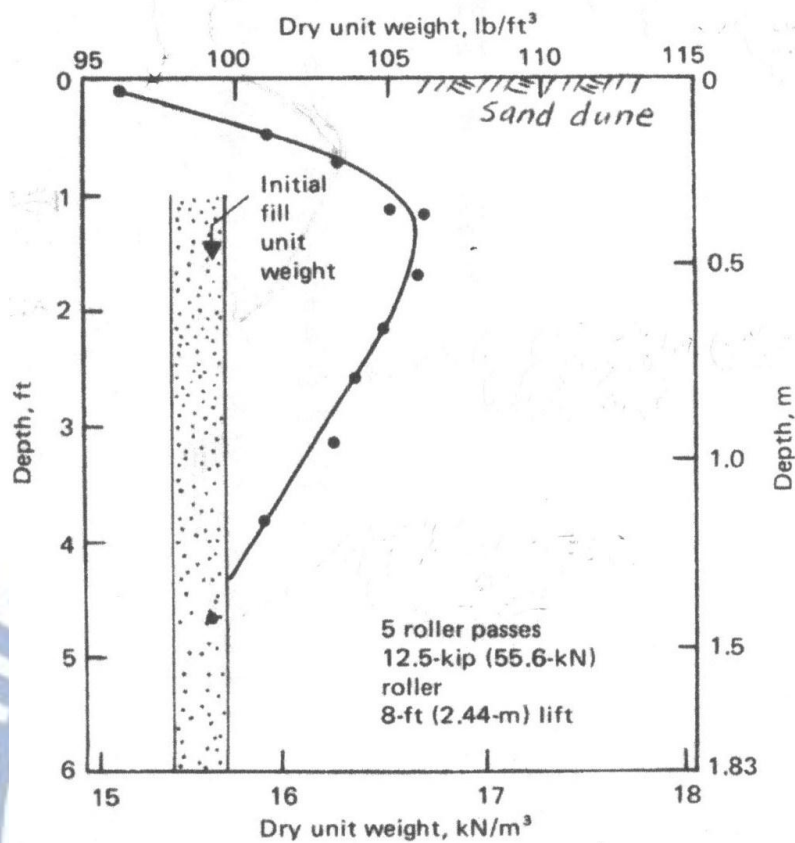


Fig. 2.2. Unit weight vs. depth relation for vibratory roller compaction
(after Whitman and D'Appolonia, 1969)

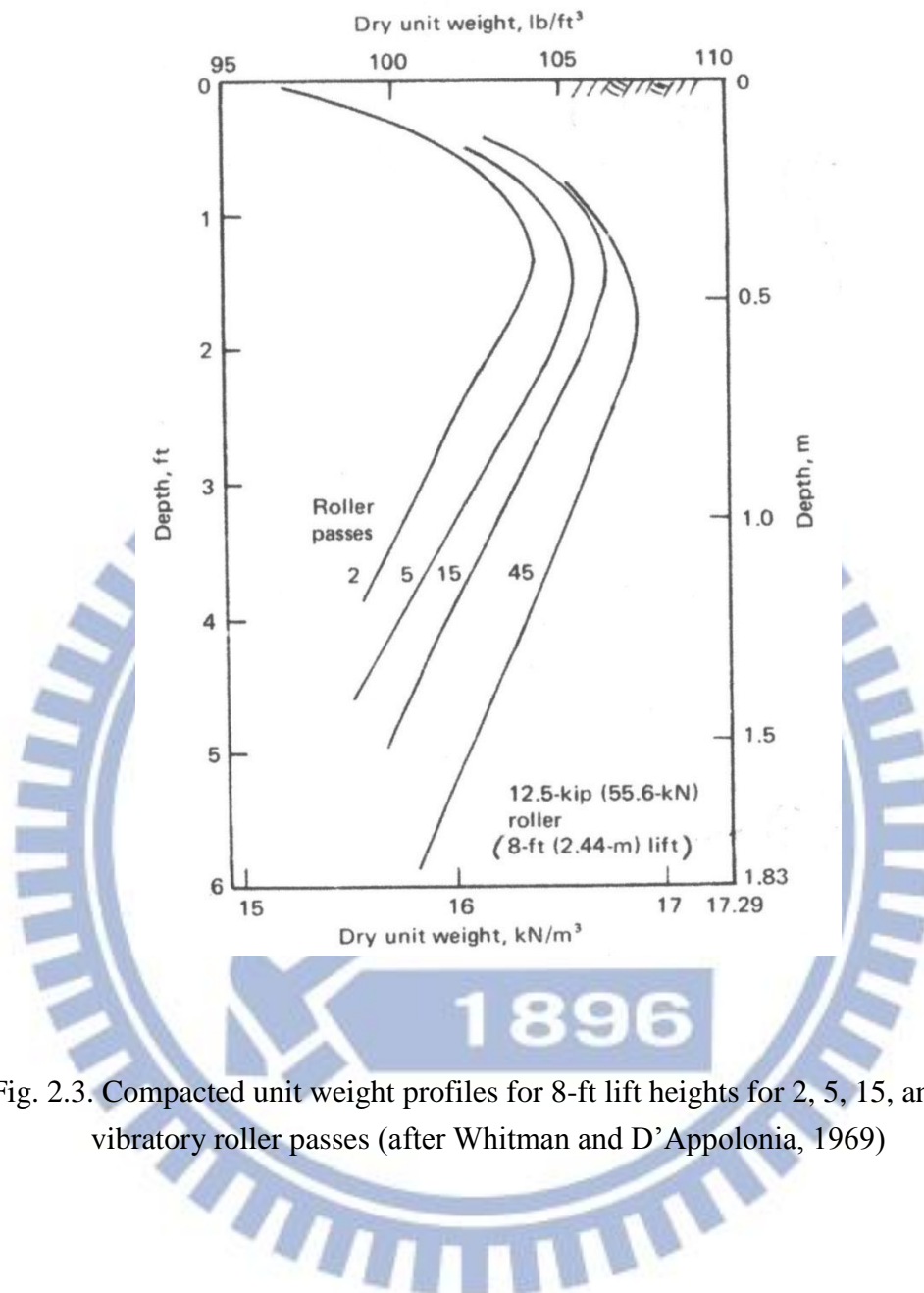


Fig. 2.3. Compacted unit weight profiles for 8-ft lift heights for 2, 5, 15, and 45 vibratory roller passes (after Whitman and D'Appolonia, 1969)

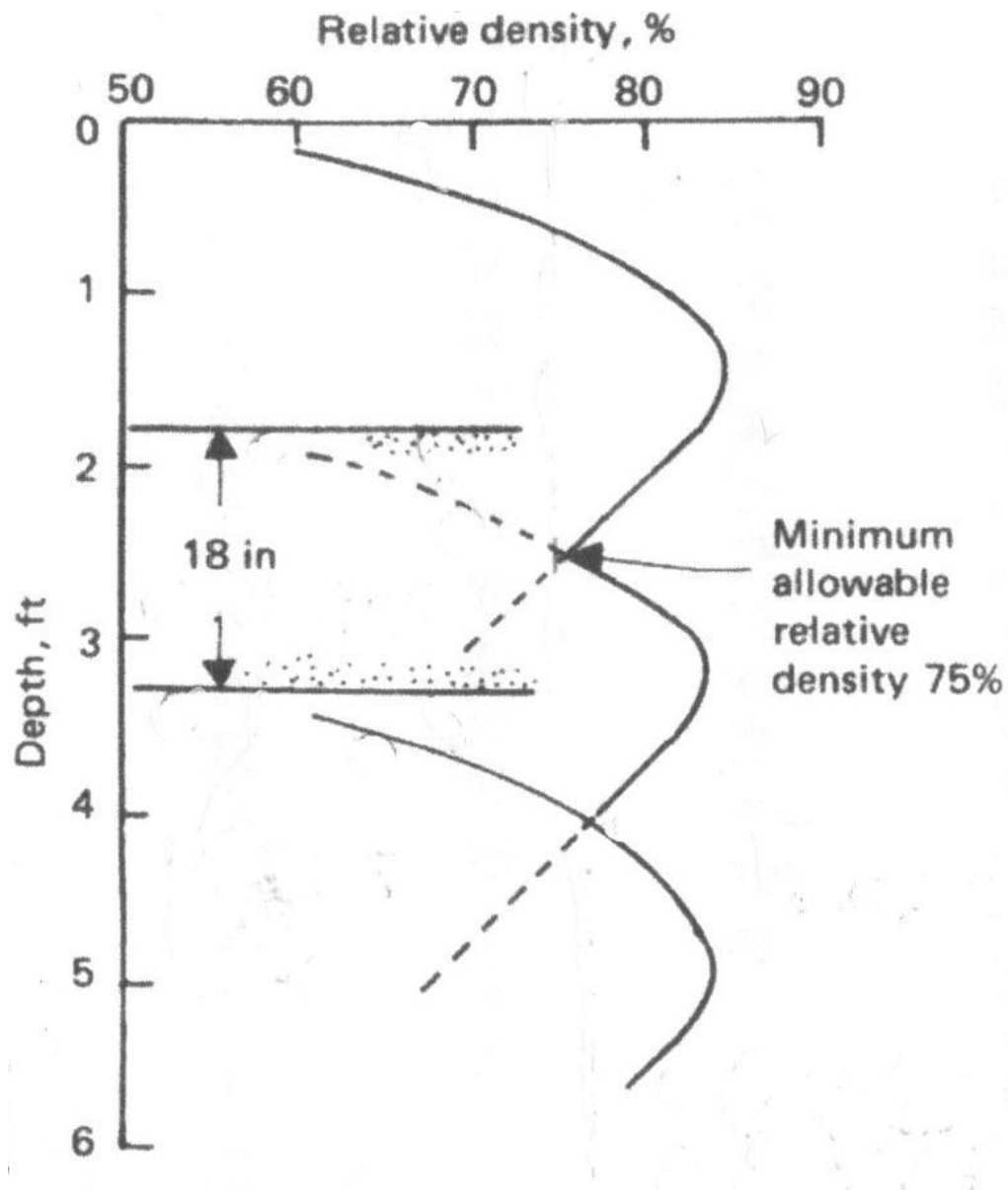


Fig. 2.4. Approximate method for determining lift height required to achieve a minimum compacted relative density of 75% with five roller passes using data for a large lift height
(after Whitman and D'Appolonia, 1969)

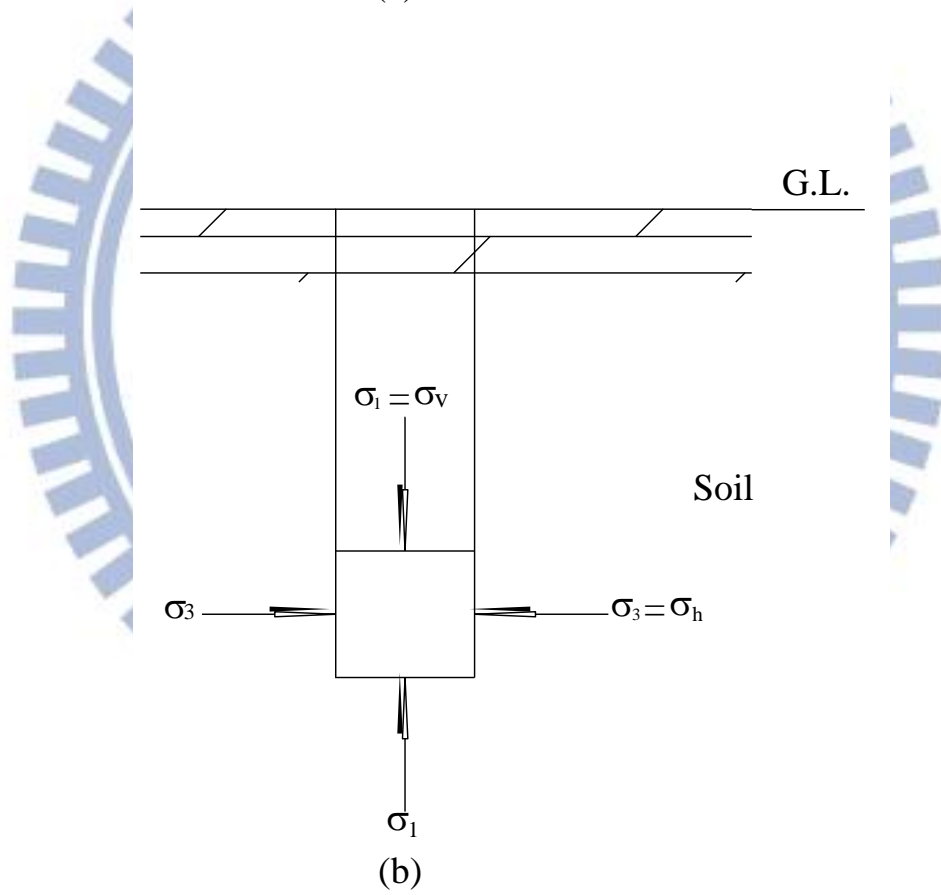
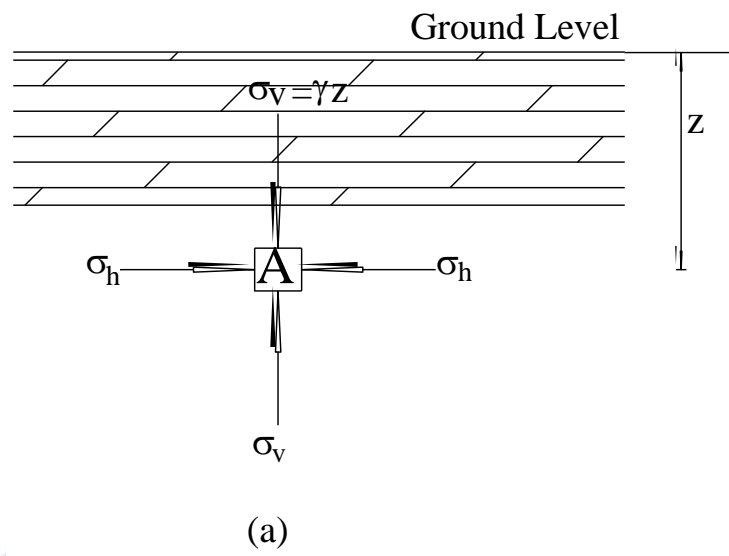


Fig. 2.5. Development of in-situ stresses (after Chen, 2003)

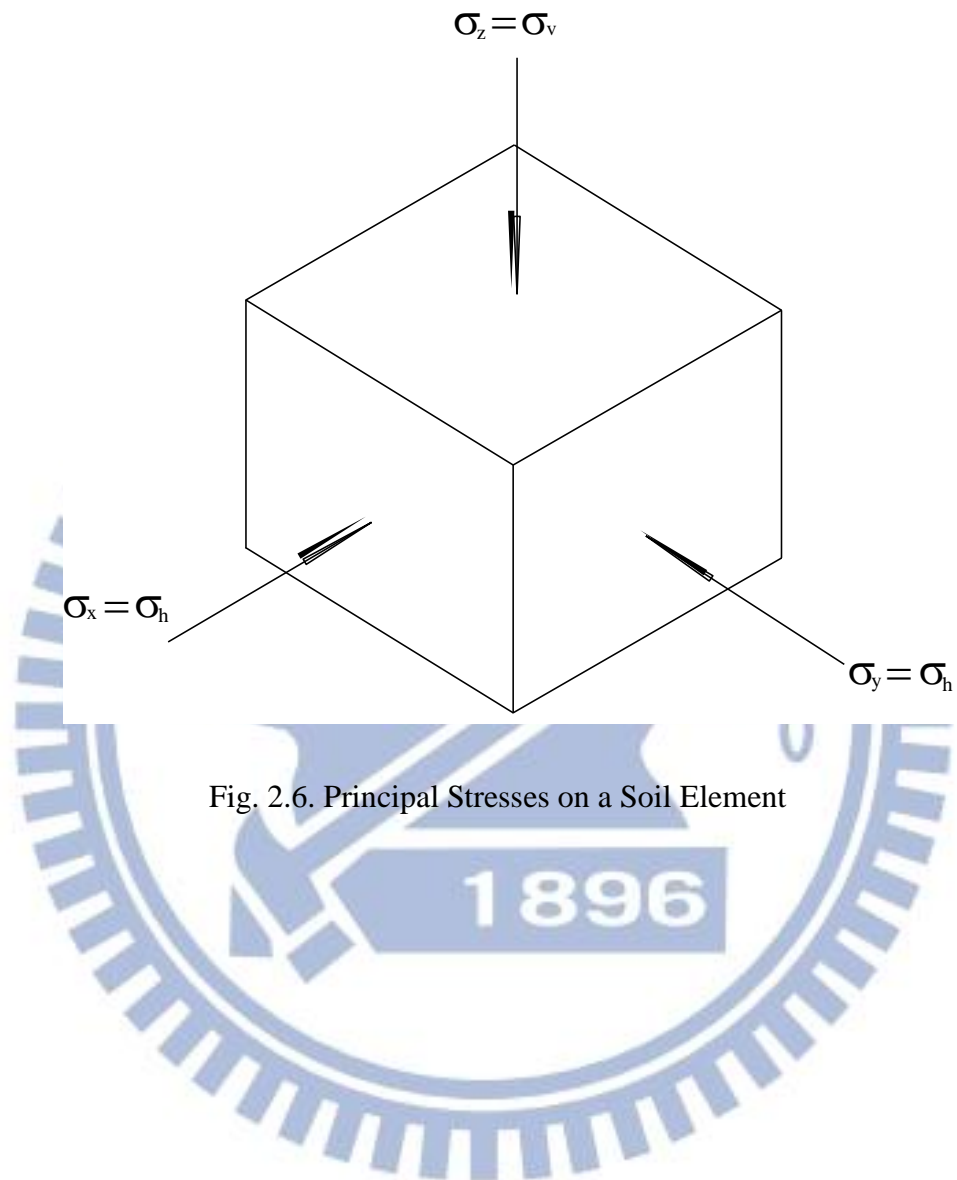


Fig. 2.6. Principal Stresses on a Soil Element

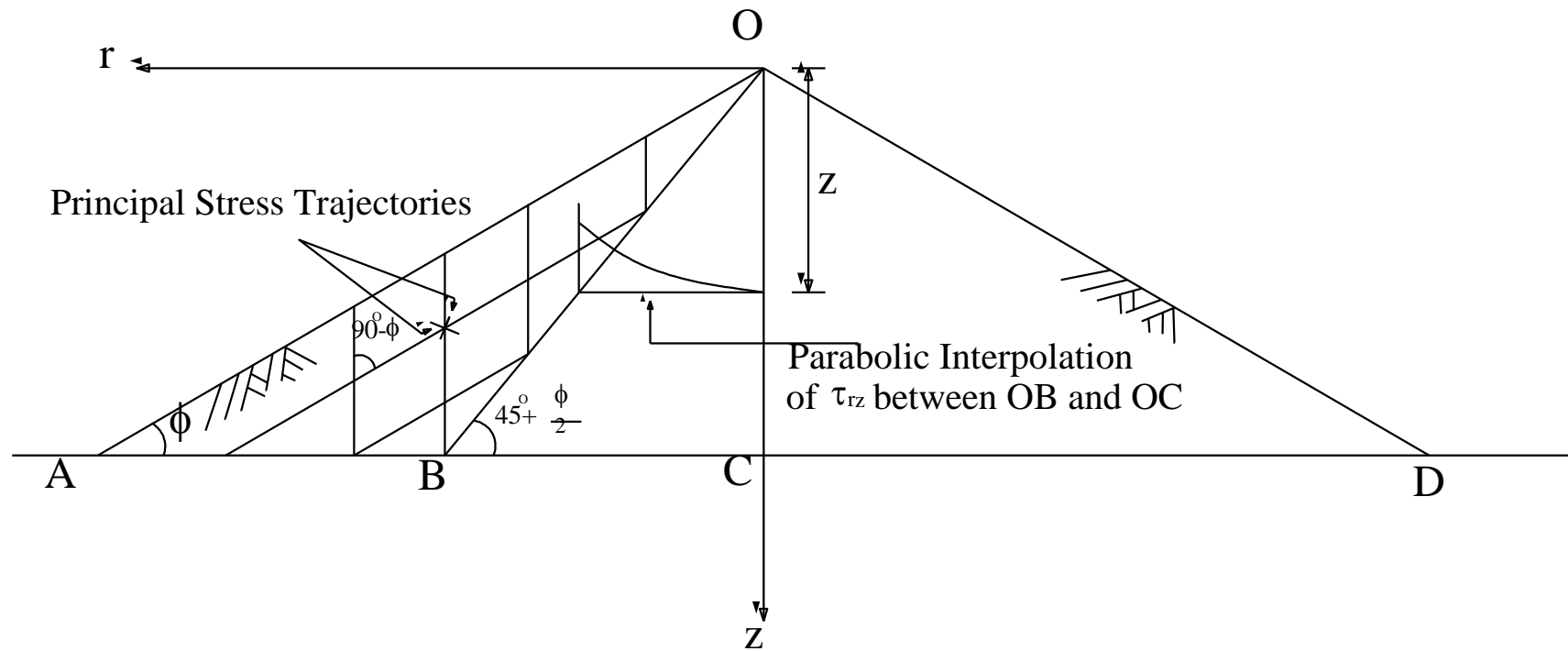


Fig. 2.7. Jaky's Formulation of the Relationship between K_o on OC and Mobilized in OAB (after Mesri and Hayat, 1993)

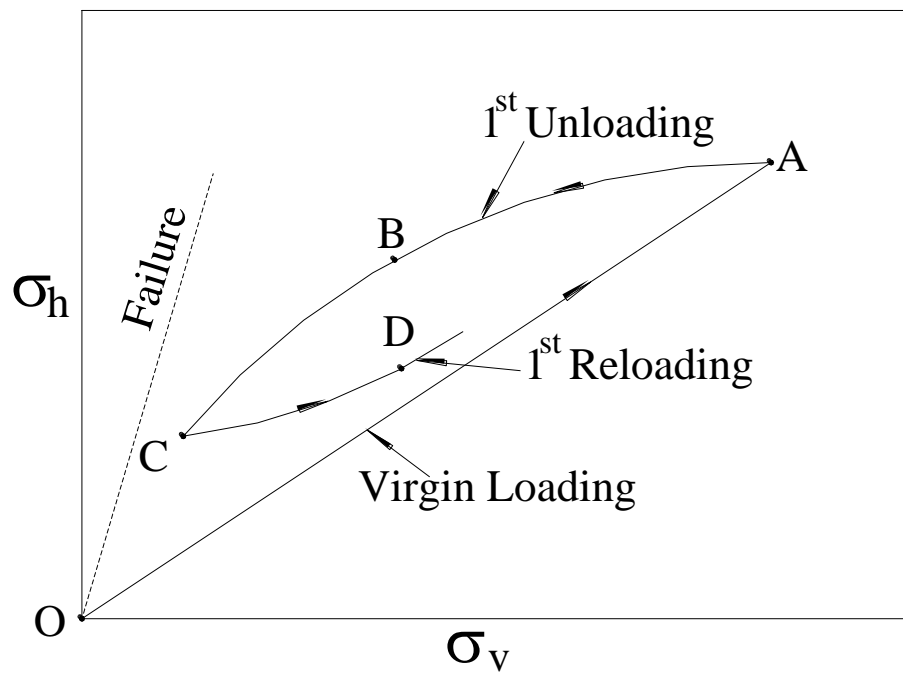


Fig. 2.8. Simplified stress history of soil under K_0 conditions (after Mayne and Kulhawy, 1982)

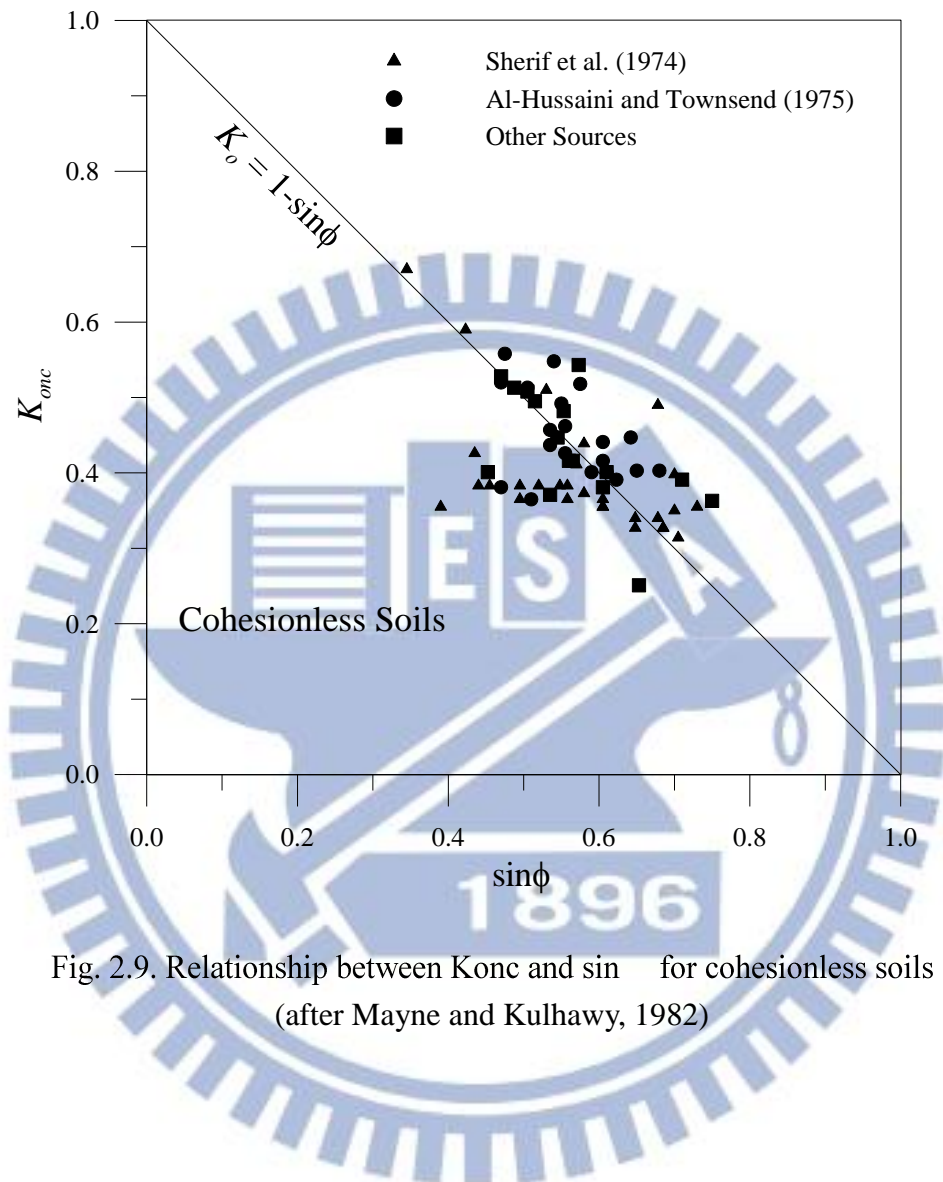


Fig. 2.9. Relationship between K_{0nc} and $\sin \phi$ for cohesionless soils
(after Mayne and Kulhawy, 1982)

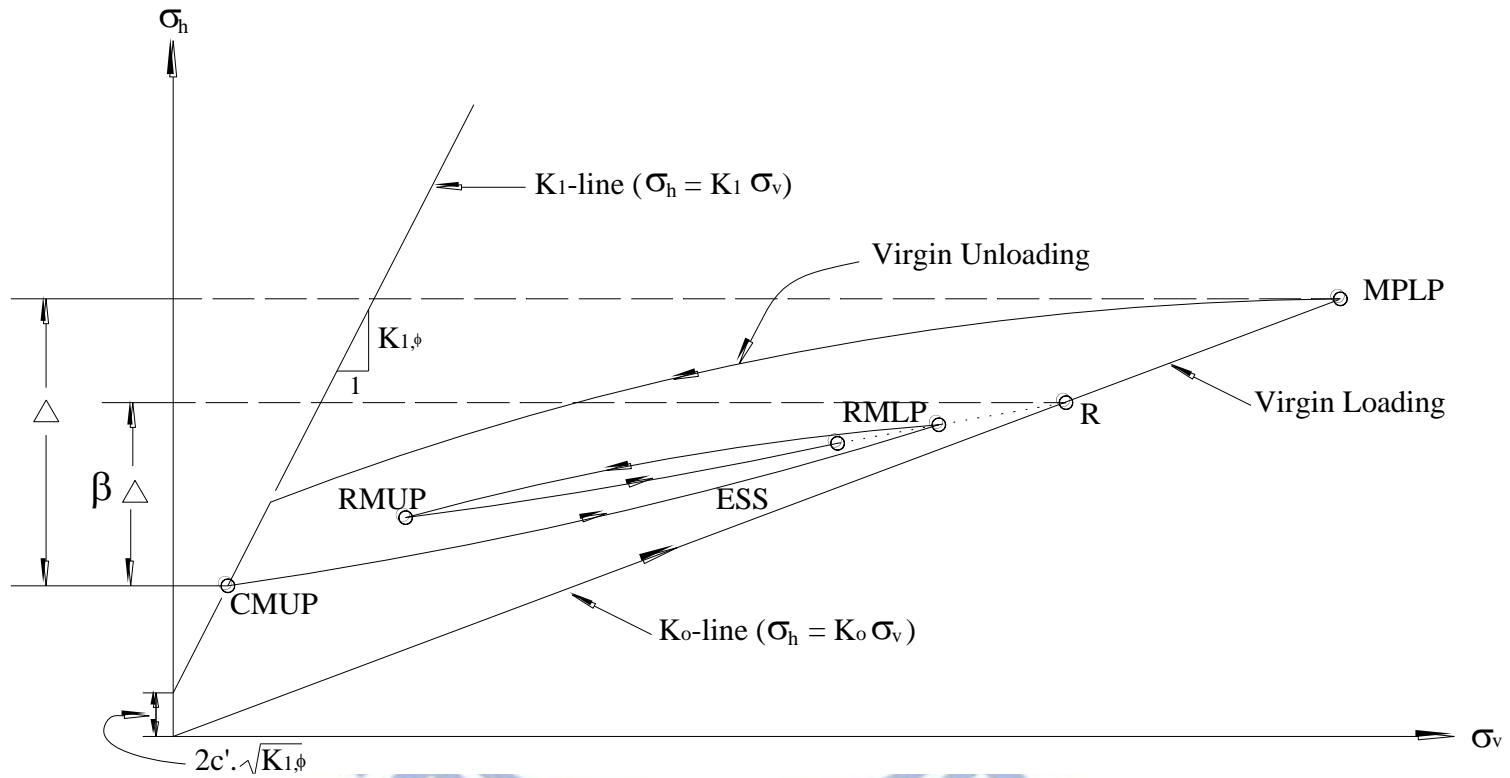


Fig. 2.10. Basic components of hysteretic K_o -loading/unloading model (after Duncan and Seed, 1986)

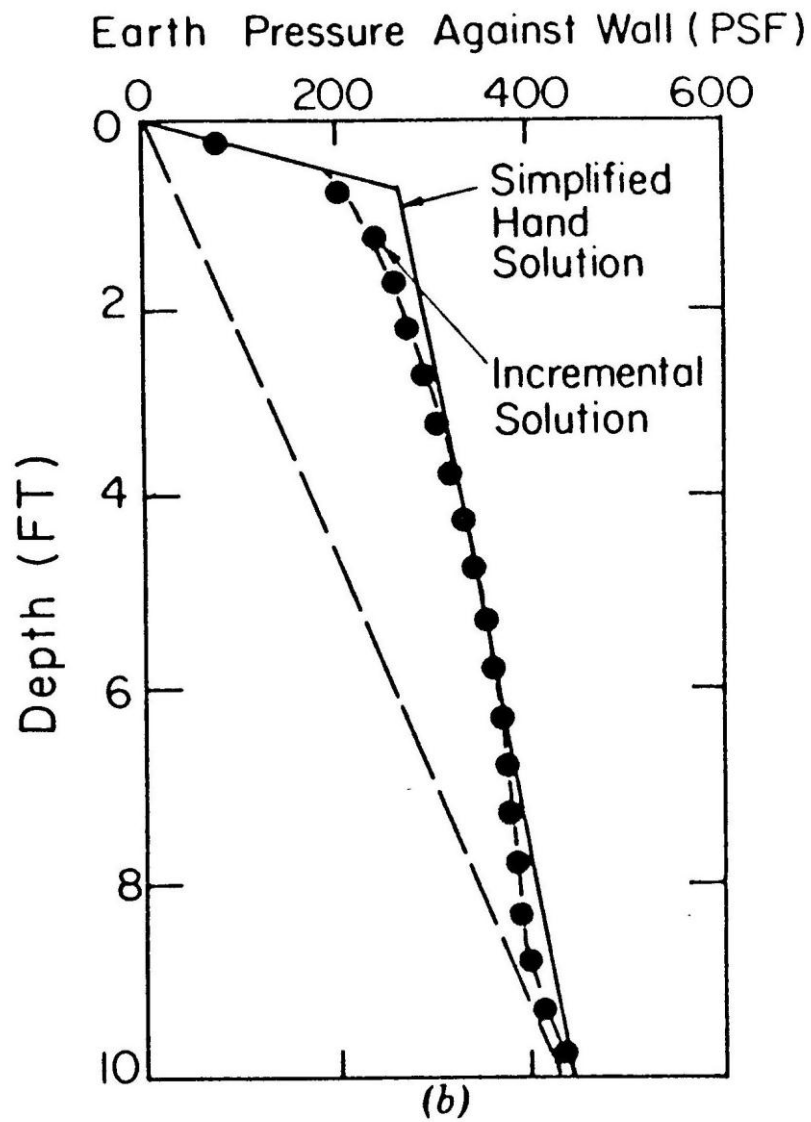


Fig. 2.11. Comparison between Final Pressure Distributions Based on Incremental Analysis and Hand Solution (after Duncan and Seed, 1983)

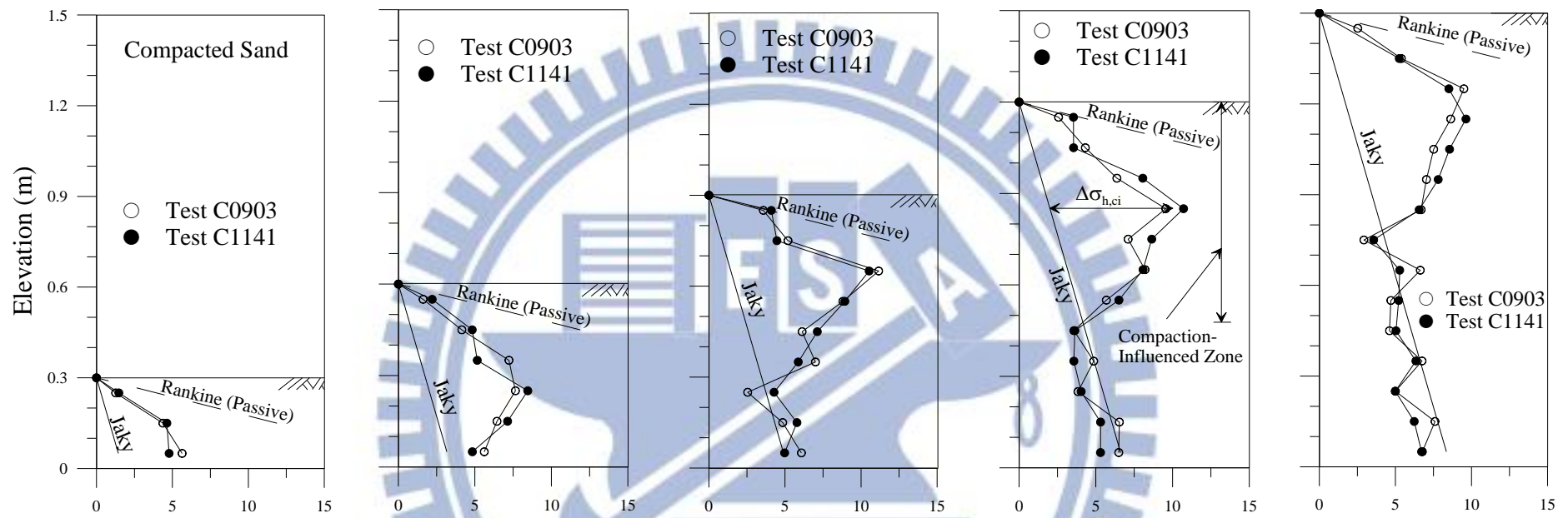


Fig. 2.12. Distribution of Horizontal Earth Pressure after Compaction (after Chen and Fang, 2008)

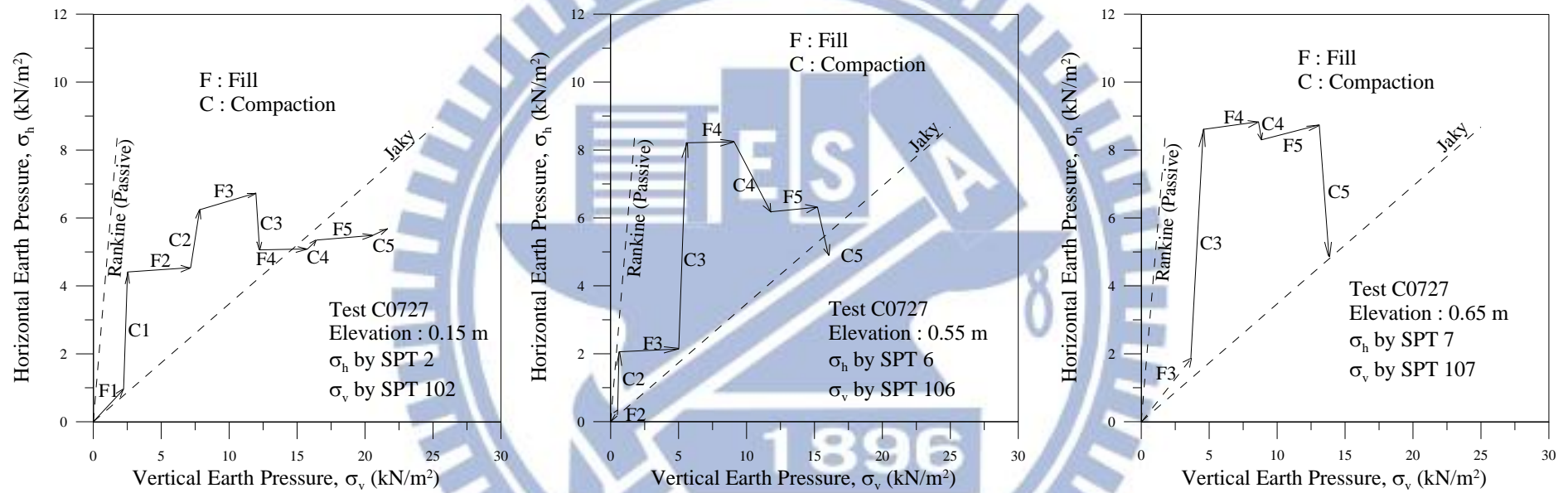


Fig. 2.13. Stress path of a soil element under compaction (after Chen and Fang, 2008)

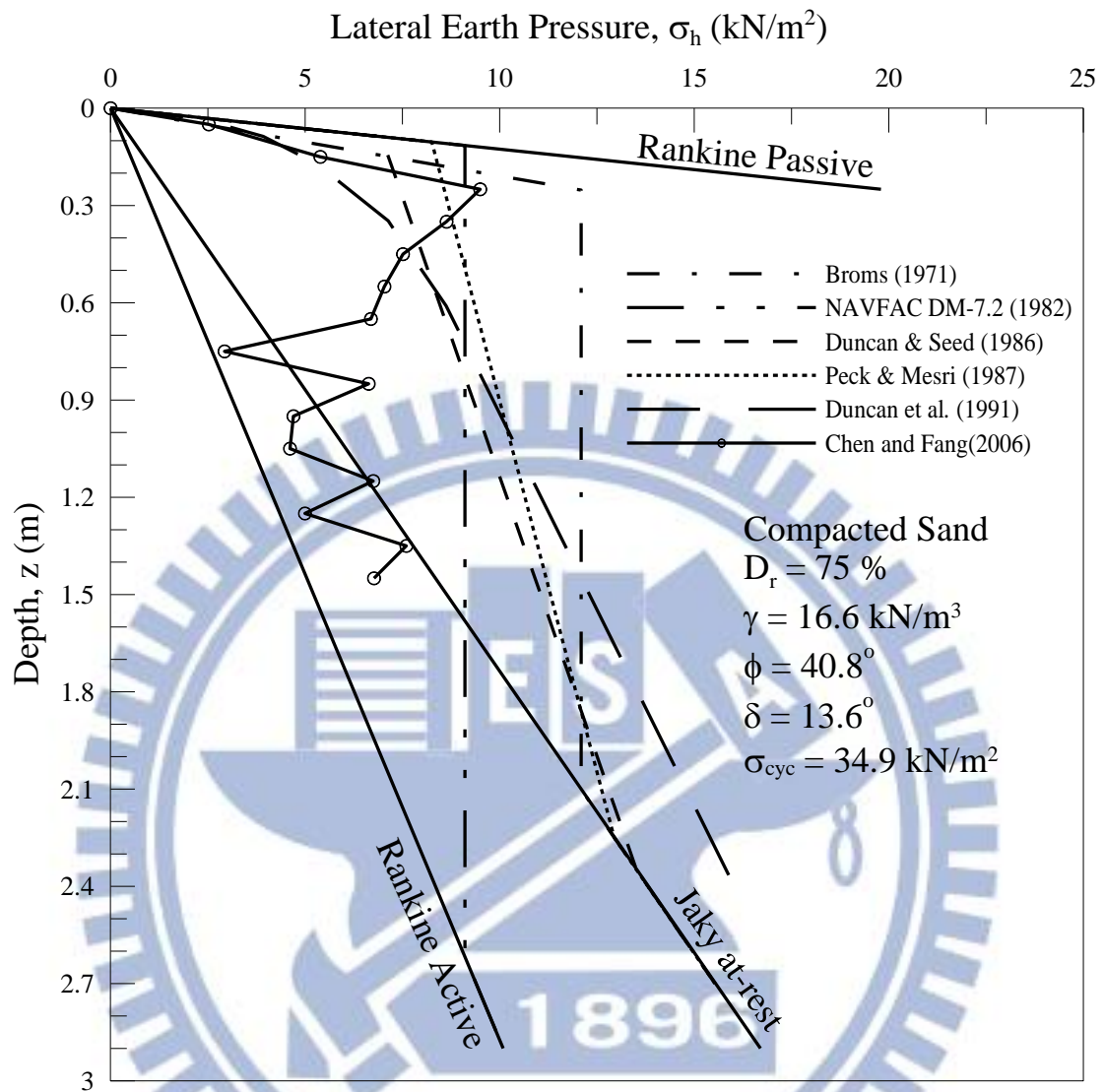


Fig. 2.14. Horizontal Earth Pressure Estimated with Various Methods after Compaction (after Chen and Fang, 2008)

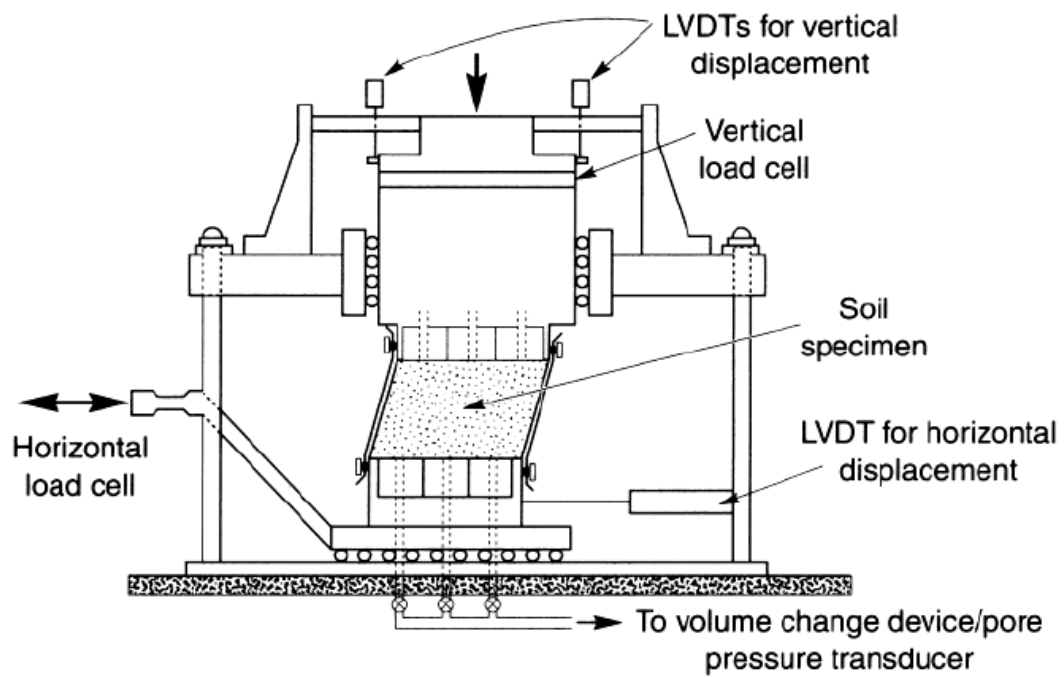


Fig. 2.15. NGI cyclic simple shear apparatus (after Airey and Wood, 1987)

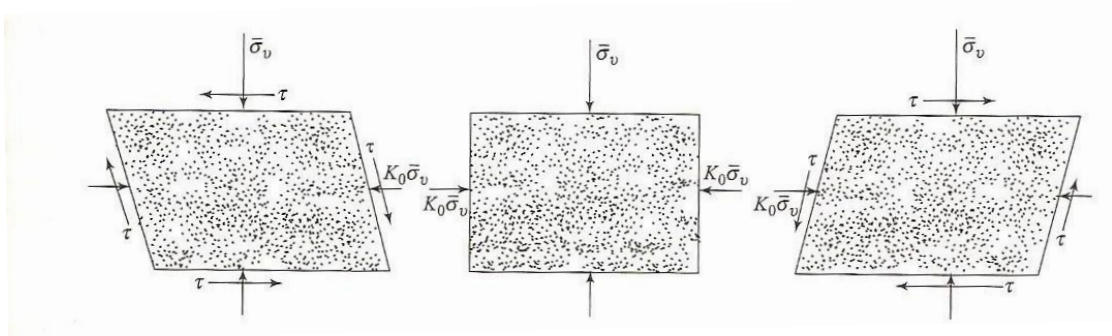
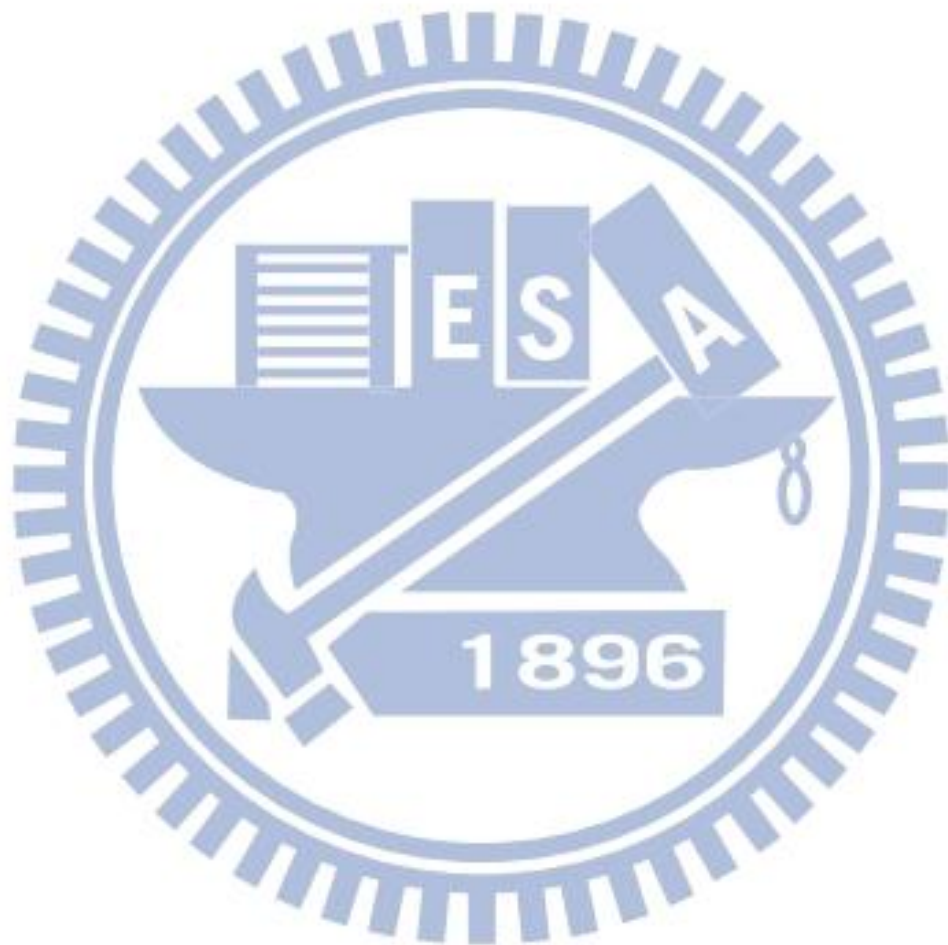


Fig. 2.16. Stress conditions of a soil specimen cyclic horizontal shear stress



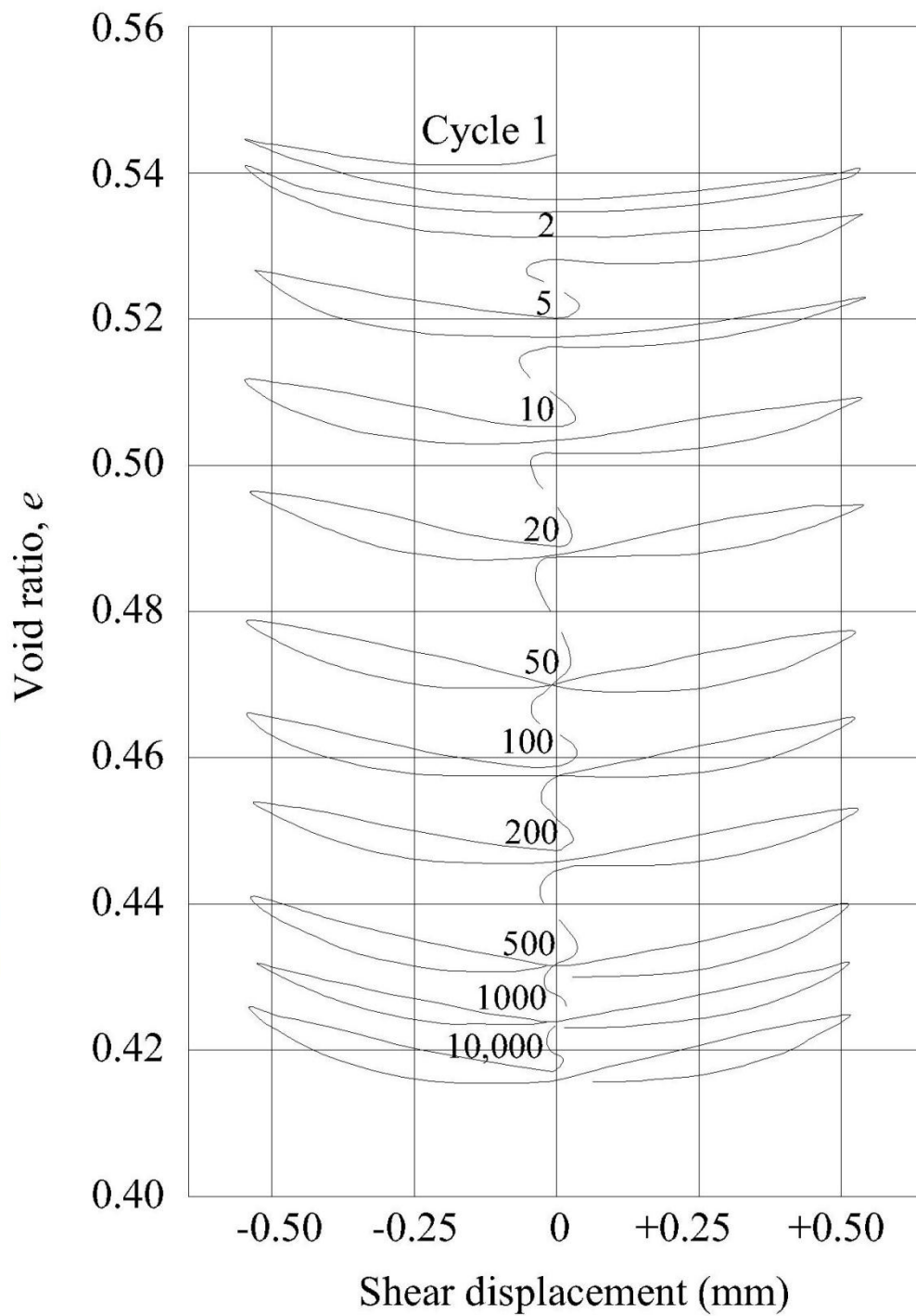


Fig. 2.17. Void ratio versus cyclic displacement for densification of a sand with successive cycles of shear (after Youd, 1972)

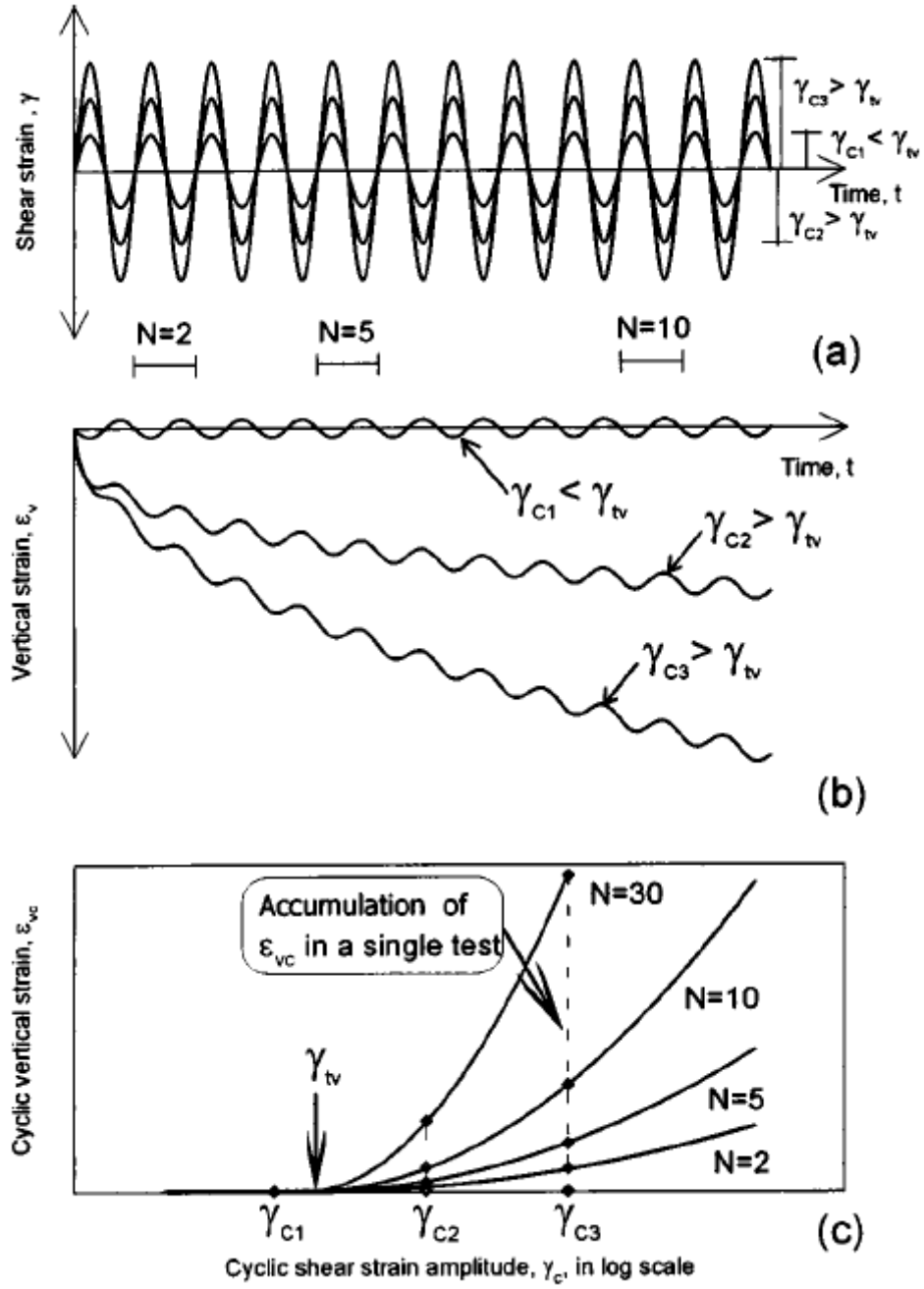


Fig. 2.18. Sketch of typical results of cyclic simple shear strain-controlled tests with definitions of volumetric cyclic threshold strain (after Hsu and Vucetic, 2004)

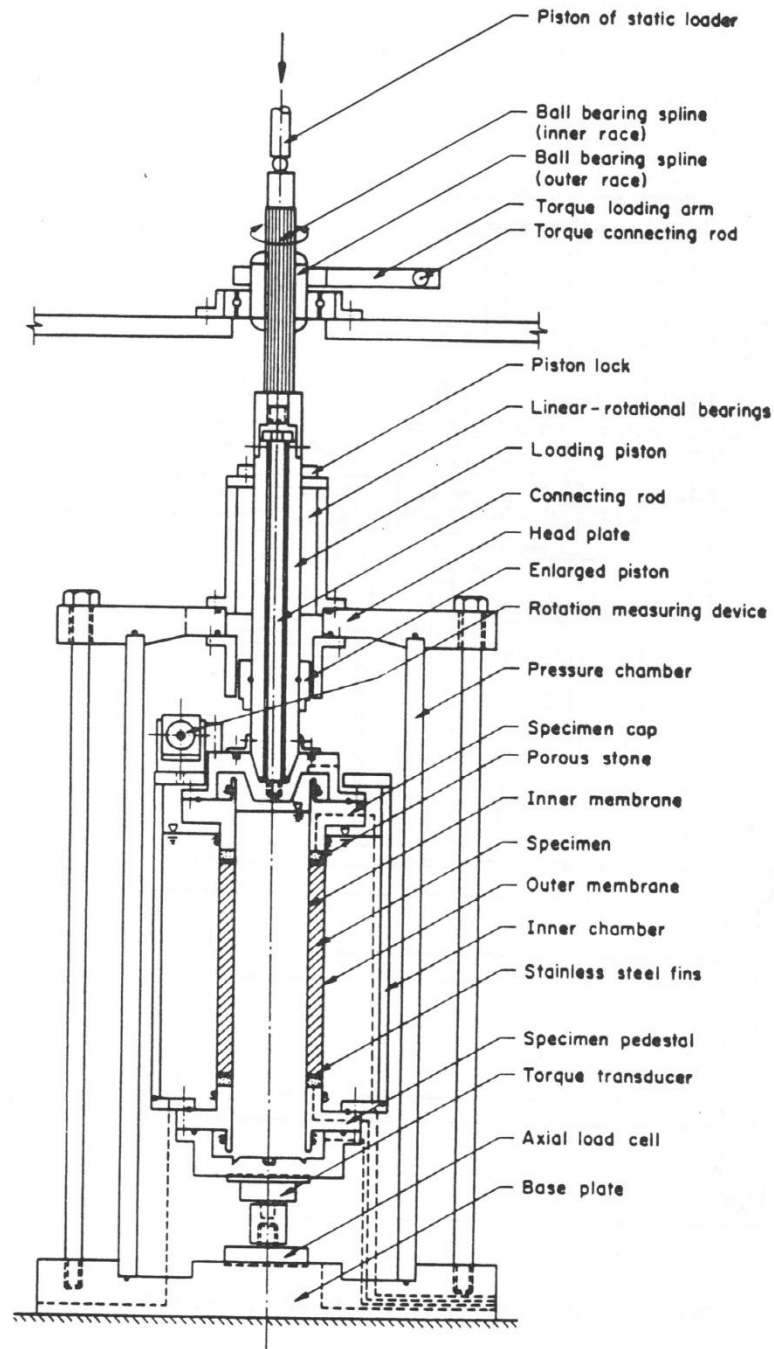


Fig. 2.19. Torsional simple shear device (after Ishibashi et al. 1985)

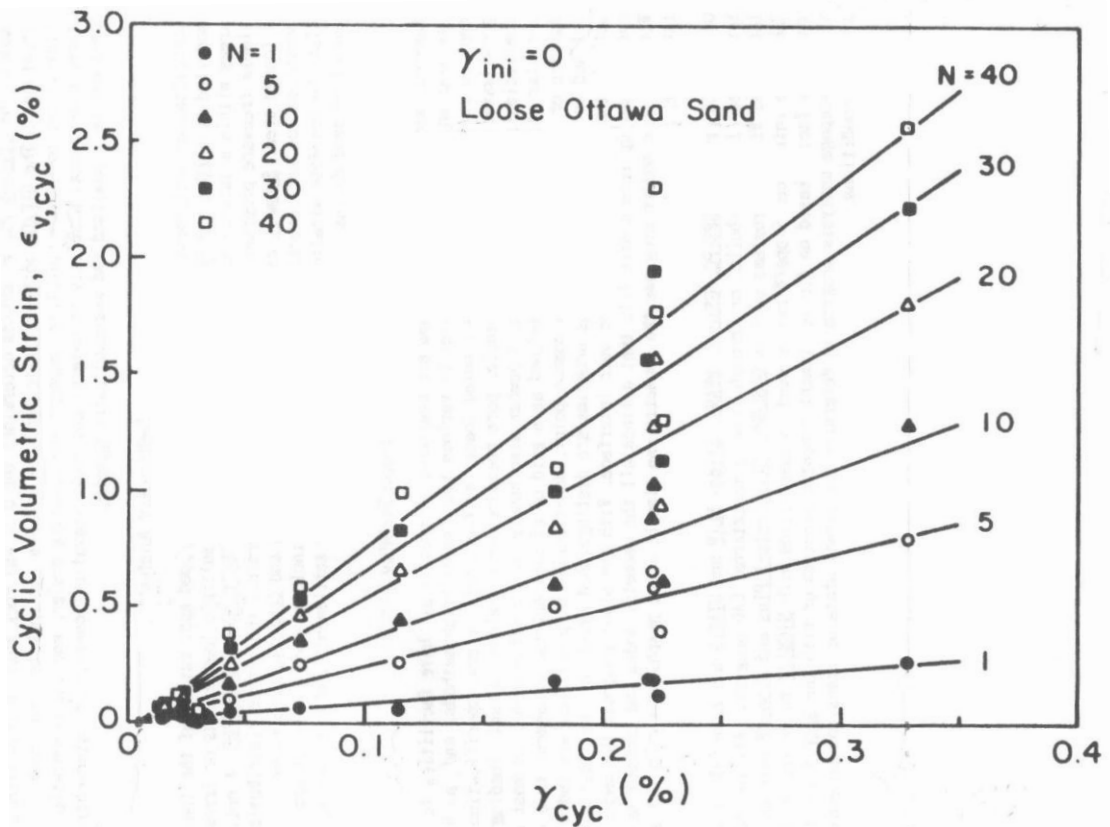


Fig. 2.20. Variation of cyclic volumetric strain as a function of cyclic shear strain (after Ishibashi et al., 1985)

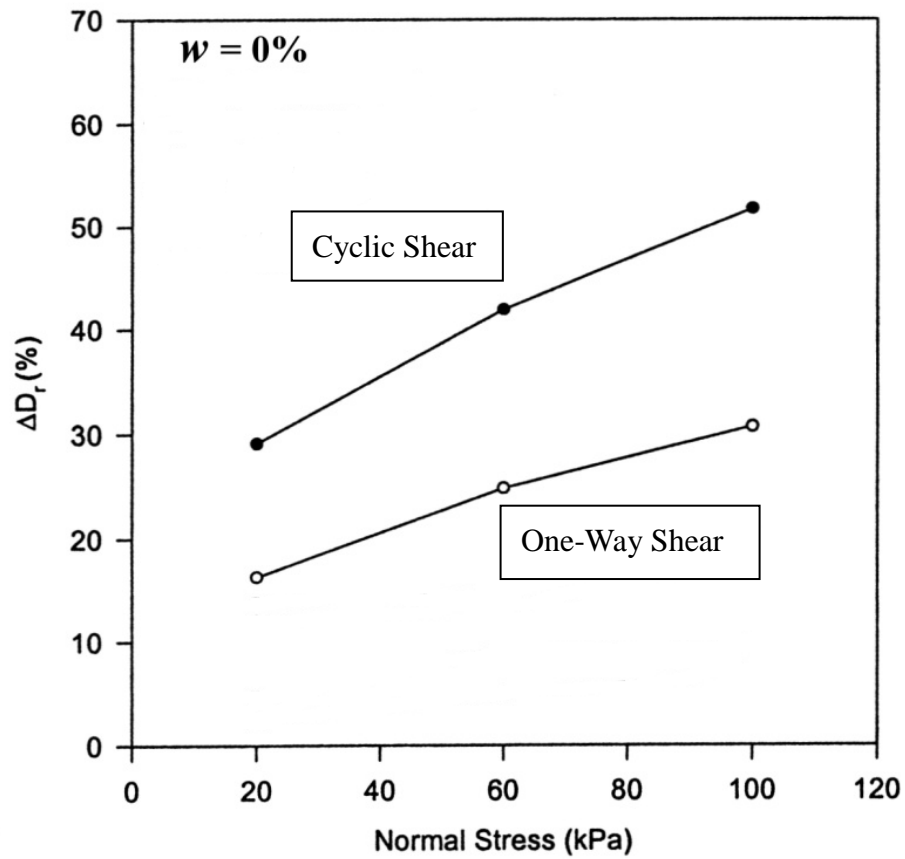


Fig. 2.21. Change of relative density with one-way and cyclic disc shearing versus normal stress (after Yang, 2002)

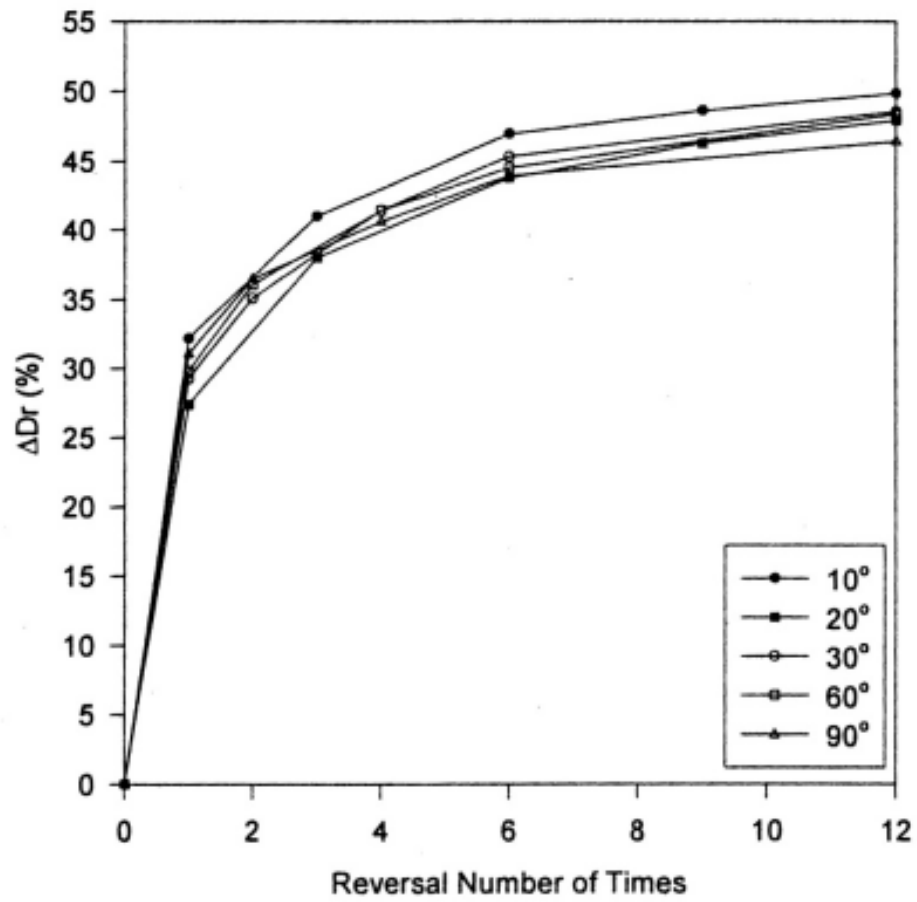


Fig. 2.22. Change of relative density due to cyclic disc shear with number of cycles
(after Ren, 2006)

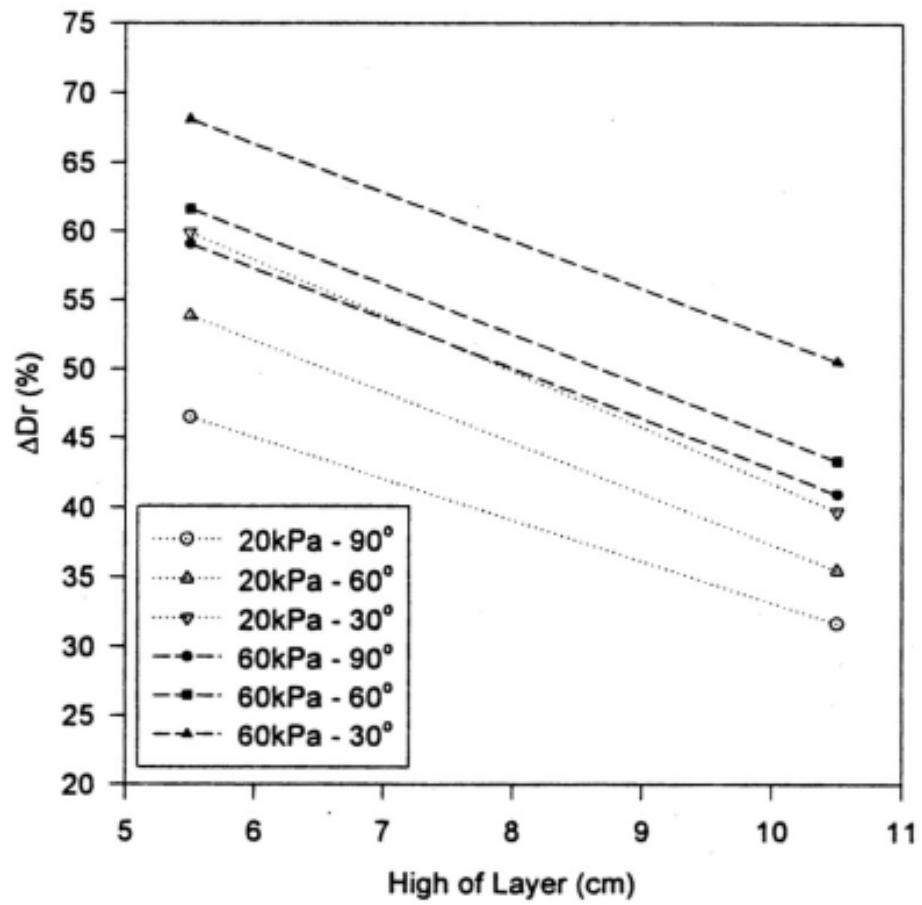


Fig. 2.23. Change of relative density due to cyclic disc shear at different depths with high of layer (after Ren, 2006)

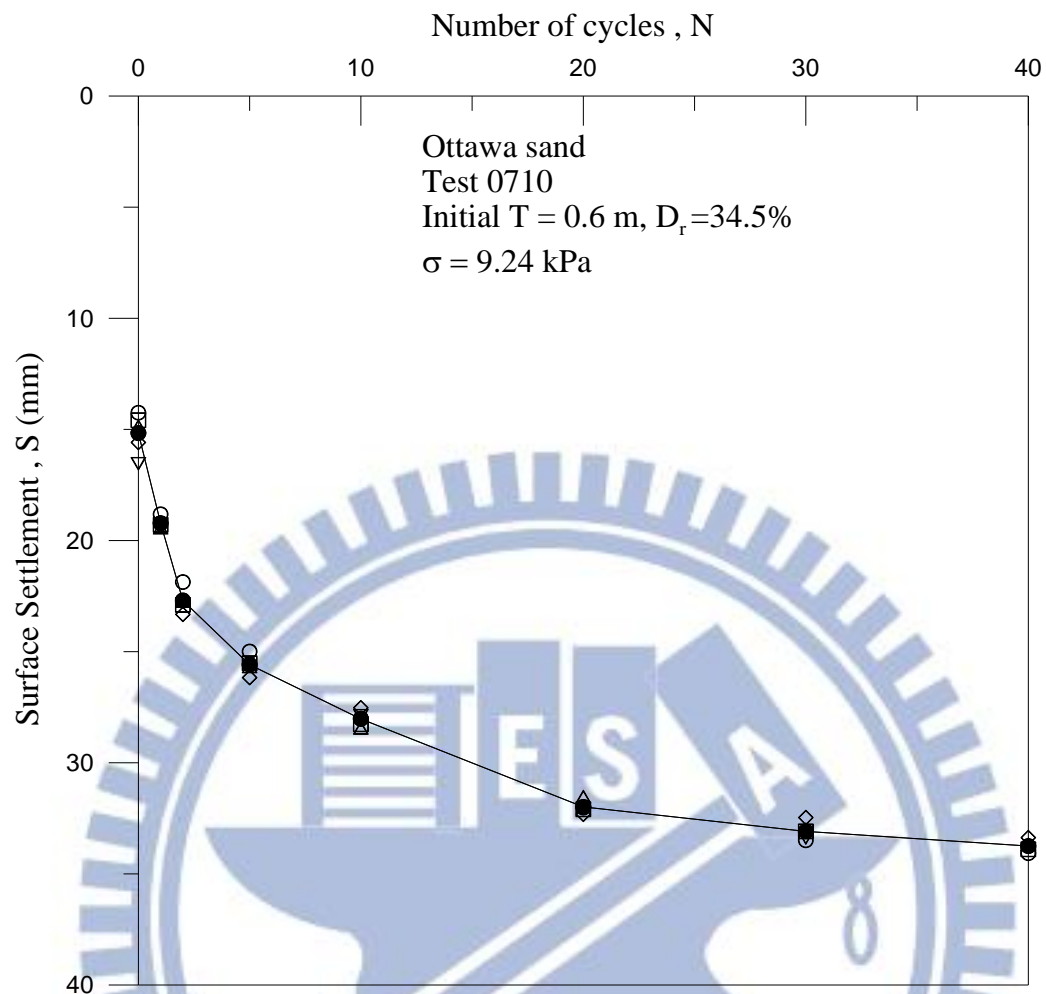


Fig. 2.24. Surface settlement due to static vertical load at N = 0 to N = 40 (after Chen, 2002)

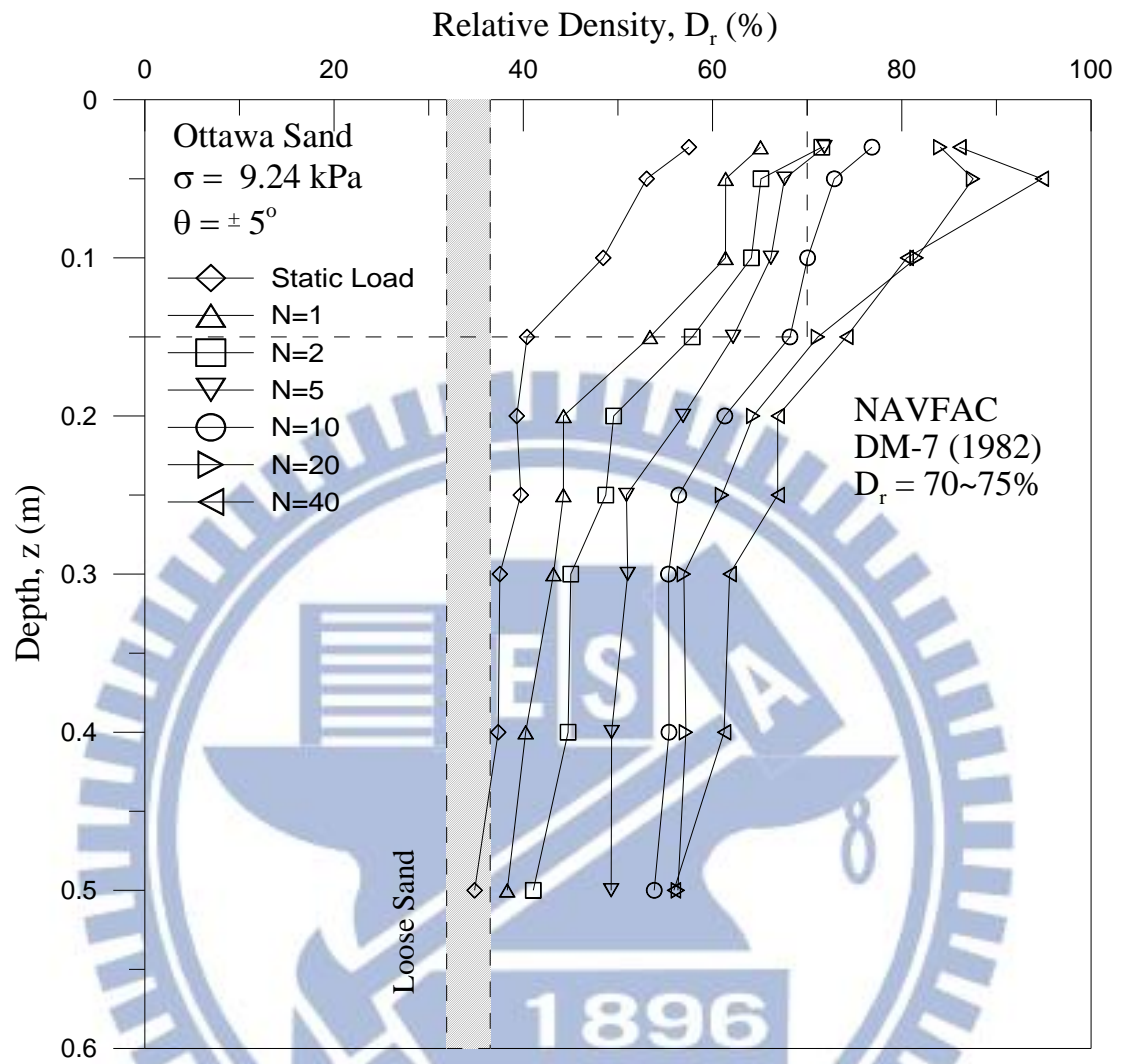


Fig. 2.25. Distribution of relative density due to cyclic torsional shearing (after Chen, 2011)

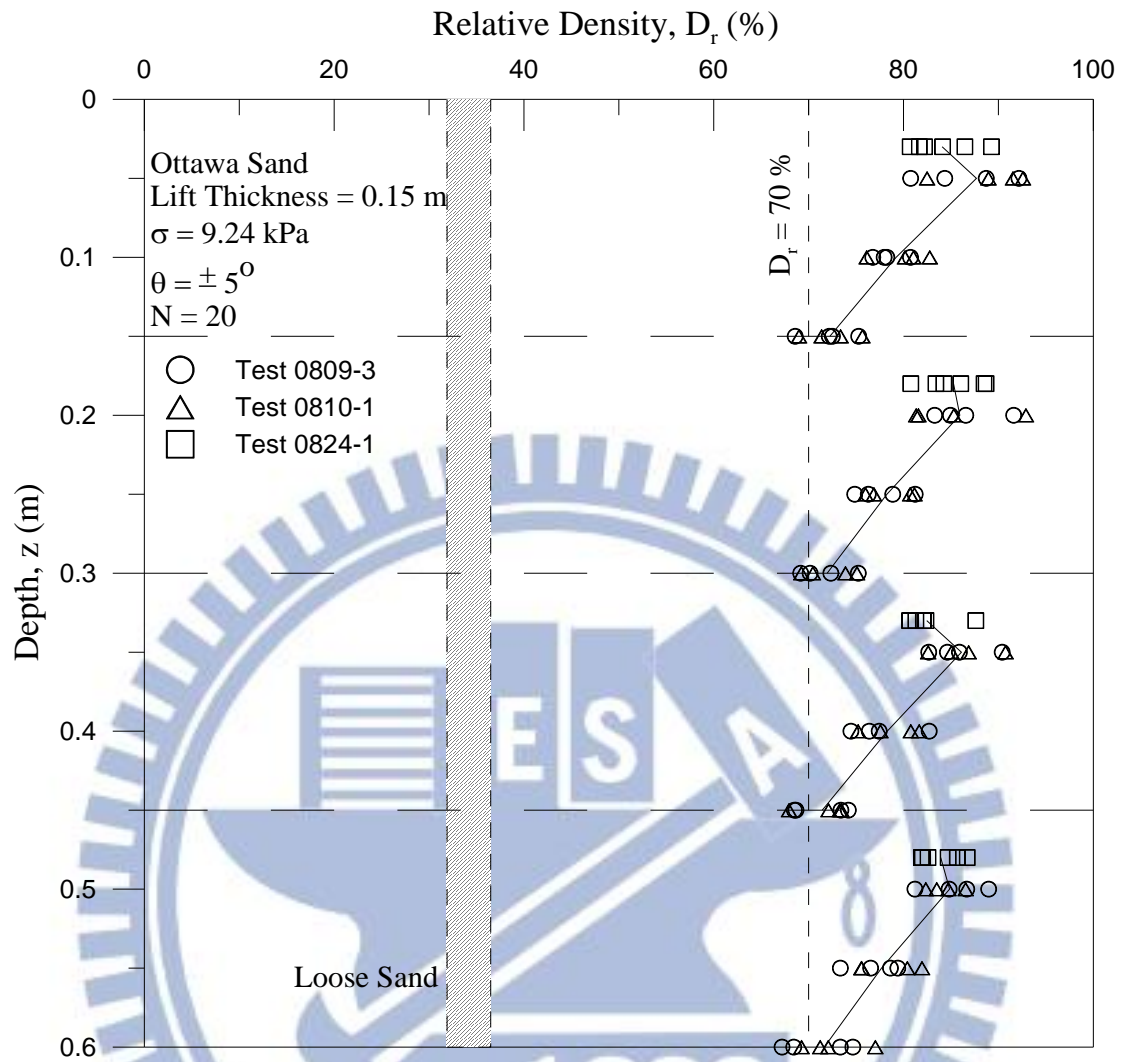


Fig. 2.26. Distribution of relative density in lift 1 to 4 (after Chen, 2011)

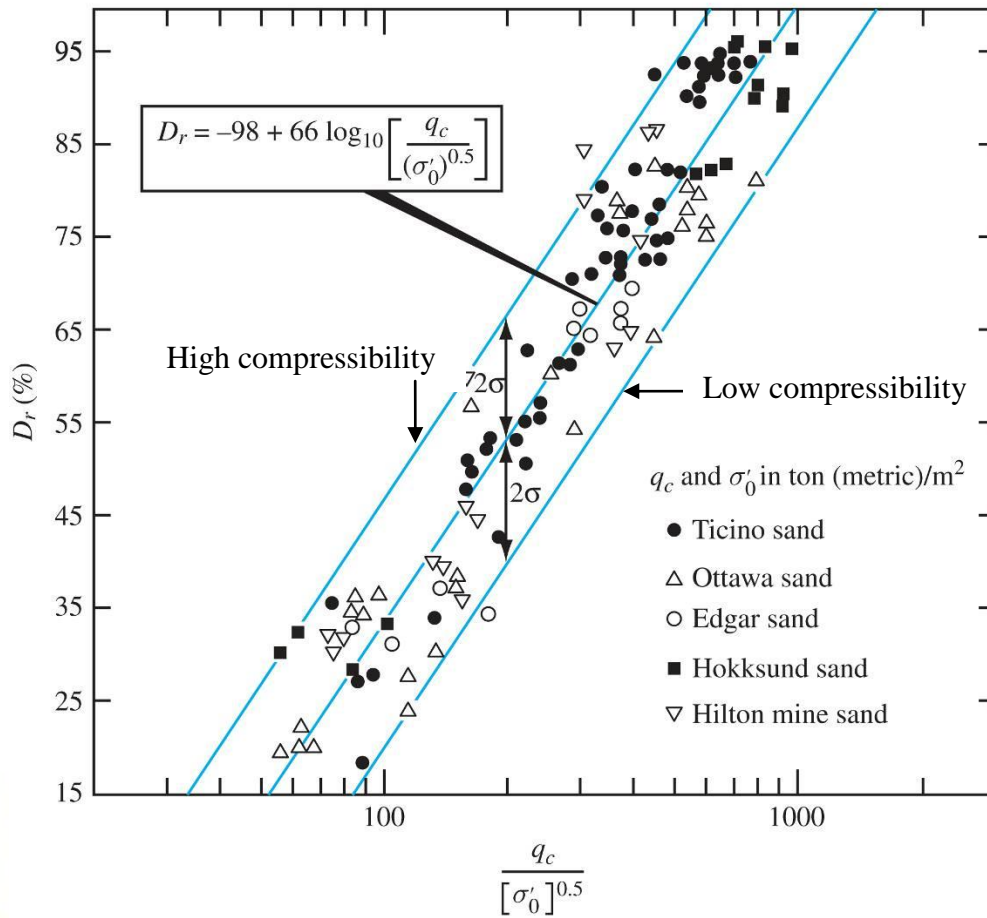
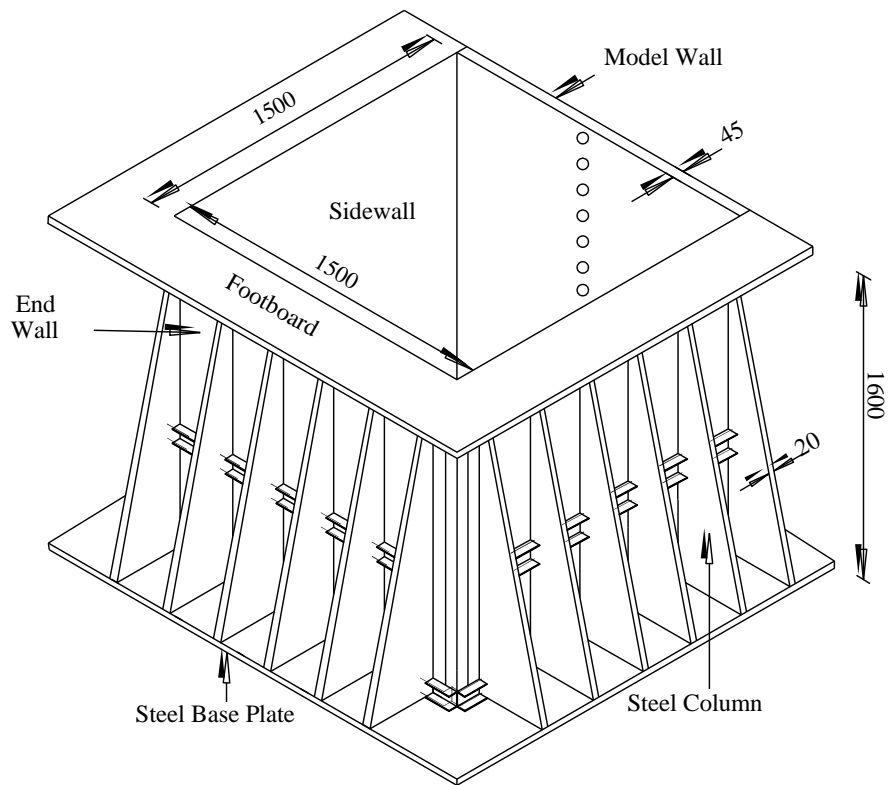


Fig. 2.27. Relationship between Relative density and q_c (Jamiołkowski et al., 1985)

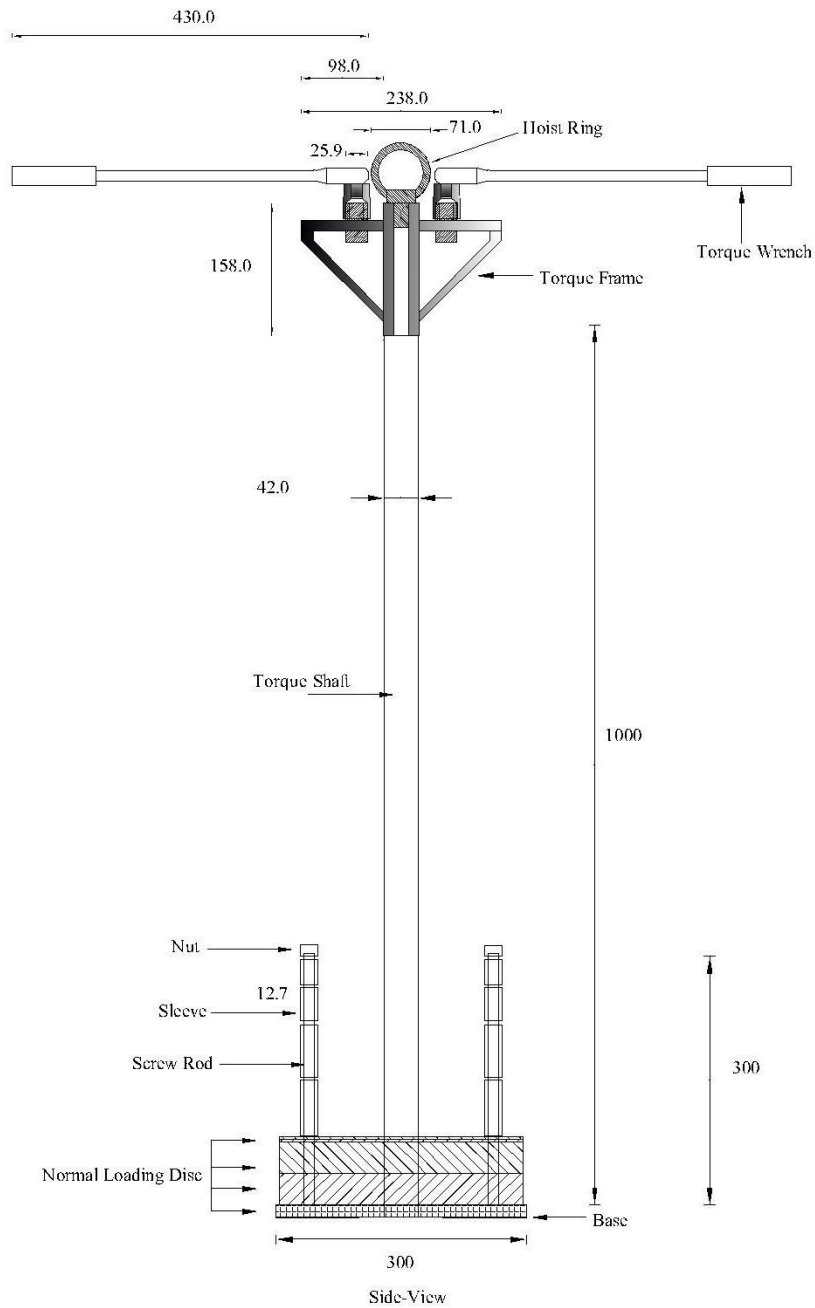


Unit : mm

Fig. 3.1. NCTU non-yielding model retaining wall and soil bin
(after Chen and Fang, 2008)



Fig. 3.2. Soil-Pressure Transducer (Kyowa BE-2KCM17) (after Chen, 2003)



Unit : mm

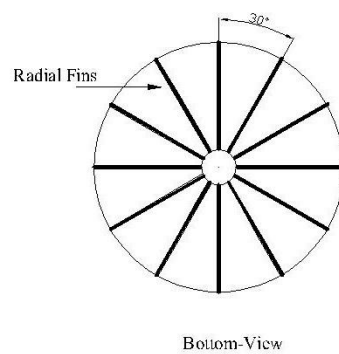


Fig. 3.3. Dimensions of cyclic torsional shear compactor (after Chen, 2011)

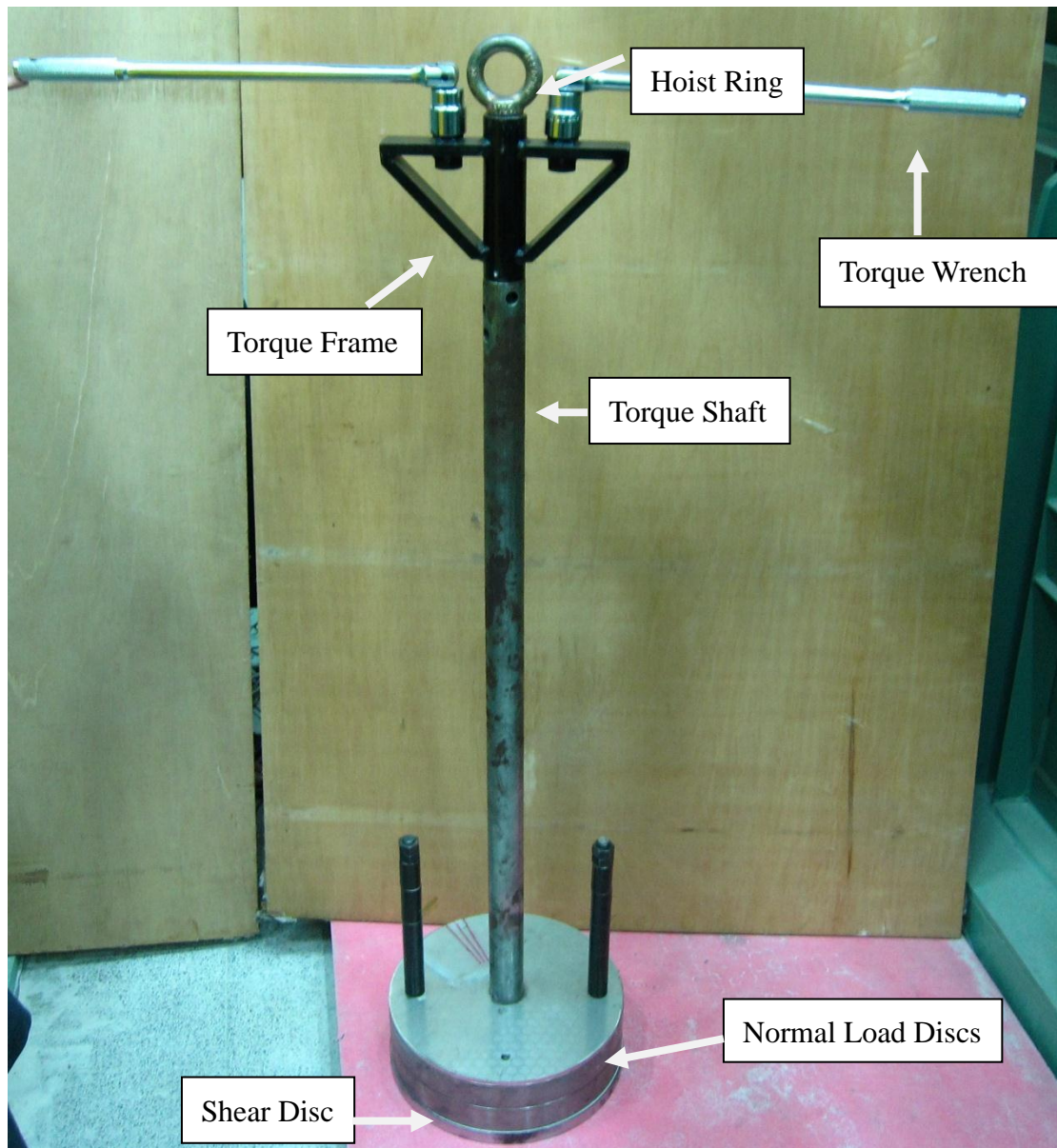
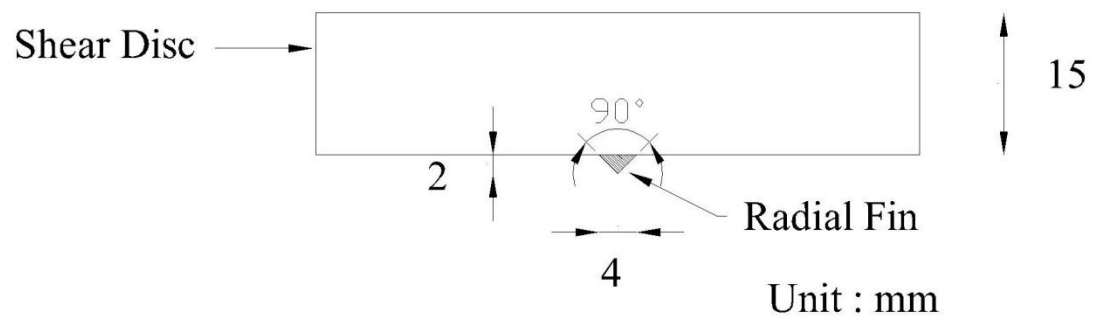


Fig. 3.4. Cyclic torsional shear compactor (after Chen, 2011)



Fig. 3.5. Bottom of shearing disc with radial fins (after Chen, 2011)



(a)



(b)

Fig. 3.6. Dimensions of a radial fin (after Chen, 2011)

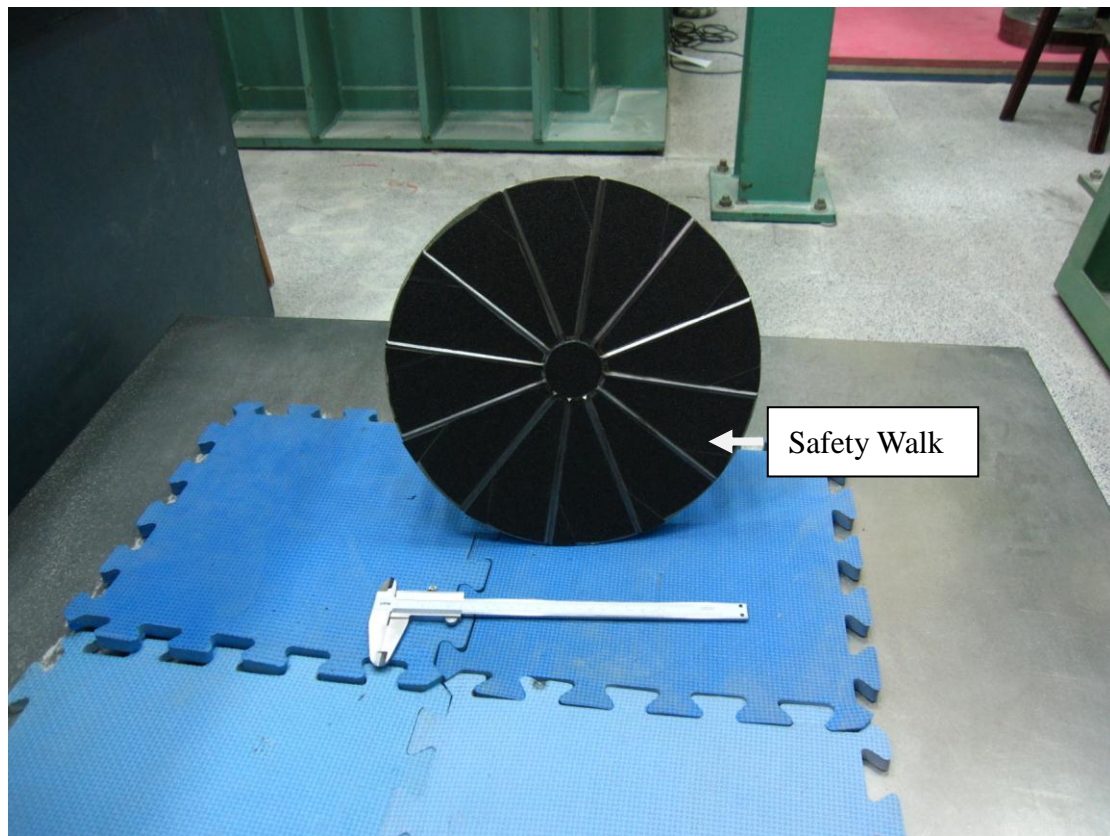
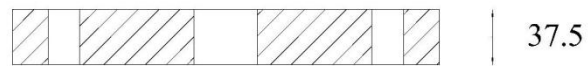
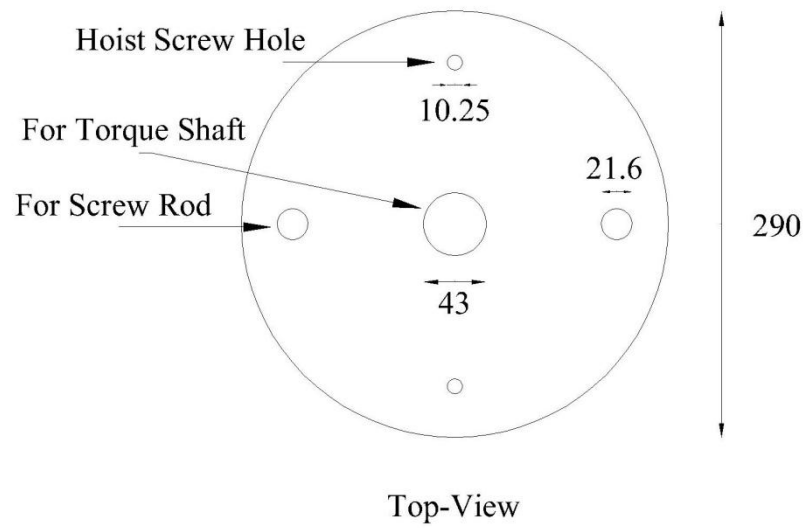


Fig. 3.7. Bottom of shearing disc with SAFETY WALK (after Chen, 2011)



Unit : mm

(a)



(b)

Fig. 3.8. Dimensions of normal loading discs (after Chen, 2011)

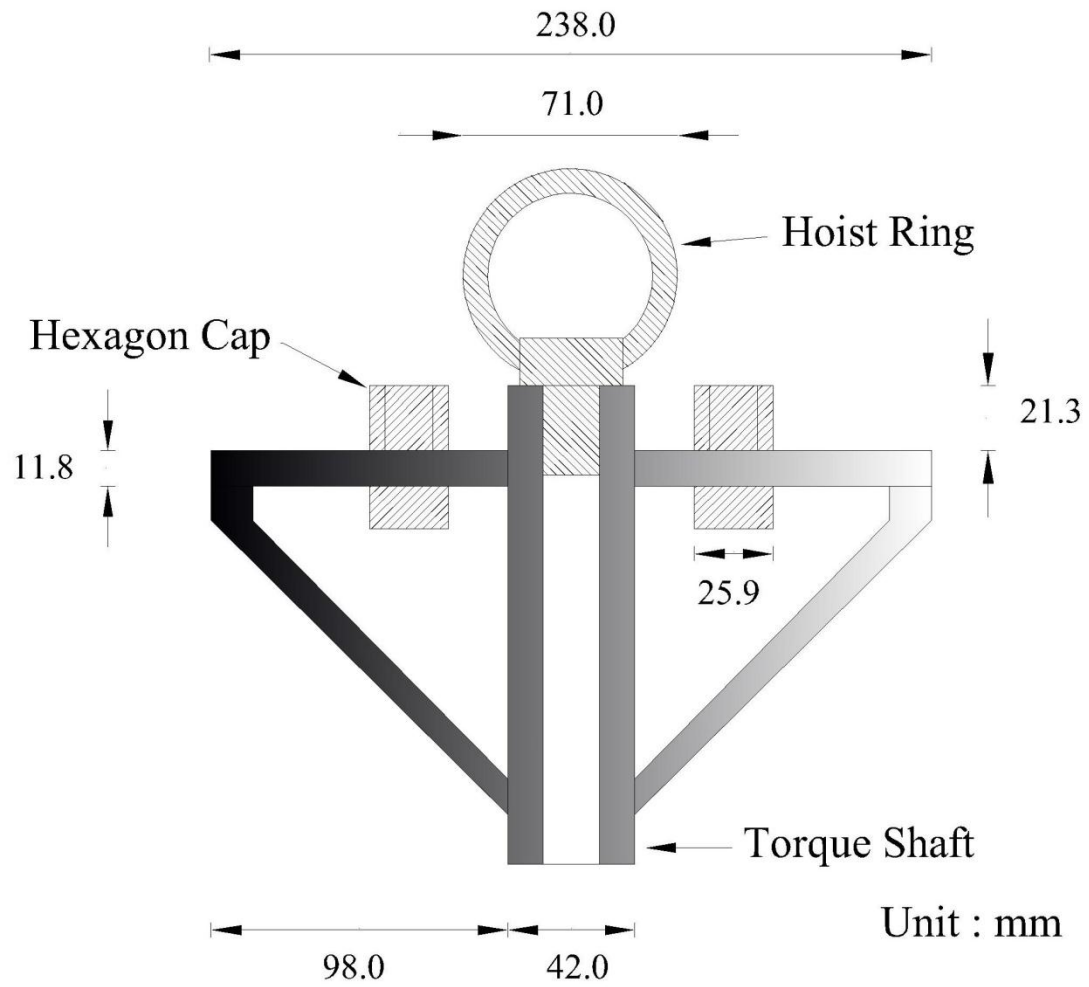


Fig. 3.9. Dimensions of torque loading frame (after Chen, 2011)

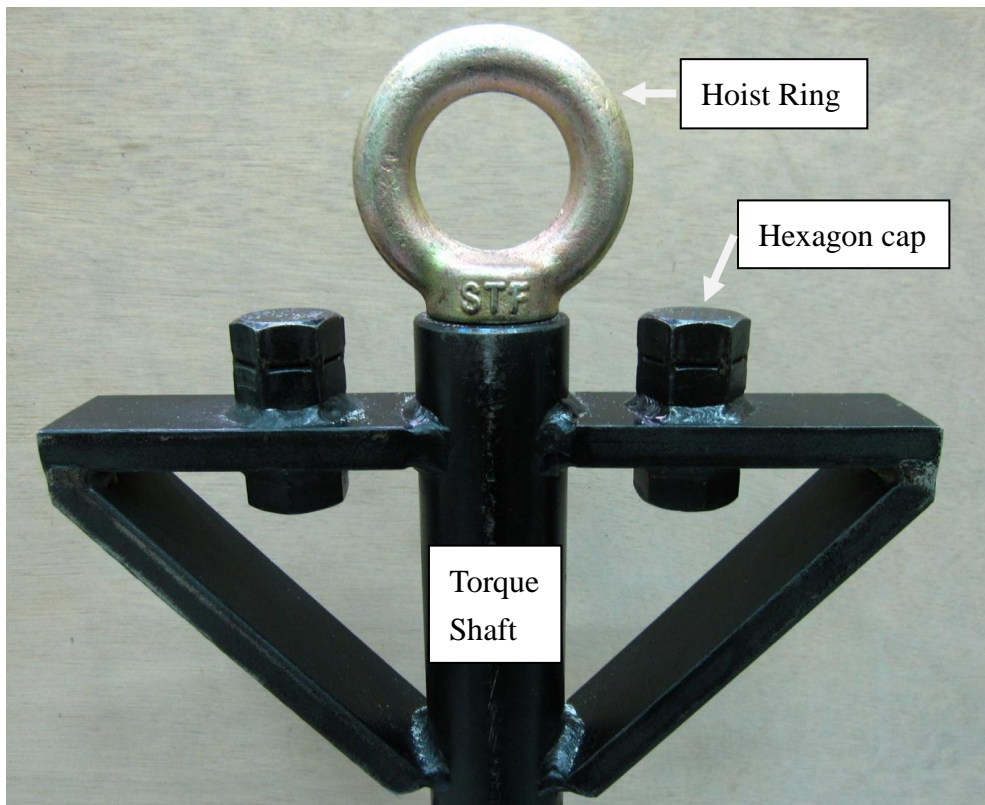
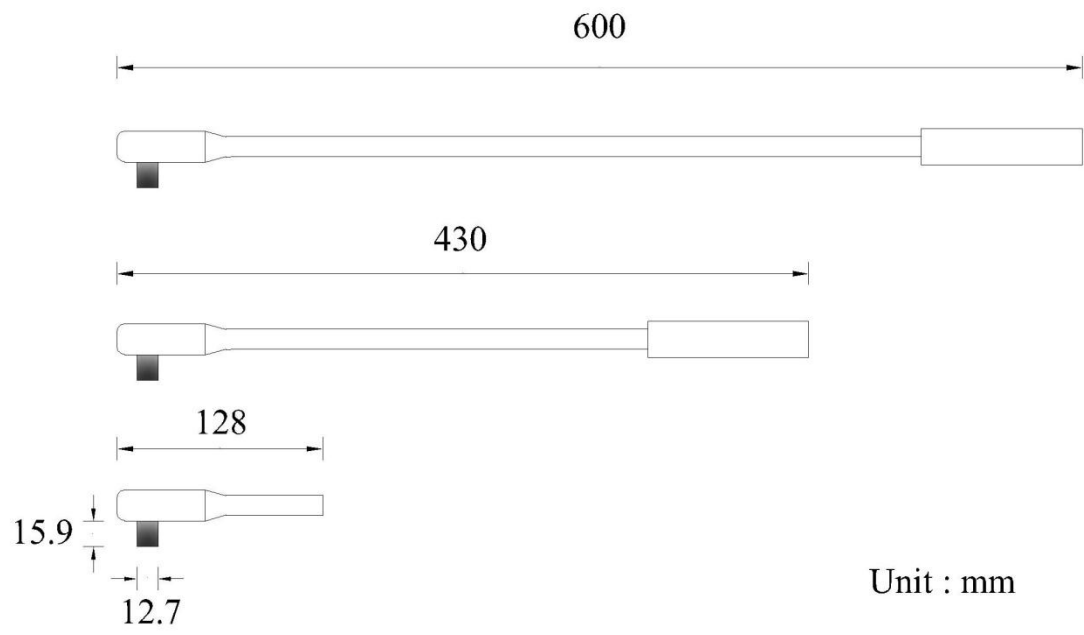
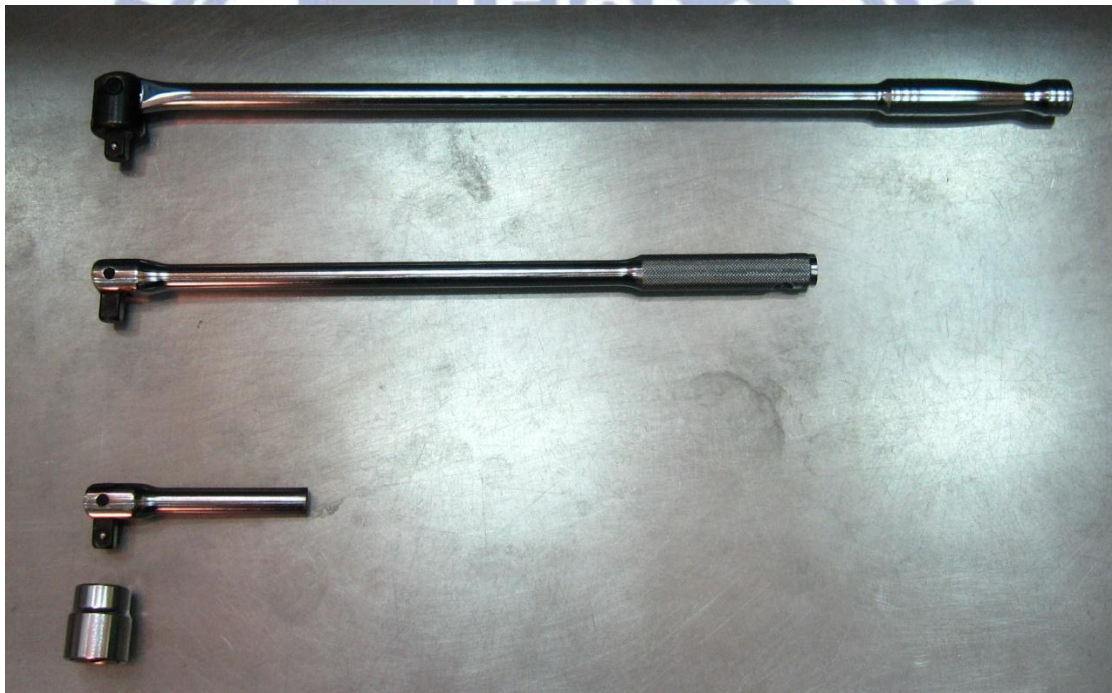


Fig. 3.10. Torque loading frame (after Chen, 2011)



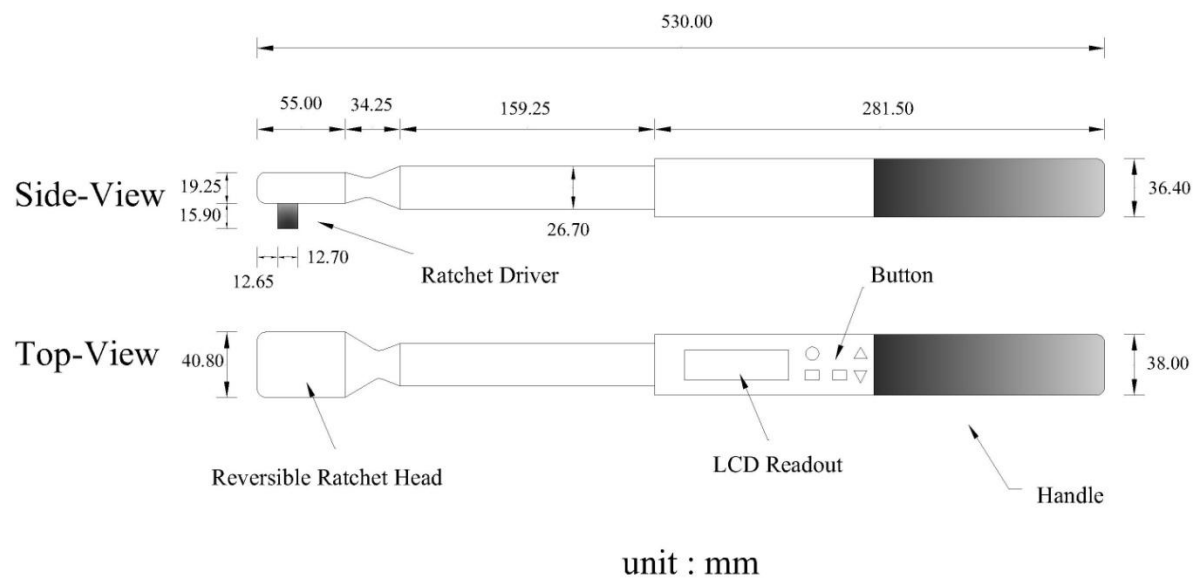


(a)



(b)

Fig. 3.11. Dimensions of torque wrench (after Chen, 2011)



(a)

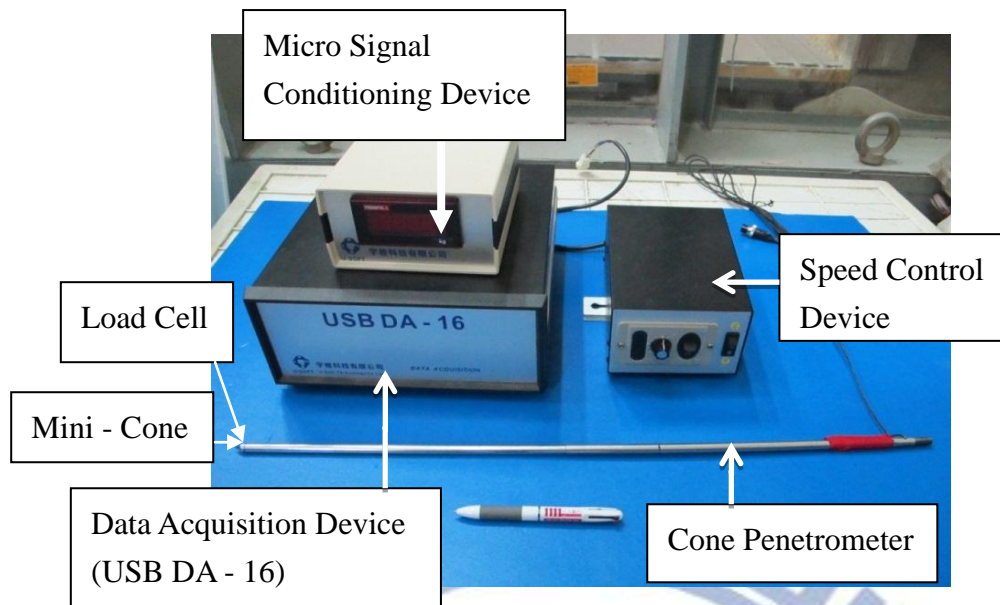


(b)

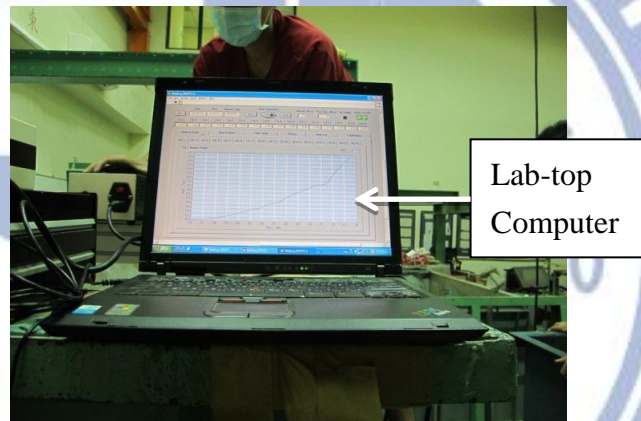
Fig. 3.12. Dimensions of digital torque wrench (after Chen, 2011)



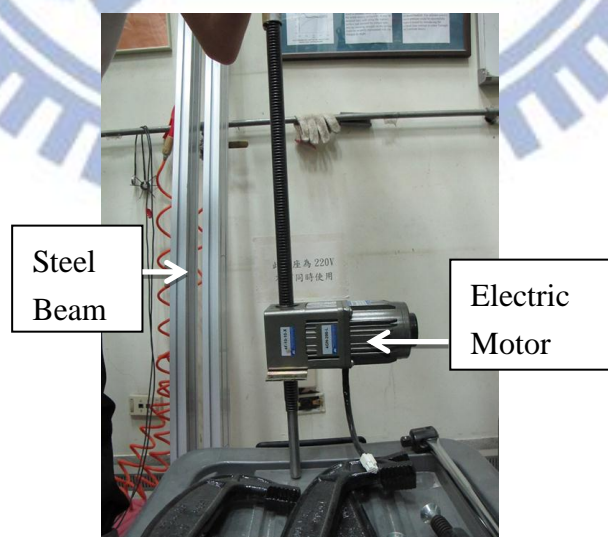
Fig. 3.13. Torque wrench are installed on the cyclic torsional loading frame (after Chen, 2011)



(a)



(b)

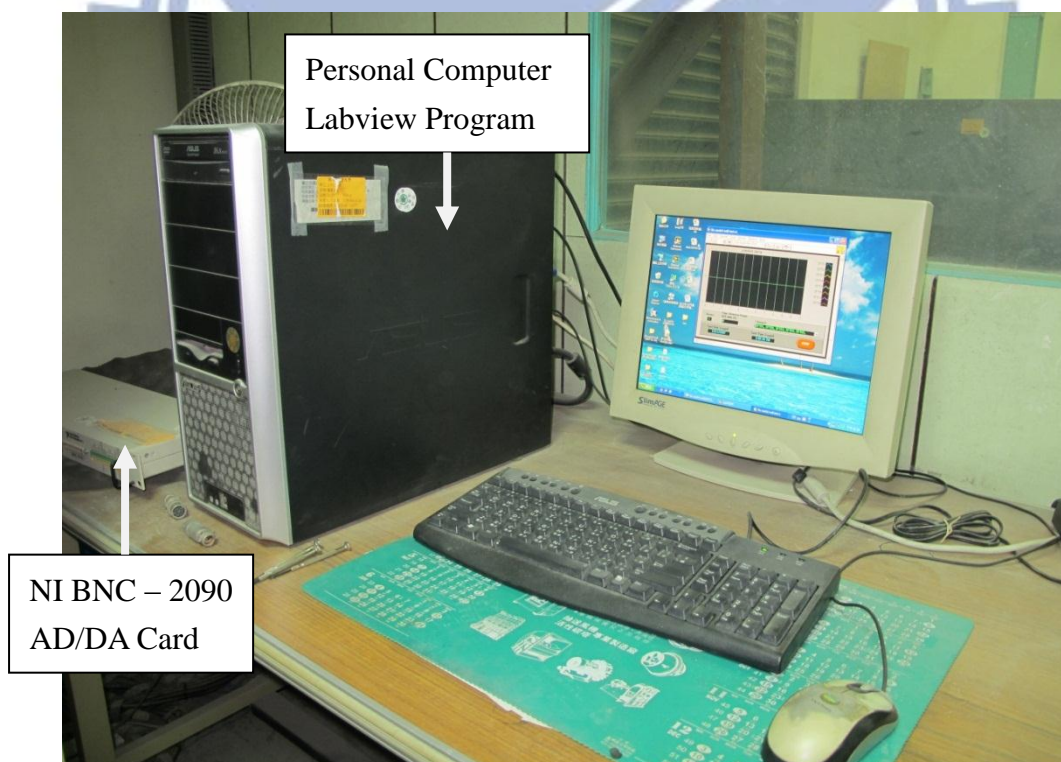


(c)

Fig. 3.14. Cone penetration facility of CYCU



(a)



(b)

Fig. 3.15. Data acquisition system

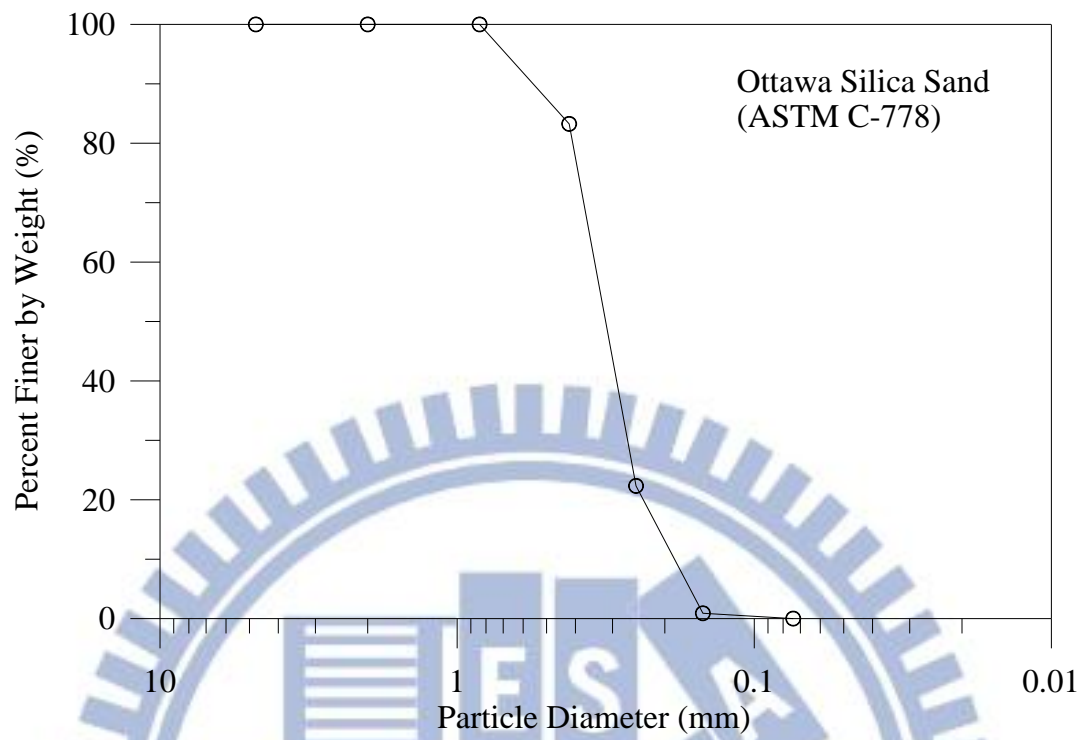
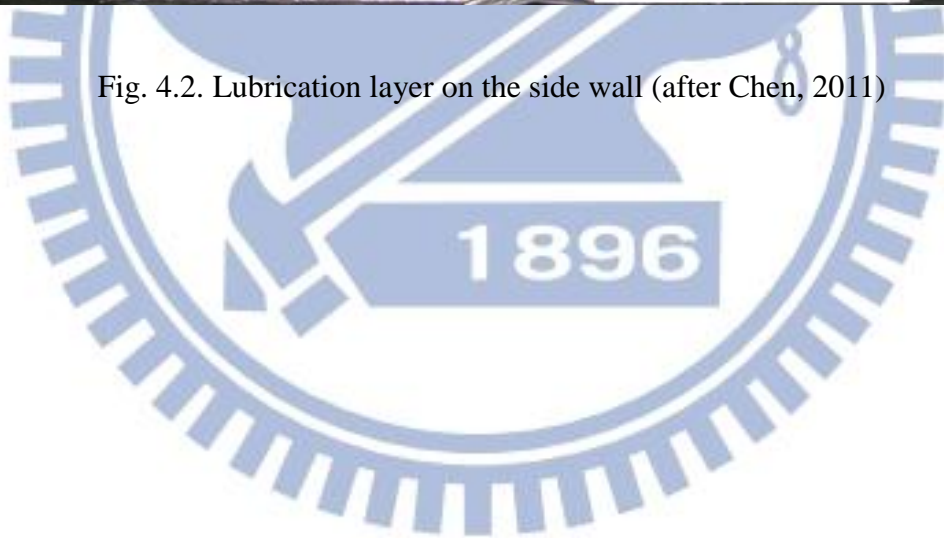


Fig. 4.1. Grain size distribution of Ottawa sand (after Chen, 2003)



Fig. 4.2. Lubrication layer on the side wall (after Chen, 2011)



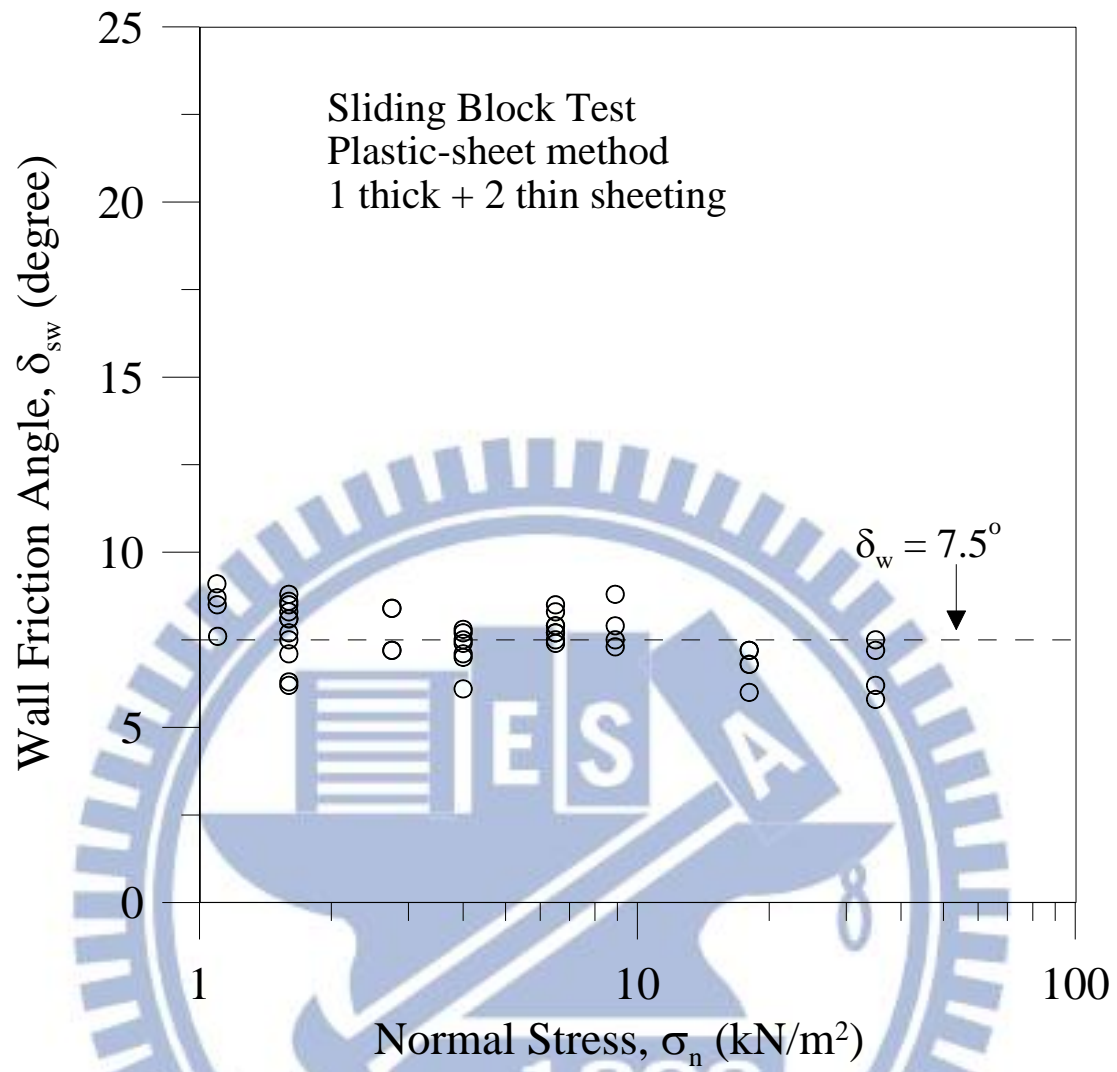
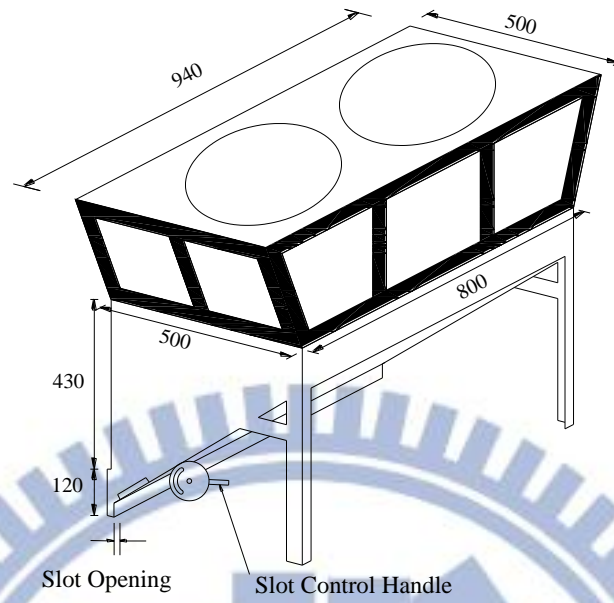
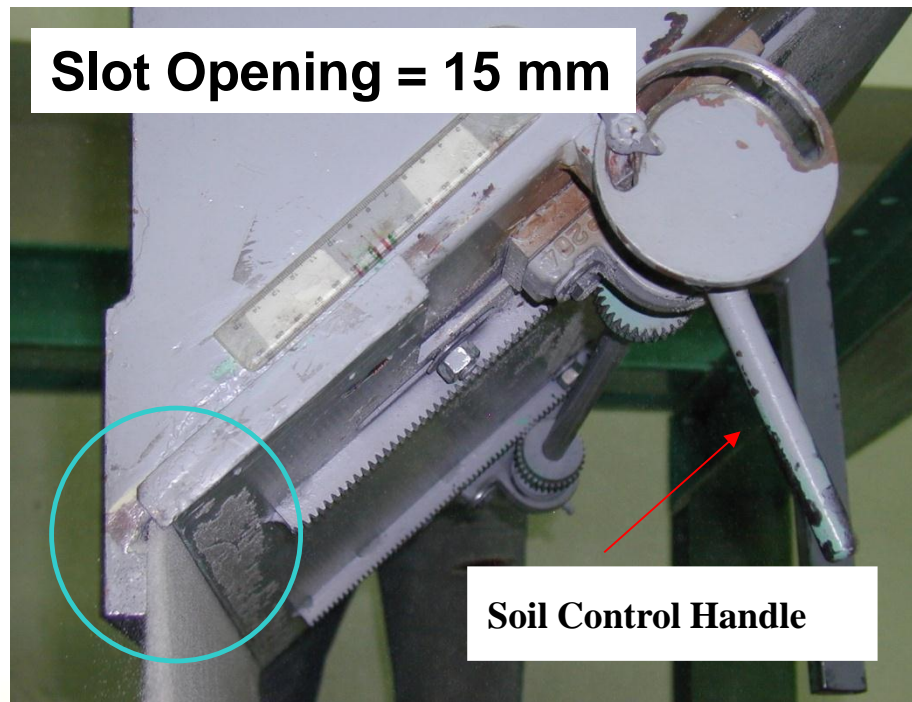


Fig. 4.3. Variation of friction Angle with normal stress (after Fang et al., 2004)

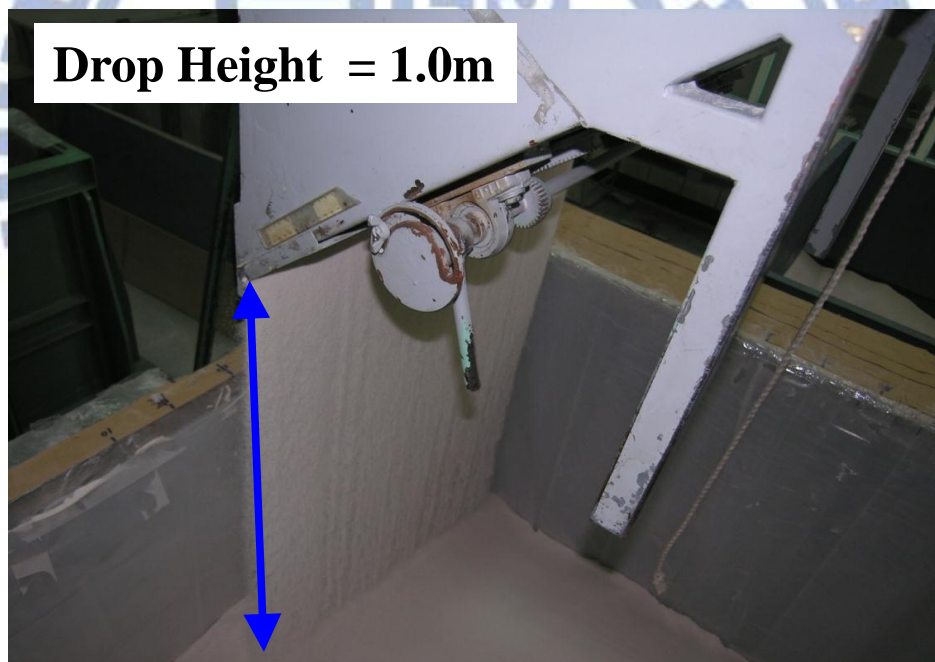


Unit:mm

Fig. 4.4. Soil hopper (after Chen, 2011)



(a)



(b)

Fig. 4.5. Pluviation of Ottawa sand into soil bin (after Chen, 2011)

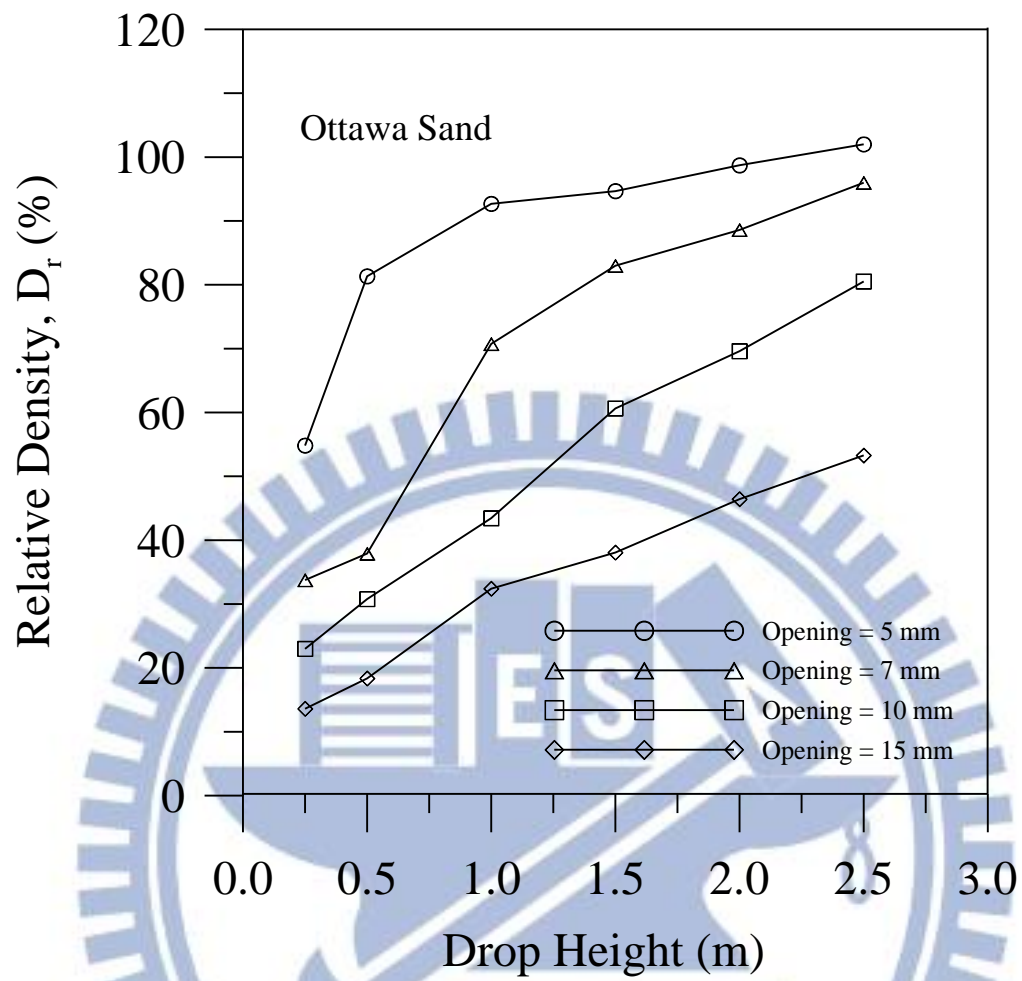
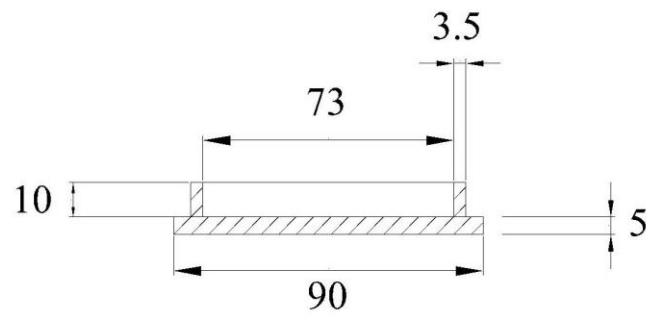
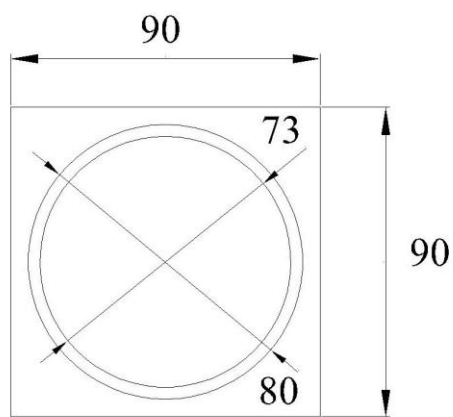


Fig. 4.6. Relationship among slot opening, drop height, and relative density (after Ho, 1999)



Side-view



Top-view

unit : mm

Fig. 4.7. Dimensions of soil density cup (after Chen, 2011)

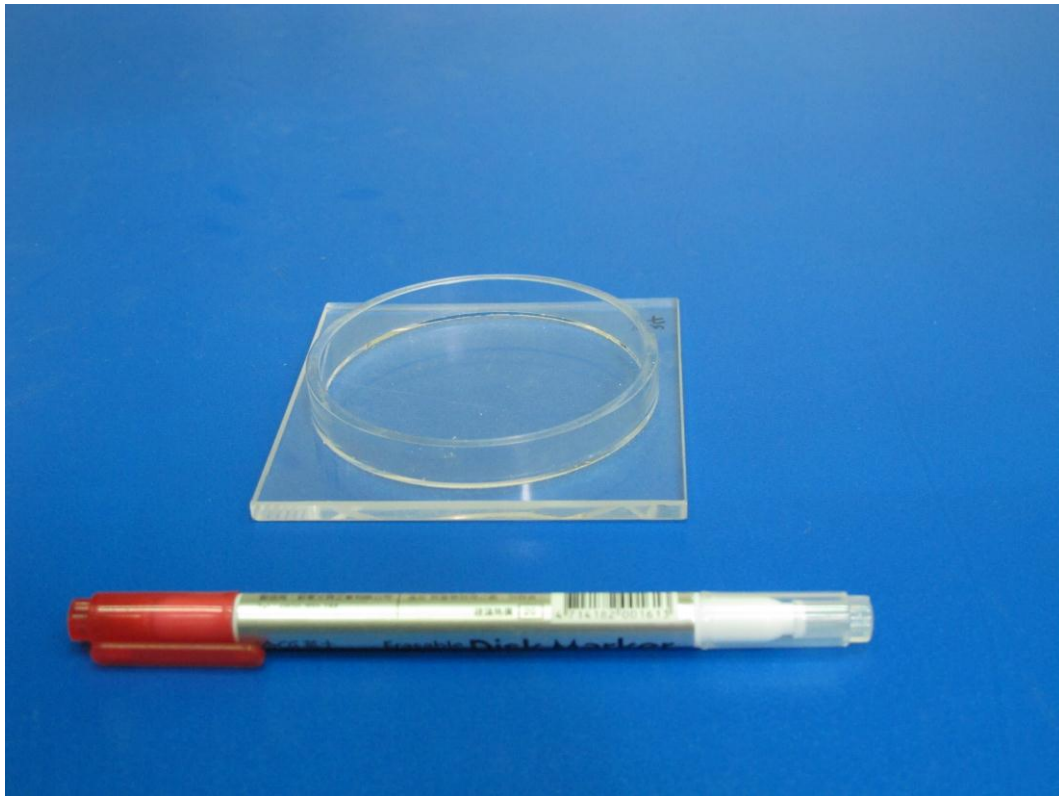
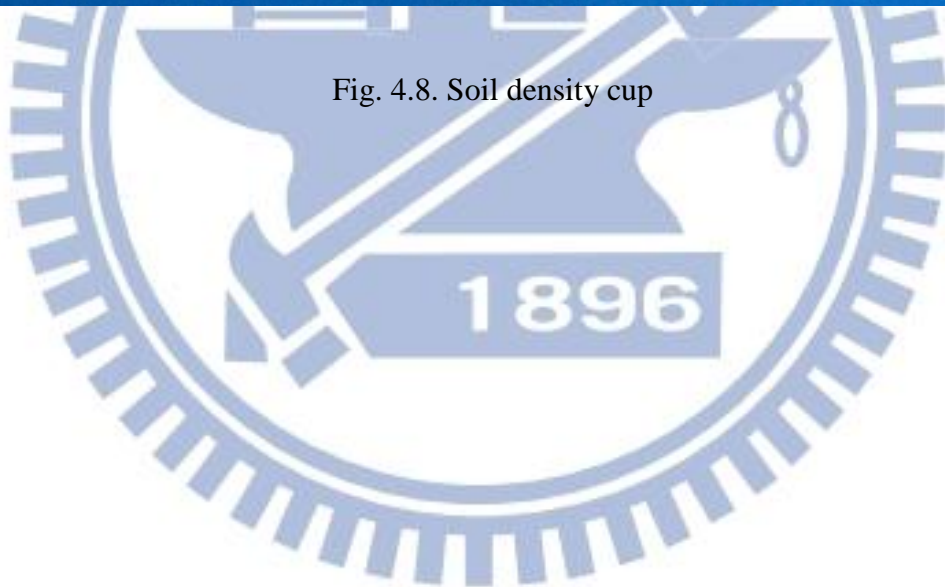


Fig. 4.8. Soil density cup



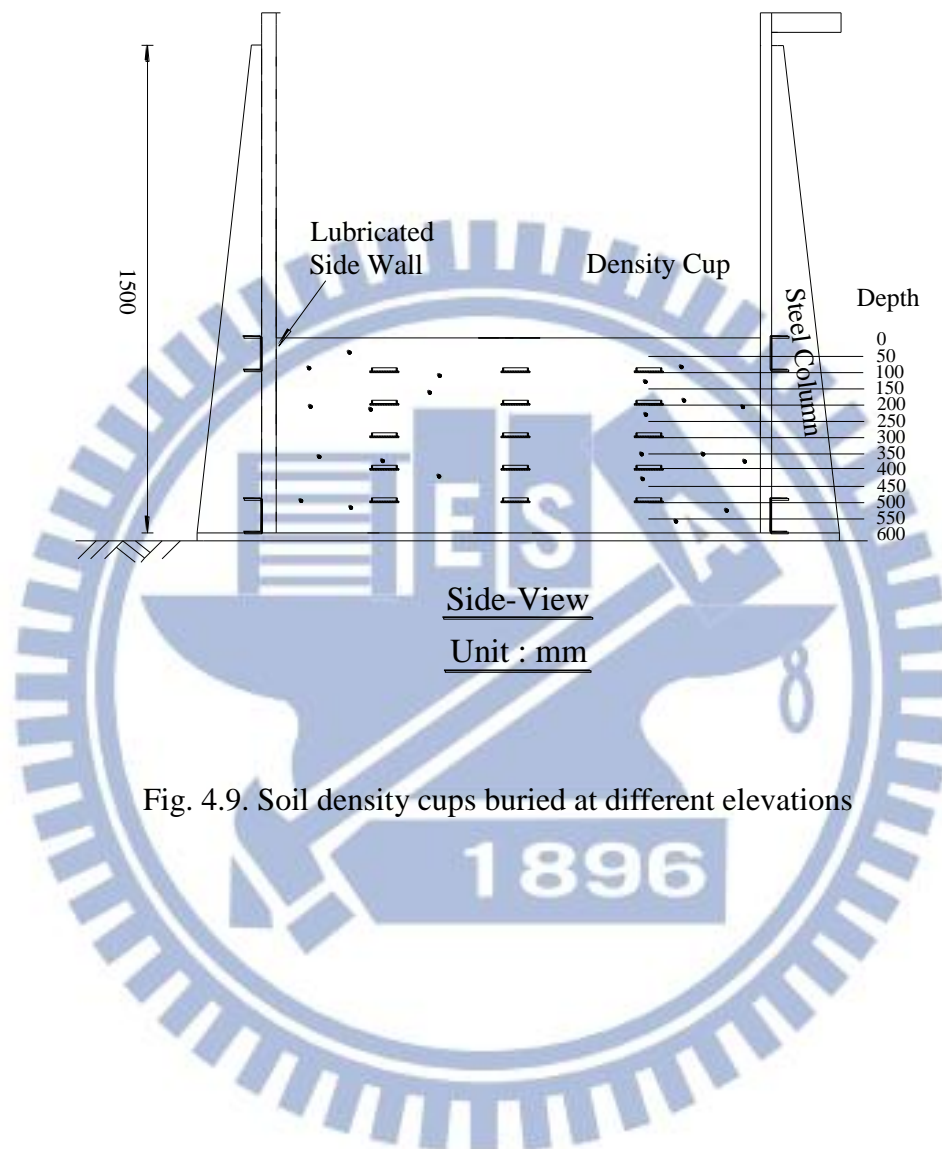


Fig. 4.9. Soil density cups buried at different elevations

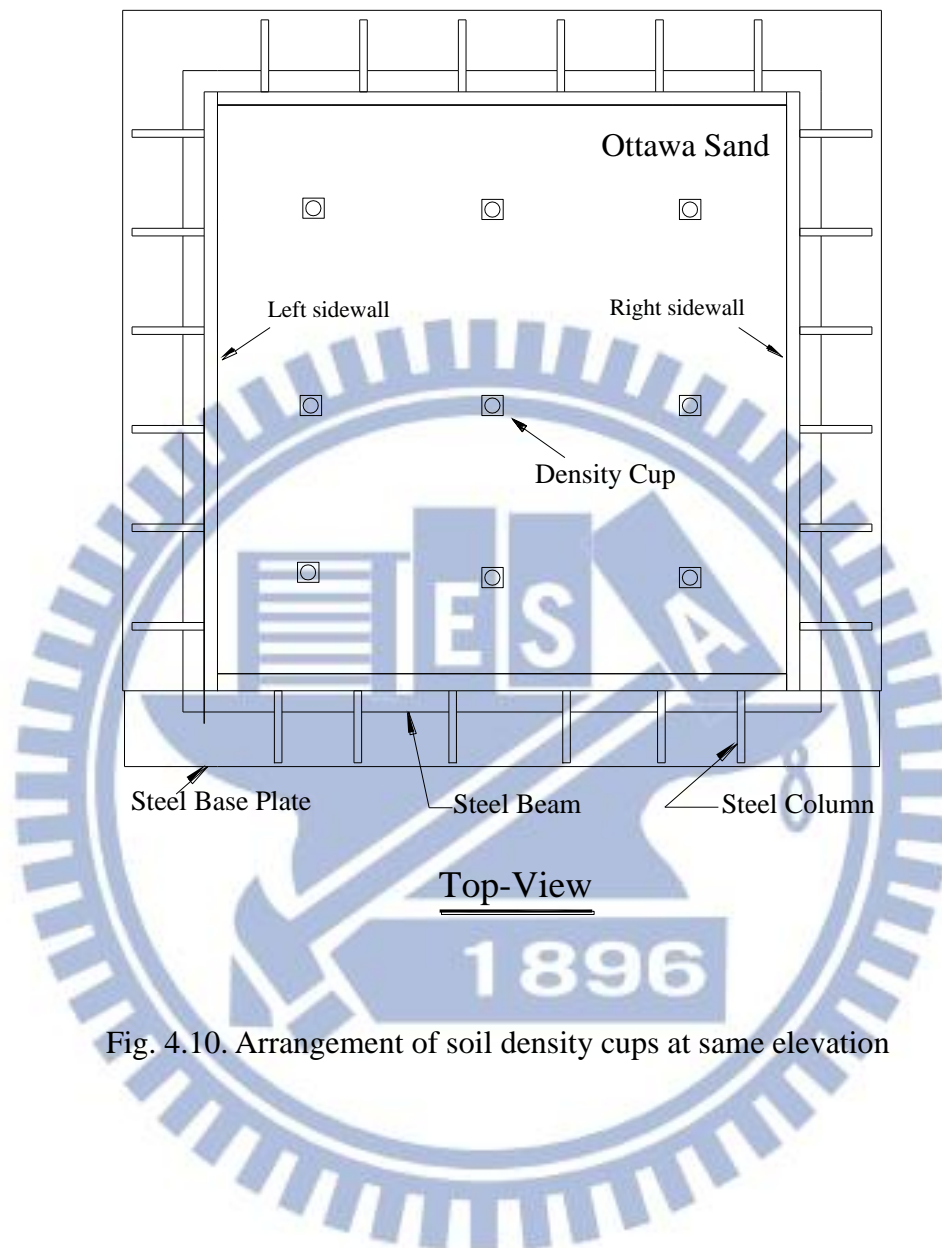


Fig. 4.10. Arrangement of soil density cups at same elevation



Fig. 4.11. Measurement of soil mass in density cup

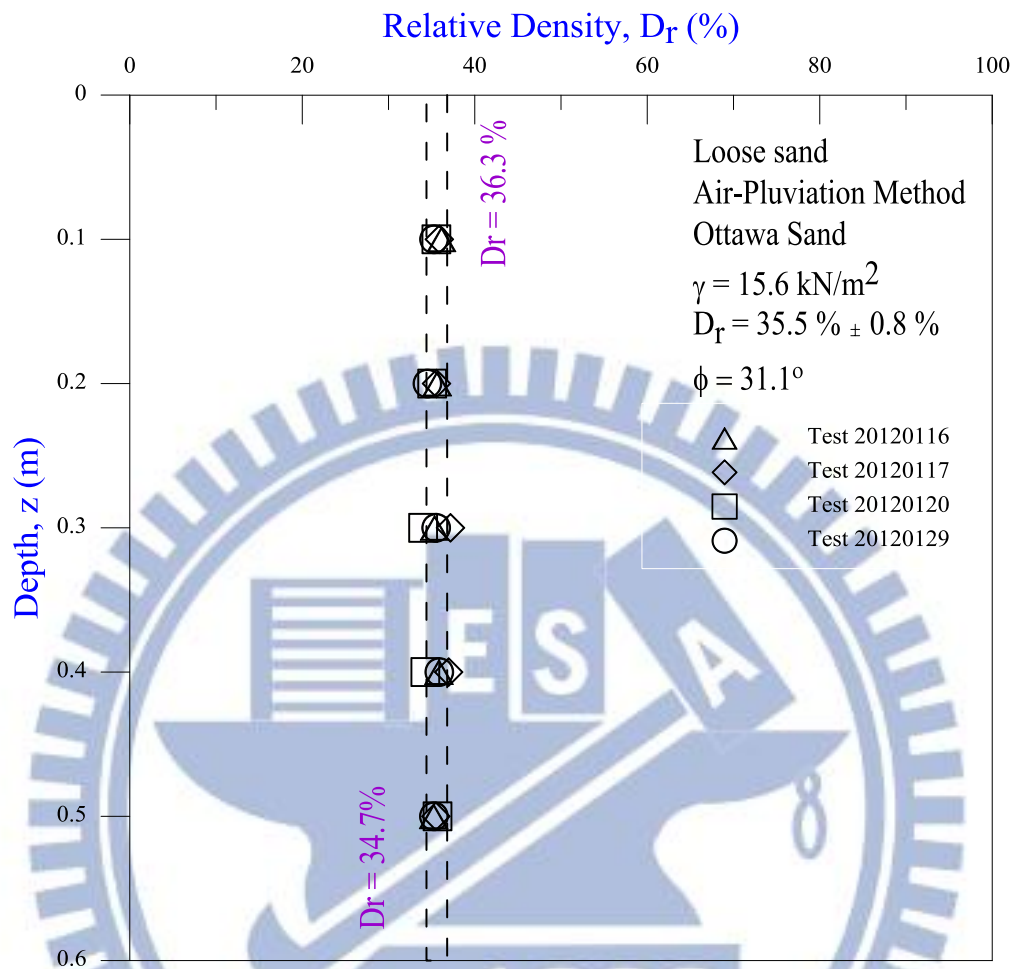


Fig. 4.12. Distribution of relative density with depth

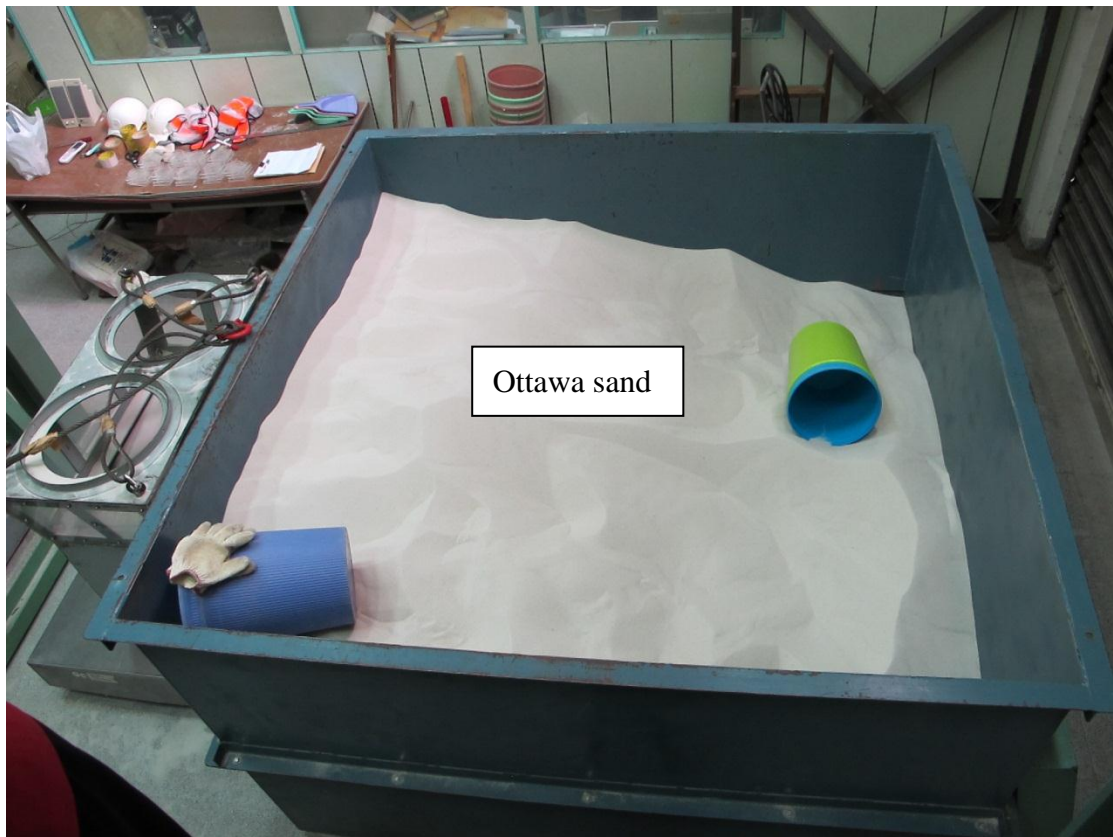


Fig. 5.1. Soil storage



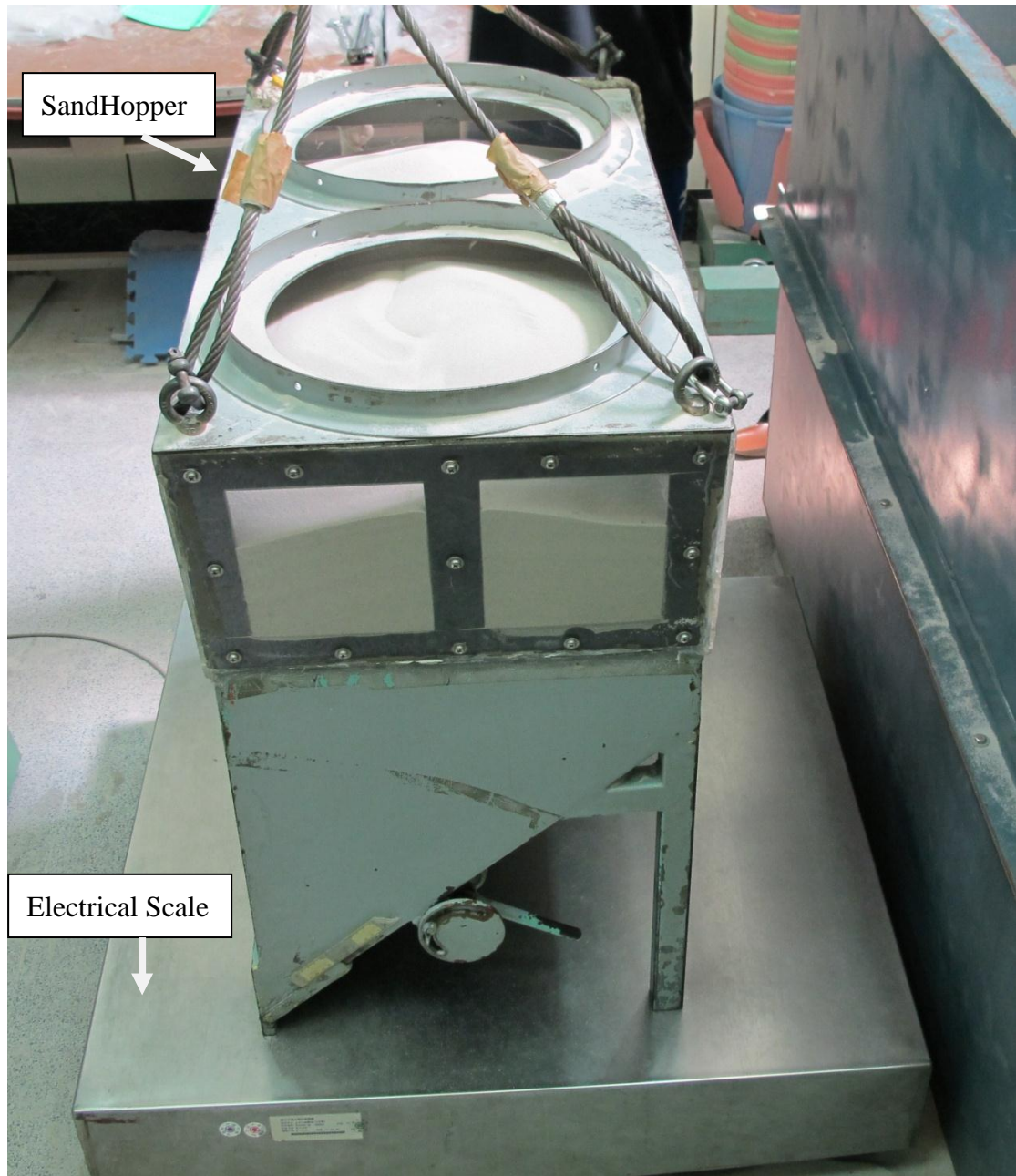


Fig. 5.2. Sand hopper and electrical scale (after Chen, 2011)

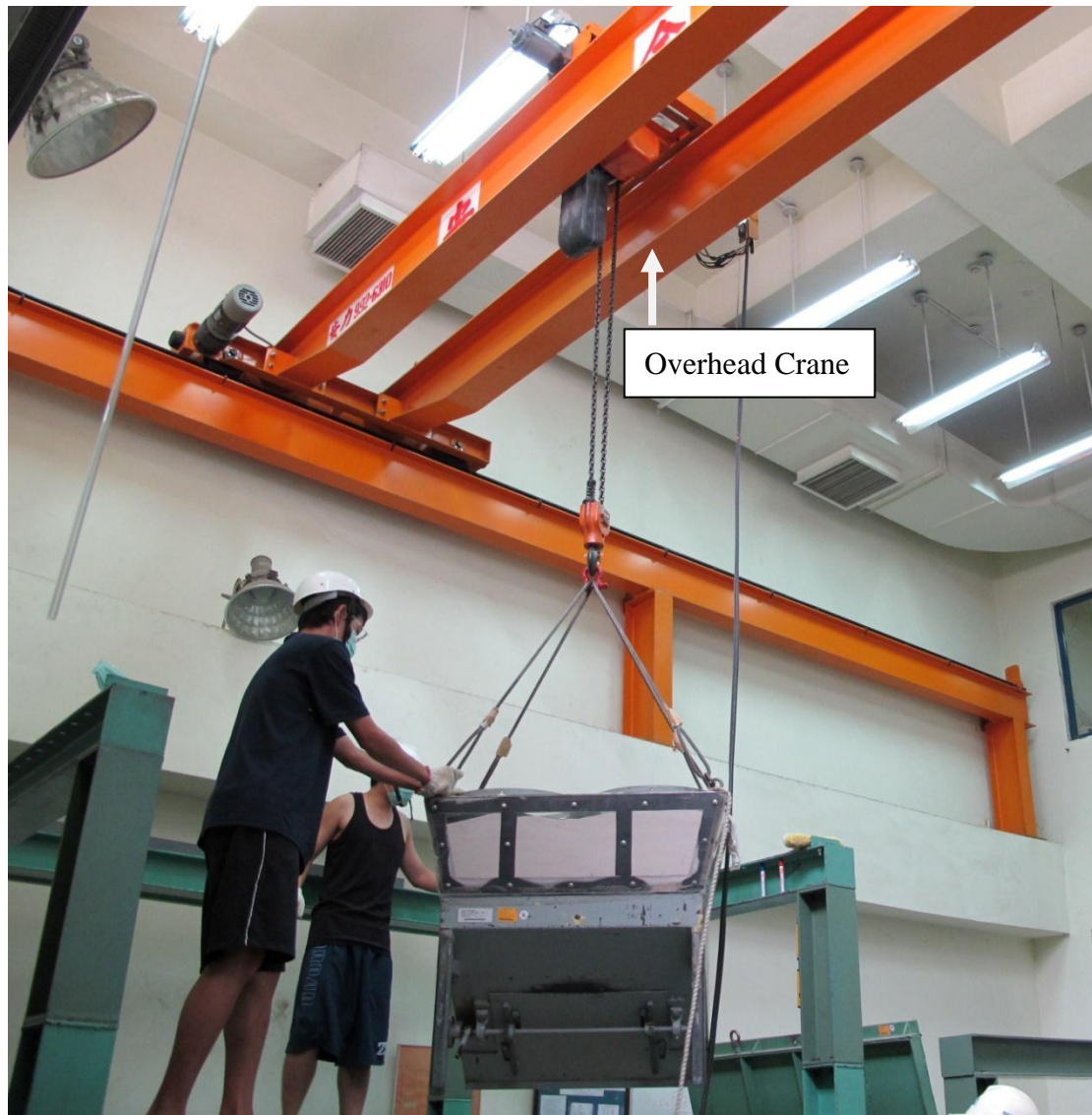


Fig. 5.3. Sand hopper lifted by overhead crane (after Chen, 2011)

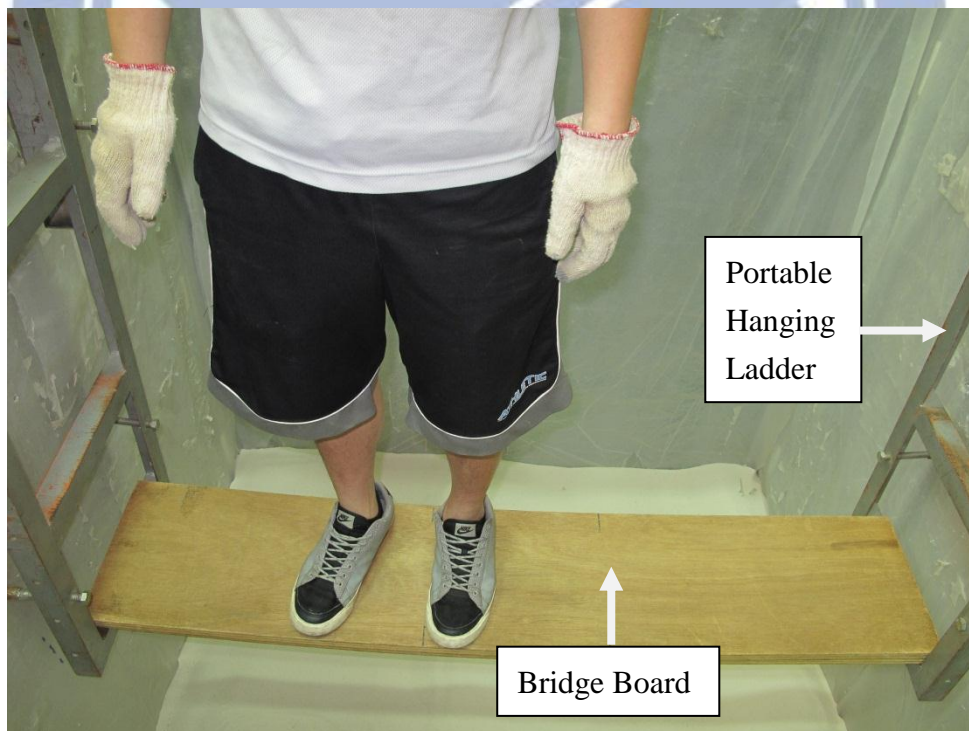


Fig. 5.4. Air-pluviation of Ottawa sand into soil bin





(a)



(b)

Fig. 5.5. Portable hanging ladders and bridge board hanging on side wall

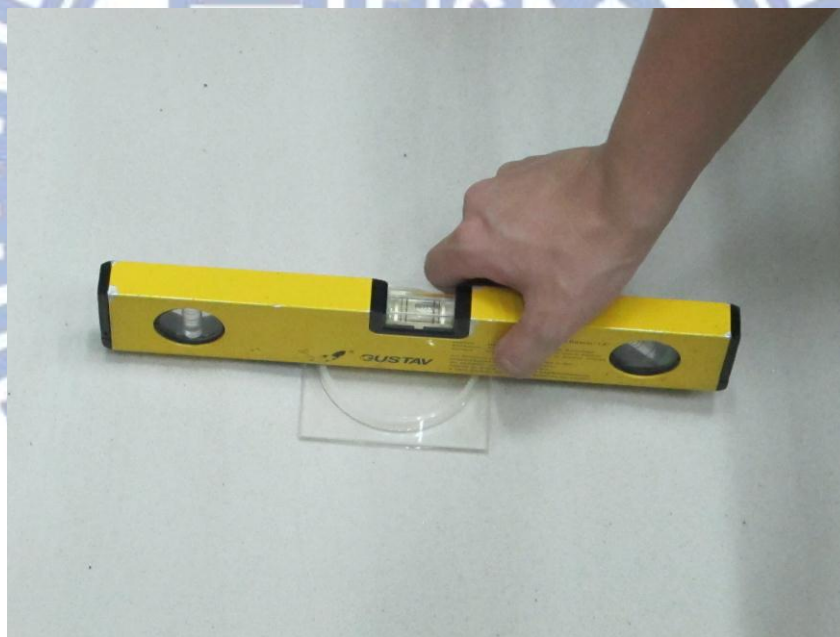


Fig. 5.6. Level soil surface with a brush





(a)



(b)

Fig. 5.7. Check density cup horizontal with a bubble level

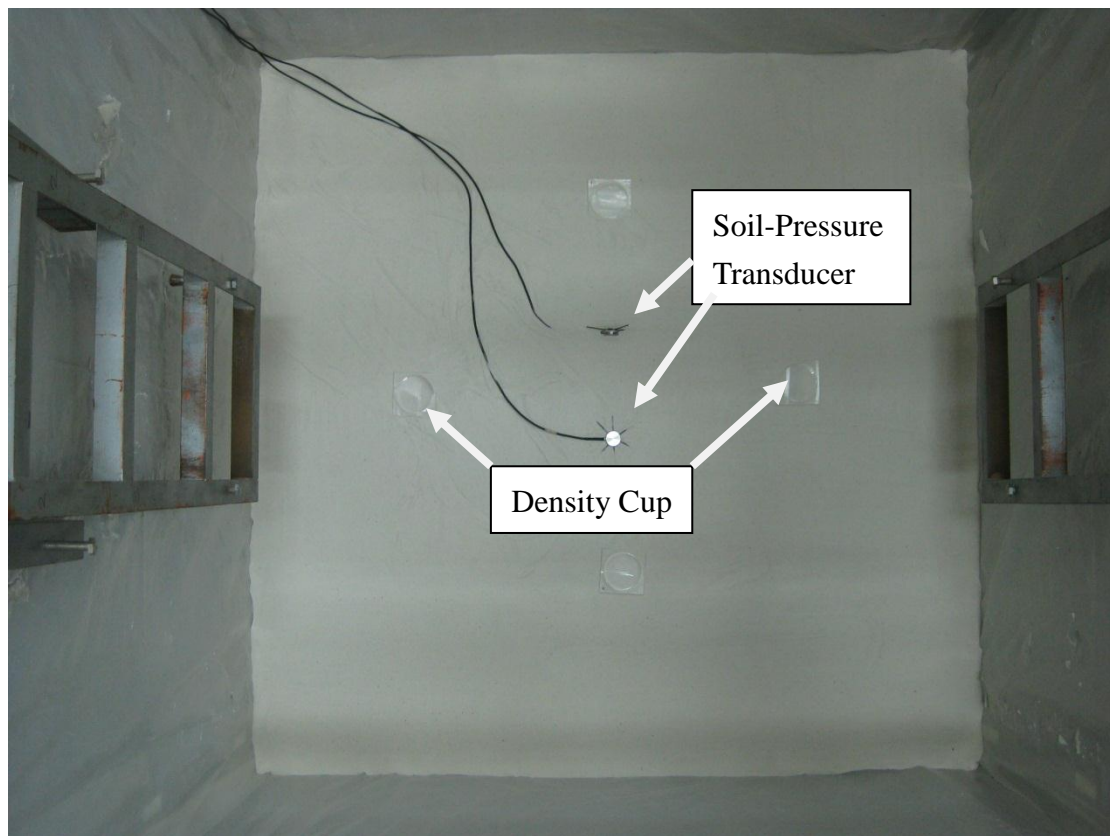


Fig. 5.8. Soil density cup and soil-pressure transducer placed on soil surface



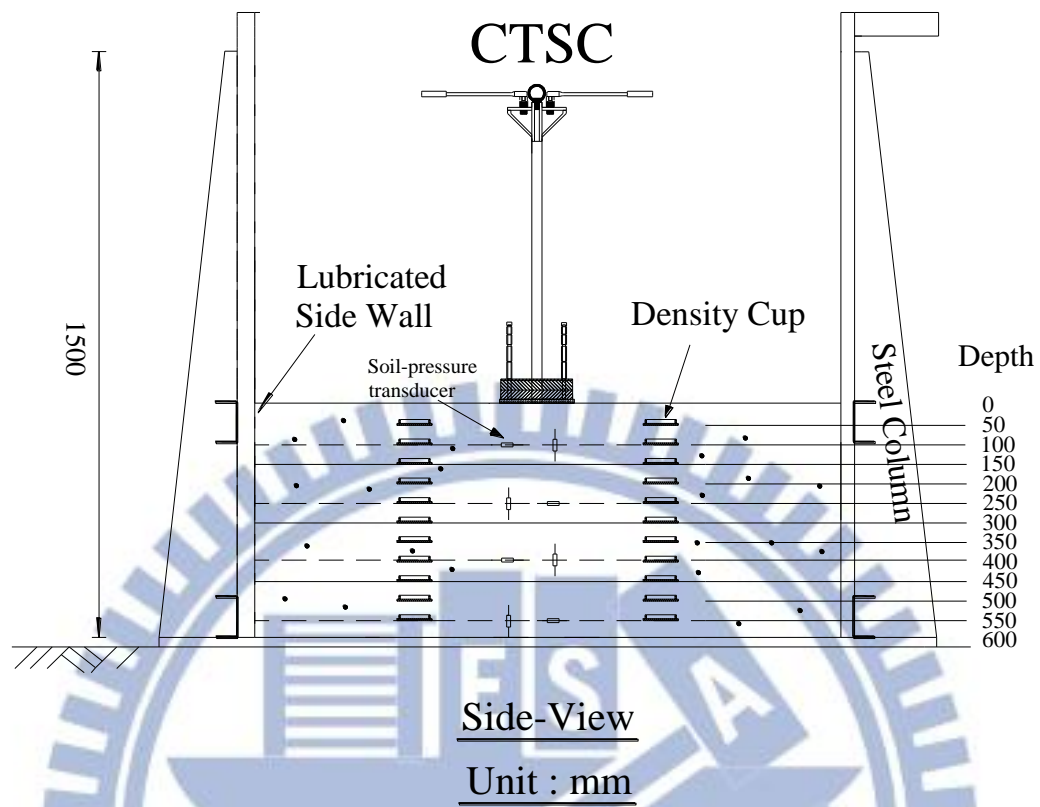


Fig. 5.9. Soil density cups and soil-pressure transducer buried at different elevations

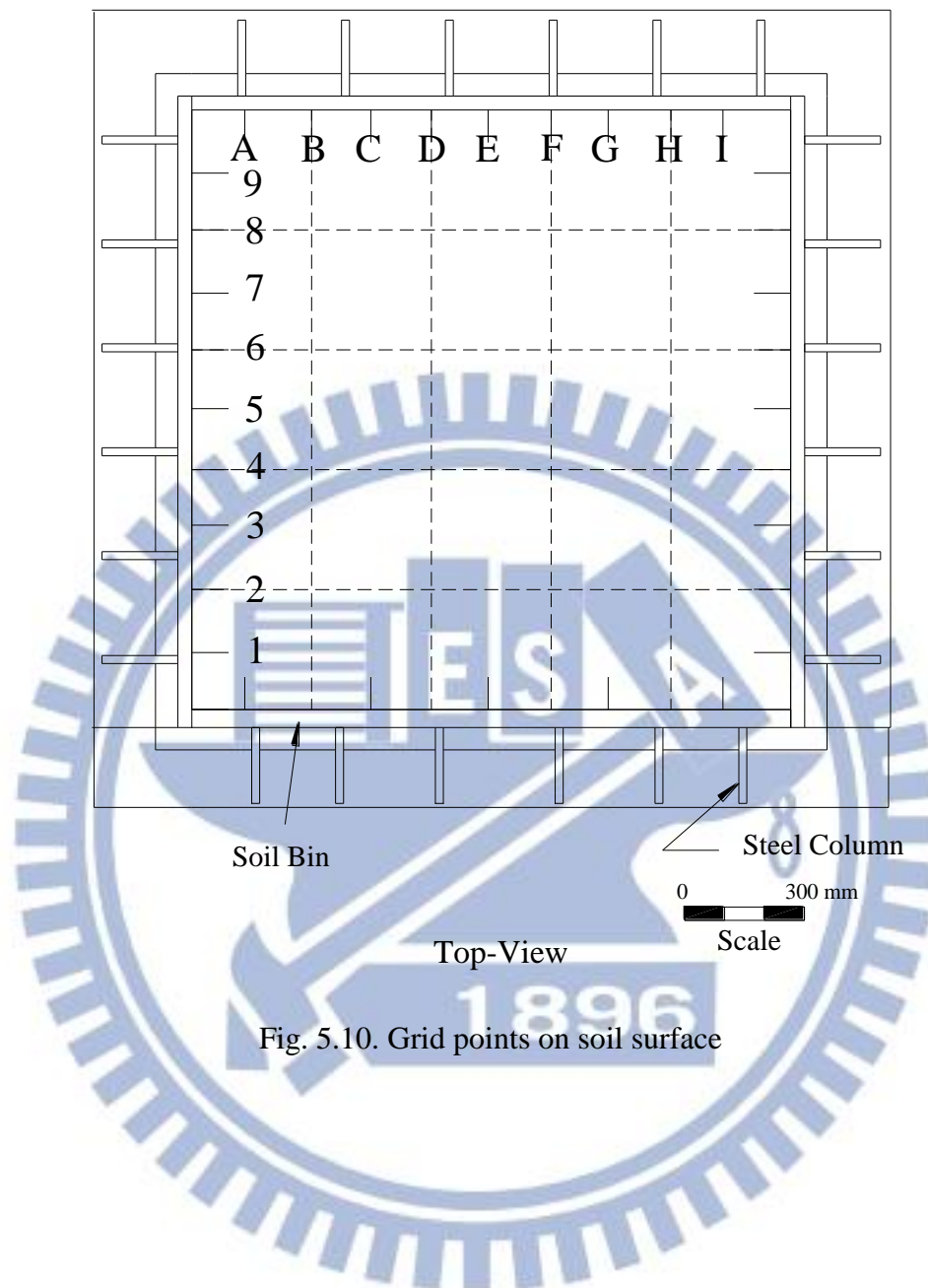
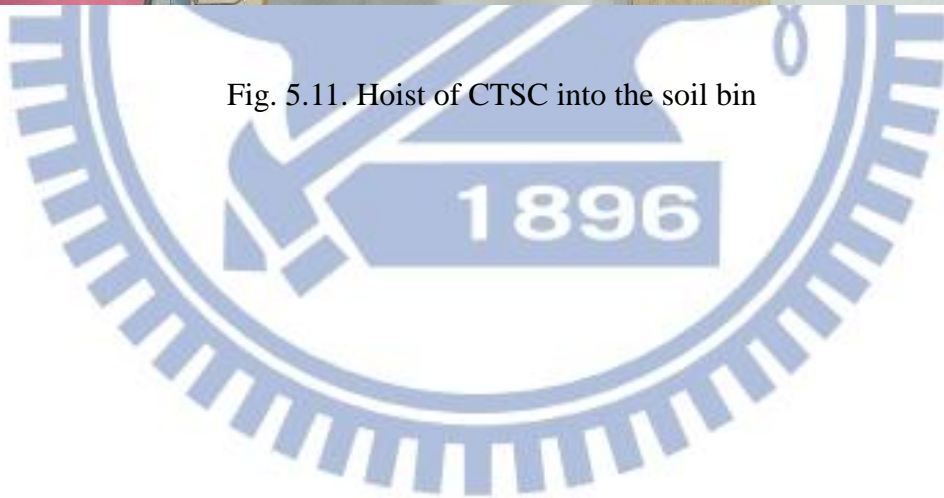
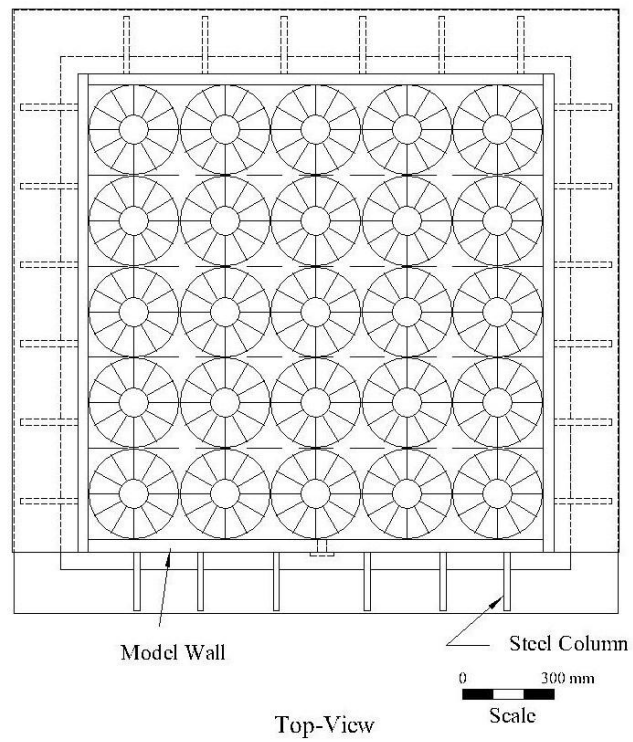


Fig. 5.10. Grid points on soil surface

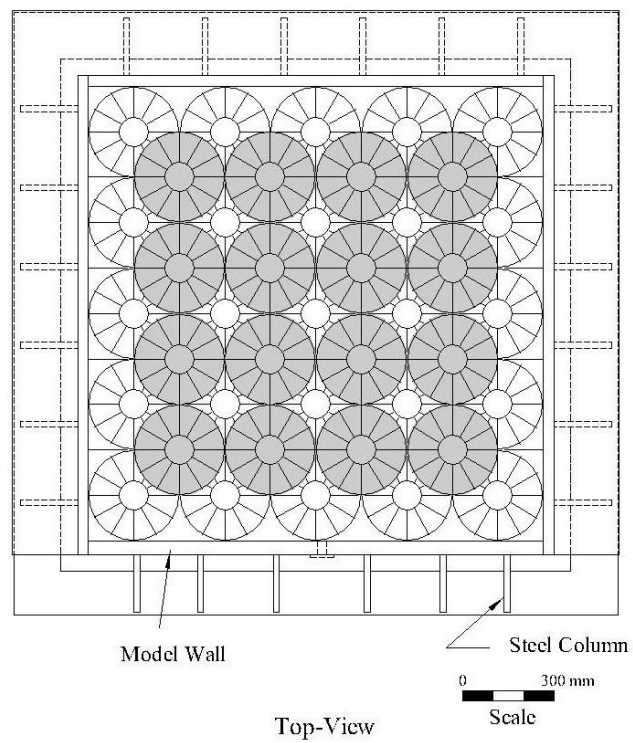


Fig. 5.11. Hoist of CTSC into the soil bin





(a) 5 x 5 loading formation



(b) 4 x 4 loading formation

Fig. 5.12. 5×5 and 4×4 loading formations of disc shearing location



Fig. 5.13. Apply vertical static load on loose sand

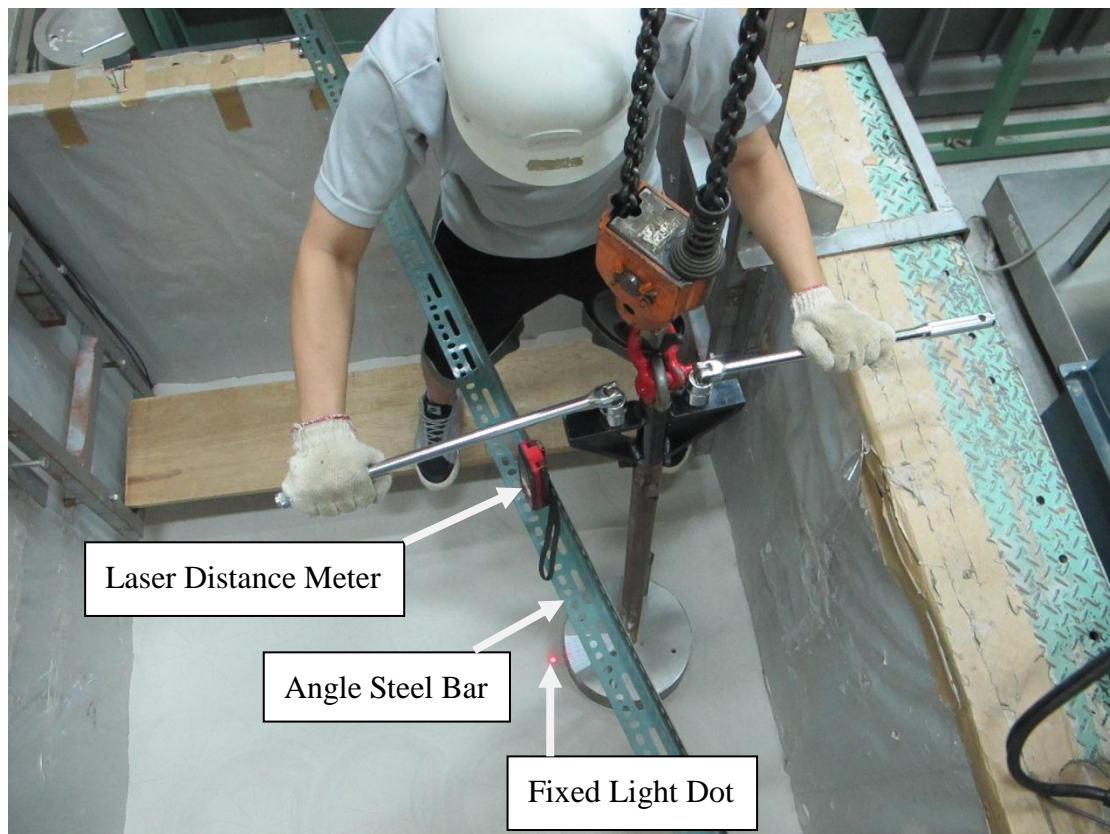


Fig. 5.14. Fixed light dot from laser distance meter



Fig. 5.15. Apply cyclic torsional shear on loose fill

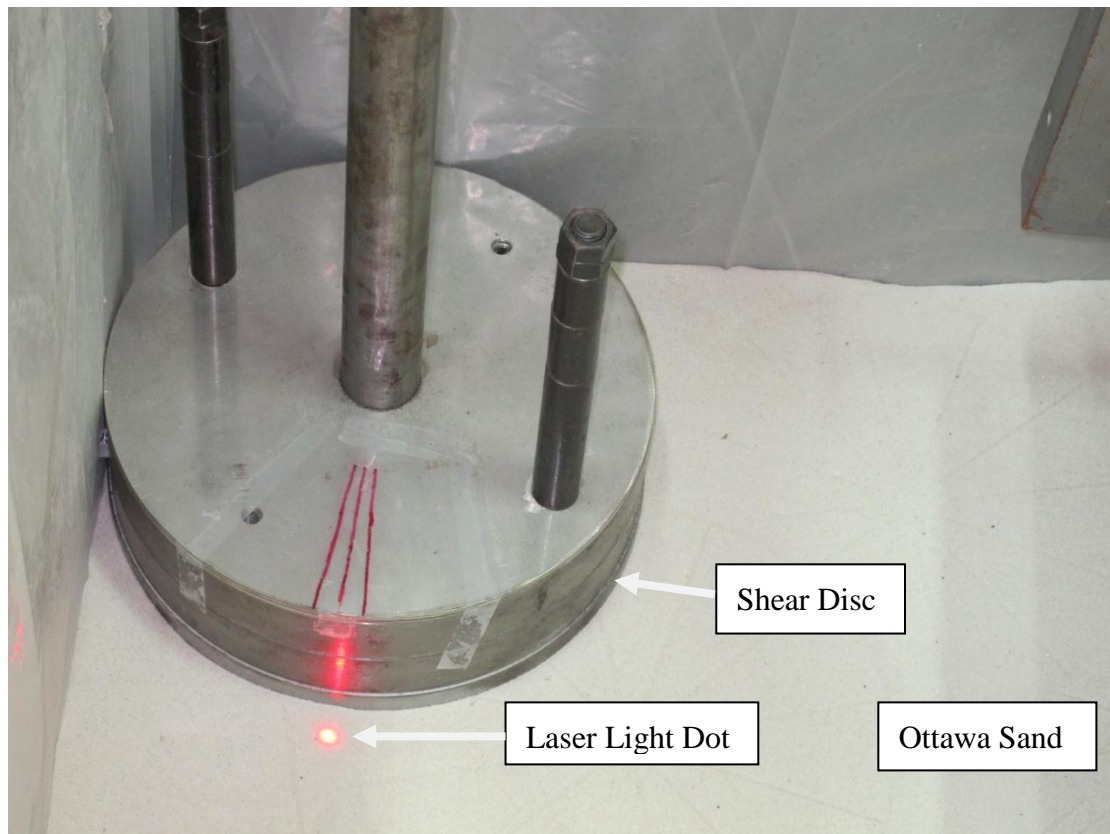
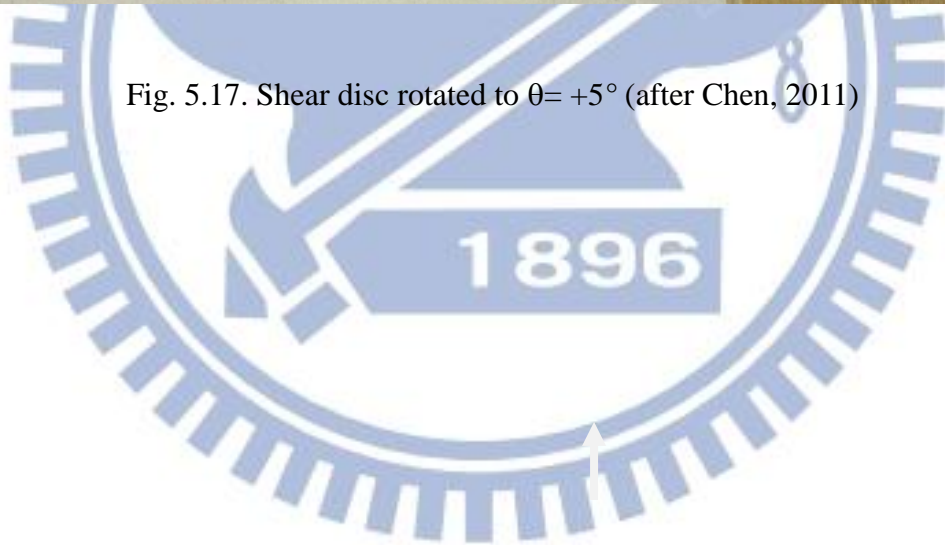


Fig. 5.16. Shear disc at initial position $\theta = 0^\circ$ (after Chen, 2011)



Fig. 5.17. Shear disc rotated to $\theta = +5^\circ$ (after Chen, 2011)



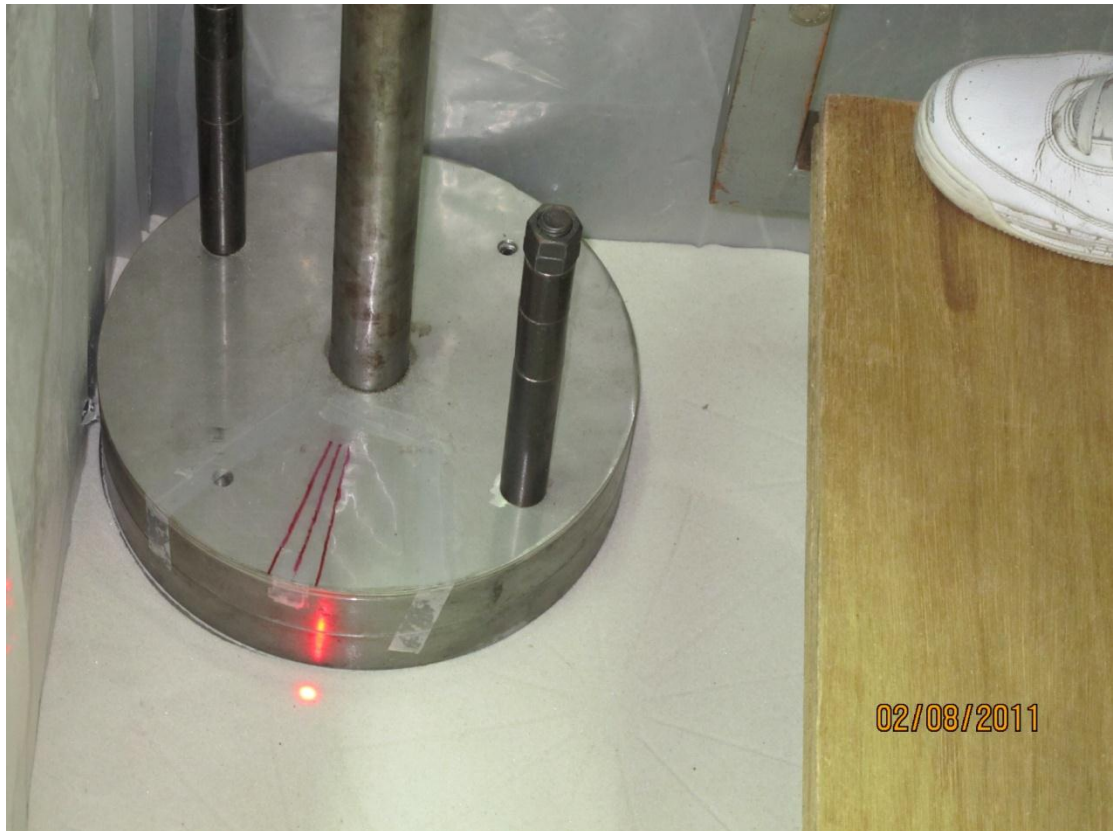


Fig. 5.18. Shear disc rotated to $\theta = -5^\circ$ (after Chen, 2011)



Fig. 5.19. Application of cyclic torsional shear to loose sand

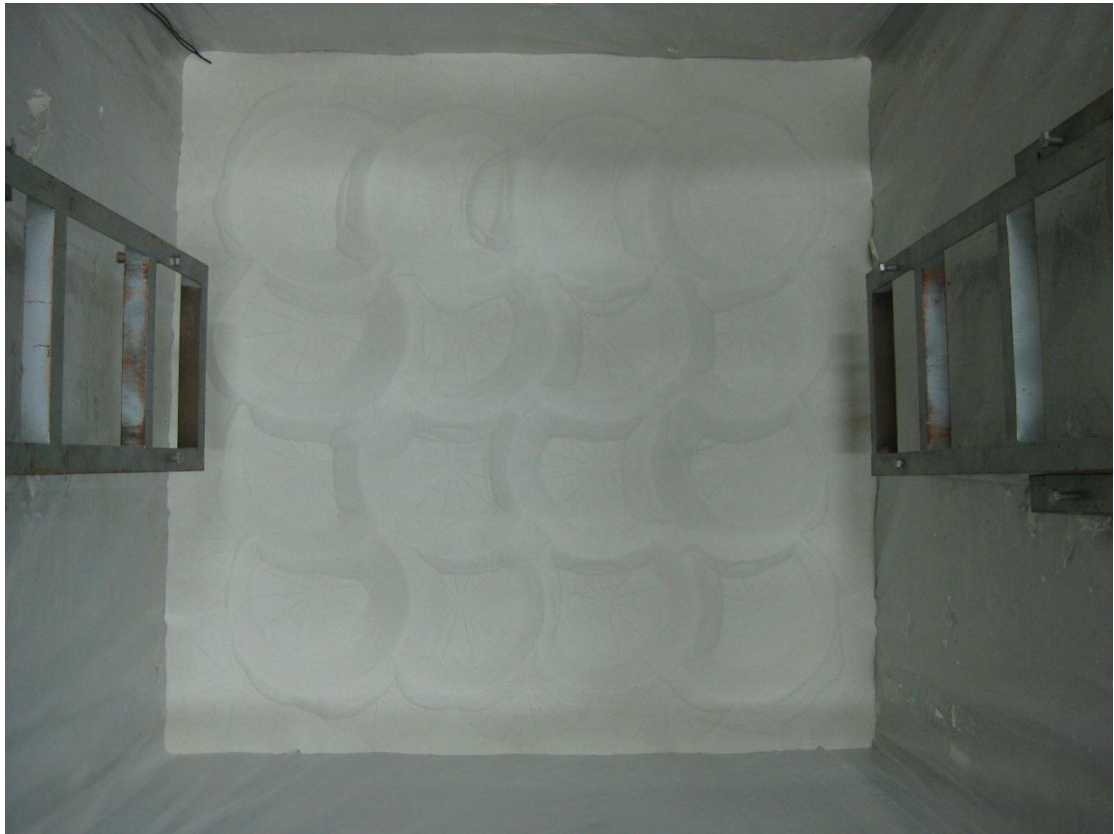


Fig. 5.20. Compacted soil surface after 4×4 formation of cyclic torsional shear at N=5

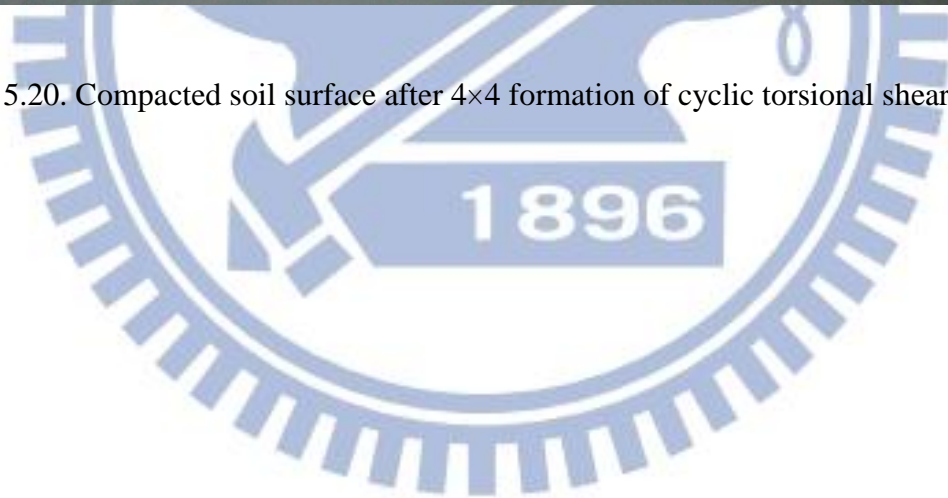




Fig. 5.21. Compacted soil surface after 5×5 formation of cyclic torsional shear at N=10

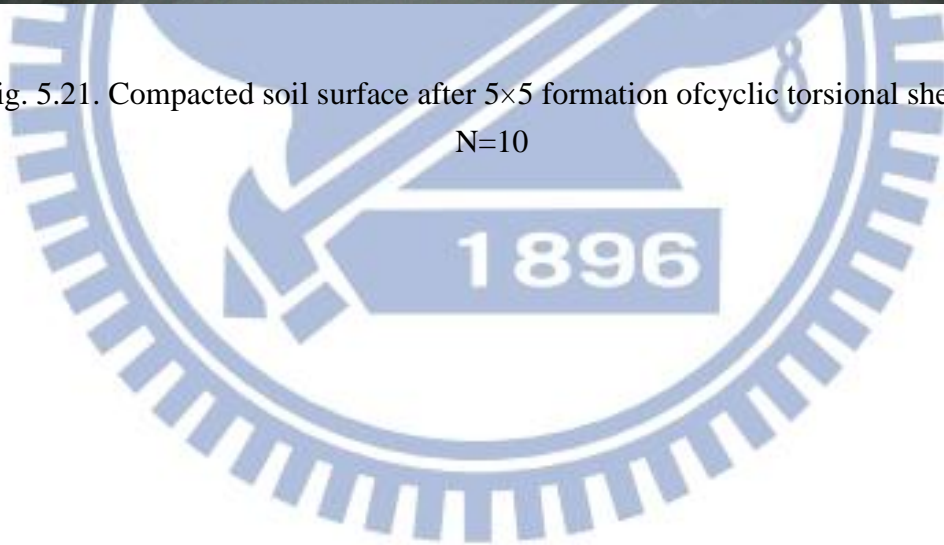




Fig. 5.22. Compacted soil surface after 4×4 formation of cyclic torsional shear at
N=20

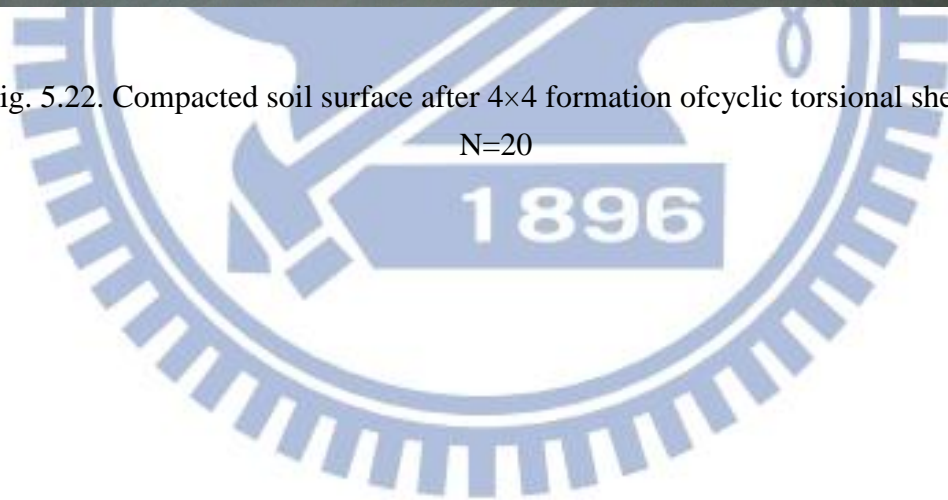




Fig. 5.23. Soil density cups dug out of compacted soil mass





(a)



(b)



(c)

Fig. 5.24. Scraping of soils toward edge of density cup with a spatula



(a)



(b)



(c)



(d)

Fig. 5.25. Brush away soil particles from base plate of density cup

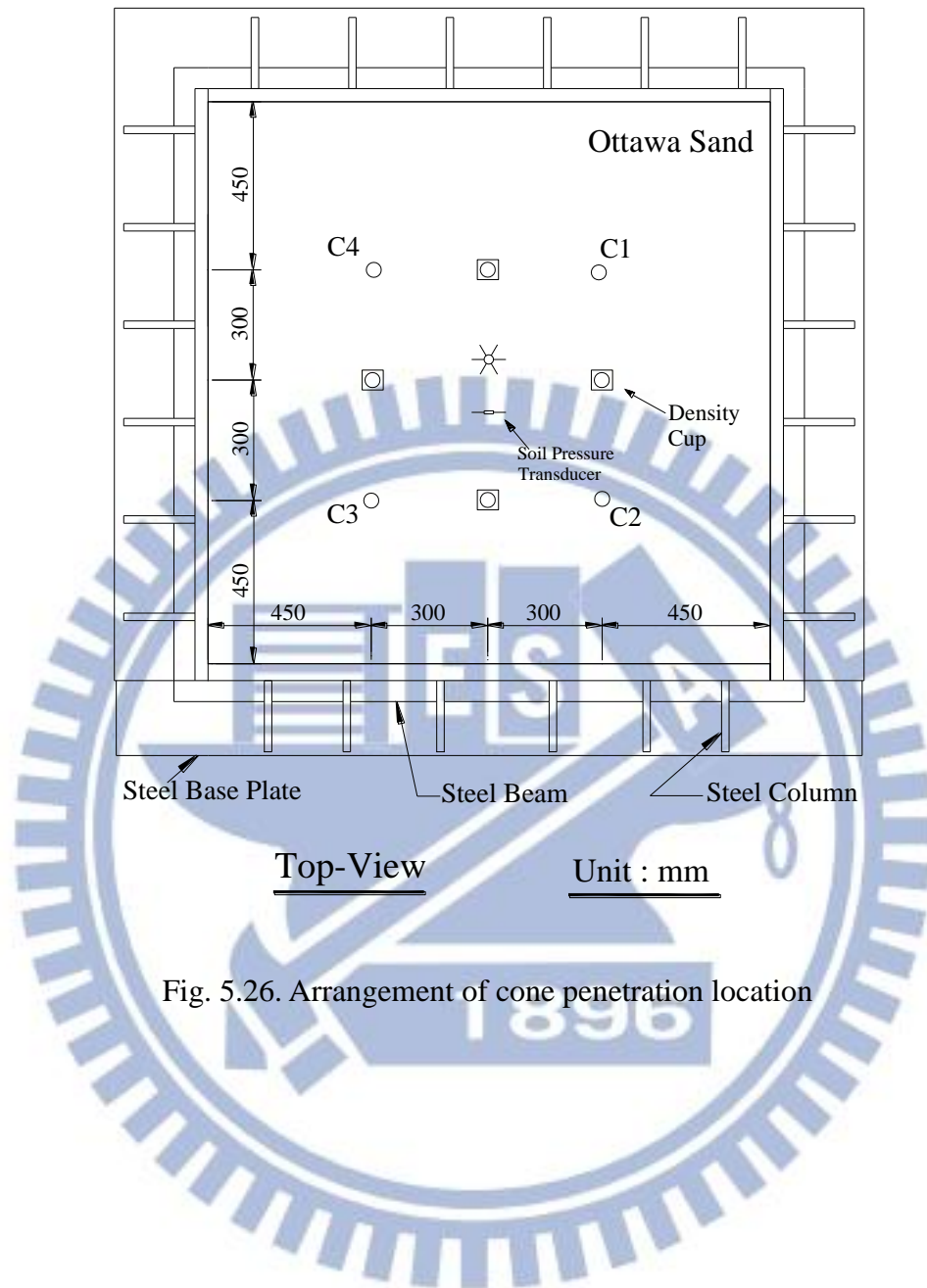
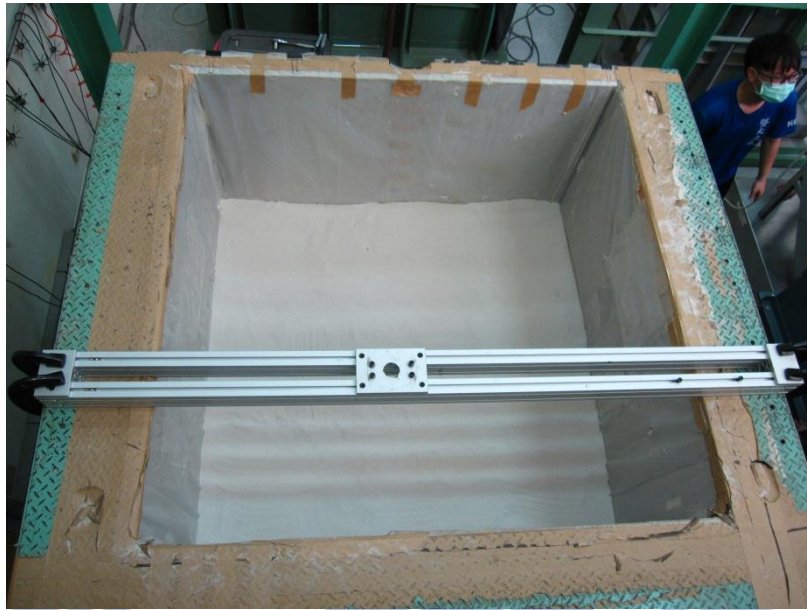


Fig. 5.26. Arrangement of cone penetration location



(a)



Steel C-clamp

(b)

Fig. 5.27. Steel beam on top of soil bin for CPT test

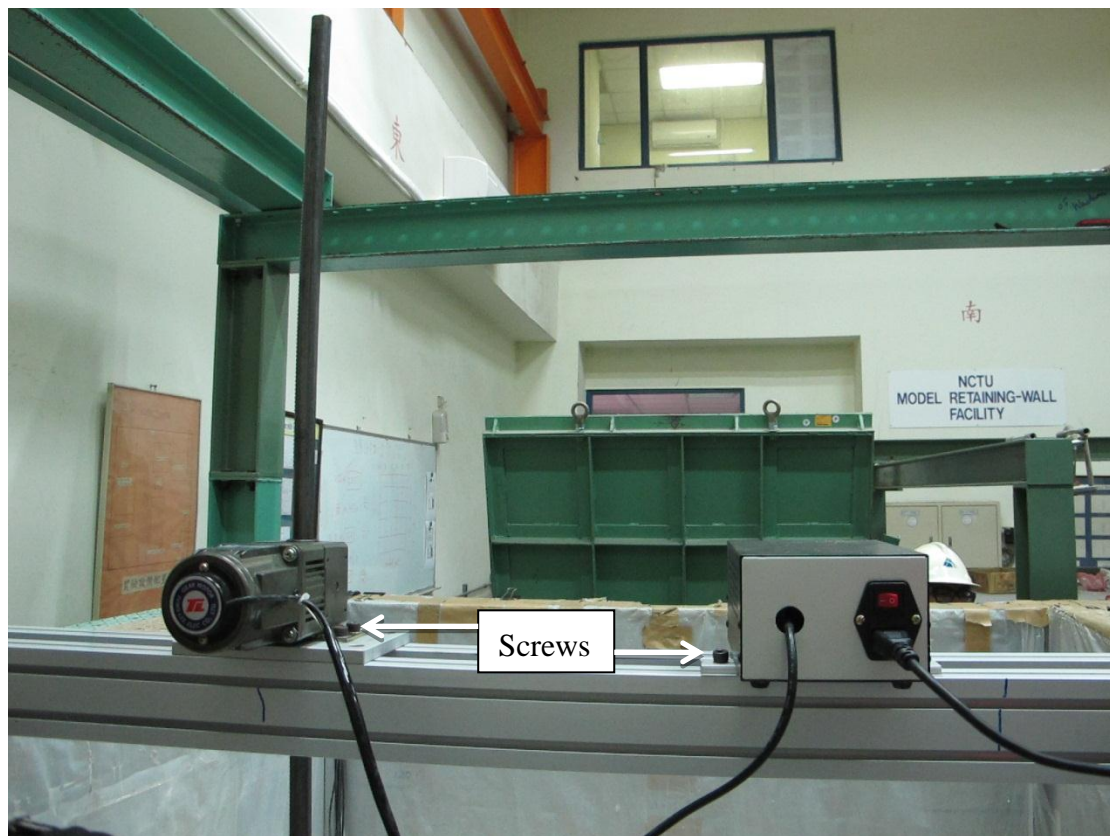


Fig. 5.28. Electric motor and movable plate fixed to the steel beam by the screws



(a)



(b)

Fig. 5.29. Connect cone penetrometer with electric motor



Fig. 5.30. Cone penetrometer on soil surface

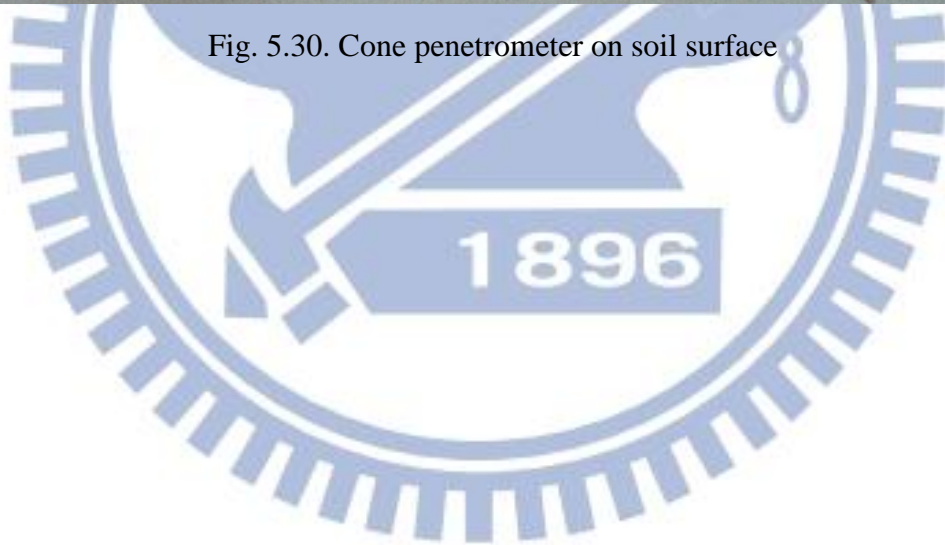




Fig. 6.1. Settlement measurement with laser distance meter



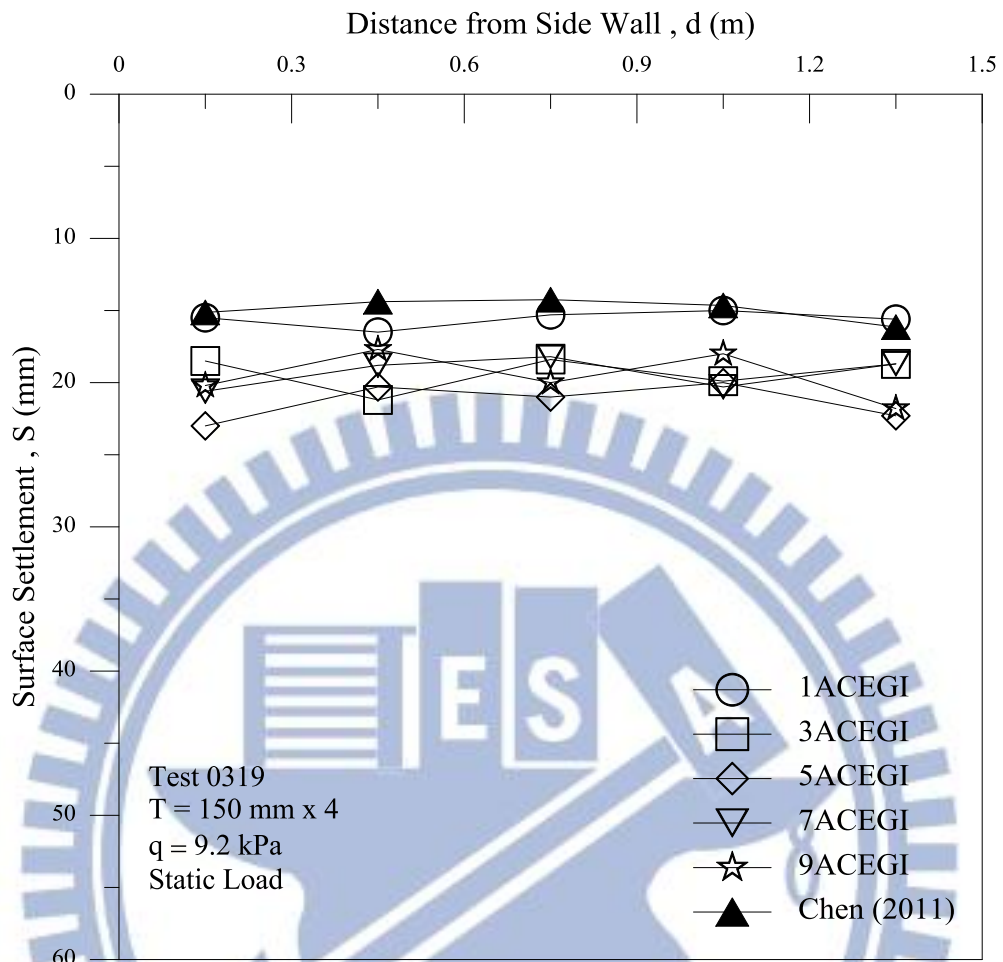


Fig. 6.2. Surface settlement due to static vertical loading

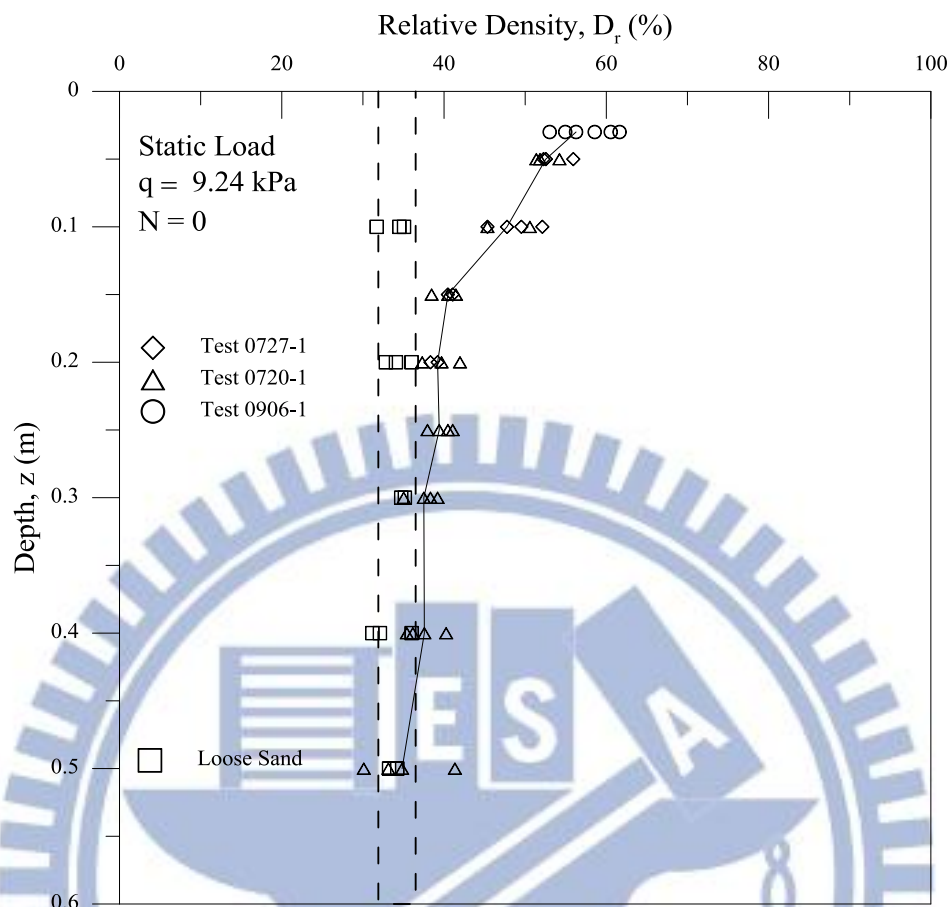


Fig. 6.3. Distribution of relative density due to static vertical loading (after Chen, 2011)

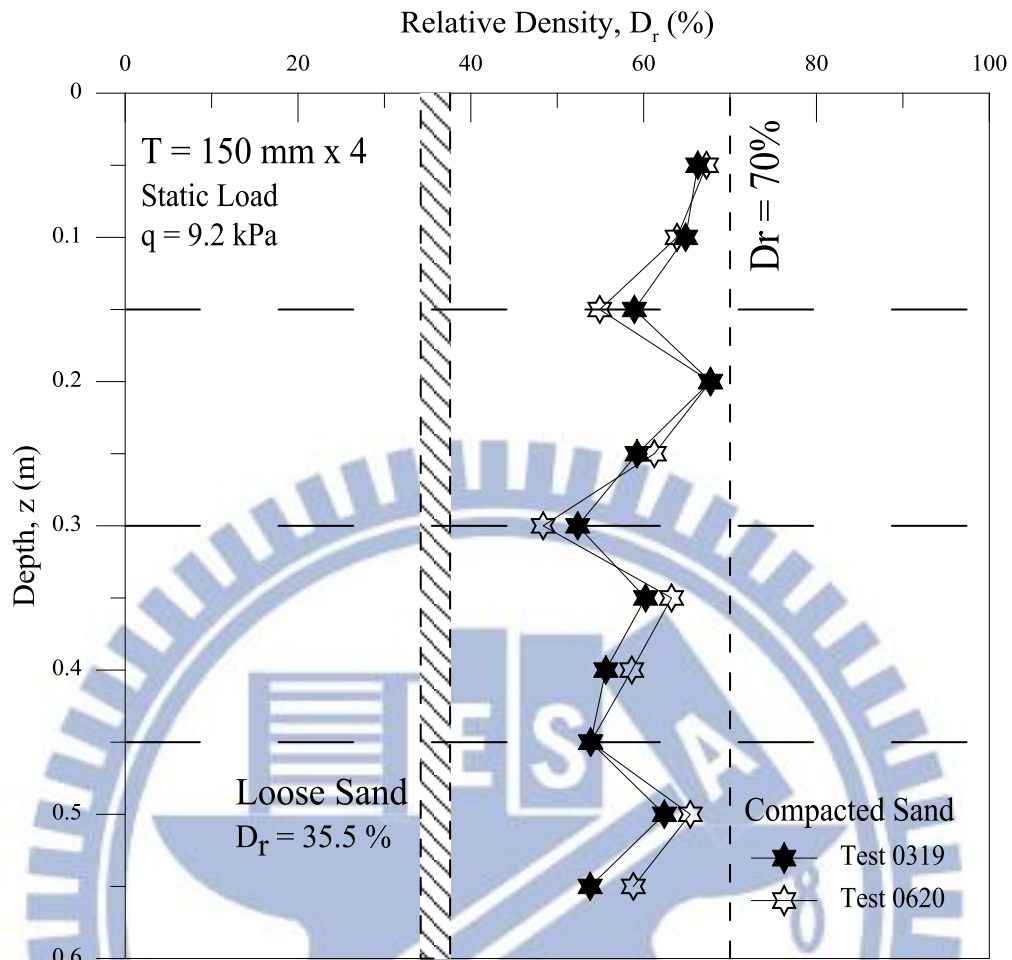
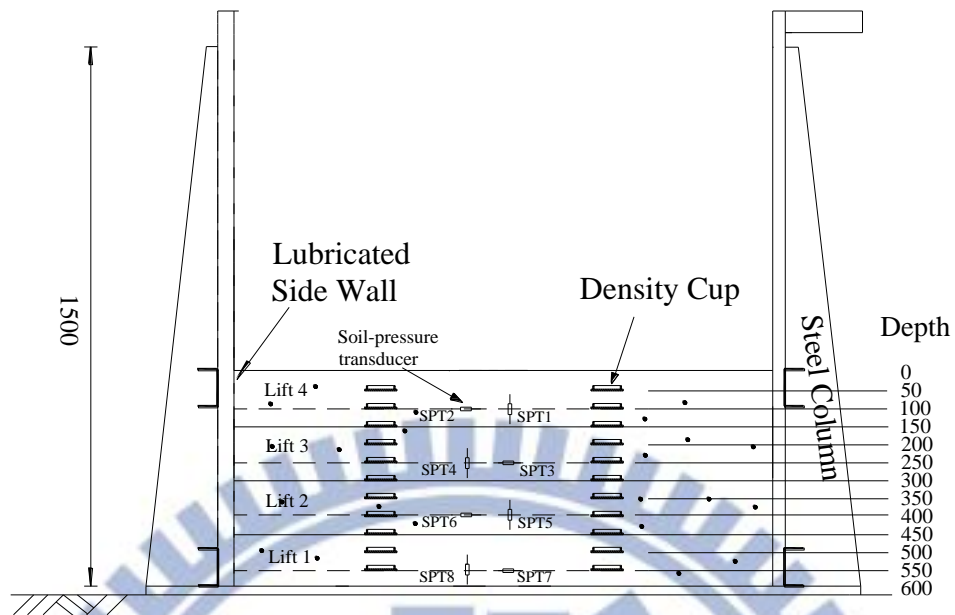


Fig. 6.4. Distribution of relative density due to static vertical loading



Side-View

Unit : mm

Fig. 6.5. Locations of SPT to measure distribution of earth pressure

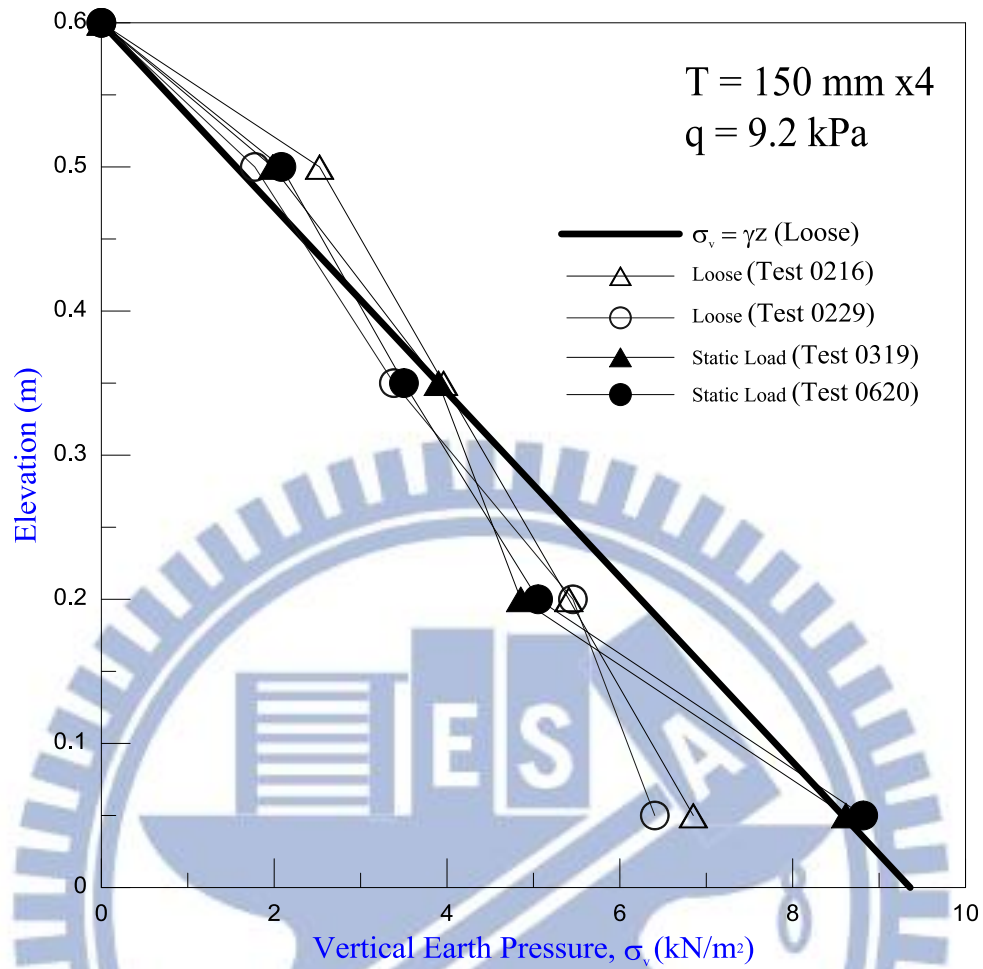


Fig. 6.6. Distribution of vertical earth pressure with depth

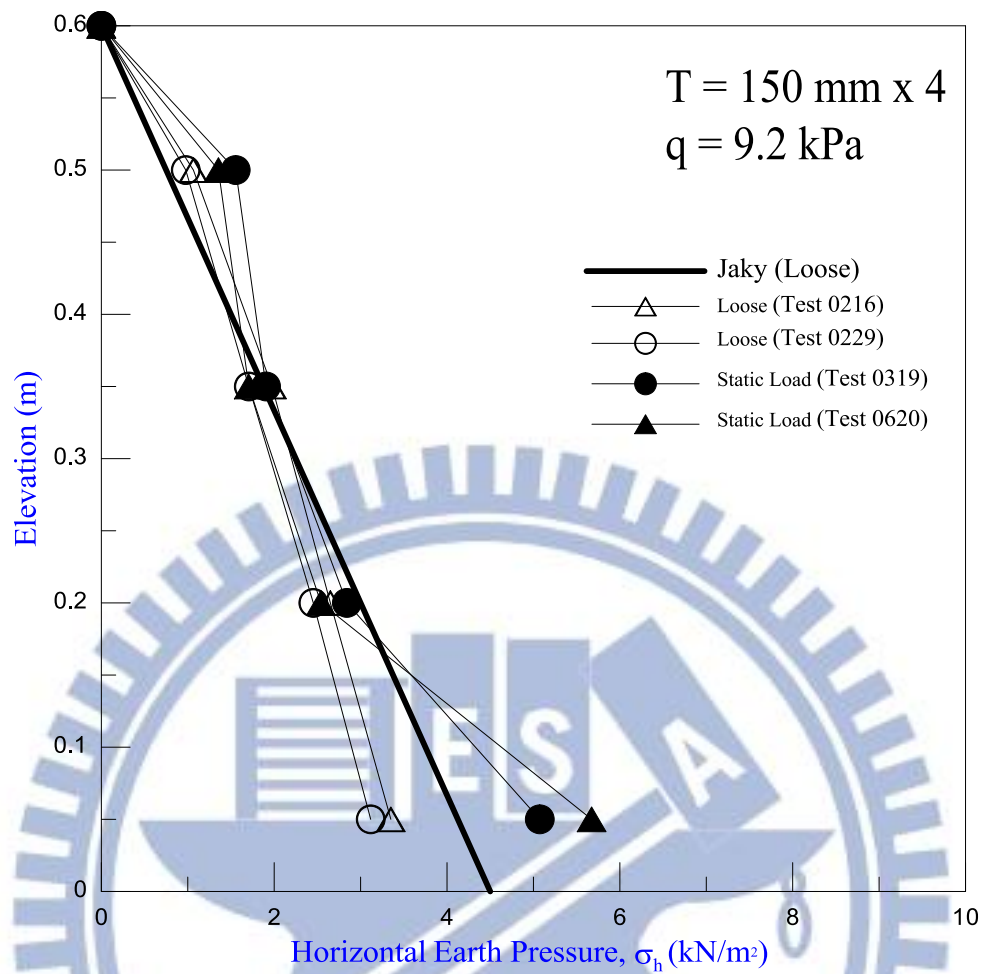


Fig. 6.7. Distribution of horizontal earth pressure with depth

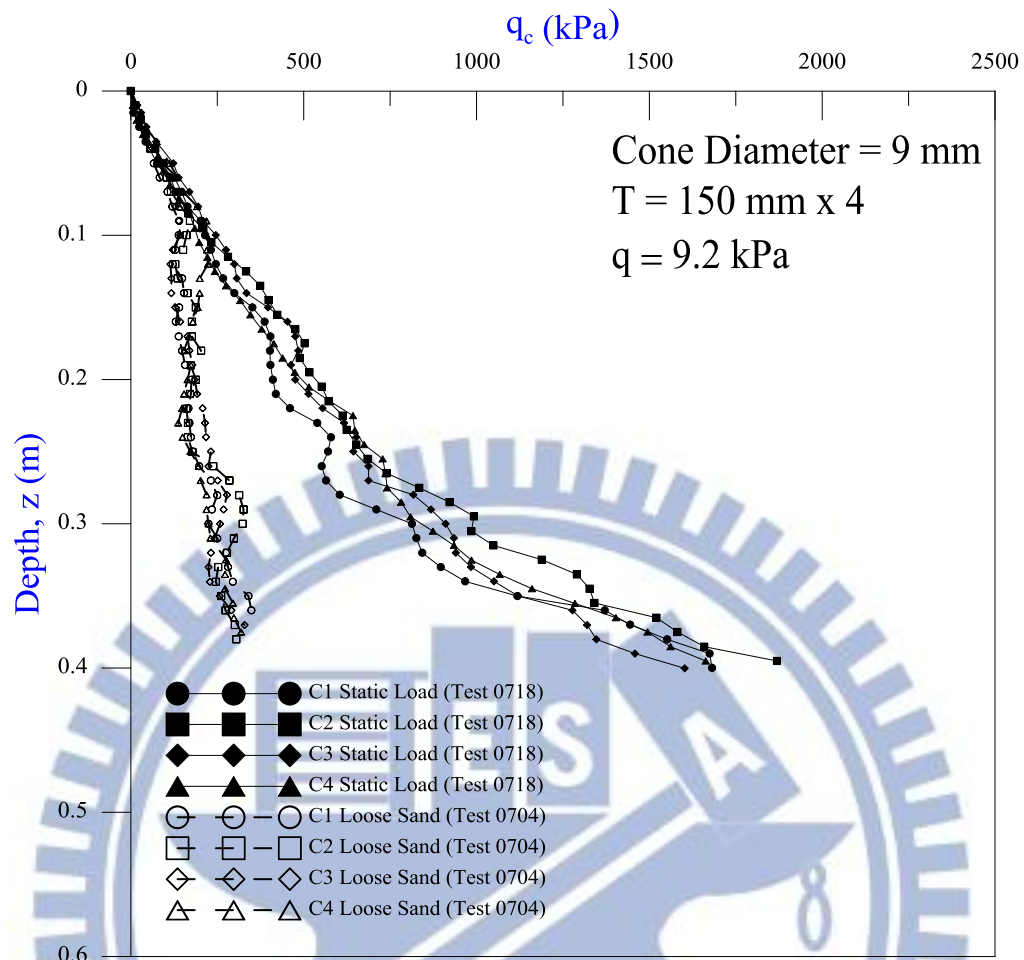


Fig. 6.8. Distribution of cone resistance in soil mass

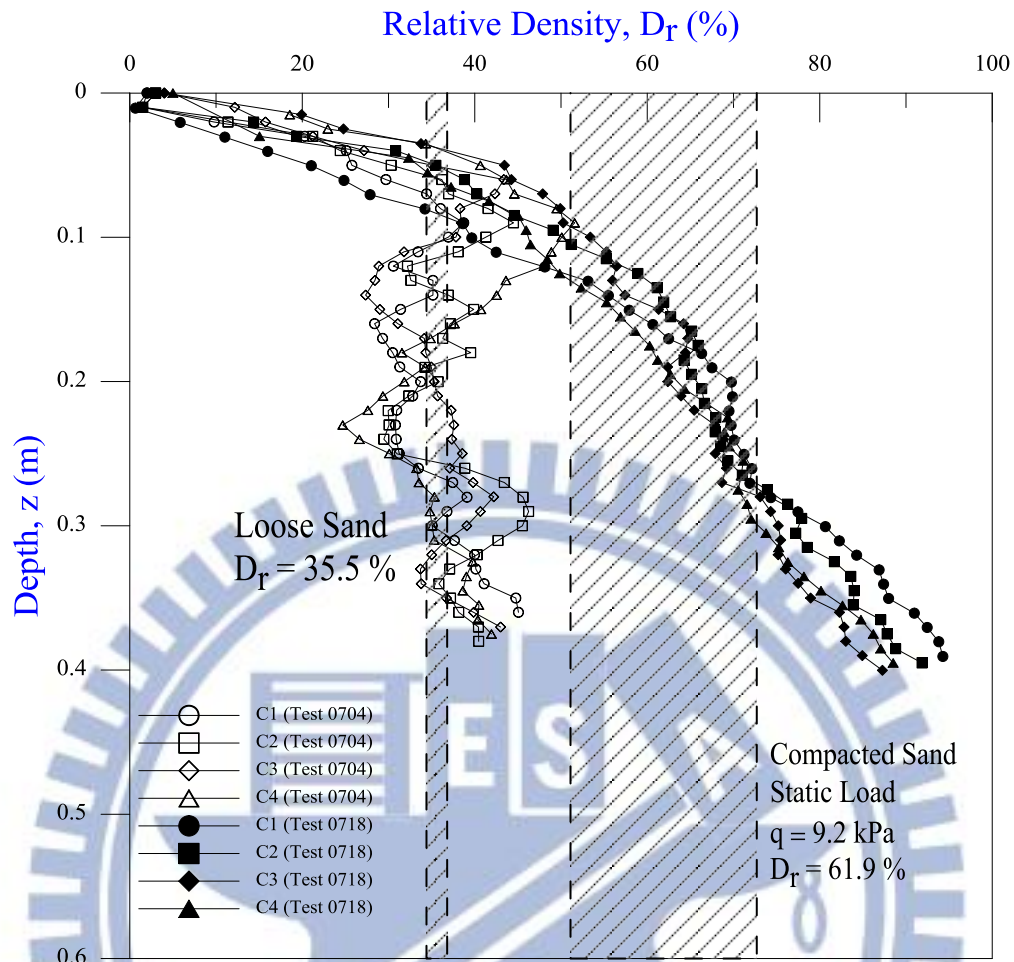


Fig. 6.9. Distribution of relative density after static load



Fig. 6.10. Digital torque wrench

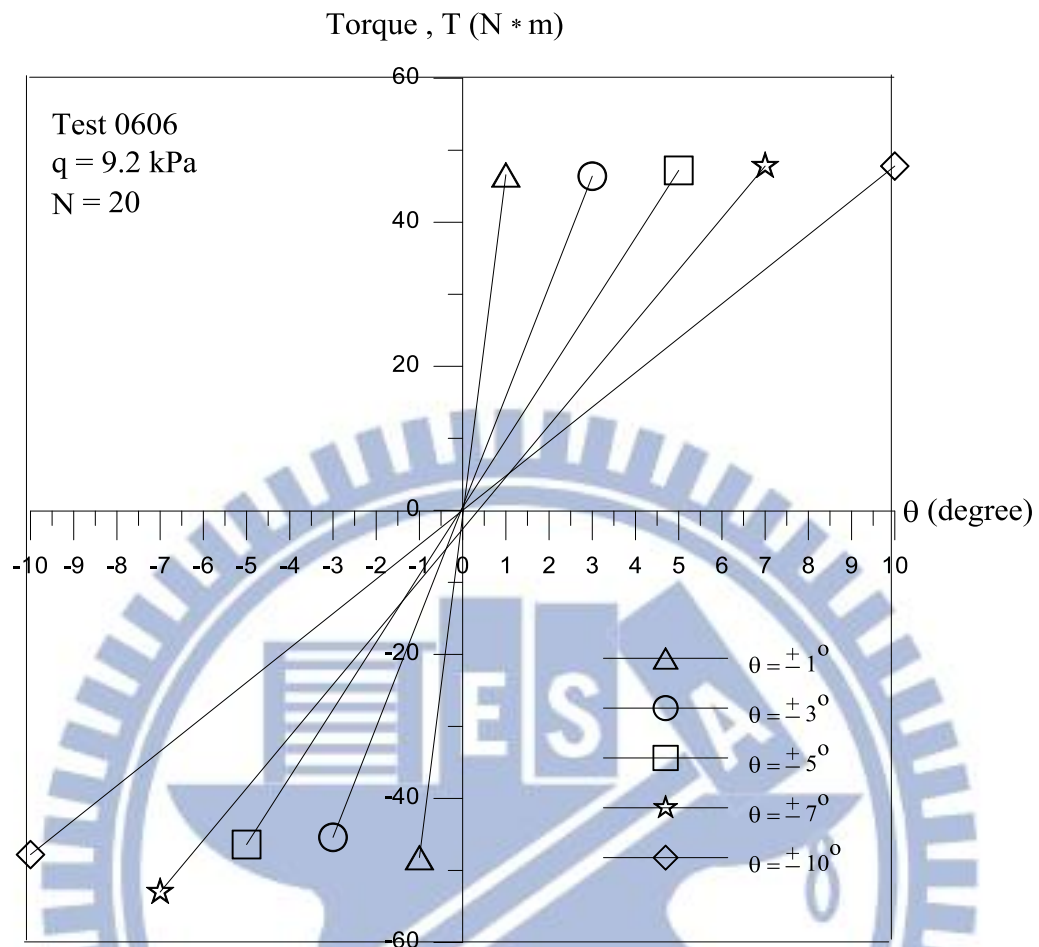


Fig. 6.11. Torque with number of cyclic for $\theta = \pm 1^\circ, \pm 3^\circ, \pm 5^\circ, \pm 7^\circ$ and $\pm 10^\circ$

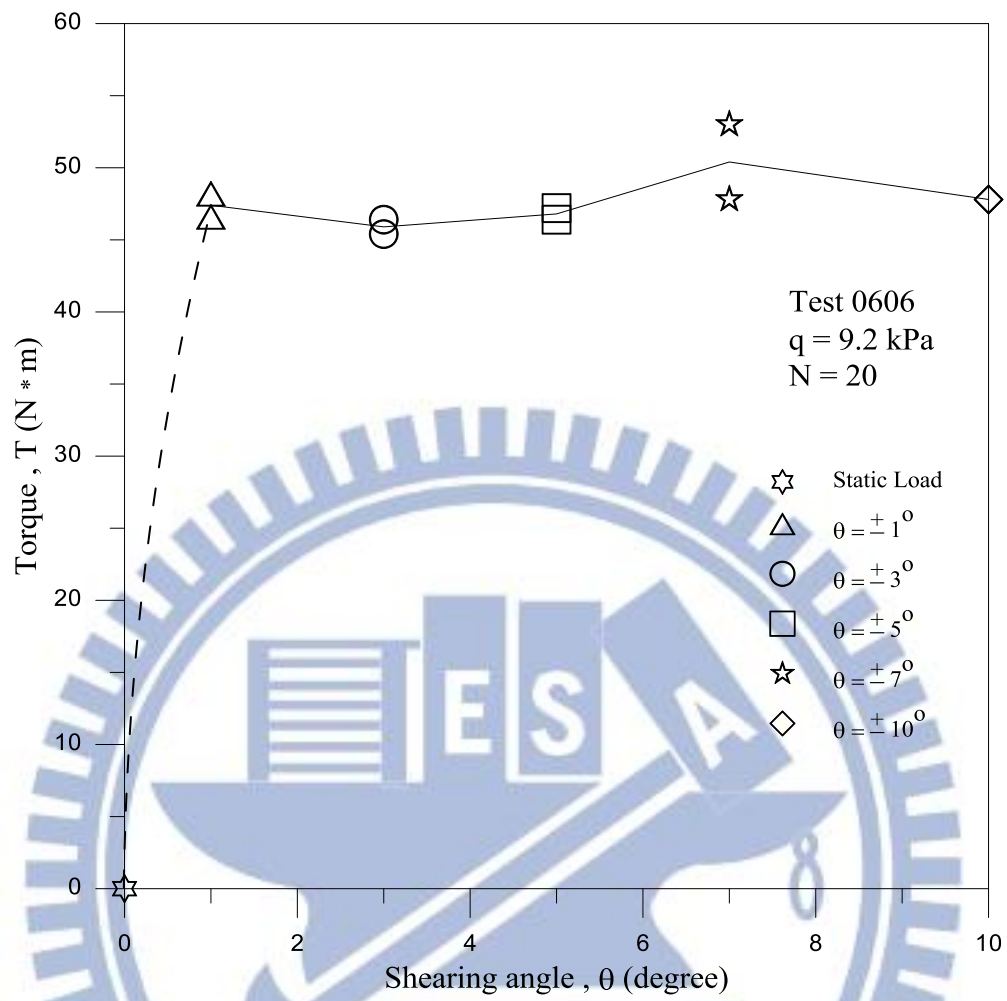
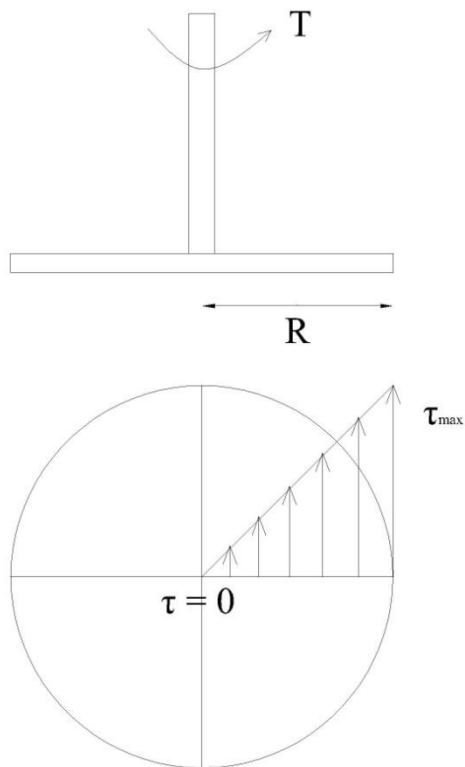


Fig. 6.12. Variation of torque with shearing angle



Maximum shear stress torsion
for a solid circular shaft :

$$\tau_{\max} = \frac{TR}{J}$$

T = Torsion

R = Radial of circular disc

J = Polar moment of inertia of
the circular cross section

$$J = \frac{\pi}{32} D^4$$

Fig. 6.13. Determine the maximum torsional shear stress at the edge of the shearing disc due to the applied torque

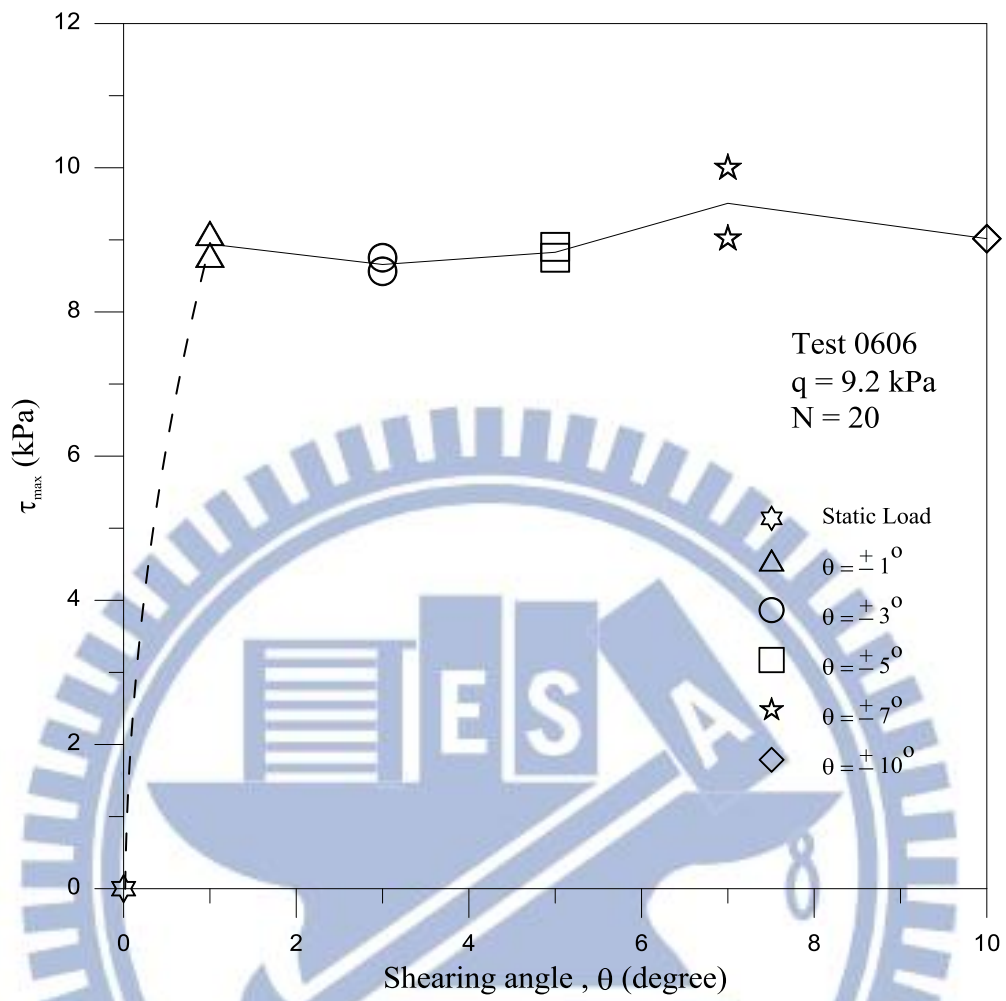


Fig. 6.14. Maximum shear stress with shearing angle

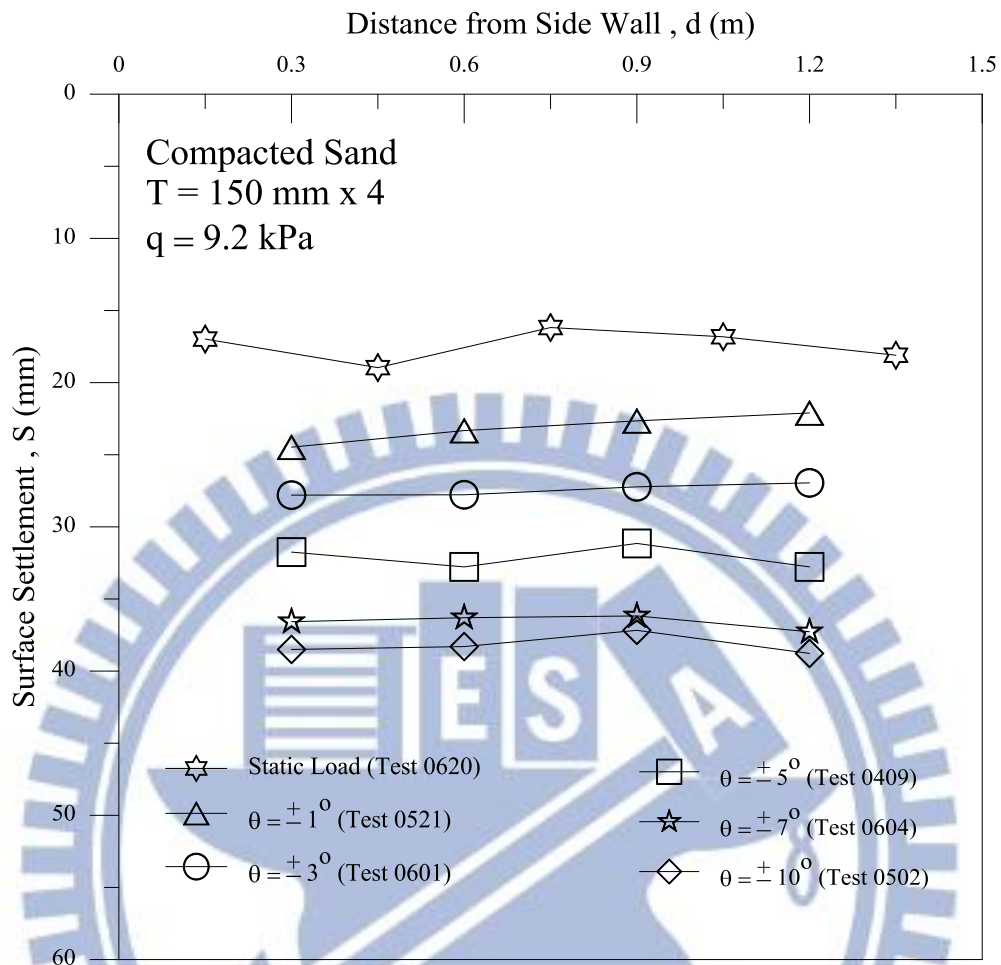


Fig. 6.15. Settlement after cyclic torsional shearing

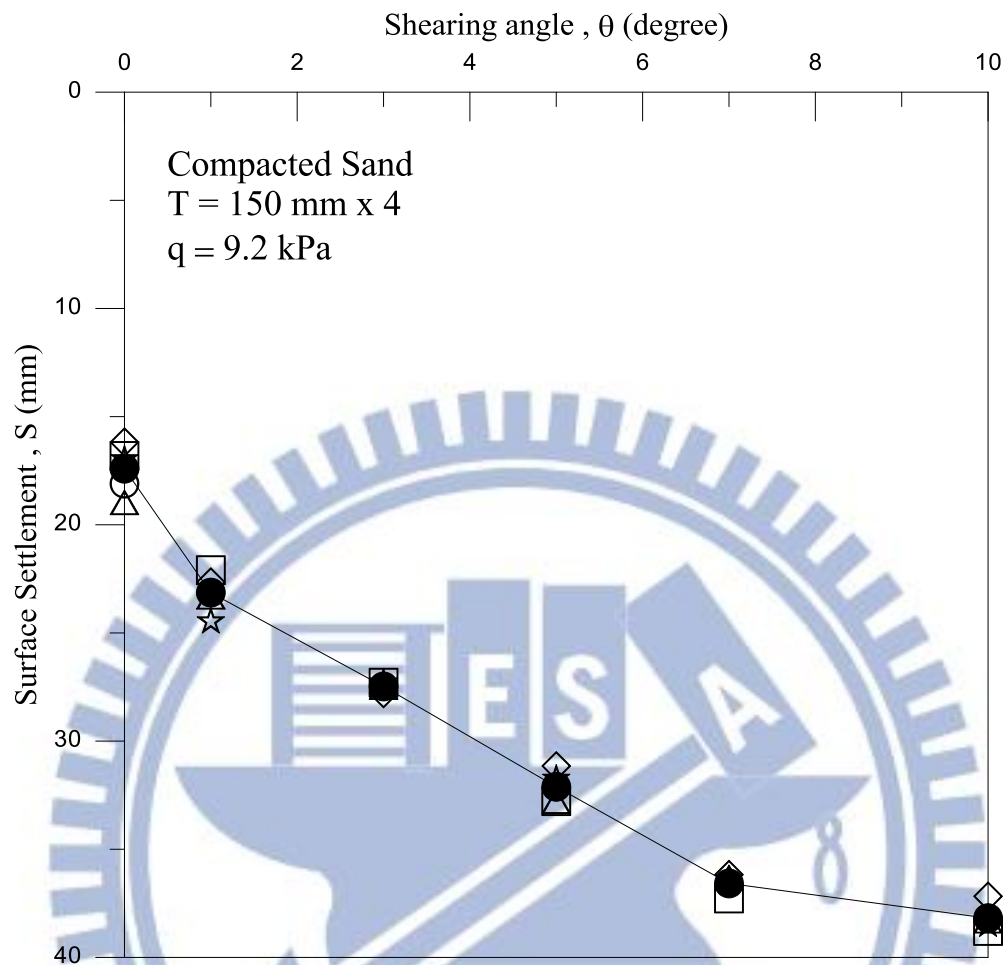


Fig. 6.16. Settlement after cyclic torsional shearing

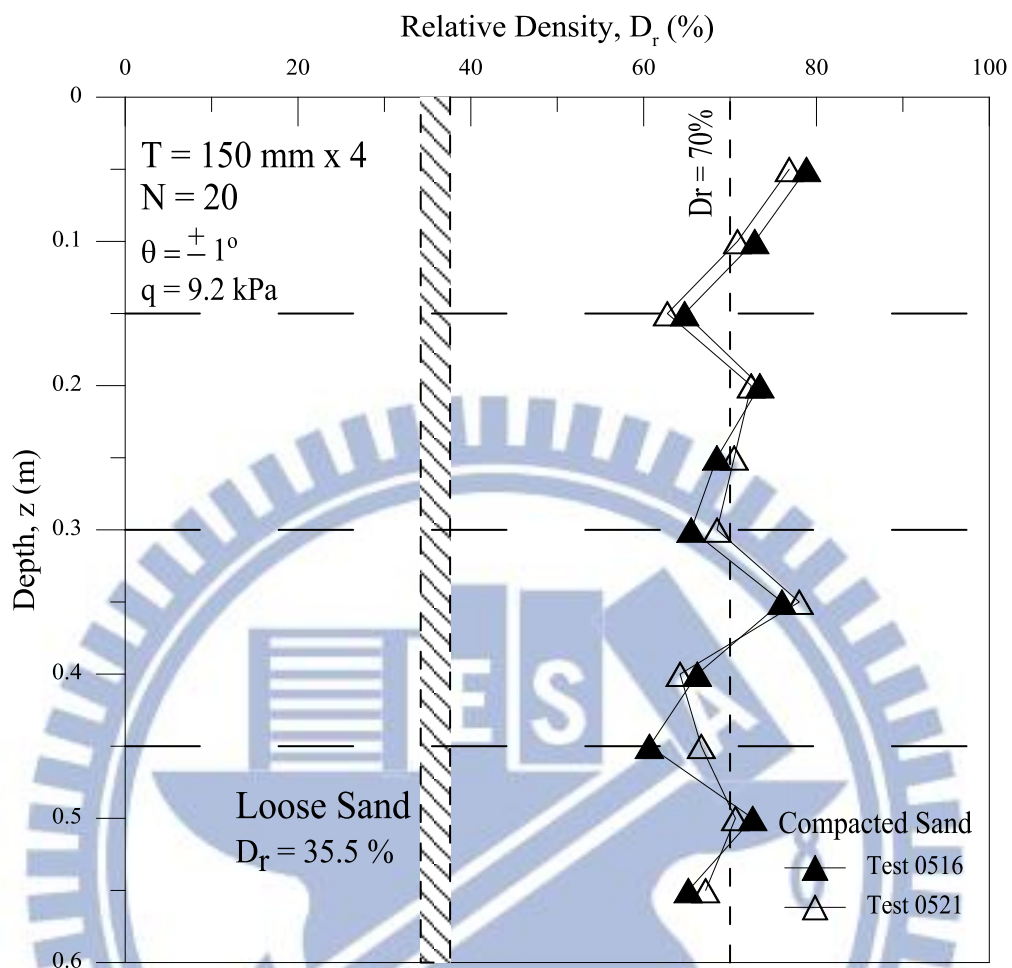


Fig. 6.17. Distribution of relative density due to cyclic torsional shearing at $\theta = \pm 1^\circ$

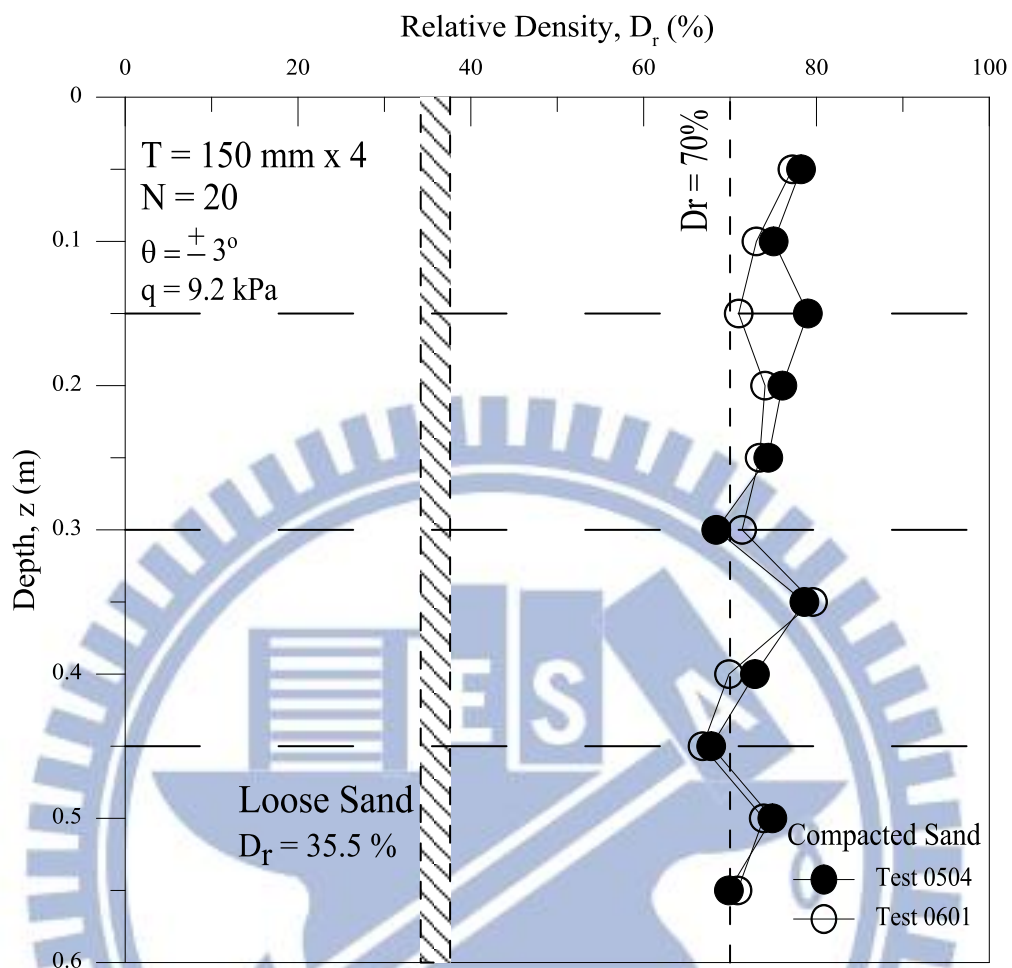


Fig. 6.18. Distribution of relative density due to cyclic torsional shearing at $\theta = \pm 3^\circ$

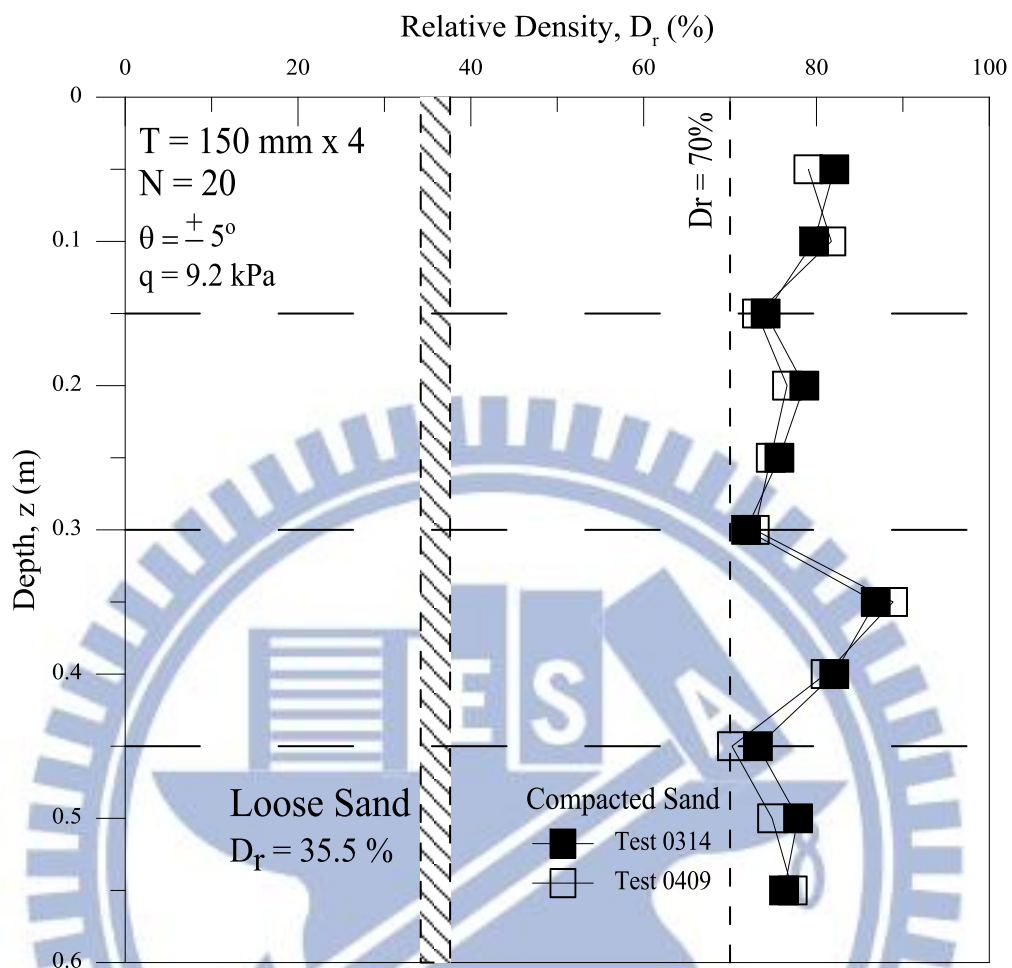


Fig. 6.19. Distribution of relative density due to cyclic torsional shearing at $\theta = \pm 5^\circ$

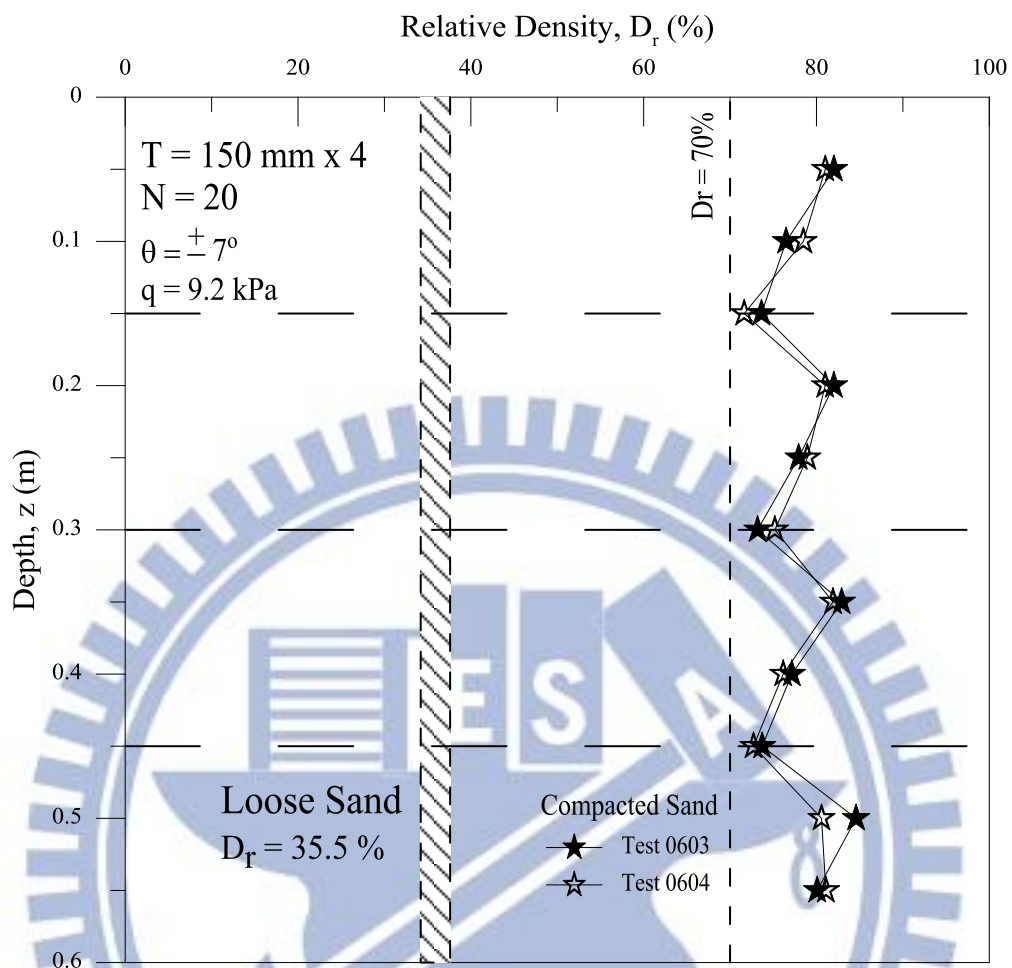


Fig. 6.20. Distribution of relative density due to cyclic torsional shearing at $\theta = \pm 7^\circ$

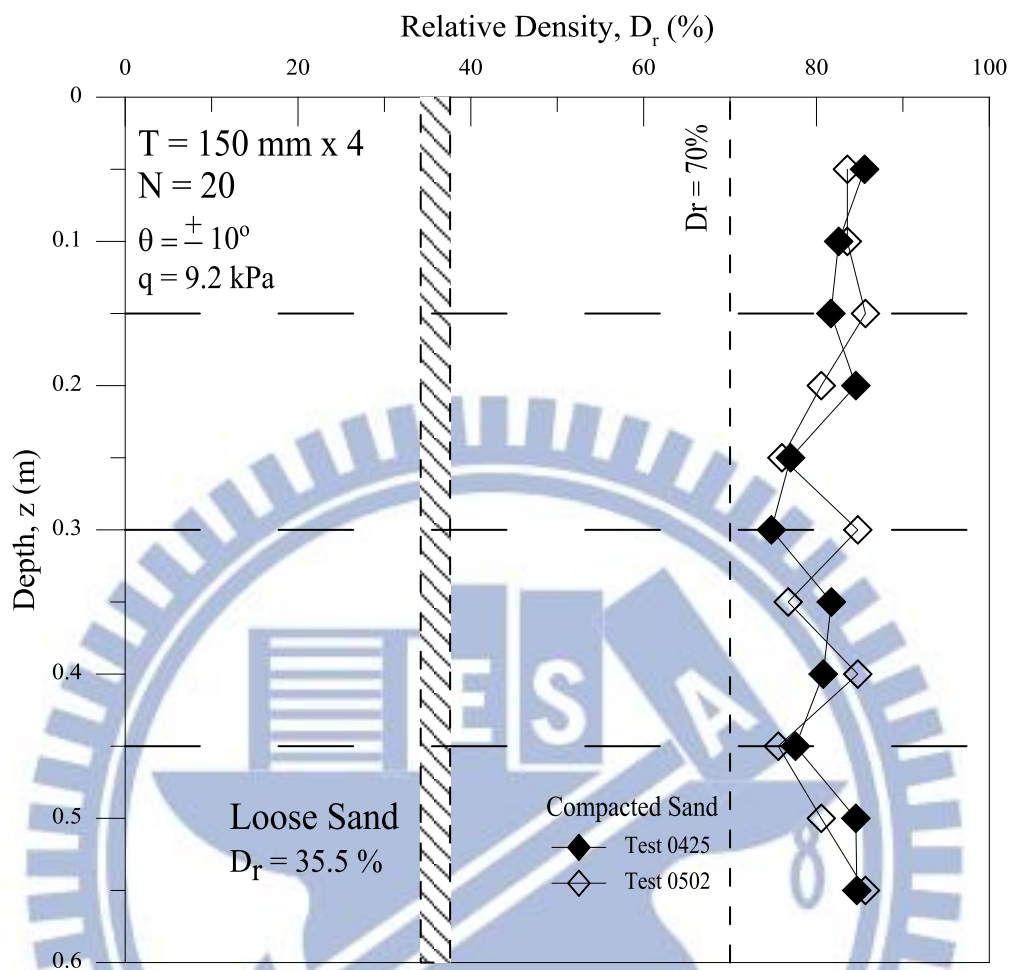


Fig. 6.21. Distribution of relative density due to cyclic torsional shearing at $\theta = \pm 10^\circ$

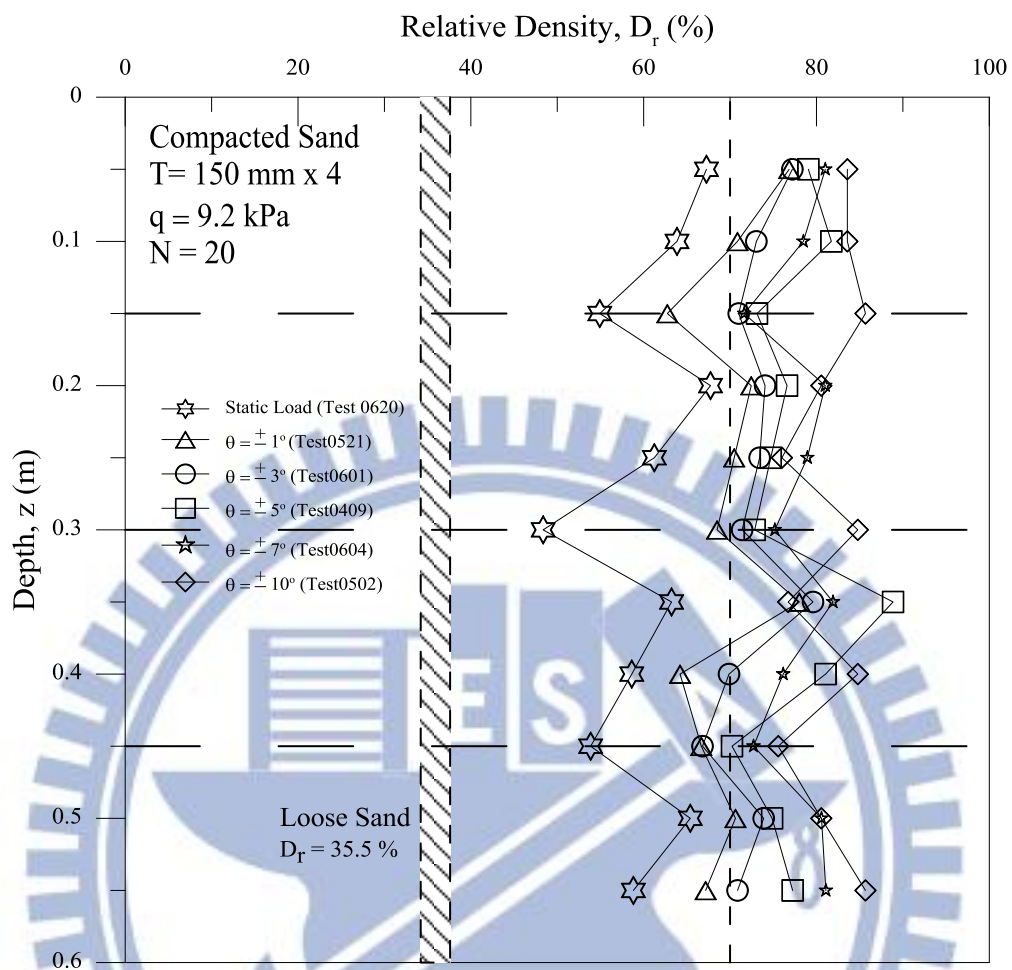


Fig. 6.22. Distribution of relative density after cyclic torsional shearing

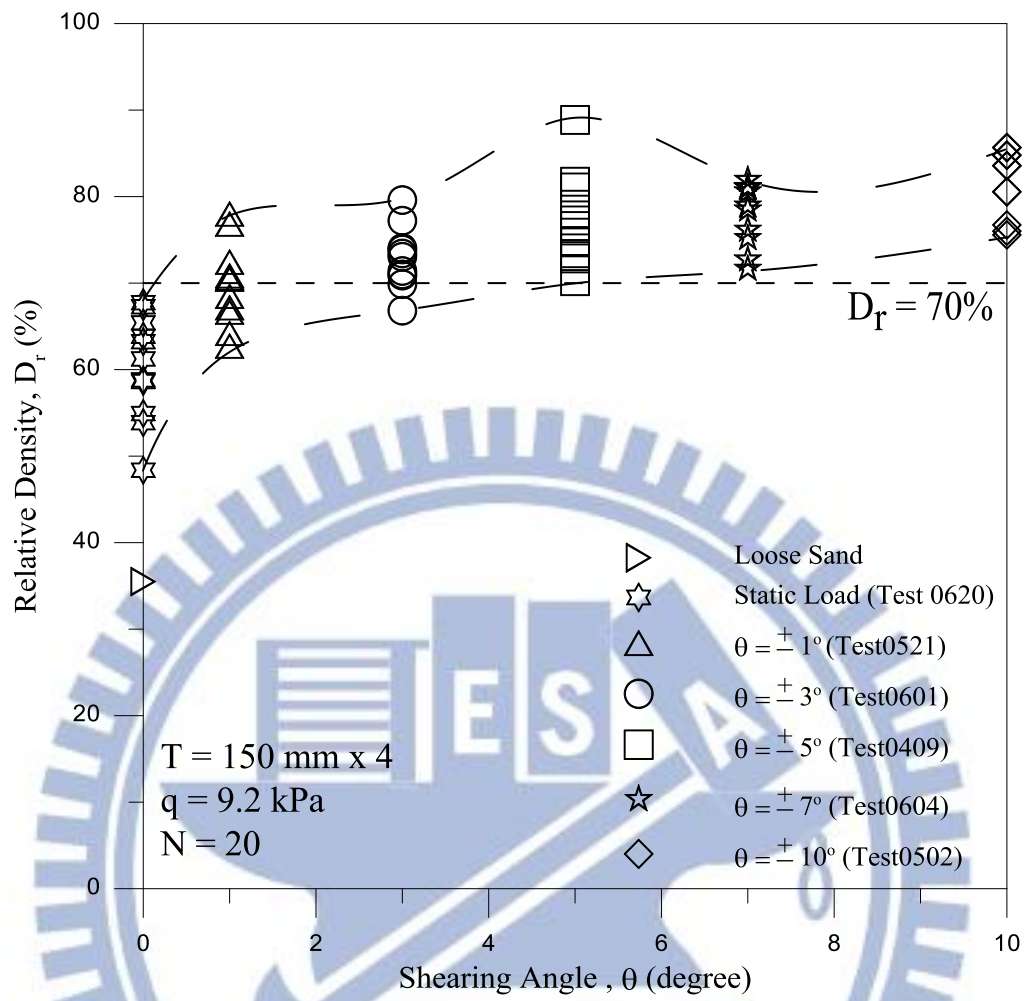


Fig. 6.23. Relative density with shearing angle

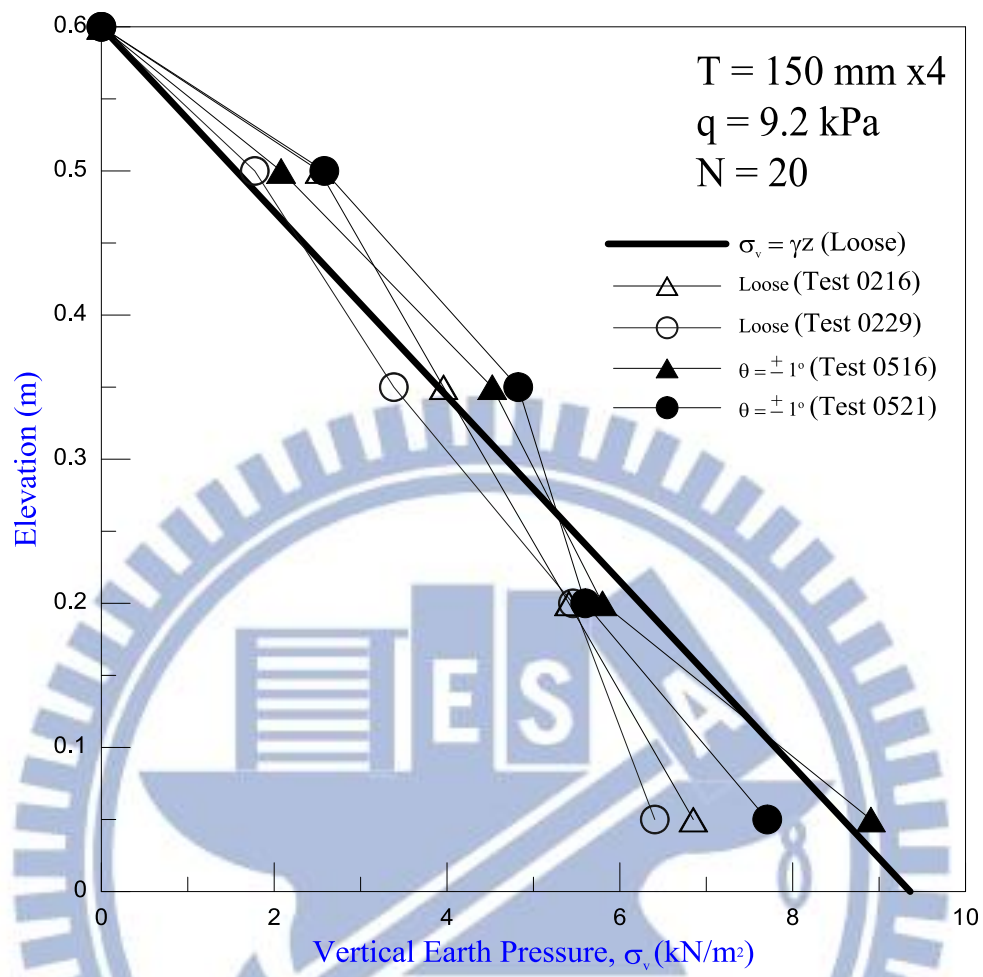


Fig. 6.24. Distribution of vertical earth pressure after cyclic torsional shear at $\theta = \pm 1^\circ$

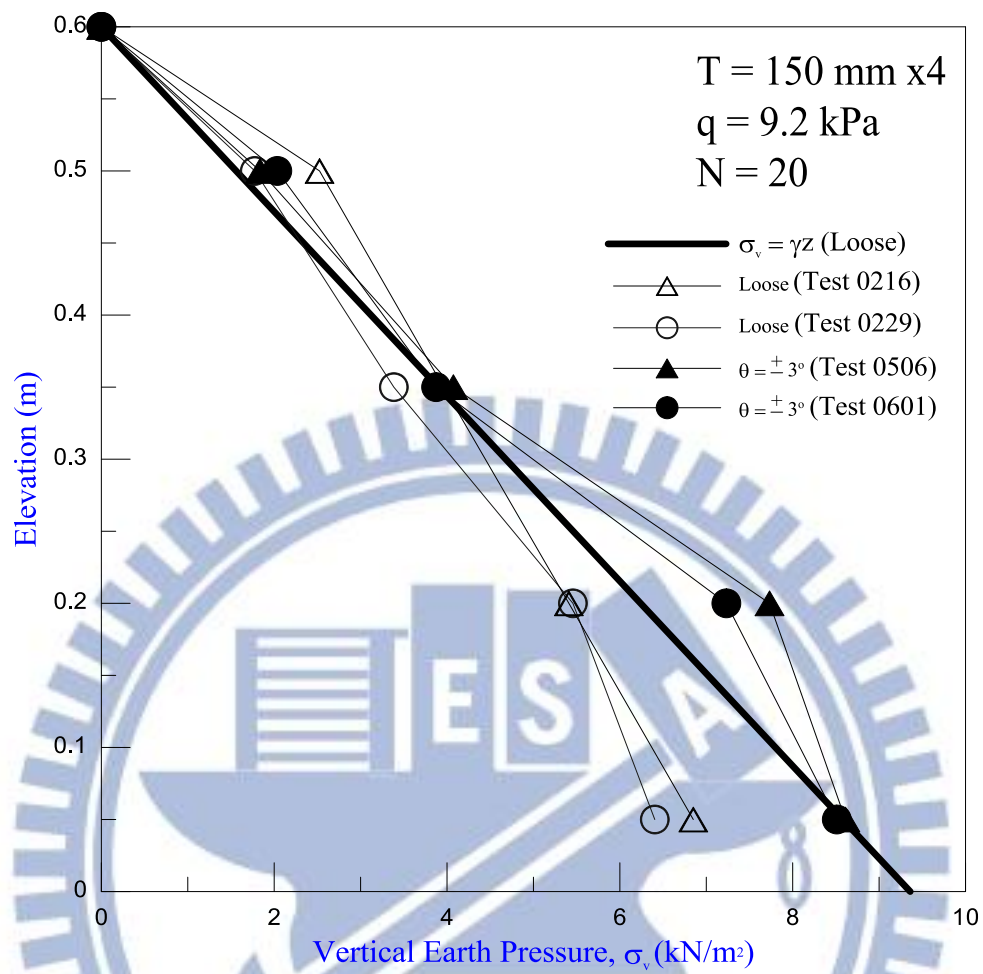


Fig. 6.25. Distribution of vertical earth pressure after cyclic torsional shear at $\theta = \pm 3^\circ$

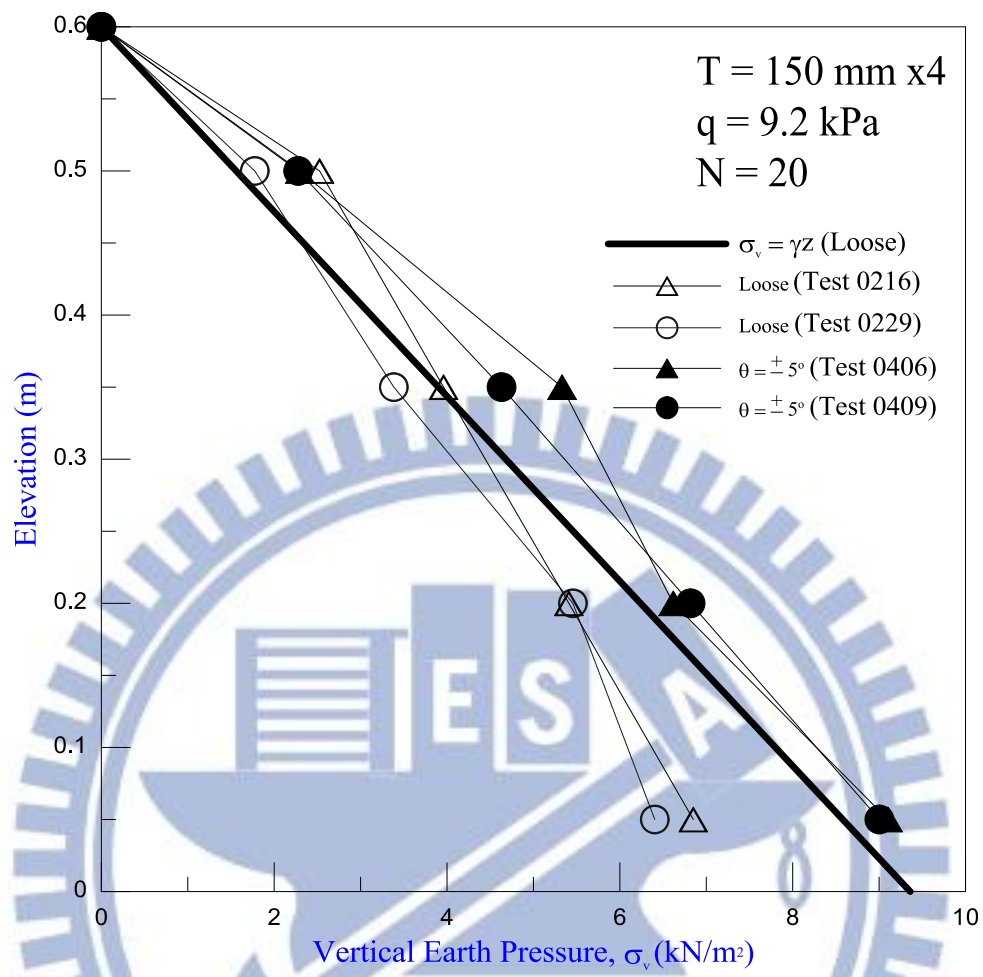


Fig. 6.26. Distribution of vertical earth pressure after cyclic torsional shear at $\theta = \pm 5^\circ$

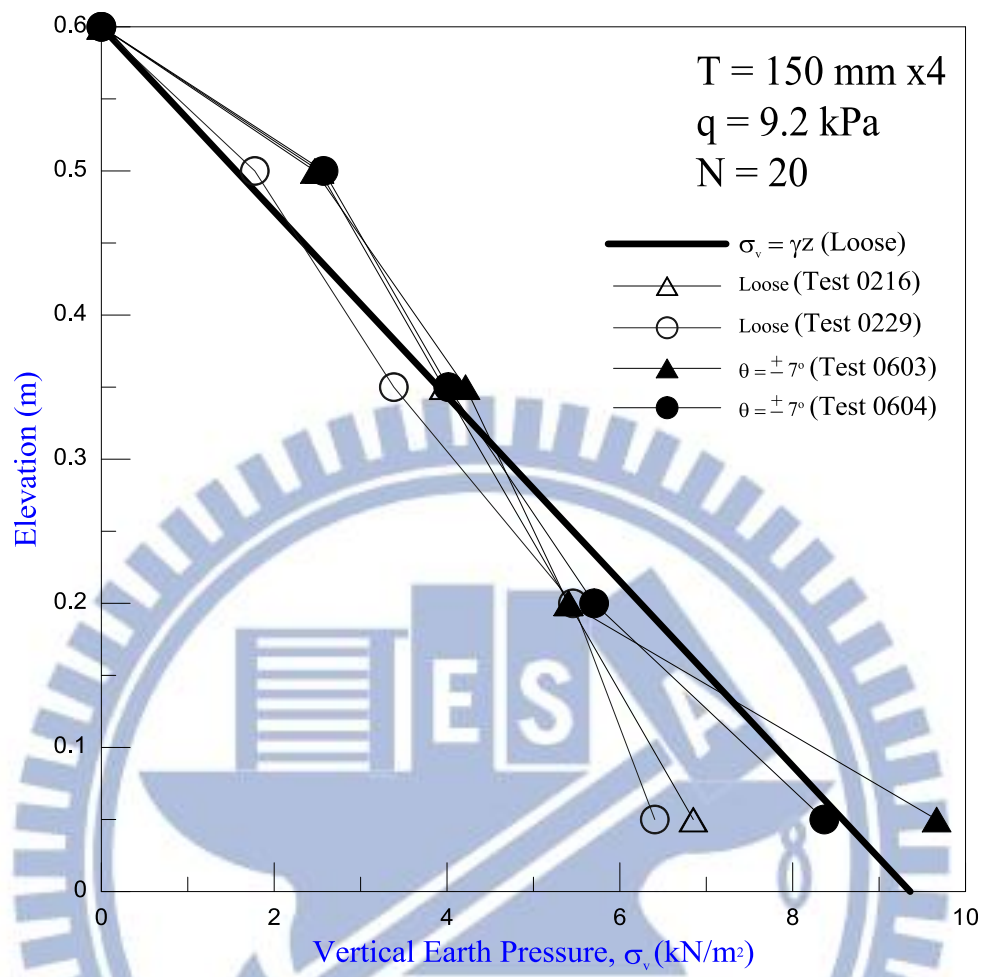


Fig. 6.27. Distribution of vertical earth pressure after cyclic torsional shear at $\theta = \pm 7^\circ$

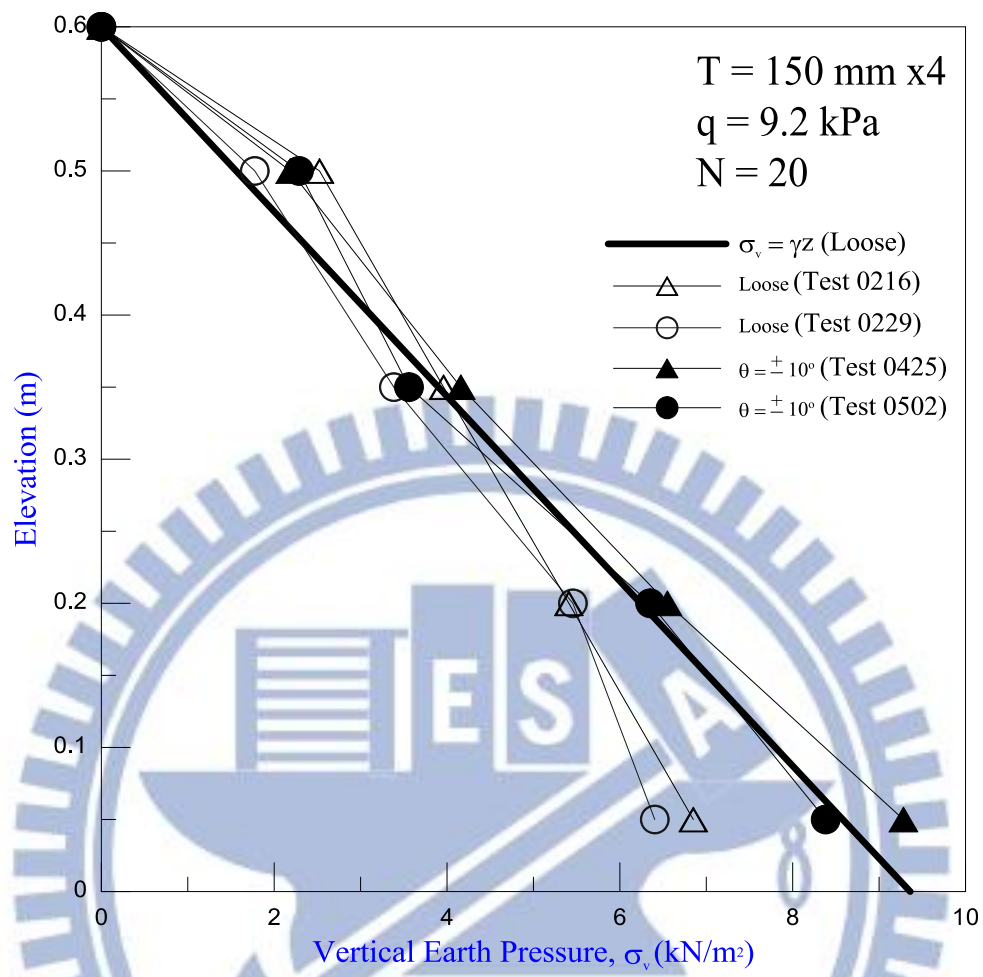


Fig. 6.28. Distribution of vertical earth pressure after cyclic torsional shear at $\theta = \pm 10^\circ$

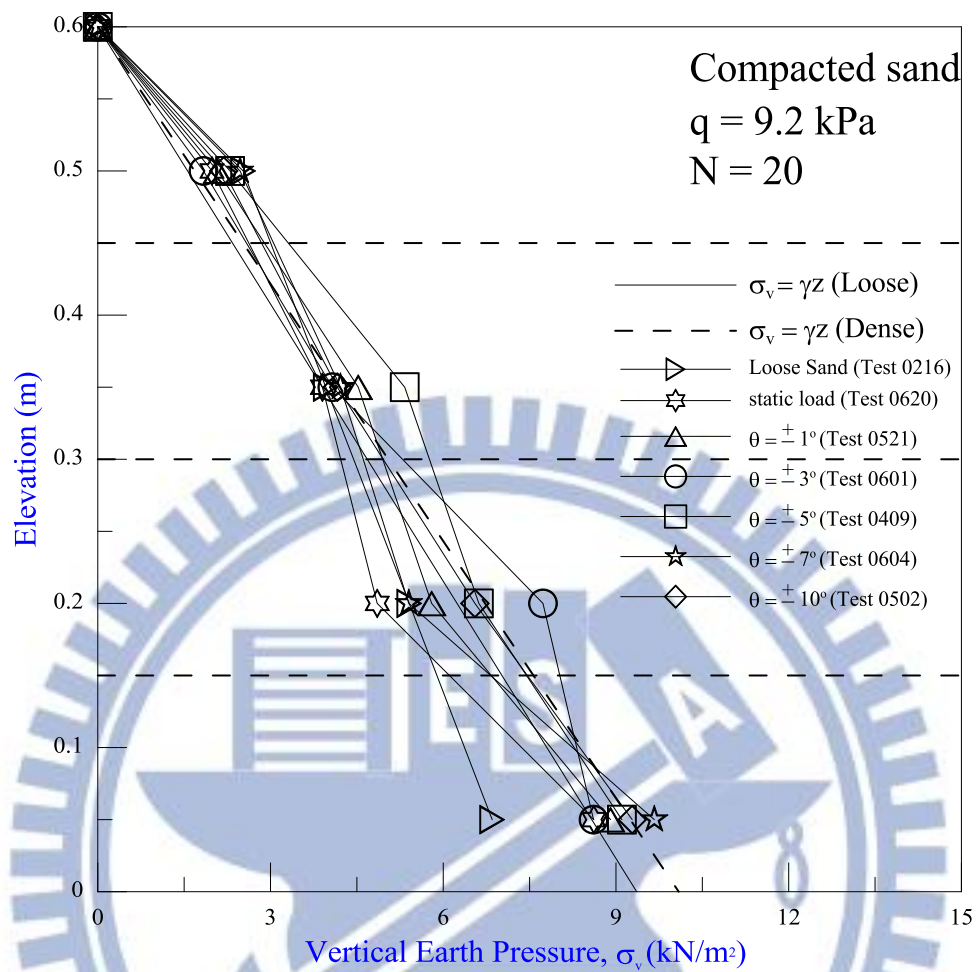


Fig. 6.29. Distribution of vertical stress after static loading and cyclic torsional shearing

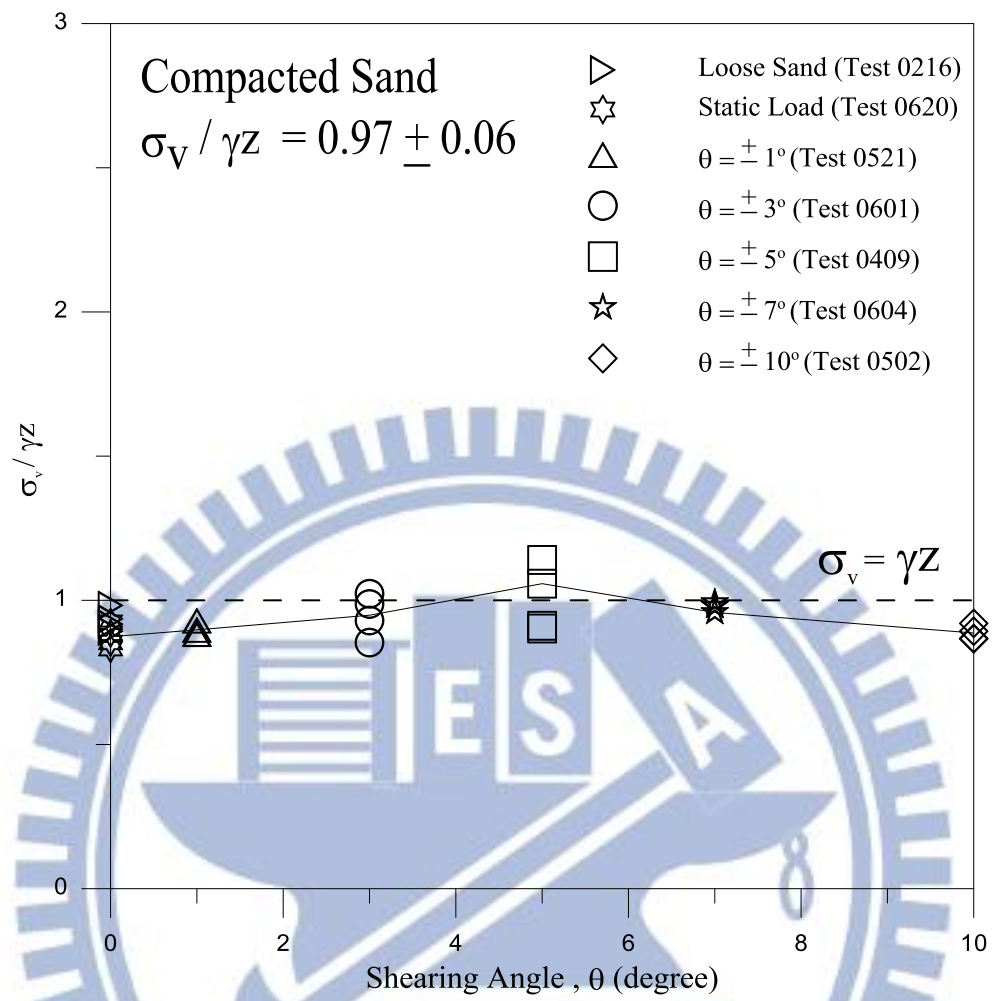


Fig. 6.30. Normalized vertical stress after cyclic torsional shearing

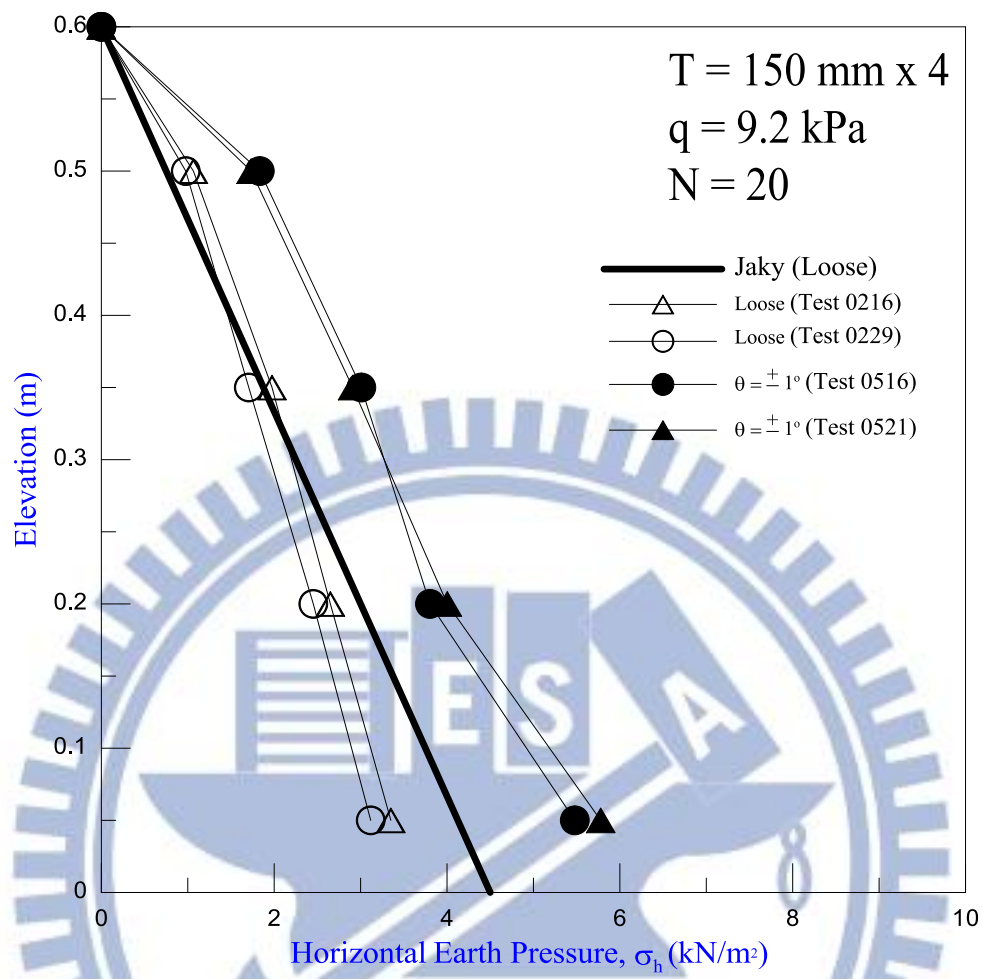


Fig. 6.31. Distribution of horizontal earth pressure after cyclic torsional shear at $\theta = \pm 1^\circ$

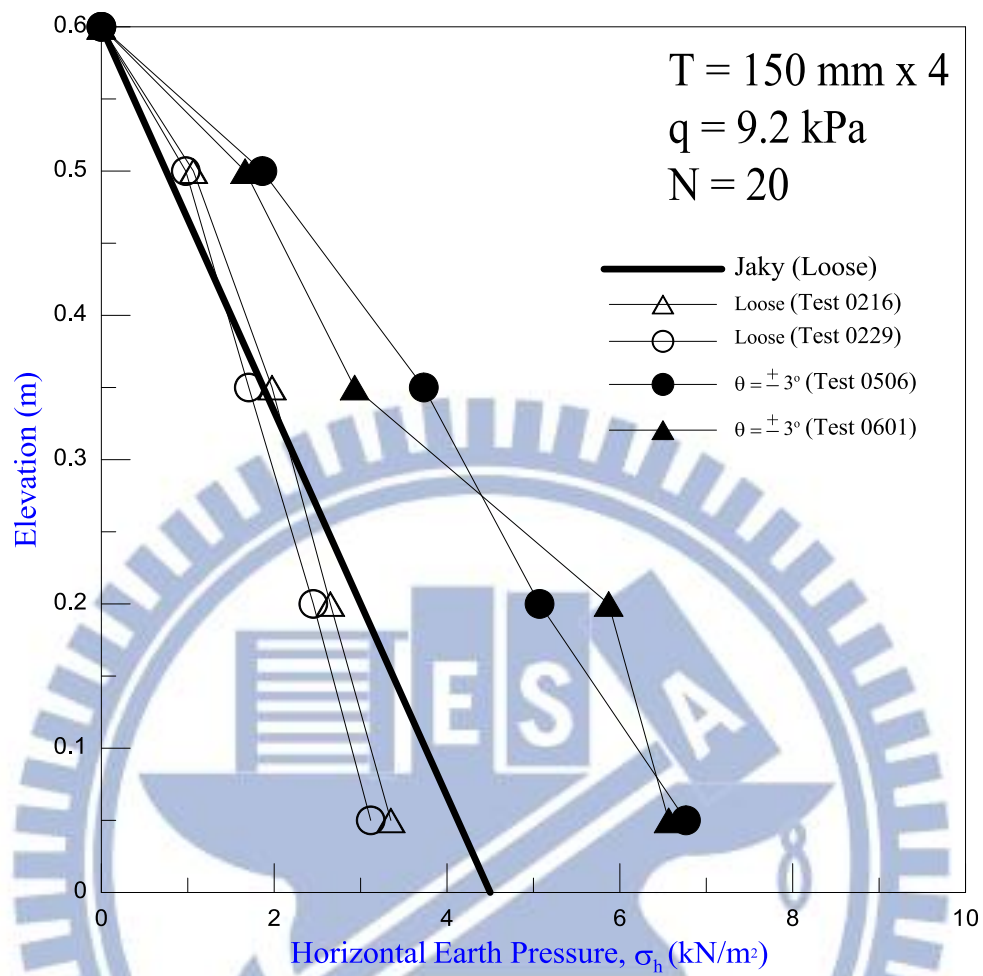


Fig. 6.32. Distribution of horizontal earth pressure after cyclic torsional shear at $\theta = \pm 3^\circ$

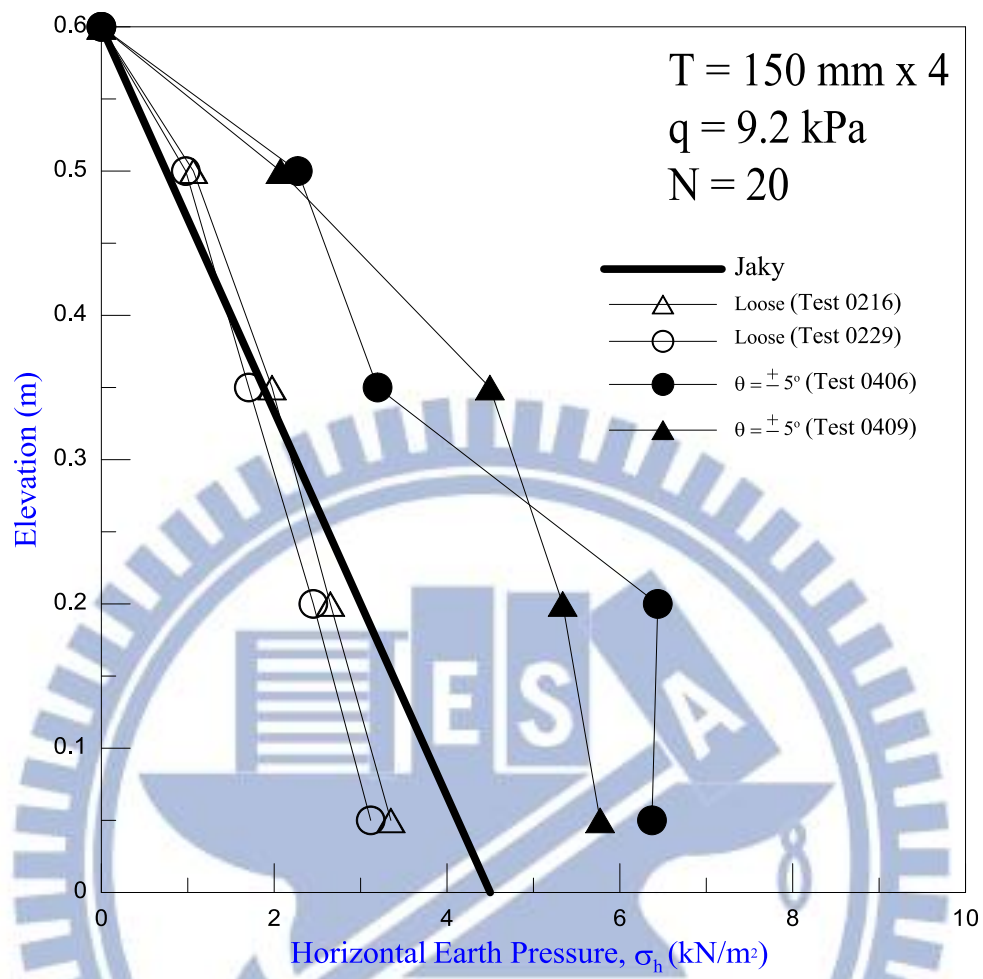


Fig. 6.33. Distribution of horizontal earth pressure after cyclic torsional shear at $\theta = \pm 5^\circ$

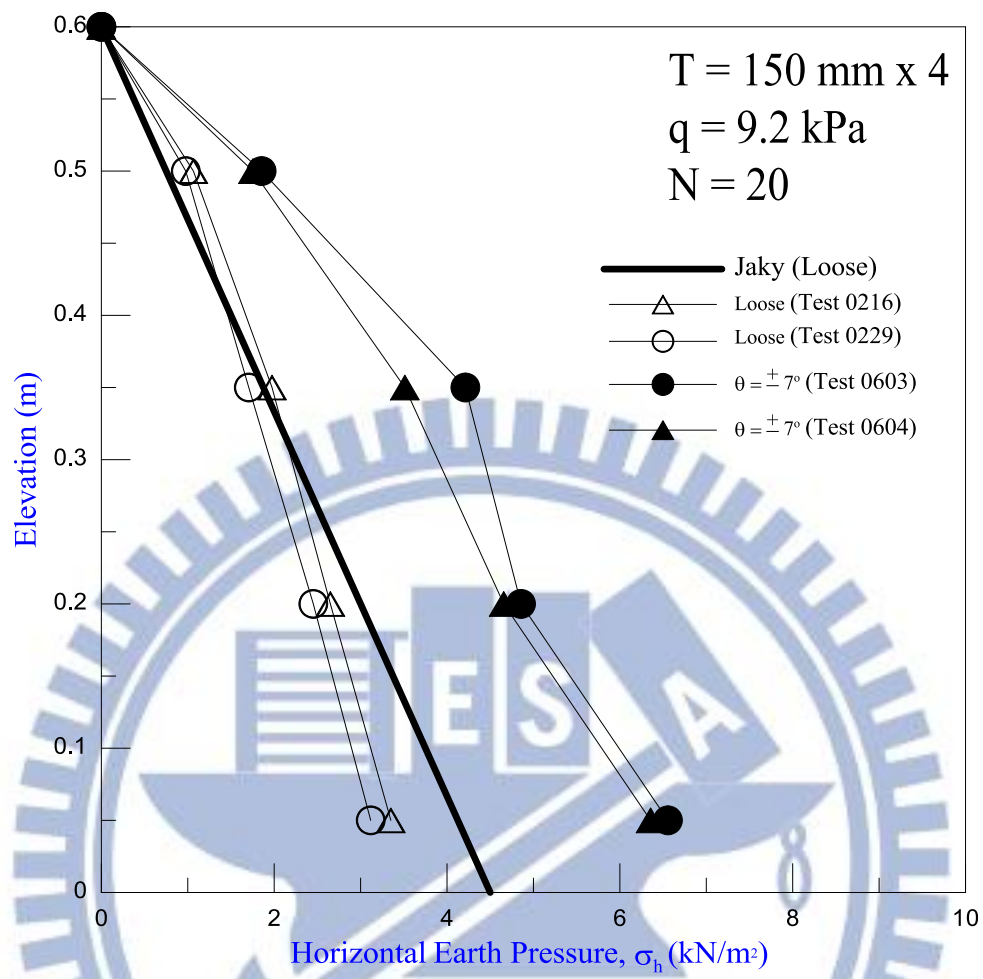


Fig. 6.34. Distribution of horizontal earth pressure after cyclic torsional shear at $\theta = \pm 7^\circ$

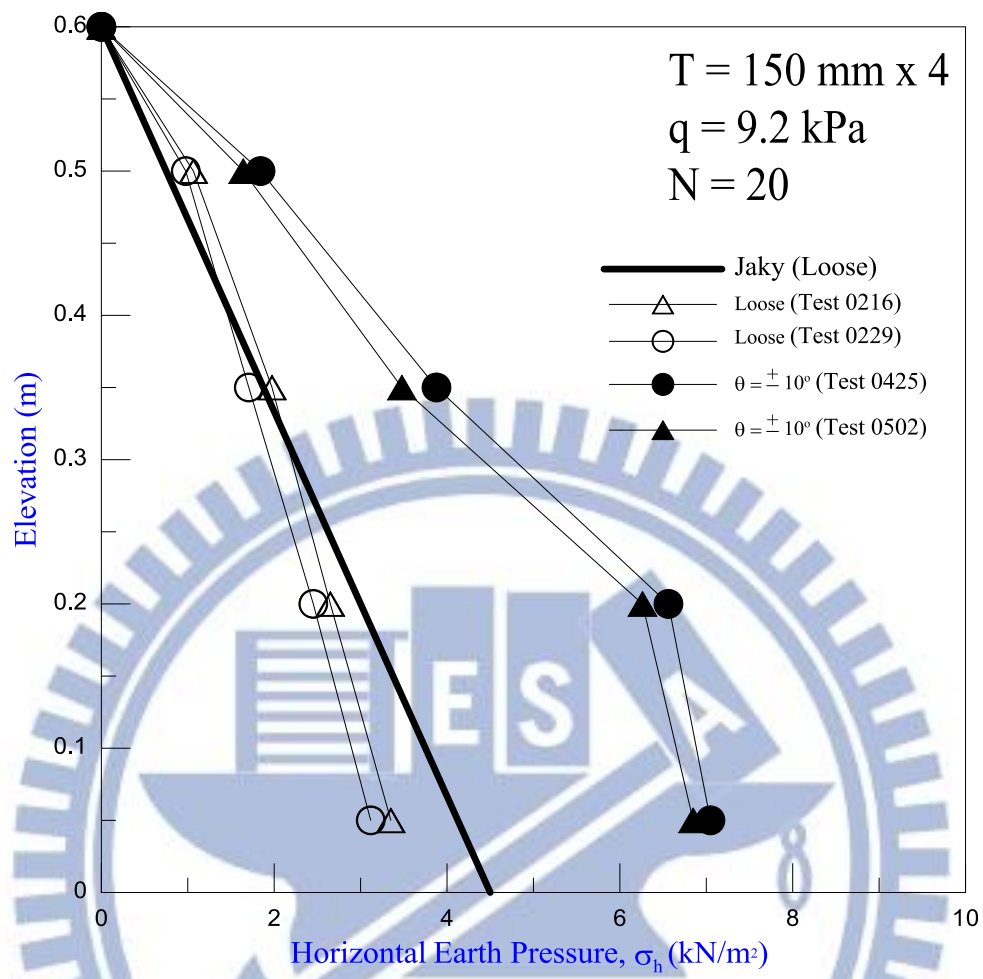


Fig. 6.35. Distribution of horizontal earth pressure after cyclic torsional shear at $\theta = \pm 10^\circ$

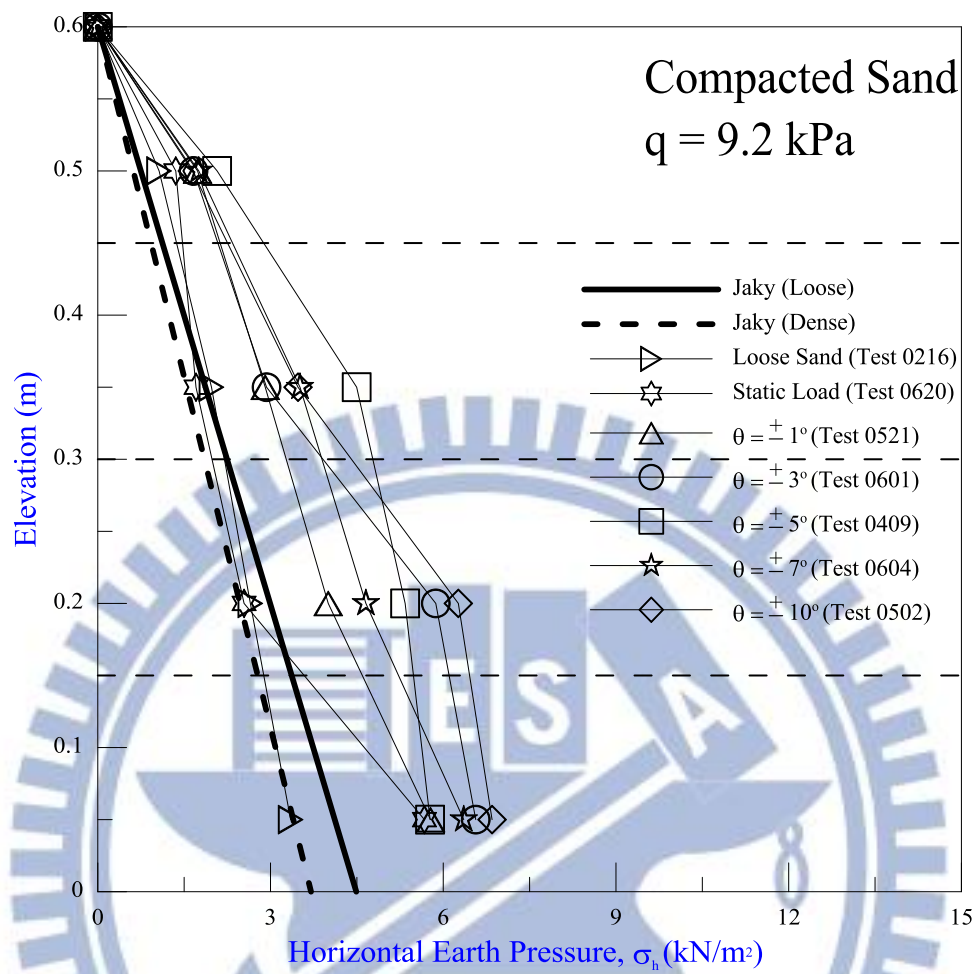


Fig. 6.36. Distribution of horizontal stress after static loading and cyclic torsional shearing

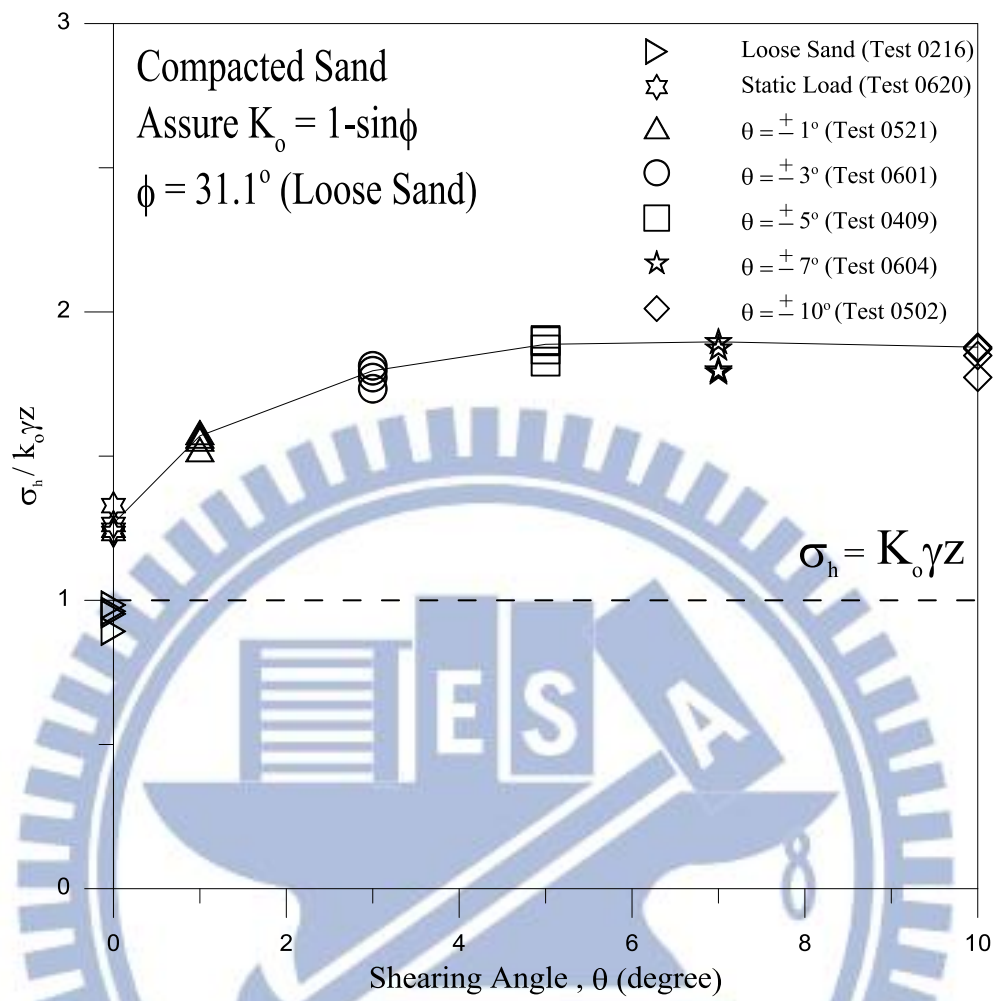


Fig. 6.37. Normalized horizontal stress after cyclic torsional shearing

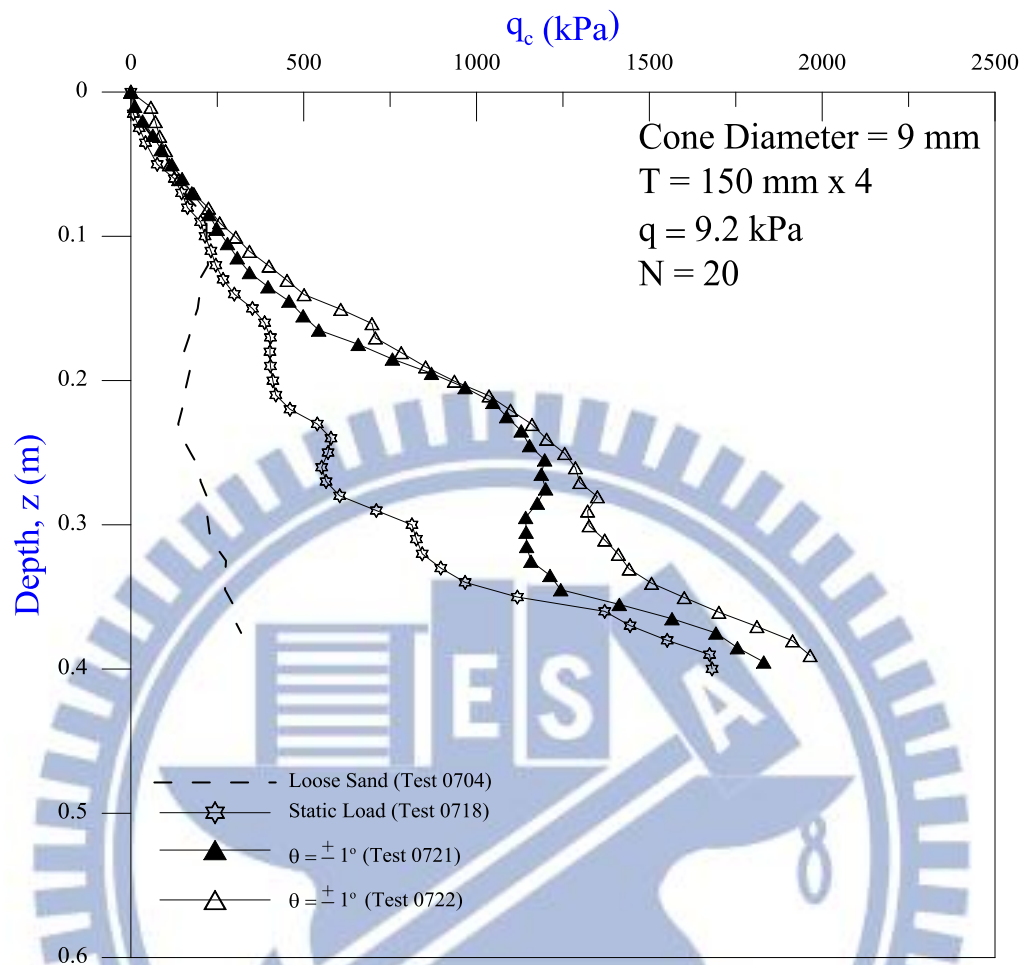


Fig. 6.38. Distribution of cone resistance after cyclic torsional shear at $\theta = \pm 1^\circ$

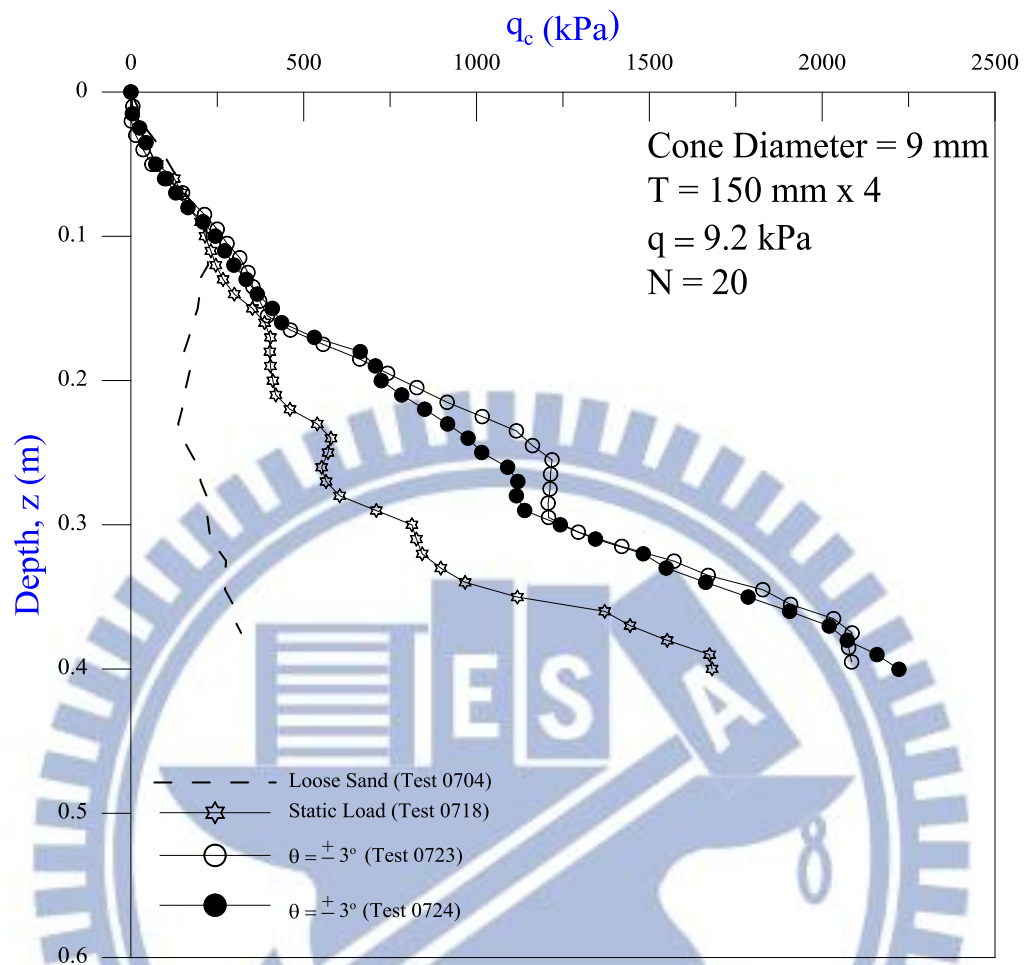


Fig. 6.39. Distribution of cone resistance after cyclic torsional shear at $\theta = \pm 3^\circ$

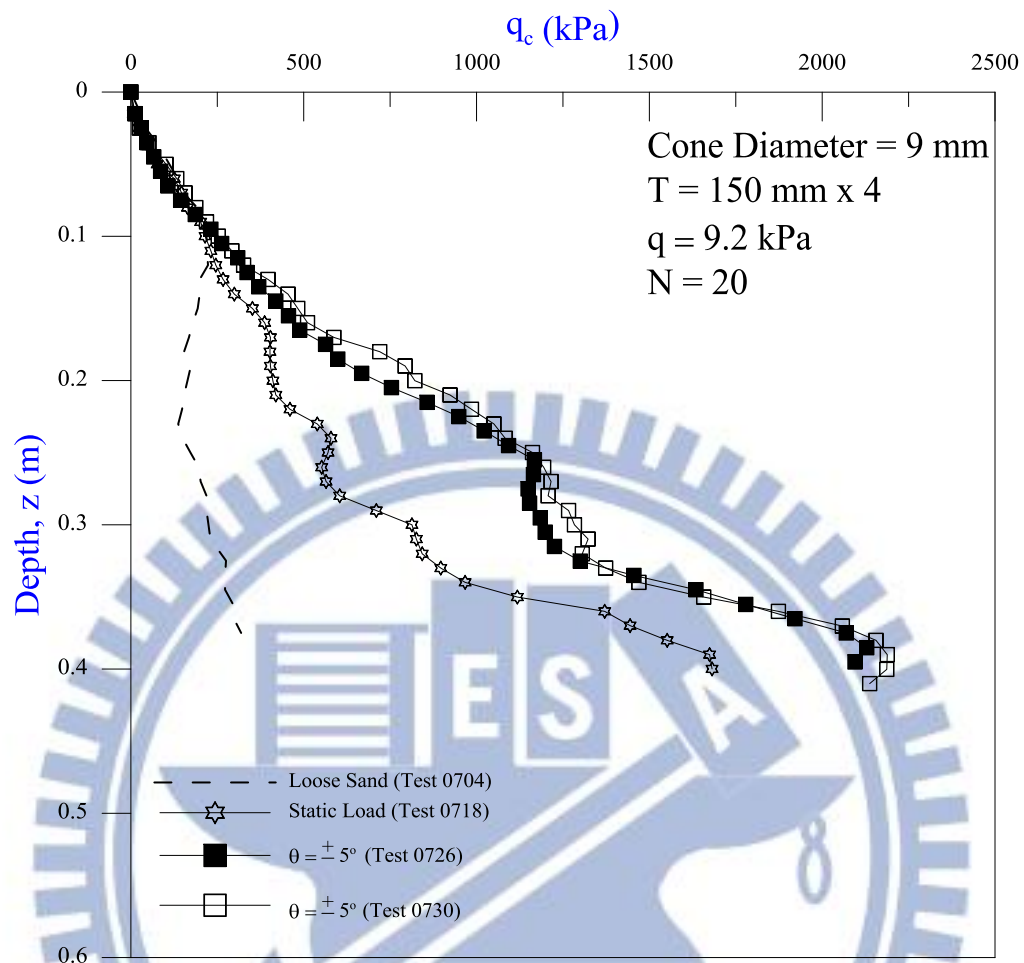


Fig. 6.40. Distribution of cone resistance after cyclic torsional shear at $\theta = \pm 5^\circ$

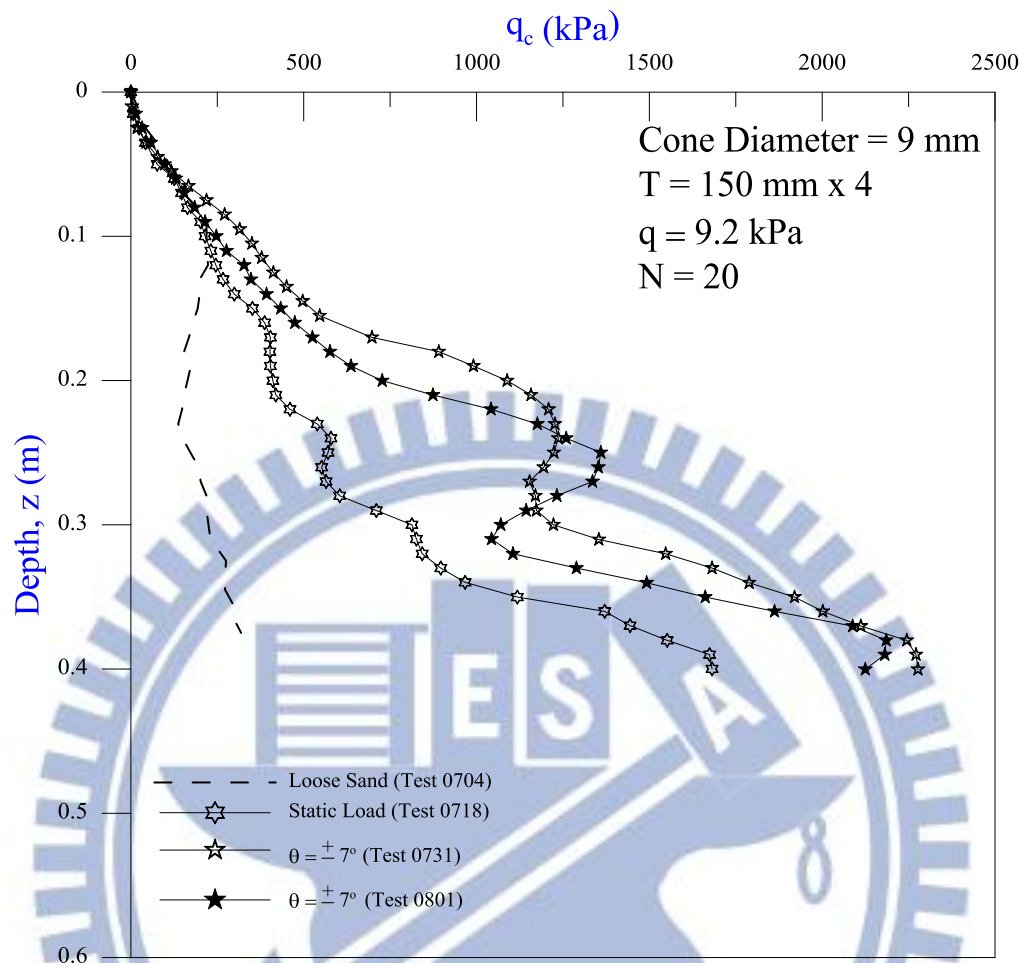


Fig. 6.41. Distribution of cone resistance after cyclic torsional shear at $\theta = \pm 7^\circ$

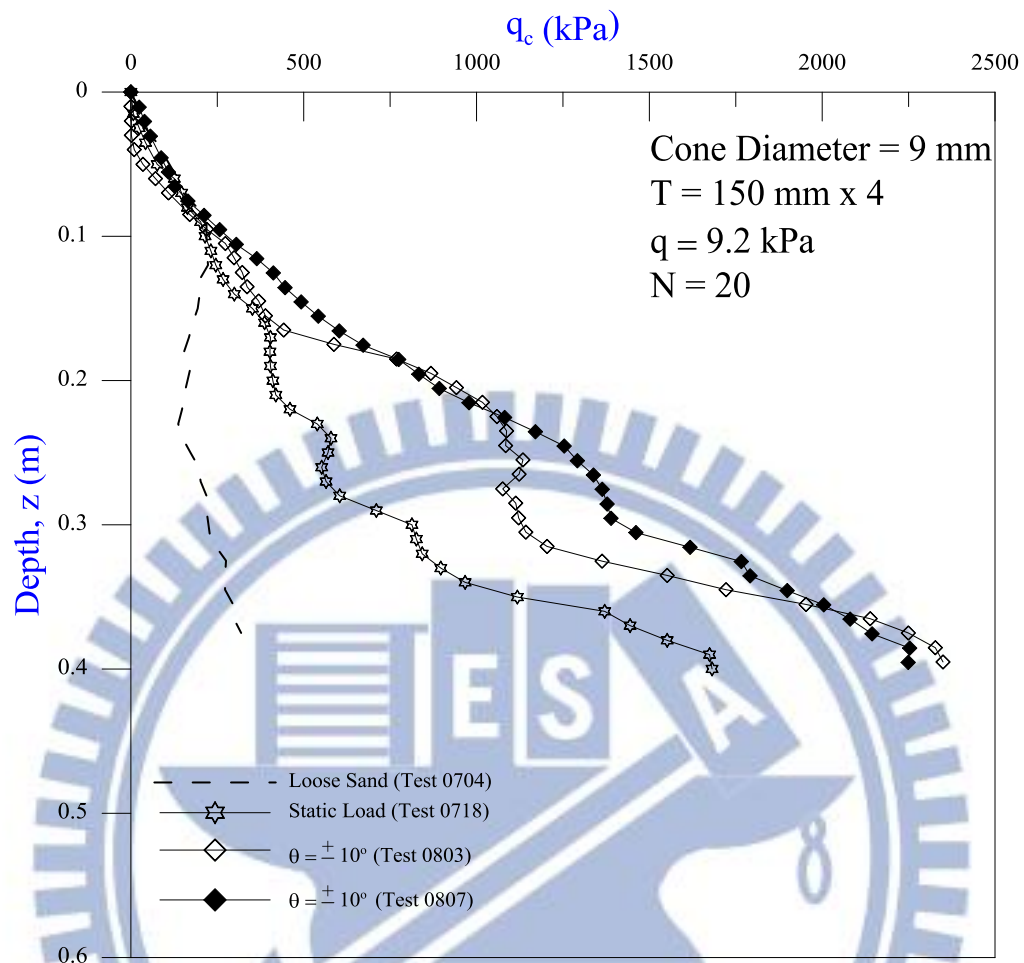


Fig. 6.42. Distribution of cone resistance after cyclic torsional shear at $\theta = \pm 10^\circ$

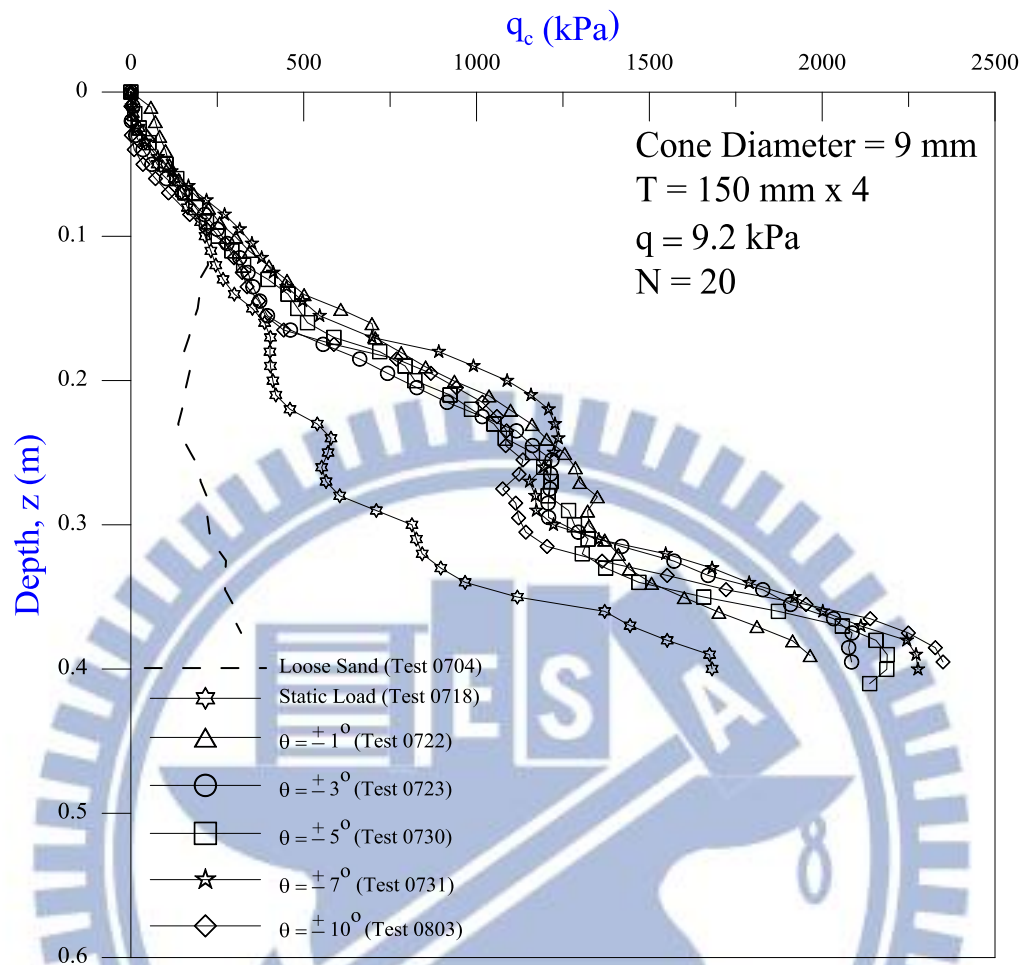


Fig. 6.43. Distribution of cone resistance after cyclic torsional shearing

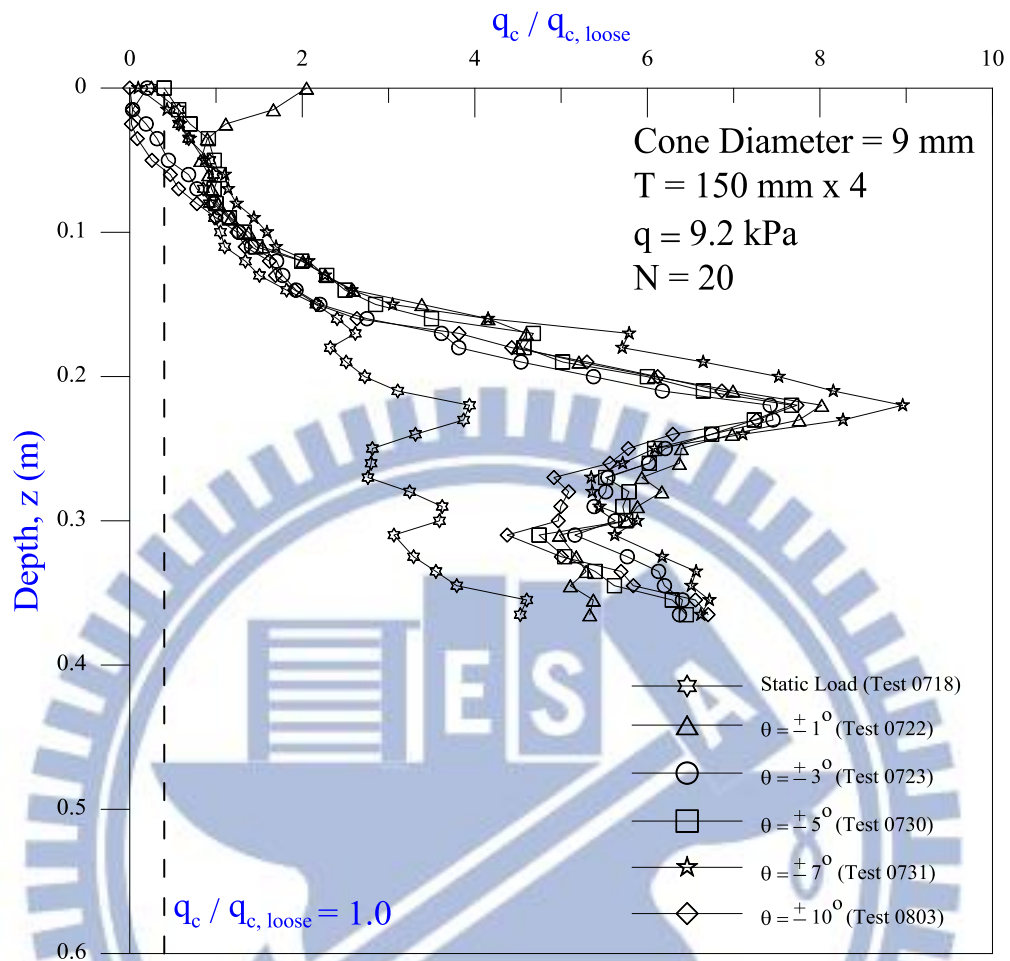


Fig. 6.44. Distribution of $q_c / q_{c, \text{loose}}$ after cyclic torsional shearing

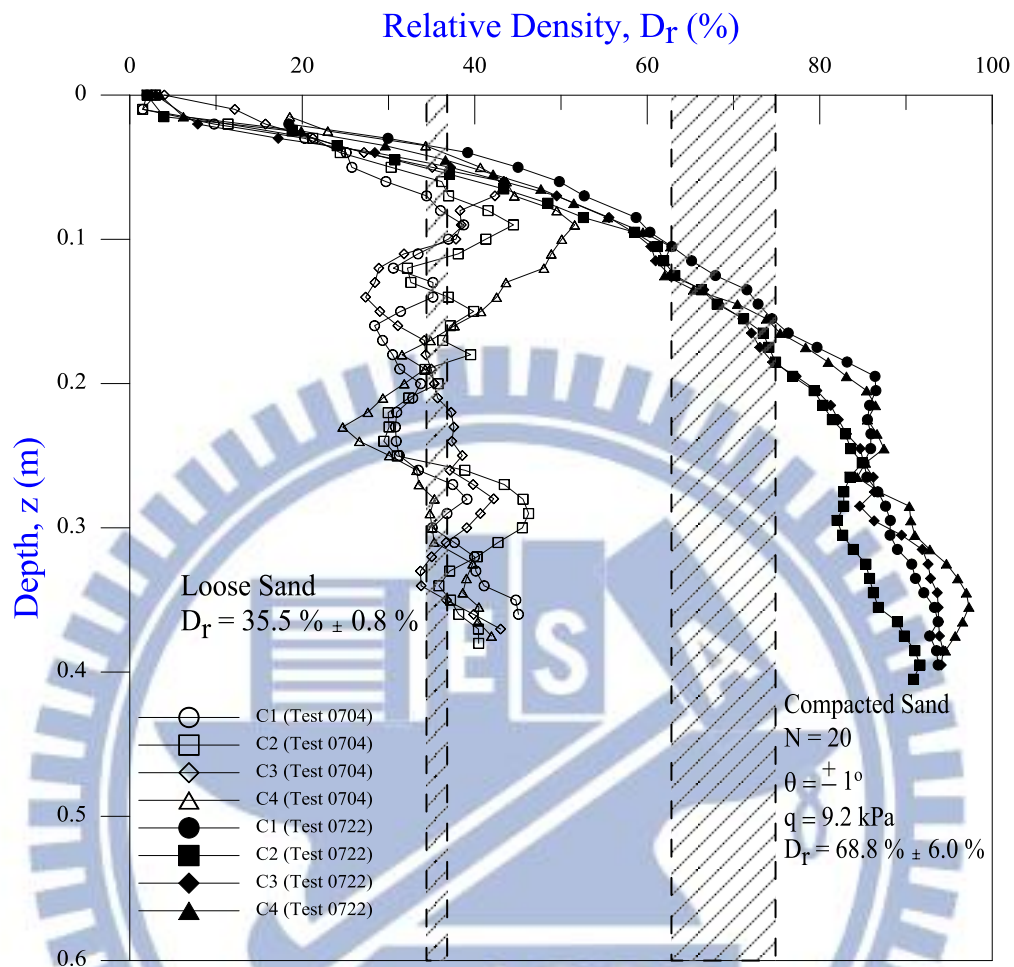


Fig. 6.45. Distribution of relative density after cyclic torsional shear at $\theta = \pm 1^\circ$

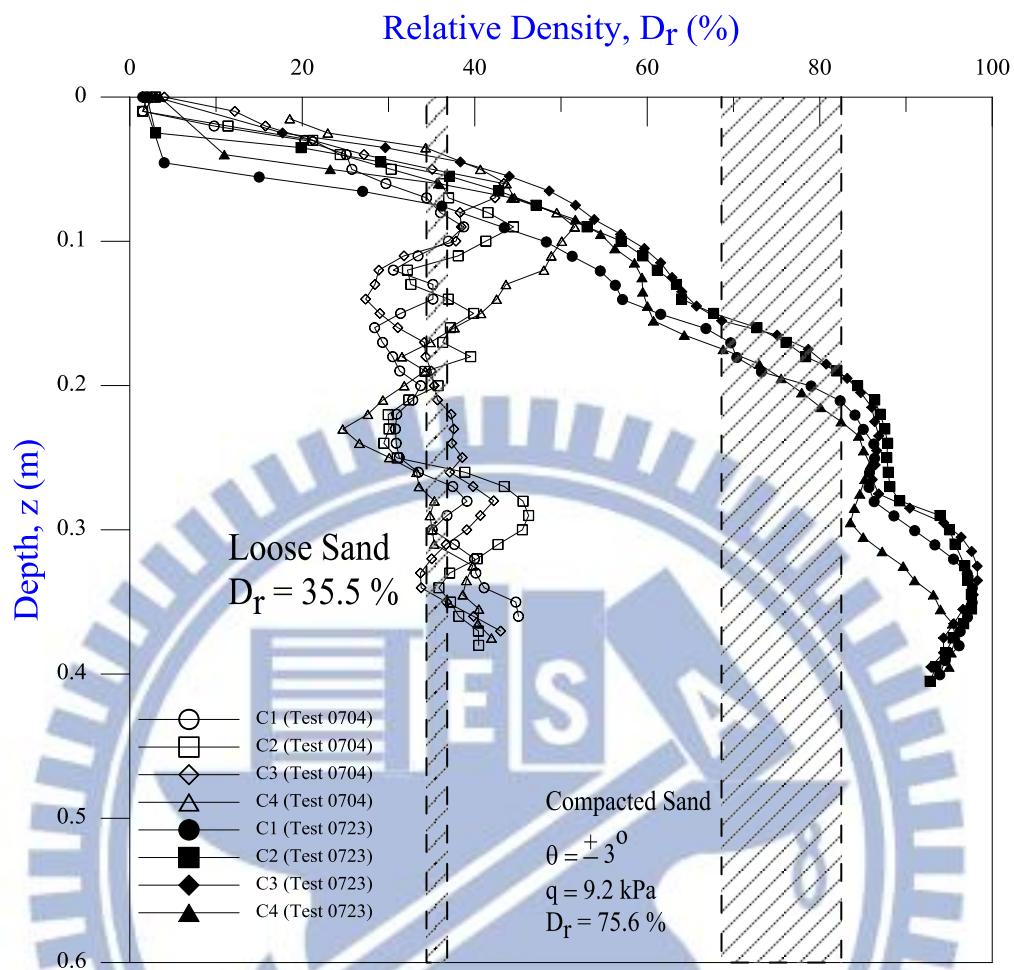


Fig. 6.46. Distribution of relative density after cyclic torsional shear at $\theta = \pm 3^\circ$

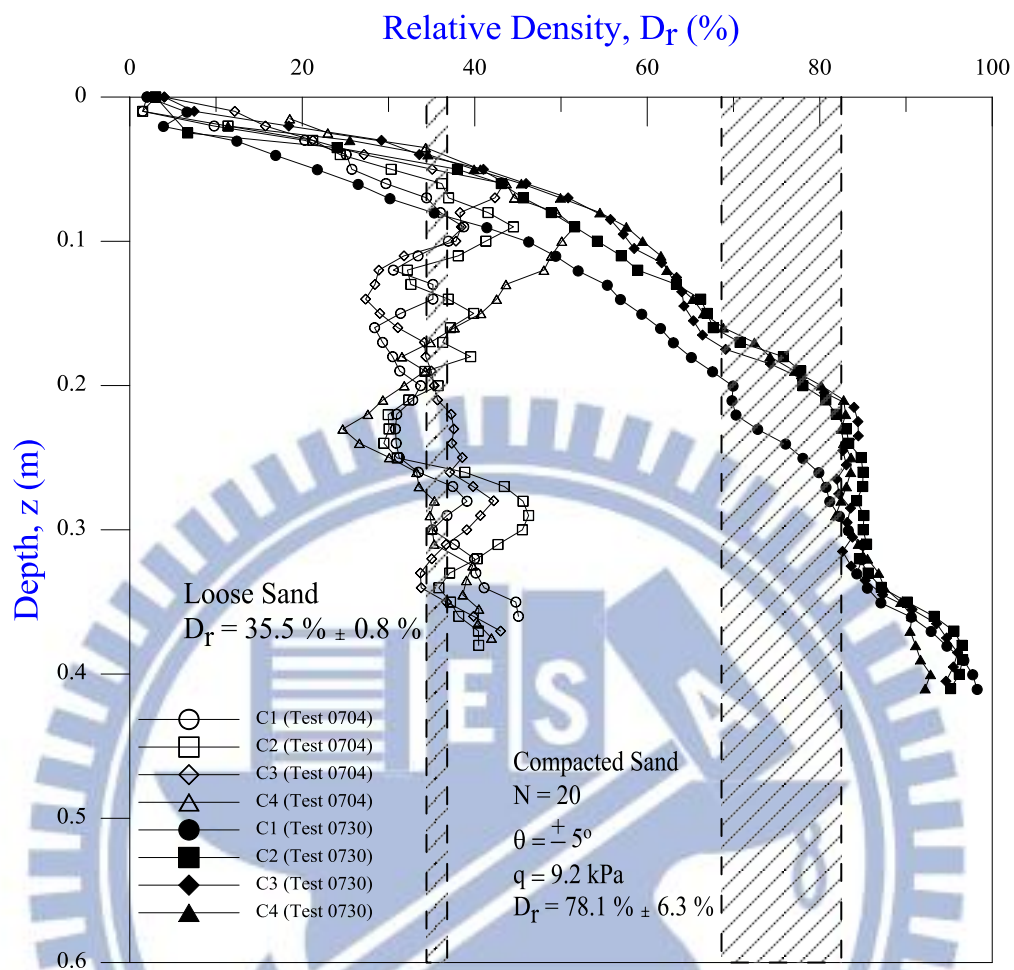


Fig. 6.47. Distribution of relative density after cyclic torsional shear at $\theta = \pm 5^\circ$

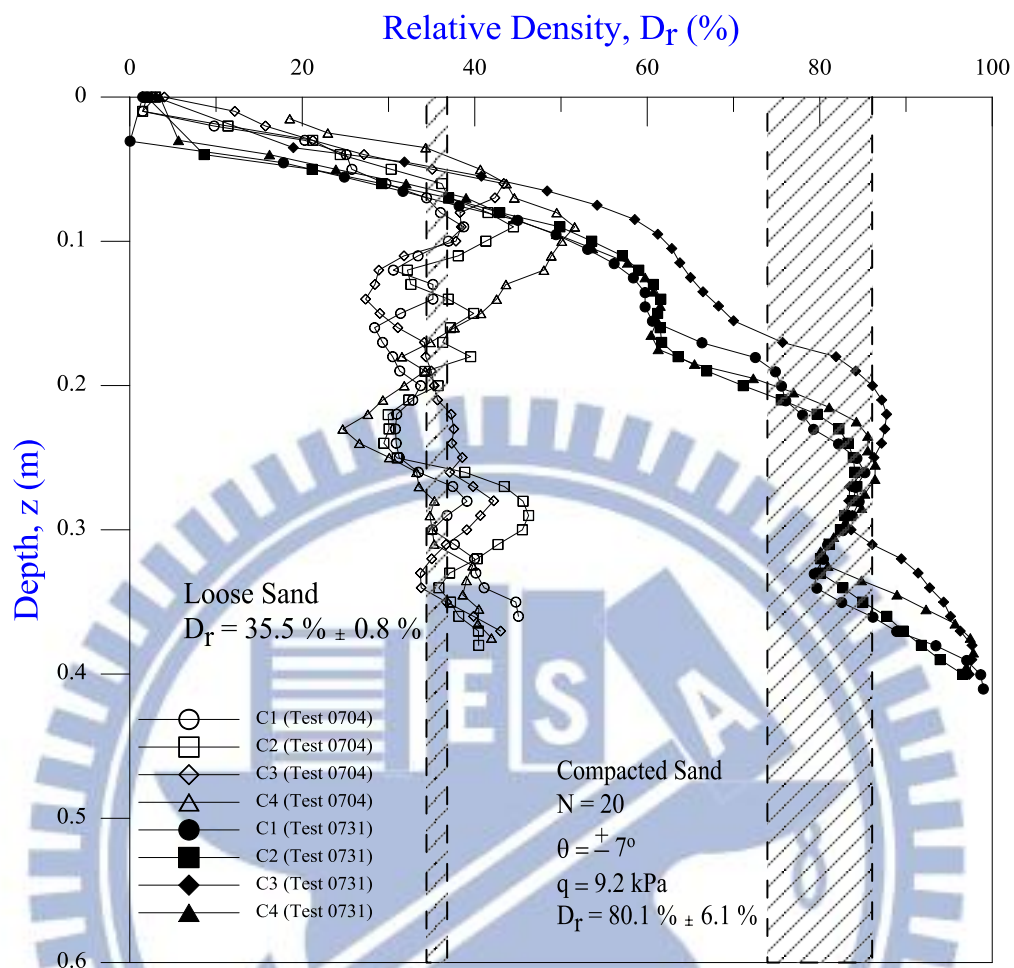


Fig. 6.48. Distribution of relative density after cyclic torsional shear at $\theta = \pm 7^\circ$

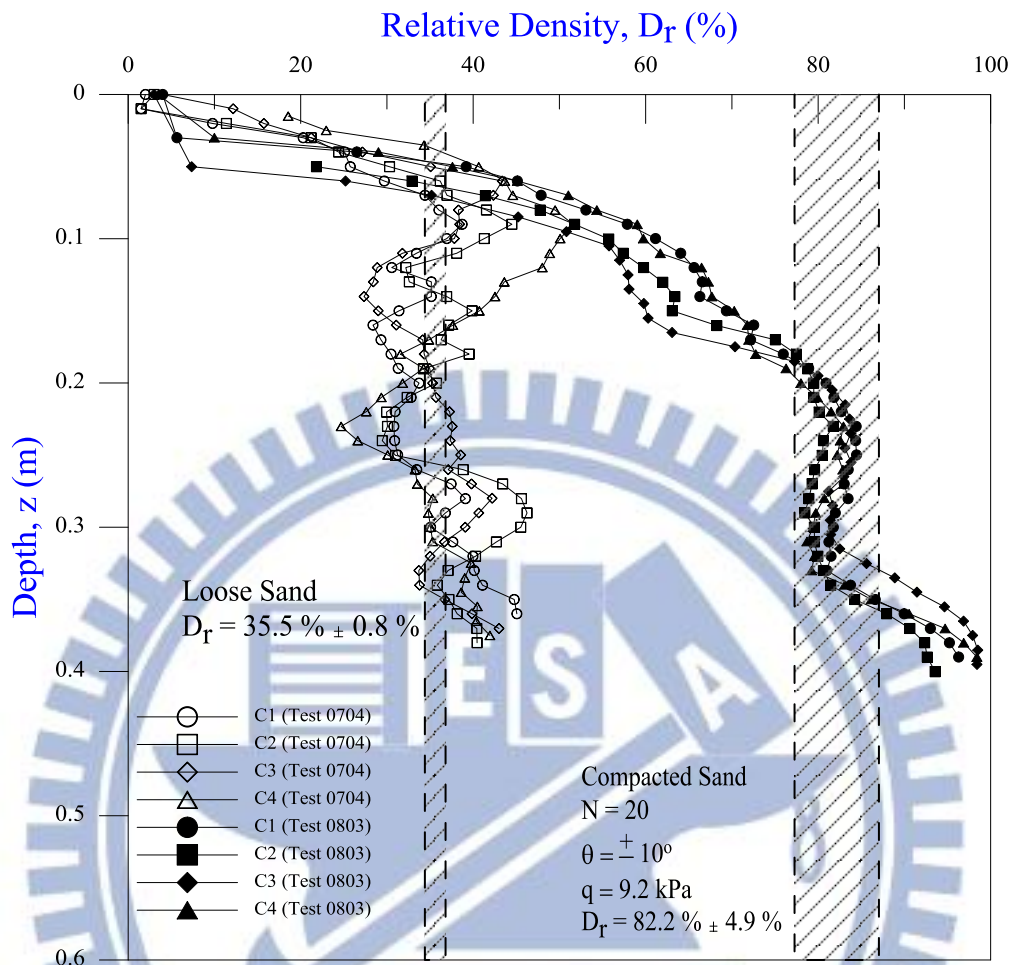


Fig. 6.49. Distribution of relative density after cyclic torsional shearing at $\theta = \pm 10^\circ$

Appendix A

CALIBRATION OF SOIL PRESSURE TRANSDUCERS

To investigate the vertical and horizontal earth pressure in the backfill, five types of strain-gage type soil pressure transducers (SPT) were used. The transducers BE-2KRS17, BE-5KRS17, PGM-02KG and PGM-05KG manufactured by KYOWA were mounted on the model wall to measure the horizontal earth pressure against the retaining wall. The effective diameter of diaphragm of transducers, BE-2KRS17 and BE-5KRS17 is 30 mm, and 12 mm for both types PGM-02KG and PGM-05KG. The soil pressure transducer type BE-2KCM17 has an effective diameter of 22 mm and was embedded in the backfill to monitor the earth pressure variation in the soil mass. Since the pressure acts between soil particles and the transducer is quite different from the pressure that acts between liquid and transducer, it is necessary to calibrate the transducer in an environment similar to that for the actual testing condition. Two systems were designed for the calibration of the on-wall and in soil transducers. These systems consist of the calibration device, air-pressure control system, signal conditioner, and data acquisition system, as indicated in Fig. A1 and Fig. A2. The typical photograph of the system is shown in Fig. A3.

Dunnicliff (1988) described that, if measurement accuracy must be maximized, each cell should be calibrated in a large calibration chamber, using the soil in which it will be embedded. The chamber should be at least 3 times, and preferably 5 times the diameter of the cell. Following Dunnicliff's recommendation, the calibration devices

shown in Fig.A3 is a shallow cylindrical chamber with an inner diameter of 400 mm and a height of 30 mm and is made of a solid steel plate, which is the same material as the model retaining wall.

To avoid point load effects, Weiler and Kulhawy (1982) concluded that the ratio of the active diaphragm to the mean soil grain size, d/D_{50} , needs to be greater than or equal to 10. In this study, the diameters of active diaphragm of the transducers, BE-2(5)KRS17, PGM-02(5)KG and BE-2KCM17 are 30, 12 and 22 mm, respectively. The mean soil grain size of Ottawa sand is $D_{50} = 0.36$ mm. The ratio $d/D_{50} = 83, 33$ and 61 are apparently greater than the required ratio of 10. In this study, the eccentric, non-uniform and point load conditions will not occur during calibration.

As shown in Fig. A1, it is important that the surface of the sensor was installed flush with the upper face of the chamber. To calibrate the in-soil transducer, as indicated in Fig. A2, a thin layer of sand was placed into the chamber to form a sand bed then the soil pressure transducer was placed on the sand bed. On top of the transducer, a 10 mm-thick sand layer was placed in the calibration device. Then the 0.2 mm-thick rubber membrane was placed over the sandy layer. As indicated in Fig. A1 and Fig. A2, a uniformly distributed air-pressure was applied on the membrane, carried-over through the soil particles, and transmitted to the transducer.

In Fig. A1 and Fig. A2, rubber O-rings were arranged to prevent air leakage between the chamber and the cap. It should be noted that the air pressure applied for the calibration of transducer should be consistent with the operating pressure range for model wall experiments. For this study, the transducers were calibrated for the pressure range of $0 \sim 9.81 \text{ kN/m}^2$ or $0 \sim 98.1 \text{ kN/m}^2$ depending on the type of soil pressure transducer. To reduce the effect of sidewall friction, the thickness of sand layer in the chamber should be limited, so that the side-friction between the sand the sidewall of the chamber could be minimized.

Table A1, A2 and A3 summarizes of the calibration factors of soil pressure transducers used in this study.

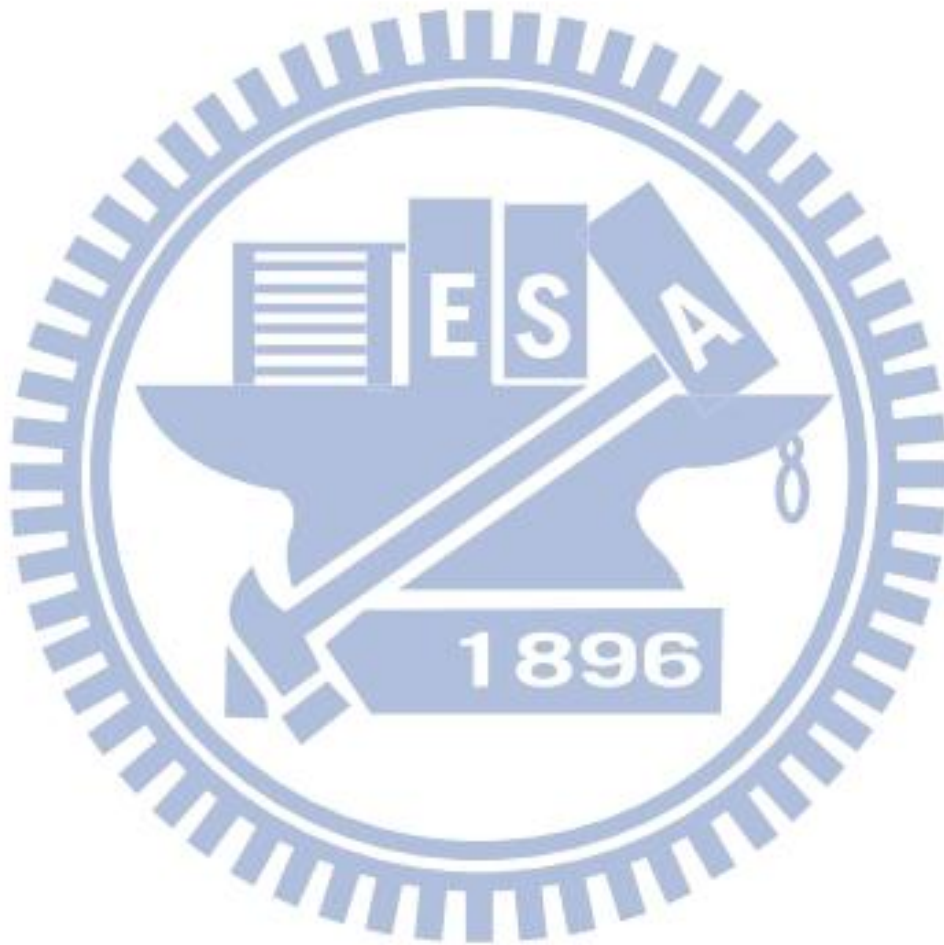


Table A.3. Soil Pressure Transducer Calibration Factors

No.	Type	Transducer No.	Dynamic Strain Amplifier	Capacity (kN/m ²)	Ave. Calibration Factor [(kN/m ²)/Volt]
			Calibration Setter (μξ)		
1	BE-2KCM17	9Z0080001	305	98.1	34.13
2	BE-2KCM17	9Z0080002	340	98.1	31.82
3	BE-2KCM17	9Z0080007	378	98.1	39.29
4	BE-2KCM17	9Z0080008	325	98.1	39.35
5	BE-2KCM17	090170001	283	98.1	38.61
6	BE-2KCM17	090170003	302	98.1	40.39
7	BE-2KCM17	090170004	288	98.1	39.13
8	BE-2KCM17	090170005	282	98.1	32.76
9	BE-2KCM17	090170006	289	98.1	34.13
10	BE-2KCM17	090170007	300	98.1	31.82
11	BE-2KCM17	090170008	269	98.1	39.29

Calibration pressure range : 0 ~ 98.1 kN/m²

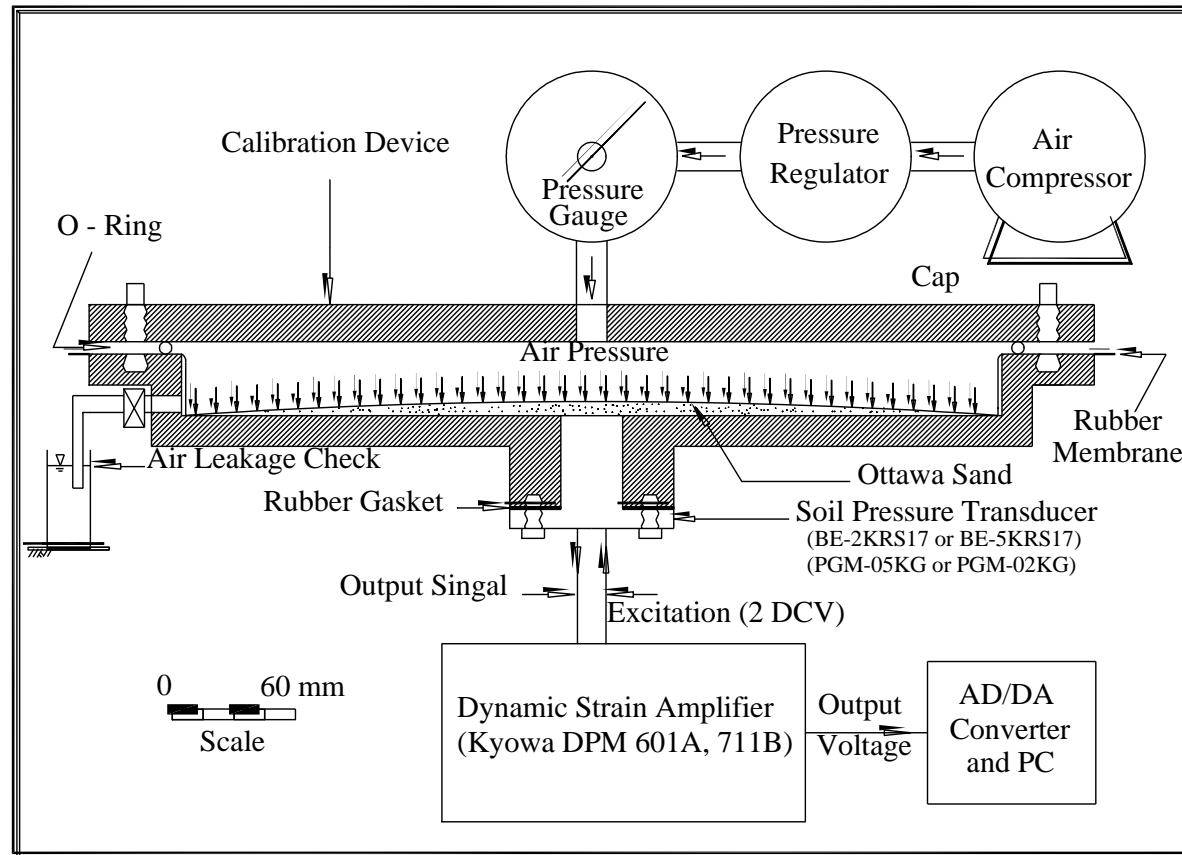


Fig. A1. Schematic diagram of on-wall soil pressure transducer calibration system

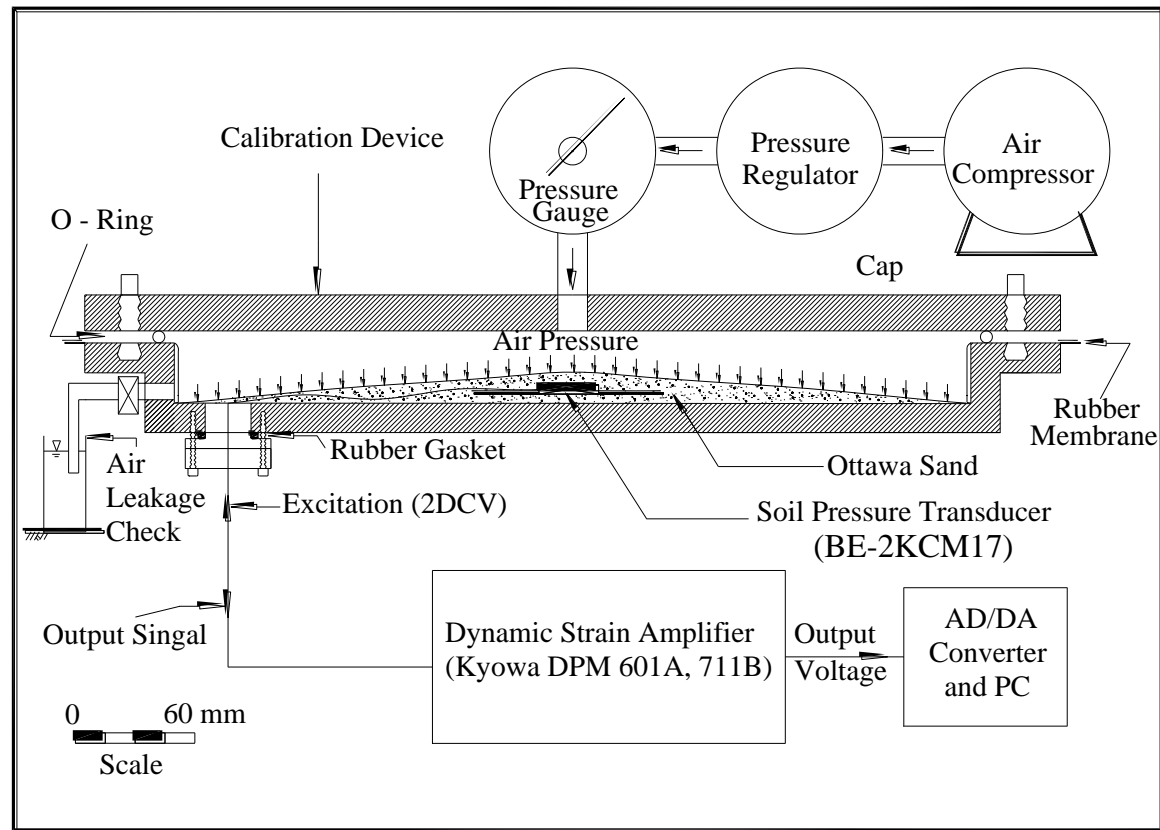


Fig. A2. Schematic diagram of in-soil soil pressure transducer calibration system

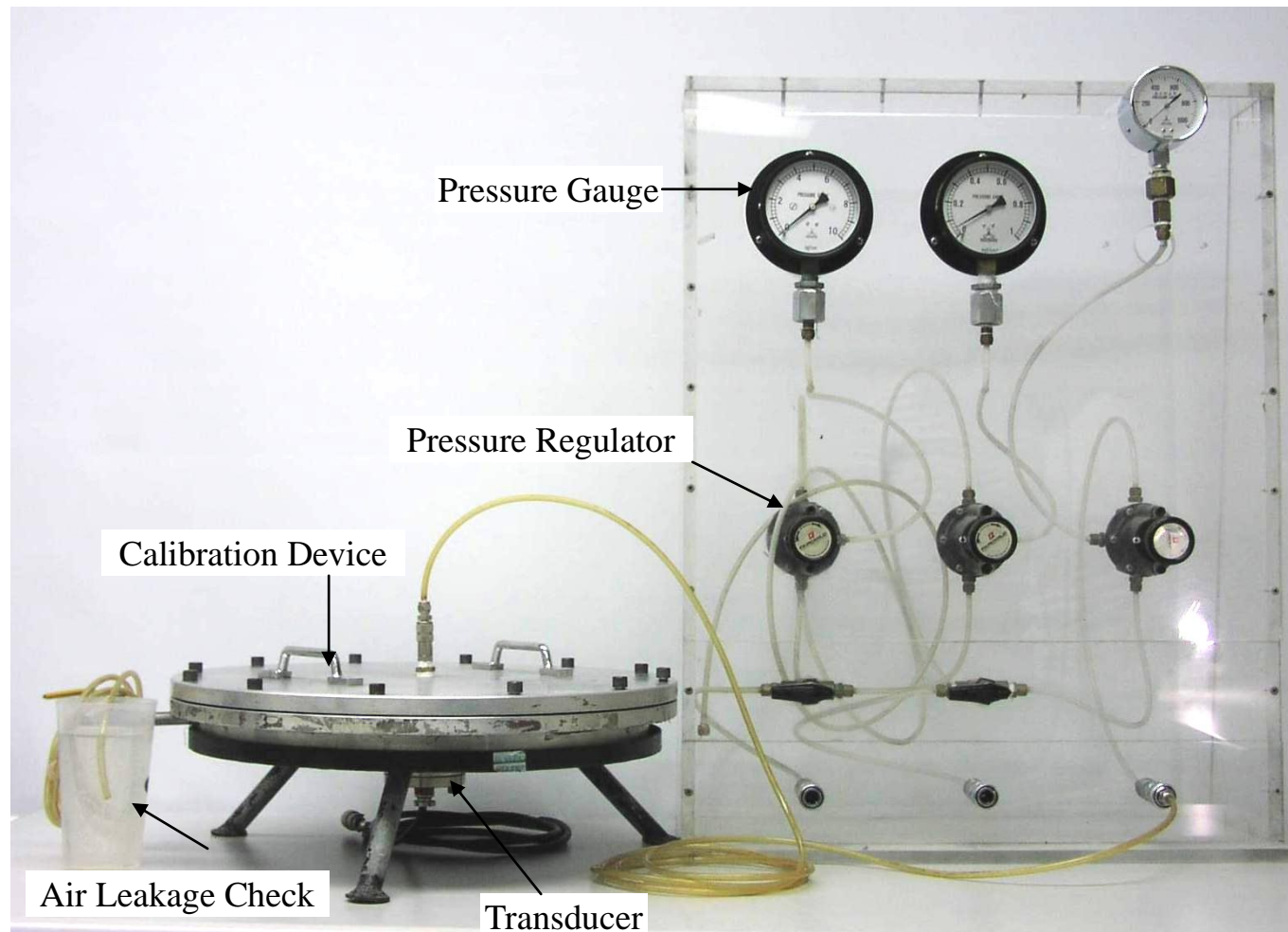


Fig. A3. Soil pressure transducer calibration system